

Cite this: *Energy Environ. Sci.*, 2025, 18, 5740

## Recent progress in underground hydrogen storage

Muhammad Ali,<sup>a</sup> Abubakar Isah,<sup>\*b</sup> Nurudeen Yekeen,<sup>\*c</sup> Aliakbar Hassanpouryouzband,<sup>d</sup> Mohammad Sarmadivaleh,<sup>e</sup> Esuru Rita Okoroafor,<sup>b</sup> Mohammed Al Kobaisi,<sup>f</sup> Mohamed Mahmoud,<sup>g</sup> Volker Vahrenkamp<sup>a</sup> and Hussein Hoteit<sup>a</sup>

With the global population anticipated to reach 9.9 billion by 2050 and rapid industrialization and economic growth, global energy demand is projected to increase by nearly 50%. Fossil fuels meet 80% of this demand, resulting in considerable greenhouse gas emissions and environmental challenges. Hydrogen (H<sub>2</sub>) offers a promising alternative due to its potential for clean combustion and integration into renewable energy systems. Underground H<sub>2</sub> storage (UHS) enables long-term, large-scale storage to achieve equilibrium between seasonal supply and demand. This review synthesizes recent advancements in UHS, highlighting progress and persistent challenges. The review explores the complex mechanisms of H<sub>2</sub> trapping and its implications for storage security and efficiency. The challenges these mechanisms present compared to other gases are discussed, emphasizing the unique properties of H<sub>2</sub>. The exploration covers interactions between H<sub>2</sub> and geological formations, focusing on the wettability, interfacial tension, and sorption characteristics of rock–H<sub>2</sub>–brine systems. Advanced experimental methods are evaluated alongside the effects of critical parameters, including temperature, pressure, salinity, and organic contaminants. Findings from innovative imaging, core-flooding techniques, and computational methods (e.g., molecular dynamics simulations and machine learning) are incorporated. These approaches are vital for understanding H<sub>2</sub> behavior in subsurface environments and developing robust, efficient storage solutions. This review offers a comprehensive update on recent progress, identifying and addressing the remaining gaps in UHS research. This work also highlights the significance of interdisciplinary research and technological innovation in overcoming these challenges. By providing insight into recent theoretical research, practical applications, and technological development, the findings support the successful incorporation of H<sub>2</sub> into the global energy infrastructure, contributing to implementing a sustainable H<sub>2</sub> economy successfully and fostering energy security and environmental protection for future generations.

Received 4th October 2024,  
Accepted 31st March 2025

DOI: 10.1039/d4ee04564e

rsc.li/ees

### Broader context

The global population is projected to reach 9.9 billion by 2050, driving a nearly 50% rise in energy demand. Fossil fuels currently supply around 80% of global energy, but their environmental impact necessitates cleaner alternatives. Hydrogen (H<sub>2</sub>) is a promising energy source due to its clean combustion and compatibility with renewable systems. A crucial aspect of H<sub>2</sub>'s role in the energy transition is its large-scale underground storage (UHS), which helps balance seasonal supply and demand fluctuations. UHS is a viable method for long-term H<sub>2</sub> storage, but its implementation presents scientific and technical challenges. H<sub>2</sub>'s interactions with geological formations, particularly in rock–H<sub>2</sub>–brine systems, involve factors such as wettability, interfacial tension, and sorption, which must be thoroughly understood for secure storage. Advanced experimental and computational techniques, including molecular dynamics simulations, machine learning, and core-flooding experiments, have provided deeper insights into H<sub>2</sub> behavior under varying subsurface conditions. Despite progress, further interdisciplinary research is needed to optimize UHS. Advancing this technology will enhance H<sub>2</sub>'s integration into global energy systems, supporting the transition from fossil fuels while ensuring energy security and environmental sustainability for future generations.

<sup>a</sup> Physical Science and Engineering Division, King Abdullah University of Science and Technology (KAUST), Thuwal, 23955, Saudi Arabia.  
E-mail: Muhammad.ali.2@kaust.edu.sa

<sup>b</sup> Harold Vance Department of Petroleum Engineering, Texas A&M University, College Station, TX 77843, USA. E-mail: abubakar.isah@tamu.edu

<sup>c</sup> School of Engineering, Edith Cowan University, Joondalup 6027, WA, Australia. E-mail: N.Yekeen@ecu.edu.au

<sup>d</sup> Grant Institute, School of Geosciences, University of Edinburgh, West Main Road, Edinburgh EH9 3FE, UK

<sup>e</sup> Western Australia School of Mines, Minerals, Energy and Chemical Engineering, Curtin University, 26 Dick Perry Avenue, Kensington, 6151, WA, Australia

<sup>f</sup> Department of Chemical and Petroleum Engineering, Khalifa University of Science and Technology, Abu Dhabi 127788, United Arab Emirates

<sup>g</sup> College of Petroleum Engineering and Geosciences, King Fahd University of Petroleum and Minerals, 31261, Dhahran, Saudi Arabia



## 1. Introduction

The global population is projected to increase to 9.9 billion by 2050 from 7.8 billion in 2020, representing an over 25% increase from today.<sup>1–5</sup> The expanding world population, rapid industrialization, and swiftly growing global economy are anticipated to cause a nearly 50% increase in the worldwide demand for energy within the next 30 years.<sup>2,6</sup> Carbon-based fuel is the world's principal energy source, contributing almost 80% of global energy requirements.<sup>7,8</sup> However, burning fossil fuels releases significant quantities of greenhouse gases and carbon into the air, trapping heat, causing environmental

pollution, depleting the ozone layer, and causing global warming.<sup>9–11</sup>

Recent statistics have indicated that anthropogenic carbon dioxide (CO<sub>2</sub>) emissions have outpaced nature's CO<sub>2</sub> recycling capacity from burning nonrenewable fossil fuels (e.g., coal, gas, and oil), and hydrocarbon production from new oil and gas wells could be noncompliant with the 1.5 °C global temperature target.<sup>12,13</sup> Almost 36.8 billion tons of CO<sub>2</sub> were emitted globally in 2020. The global CO<sub>2</sub> emissions increased considerably by 32% between 1750 and 2020 (from 280 to 410 ppm),<sup>14,15</sup> attaining a new record high of 37.4 Gt (billion tonnes) in 2023. An estimated 67% of the worldwide fossil-fuel-proven conventional and unconventional reserves should be undeveloped by 2050 to curtail a more than 2 °C rise in global temperature.<sup>8</sup>

However, these energy sources are erratic<sup>16</sup> and significantly influenced by seasonally changing atmospheric occurrences, such as wind strength, site meteorology, and sunlight.<sup>17–21</sup> The fluctuations in renewable energy sources usually result in interim inequalities (imbalance) between demand and supply.<sup>15,21,22</sup>

In the last few decades, global efforts have targeted CO<sub>2</sub> capturing and sequestration, carbon fuel replacement with hydrogen (H<sub>2</sub>), and the implementation of an H<sub>2</sub> economy as a more realistic and sustainable option for achieving a CO<sub>2</sub>-free economy and offsetting the mismatch between energy supply and demand.<sup>10,12,15,17,23</sup> Fig. 1 illustrates H<sub>2</sub> generation relevant to global energy demands and geological storage, aiming for net zero emissions. An example of such international efforts is the European Union's member nations' "2020 Climate & Energy Package".<sup>24,25</sup>

Hydrogen (H<sub>2</sub>) is anticipated to play a significant part in actualizing the objectives regarding global warming and climate change and restricting global warming to a value lower than 2 °C.<sup>4,15,26,27</sup> Unlike fossil fuel combustion characterized by the release of CO<sub>2</sub>, H<sub>2</sub> combustion cleanly emits water vapor into the atmosphere.<sup>28–34</sup>



**Muhammad Ali**

*Muhammad Ali holds a BE in petroleum and natural gas engineering from Mehran University of Engineering and Technology, Pakistan (2009). He worked as a research engineer at King Fahd University of Petroleum and Minerals, Saudi Arabia (2010–2016) and as a technical support engineer at Edith Cowan University, Australia (2018–2020). He earned an MPhil (2018) and PhD (2021) in petroleum engineering from Curtin University, Australia. Since August 2021, he has been a research scientist at King Abdullah University of Science and Technology, Saudi Arabia, focusing on carbon dioxide and hydrogen geo-storage, enhanced oil recovery, nano-energy, drilling fluid rheology, and reservoir characterization.*

*Muhammad Ali holds a BE in petroleum and natural gas engineering from Mehran University of Engineering and Technology, Pakistan (2009). He worked as a research engineer at King Fahd University of Petroleum and Minerals, Saudi Arabia (2010–2016) and as a technical support engineer at Edith Cowan University, Australia (2018–2020). He earned an MPhil (2018) and PhD (2021) in petroleum engineering from Curtin University, Australia. Since August 2021, he has been a research scientist at King Abdullah University of Science and Technology, Saudi Arabia, focusing on carbon dioxide and hydrogen geo-storage, enhanced oil recovery, nano-energy, drilling fluid rheology, and reservoir characterization.*



**Abubakar Isah**

*Abubakar Isah holds a BE in petroleum engineering from Abubakar Tafawa Balewa University, Nigeria (2014), and an MSc (2020) and PhD (2024) in petroleum engineering from King Fahd University of Petroleum and Minerals. He specializes in fluid-rock interactions for CCUS, hydrogen storage/generation, and EOR applications. He is a postdoctoral researcher at Texas A&M University. His expertise includes subsurface fluid-brine-rock interactions, experimental petrophysics, high-pressure, high-temperature core flooding, and geochemical analyses of reaction effluents. He has extensive experience using commercial and in-house-designed reactors to study rock-fluid interactions in porous media.*

*Abubakar Isah holds a BE in petroleum engineering from Abubakar Tafawa Balewa University, Nigeria (2014), and an MSc (2020) and PhD (2024) in petroleum engineering from King Fahd University of Petroleum and Minerals. He specializes in fluid-rock interactions for CCUS, hydrogen storage/generation, and EOR applications. He is a postdoctoral researcher at Texas A&M University. His expertise includes subsurface fluid-brine-rock interactions, experimental petrophysics, high-pressure, high-temperature core flooding, and geochemical analyses of reaction effluents. He has extensive experience using commercial and in-house-designed reactors to study rock-fluid interactions in porous media.*



**Nurudeen Yekeen**

*Nurudeen Yekeen earned a BSc in chemical engineering from the Federal University of Technology Owerri, Nigeria (2007), an MSc in petroleum engineering from the University of Ibadan, Nigeria (2012), and a PhD in petroleum engineering from the Universiti Teknologi Malaysia (2017), receiving the Best Postgraduate Student award. He was a postdoctoral researcher at Universiti Teknologi PETRONAS (2018–2020), then an assistant professor at UCSI University (2020–2022) and a senior lecturer at Universiti Teknologi PETRONAS (2022–2023). He is currently affiliated with Edith Cowan University in Australia. His research focuses on carbon dioxide and hydrogen geo-storage, enhanced oil recovery, nanotechnology, and unconventional energy resources.*

*Nurudeen Yekeen earned a BSc in chemical engineering from the Federal University of Technology Owerri, Nigeria (2007), an MSc in petroleum engineering from the University of Ibadan, Nigeria (2012), and a PhD in petroleum engineering from the Universiti Teknologi Malaysia (2017), receiving the Best Postgraduate Student award. He was a postdoctoral researcher at Universiti Teknologi PETRONAS (2018–2020), then an assistant professor at UCSI University (2020–2022) and a senior lecturer at Universiti Teknologi PETRONAS (2022–2023). He is currently affiliated with Edith Cowan University in Australia. His research focuses on carbon dioxide and hydrogen geo-storage, enhanced oil recovery, nanotechnology, and unconventional energy resources.*



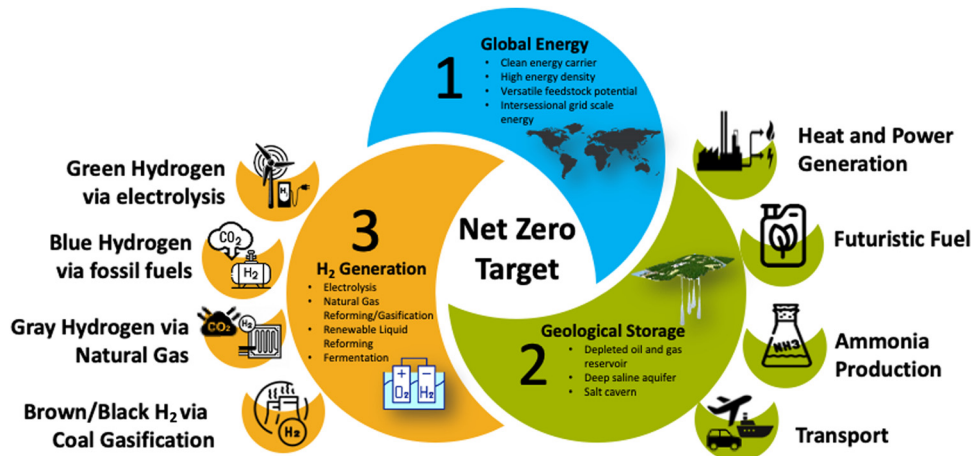


**Fig. 1** Integrated framework for hydrogen ( $H_2$ ) generation, geological storage, and global energy needs to achieve net zero emissions. Critical components of the  $H_2$  economy include (1) global energy, highlighting  $H_2$  as a clean energy carrier with high energy density, versatile feedstock potential, and suitability for interseasonal grid-scale energy storage; (2) geological storage, detailing storage methods in depleted hydrocarbon reservoirs, deep saline aquifers, and salt caverns; and (3)  $H_2$  generation, outlining production methods, including electrolysis, natural gas reforming/gasification, renewable liquid reforming, and fermentation. This integrated approach underscores the importance of  $H_2$  in sustaining global energy demands.

Despite the opportunities of attaining decarbonization goals and a carbon-free worldwide economy offered by successfully implementing an  $H_2$  economy, the research frontiers on the  $H_2$  economy have yet to be fully extended to real-world applications due to insufficient information on the conditions

and parameters governing the industrial-scale storage and withdrawal of  $H_2$ . Renewable energy in the  $H_2$  economy encompasses production, utilization, underground storage, and retrieval processes, as depicted in Fig. 2. Large-scale UHS is affected by rock-wetting phenomena, sealing integrity, other gases

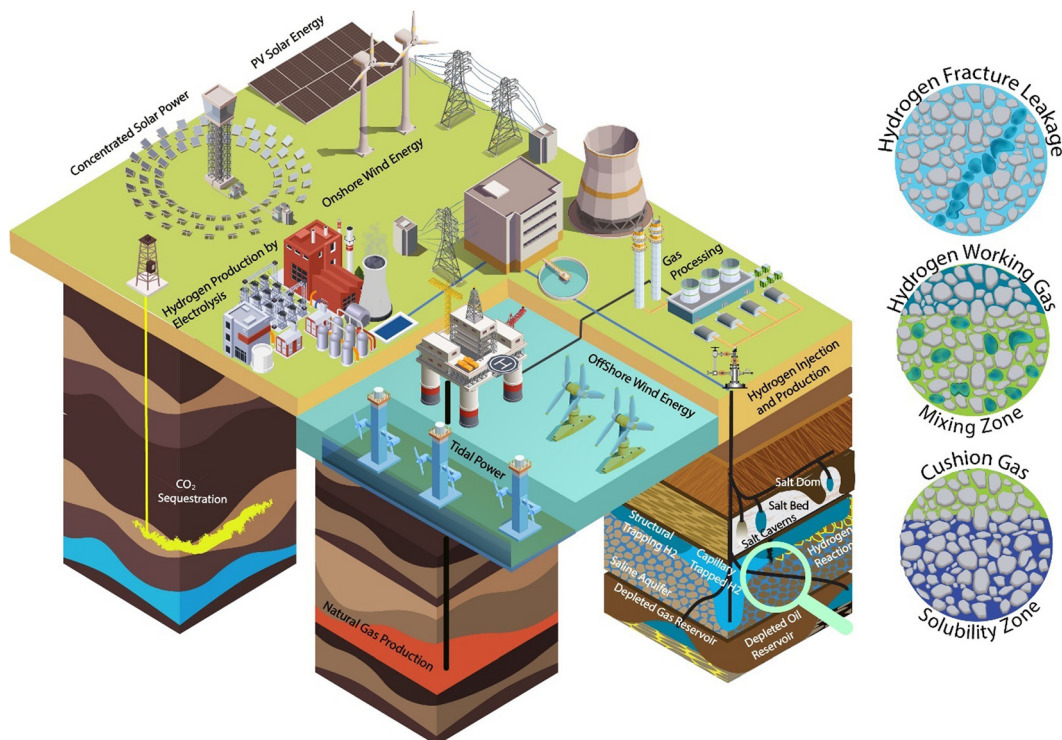


**Fig. 2** Renewable energy and hydrogen ( $H_2$ ) economy: production, underground  $H_2$  storage (UHS), and withdrawal processes. Integrated renewable energy sources (concentrated solar power, photovoltaic solar energy, onshore and offshore wind energy, and tidal power) with  $H_2$  production via electrolysis and gas processing, highlighting the significance of UHS in geological formations (e.g., salt caverns, depleted hydrocarbon reservoirs, and saline aquifers). Inset:  $H_2$  storage mechanisms, including cushion gas, mixing zones,  $H_2$  working gas, and fracture leakage. This comprehensive approach underscores the potential of  $H_2$  as a critical component in achieving a sustainable and balanced energy system.



(cushion gas), microbial actions, and geochemical reactions. These factors are critical because they determine the interaction between H<sub>2</sub>, rock matrices, organics, and brines in geological formations.<sup>28,31,33,35–37</sup> Understanding these interactions is essential for effective and efficient H<sub>2</sub> storage because they affect the storage capacity, retention, and retrievability of H<sub>2</sub>.

Although considerable literature exists on the subsurface storage of CO<sub>2</sub> and natural gas, providing a well-established understanding of their storage and withdrawal processes, UHS is relatively new and has not been reported as extensively. Research on CO<sub>2</sub> storage has provided insight into geological sequestration and reactions between CO<sub>2</sub>, rock, and brine. In contrast, natural gas storage studies have focused on maximizing retrieval efficiency and managing pressure and flow rates.<sup>38–44</sup> In contrast, the characteristics of H<sub>2</sub>, such as its low density and high diffusivity, pose unique challenges that are being explored. Due to its low density, H<sub>2</sub> can accumulate at the top of the formation, raising the formation pressure.<sup>45</sup> Hydrogen interactions with rock formations can significantly differ from those of CO<sub>2</sub> and natural gas,<sup>37,46–50</sup> necessitating detailed reports to understand its behavior in subsurface conditions.

Several literature reviews have been presented that document aspects of H<sub>2</sub> storage, including storage sites, methods, prospects and challenges, storage mechanisms, and characteristics.<sup>44,51</sup> The work is a state-of-the-art literature review on H<sub>2</sub> storage technology and areas that require further research and development.

Despite the numerous existing reviews on H<sub>2</sub> storage in subsurface environments, no comprehensive review has addressed H<sub>2</sub> interfacial properties under geological conditions, analyzed data discrepancies, or discussed the effects of cushion gas on rock/H<sub>2</sub>/brine interactions relevant to UHS and retrieval processes. This review addresses this gap by examining the H<sub>2</sub> economy, experimental methods, and realities of H<sub>2</sub> storage in actual subsurface settings involving pressures, temperatures, diverse brine compositions, and organic-acid molecules in storage and caprock formations. Furthermore, this review critically compares published data on rock/H<sub>2</sub>/brine wettability and interfacial tension (IFT) across reservoir and caprock mineralogy types, including calcite, quartz, shale, mica, and clay minerals. The primary objective is to consolidate knowledge gaps and inconsistencies related to rock/H<sub>2</sub> wettability, H<sub>2</sub> biogeochemical reactivity with minerals, and its behavior under various temperature and pressure conditions. The review explores potential factors contributing to the reported disparities in the data in the existing literature.

Addressing these gaps in knowledge *via* an extensive review is crucial for overcoming challenges associated with large-scale H<sub>2</sub> storage. This approach enables the development of reliable, efficient, and safe UHS systems. Therefore, this review provides valuable insight into the characteristics, feasibility, containment security, and retrieval of H<sub>2</sub> in geological formations.

## 2. Background

Research results have revealed that vast quantities of H<sub>2</sub> could be stored in geo-storage formations at a reasonable cost, sufficient to achieve a balance between seasonal demand and supply.<sup>17,28,33,52</sup> Researchers aim to infer the economic, social, legal, technological, and geological implications of industrial-scale UHS from the knowledge of other gases, particularly stored CO<sub>2</sub> and methane (CH<sub>4</sub>).<sup>53</sup> This section extensively discusses the H<sub>2</sub> economy with H<sub>2</sub> as an alternative energy carrier, its thermodynamic properties, and UHS, including storage media and trapping mechanisms of H<sub>2</sub> in geological storage media. In addition, parameters influencing rock-wetting phenomena in the presence of H<sub>2</sub> and rock–fluid interfacial interactions are also discussed in this context.

### 2.1. Hydrogen economy

The “hydrogen economy” concept envisions using H<sub>2</sub> as a low-carbon fuel source. The concept anticipates a significant role for H<sub>2</sub> in reducing dependence on fossil fuels, mitigating greenhouse gas emissions, and addressing energy security problems. It involves several facets of the H<sub>2</sub> value chain, including H<sub>2</sub> production, transportation, storage, withdrawal, and usage as a significant fuel for industrial and commercial purposes.<sup>52,54–57</sup>

The primary components of the H<sub>2</sub> economy include H<sub>2</sub> production, involving several pathways. For example, steam CH<sub>4</sub> reforming, also called natural gas reforming or gray H<sub>2</sub>, produces most of the H<sub>2</sub> used today.<sup>58–69</sup> Fig. 3 presents an overview of the critical components of the H<sub>2</sub> economy and production.

Coal gasification is another critical pathway for producing H<sub>2</sub>. This process converts coal into synthetic gas (syngas), primarily comprising H<sub>2</sub>, carbon monoxide (CO), and CO<sub>2</sub>. Hydrogen from coal gasification is called black or brown H<sub>2</sub> if bituminous or brown coal (lignite), respectively, is used.<sup>70–72</sup>

Biomass gasification is similar to coal gasification, but the feedstock comprises organic materials.<sup>71,73</sup> More information on producing H<sub>2</sub> from biomass is presented elsewhere.<sup>74–84</sup> Electrolysis involves using electricity (preferably from renewable sources) to split water into oxygen (O<sub>2</sub>) and H<sub>2</sub>. “Green hydrogen” can be produced from the conversion of surplus renewable energy to H<sub>2</sub> *via* electrolysis and stored at the subsurface to be withdrawn and used when critical energy demand occurs. Hydrogen could also be produced from water *via* renewable resources, such as solar and wind,<sup>52,54–57</sup> and recently, from rocks.<sup>85–87</sup> The levelized cost of H<sub>2</sub> (LCOH) from various sources is presented in Fig. 4(a). The LCOH from fossil fuel sources is low, whereas H<sub>2</sub> from renewable energy results in a high LCOH.<sup>58</sup>

The produced H<sub>2</sub> is stored as a gas under high pressure and as a liquid at very low temperatures or in metal hydrides and other chemical compounds. Each method has its advantages, discharge power, and discharge duration. More considerable pressures and capacities are required for large-scale H<sub>2</sub> storage. These conditions are offered by geological storage, such as salt



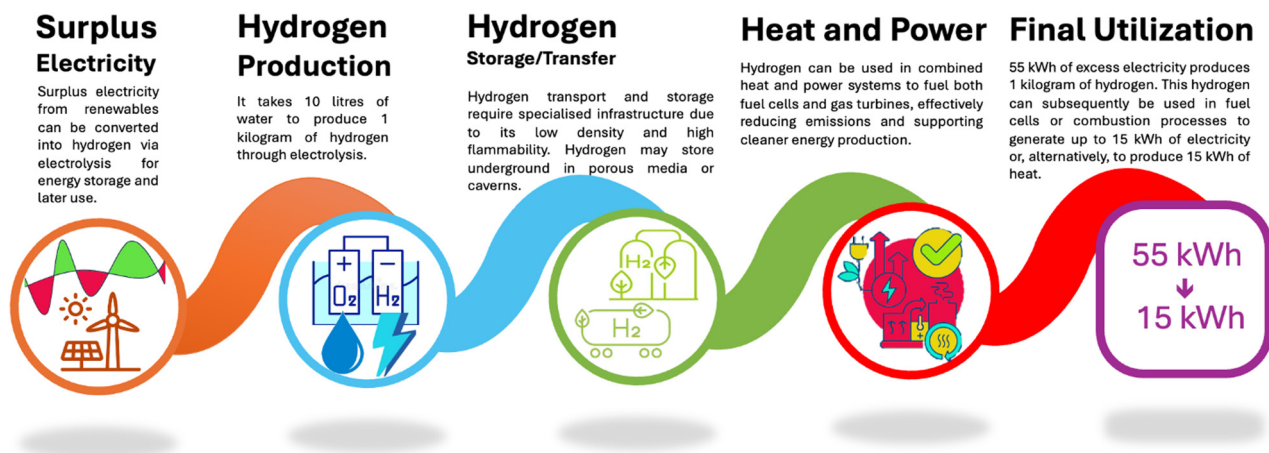


Fig. 3 Overview of critical components in hydrogen ( $H_2$ ) production and the stages of the  $H_2$  economy. The first stage represents the variability of renewable energy sources (e.g., wind and solar), generating electricity to produce  $H_2$  via electrolysis. In the second stage,  $H_2$  is stored and transported in high-pressure containers or pipelines. The third stage integrates  $H_2$  into industrial and energy systems for applications (e.g., fuel cells, heating, and power generation). The final stage highlights the efficiency challenge, where the energy loss across the  $H_2$  value chain results in a net reduction from the initial energy input (e.g., 55 kWh) to the usable energy output (e.g., 15 kWh).

caverns, depleted oil and gas fields, saline aquifers, and abandoned mine shafts, as illustrated in Fig. 4(b). Geological storage in porous media is ubiquitous, has a higher capacity, and has a longer discharge duration.<sup>29,89–91</sup>

The  $H_2$  economy offers environmental benefits, such as zero emissions from  $H_2$  combustion, reduced greenhouse gases, and energy security, as excess renewable energy can be converted to  $H_2$  via electrolyzers, in which electricity splits water into  $O_2$  and  $H_2$  via electrolysis, balancing the supply and demand and enhancing grid stability. In addition,  $H_2$  can be employed across sectors, including transportation, industry, and power generation, making it a versatile fuel source.

Enabling the  $H_2$  economy faces challenges, such as high  $H_2$  production costs, because green  $H_2$  or blue  $H_2$  is more expensive than  $H_2$  from traditional fossil fuels. The infrastructure for  $H_2$  production, storage, distribution, and refueling stations must be developed. The processes involved in producing, storing, and converting  $H_2$  can be less efficient than the direct use of electricity from renewable sources, and the low volumetric mass density of  $H_2$  necessitates consideration for transport and storage. The volumetric energy density of  $H_2$  suggests that much space is needed to store gaseous  $H_2$ , and this phenomenon is a major driver of the research on UHS.

## 2.2. Hydrogen thermodynamics

Hydrogen exists primarily in molecular form ( $H_2$ ) under standard conditions and exhibits unique thermodynamic properties due to its low molecular weight and high diffusivity in air and porous materials. Hydrogen thermodynamics encompasses  $H_2$  energy and phase behavior under varying temperature, pressure, and volume conditions. This field is crucial for  $H_2$  storage, fuel cells, and  $H_2$  production technology.<sup>92–96</sup> Moreover, this field is fundamental to understanding the role of  $H_2$  in energy systems, particularly its potential as a clean and efficient fuel.<sup>97,98</sup> The thermodynamic properties of  $H_2$  include its enthalpy, entropy, Gibbs free energy,

and heat capacity, which are crucial for designing and optimizing  $H_2$  storage, transportation, and utilization technology.<sup>89,95,99</sup>

One of the critical aspects of  $H_2$  thermodynamics is its phase behavior. Hydrogen exists primarily as para- or ortho- $H_2$ , with various spin configurations and energy states.<sup>92,98</sup> At standard conditions,  $H_2$  is a diatomic gas. Nonetheless,  $H_2$  can also exist as a liquid at very low temperatures (below 20 K) and as a solid under extremely high pressure, as depicted in Fig. 5(i). The transition between these phases involves significant energy changes characterized by specific enthalpies of fusion and entropy (vaporization). For instance, the enthalpy of vaporization is relevant for storing and transporting liquid  $H_2$ , requiring careful thermal management to minimize energy loss. Solid  $H_2$ , primarily metal hydrides, offers a high-density storage option but requires careful thermodynamic management to ensure efficient absorption and desorption processes.<sup>95,100</sup>

The physical properties of  $H_2$  are compared with those of  $CH_4$  and  $CO_2$  in Fig. 5(a–h). Hydrogen has a significantly lower molecular mass and density than other gases (see Fig. 5(a and b)), approximately  $0.089 \text{ kg m}^{-3}$  at standard normal conditions.<sup>41</sup> In addition,  $H_2$  has a high diffusivity and lower density than  $CO_2$  and  $CH_4$ , suggesting that it is more likely to migrate to the surface faster than  $CO_2$  and  $CH_4$ . Hence,  $H_2$  storage sites should be located at greater depths and sites with lower permeability than  $CO_2$  and  $CH_4$  to ensure adequate confinement by the caprock and prevent potential leakages out of the formation. Deeper reservoirs could also provide the temperature and pressure conditions required for maintaining the stability of the geo-storage formations.<sup>105</sup>

Due to its high diffusivity and low density,  $H_2$  can diffuse much more quickly through tiny fissures in the sealing layer compared to  $CO_2$  and  $CH_4$ ; hence, UHS sites should have very tight, thick, and impermeable caprock or sealing layers to prevent the upward migration and leakages of  $H_2$ , particularly in areas with fractures or fault lines. Methane and  $CO_2$  with



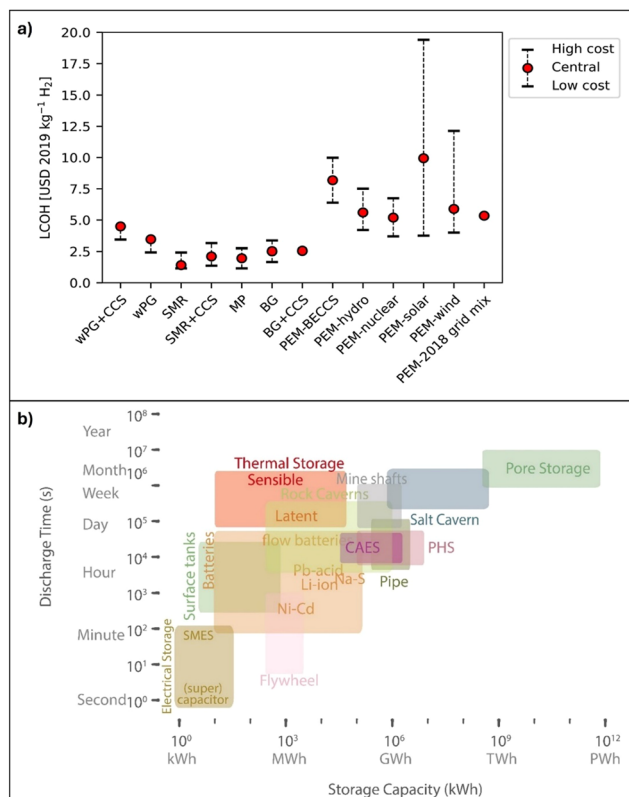


**Fig. 4** Levelized cost of hydrogen ( $H_2$ ) (LCOH) and comparison of energy storage methods by discharge time and storage capacity. These figures were extended and modified from ref. 58 and 88. (a) The LCOH for the alternative production routes is expressed in USD 2019 per kilogram of  $H_2$ . wPG, waste polymers gasification; CCS, carbon capture and storage; SMR, steam methane reforming; MP, methane pyrolysis; BG, biomass gasification; PEM, proton exchange membrane electrolysis; BECCS, electricity from bioenergy; HYDRO, hydropower; NUCLEAR, electricity from a nuclear power plant; SOLAR, electricity from photovoltaic cells; WIND, electricity from wind power; and GRID, electricity from the power grid. (b) Energy storage technology, highlighting the range of discharge times (from seconds to years) and storage capacities (from kilowatt-hours to petawatt-hours). The technology includes thermal storage (sensible and latent), batteries (e.g., Li-ion, Pb-acid, Ni-Cd, and Na-S), surface tanks, salt caverns, mine shafts, rock caverns, compressed air energy storage (CAES), pumped hydro storage (PHS), flywheels, pipes, supercapacitors, and superconducting magnetic energy storage (SMES). Each is represented by a colored block indicating its operational range, displaying the diversity and scalability of energy storage solutions.

higher density than  $H_2$  are more likely to remain in the lower parts of the formation or dissolve in the formation brine in high-pressure conditions. Special attention should be focused on secure, sufficiently deep reservoirs in  $H_2$  storage site selection.<sup>106</sup>

The operational strategies for  $H_2$  should involve careful pressure control mechanisms and management and more sophisticated and advanced leak detection systems to account for the high diffusivity of  $H_2$  and the tendency to migrate upward during UHS.<sup>89</sup> Pressure management is vital during  $H_2$  injection due to its low density, suggesting that  $H_2$  could demonstrate a high tendency to migrate upward more than  $CH_4$  and  $CO_2$ . Pressure maintenance or periodic reinjection of

$H_2$  must be practiced in a location with rapid pressure decline or where the caprock is not sufficiently impermeable to ensure long-term containment safety.<sup>107</sup>

The buoyancy of  $H_2$  could cause it to migrate easily if the pressure is not effectively controlled. Moreover,  $CH_4$  and  $CO_2$  are denser and have lower diffusivity than  $H_2$ , so they are not as buoyant and mobile as  $H_2$ . Hence, the operational strategies for their storage sites are less challenging regarding containment than  $H_2$ . However, careful management of  $CO_2$  storage sites is also required to prevent dissolution in brine, resulting in acidification and potential leakages.

The low density implies that  $H_2$  could display significantly different caprock and storage rock-wetting behavior than other gases, such as nitrogen ( $N_2$ ),  $CH_4$ , and  $CO_2$ . The literature suggests that  $H_2$  tends to wet the rock lower than  $CO_2$  and  $N_2$  at similar thermophysical conditions, which has been ascribed to its lower density than that of  $CO_2$  and  $N_2$ . For instance, at 15 MPa and 323 K, the density of  $H_2$  is approximately  $10 \text{ kg m}^{-3}$  compared to  $700 \text{ kg m}^{-3}$  for  $CO_2$ .<sup>35,108</sup> Studies on the interfacial properties of rock/ $H_2$ /brine systems have consistently demonstrated that the structural and residual trapping potential of storage and caprock is higher for  $H_2$  storage than  $CO_2$  and  $CH_4$  storage. Hence, the containment security of  $H_2$  is anticipated to be higher than that of  $CO_2$ ,  $CH_4$ , and  $N_2$  during geo-storage.<sup>108–111</sup>

Thermodynamic properties, such as the specific heat capacity, entropy, and Gibbs free energy, are essential in  $H_2$  applications. The high specific heat capacity of  $H_2$  gas makes it a practical energy source in many industrial processes. Entropy changes are critical to understanding the efficiency of  $H_2$ -based energy systems, such as water electrolysis for  $H_2$  production in fuel cells where  $H_2$  reacts with  $O_2$  to produce electricity and in underground storage applications to understand  $H_2$  diffusivity and reservoir containment. Gibbs free energy, a measure of thermodynamic potential, determines the feasibility and spontaneity of  $H_2$  reactions.<sup>92,112</sup> For instance, the Gibbs free energy change in subsurface storage could indicate the extent and feasibility of  $H_2$  regarding biogeochemical reactions.<sup>89,92–95,99,101,113</sup>

In  $H_2$  storage, thermodynamic principles guide the design of storage systems, and  $H_2$  can be stored as compressed gas or liquid. It can also be chemically bonded in hydrides or adsorbed on porous materials. Each storage method involves different thermodynamic considerations.<sup>6–8,94,112,114</sup> For example, adsorption-based storage relies on the interplay between temperature, pressure, and adsorption capacity, requiring precise control to maximize  $H_2$  uptake and release. Similarly,  $H_2$  storage in subsurface porous media involves wettability and interfacial property considerations of the  $H_2$ /rock/fluid systems, which must be optimized and managed to ensure efficient storage and retrieval.

The unique properties of  $H_2$  necessitate a comprehensive investigation of its wetting behavior, interfacial interactions, sorption characteristics, and biogeochemical reactions with rocks in the presence of fluids and under diverse physicochemical conditions. The knowledge of  $H_2$ -rock-fluid interactions is vital for optimizing  $H_2$  storage and ensuring the integrity and efficiency of the storage systems. Extensive understanding is



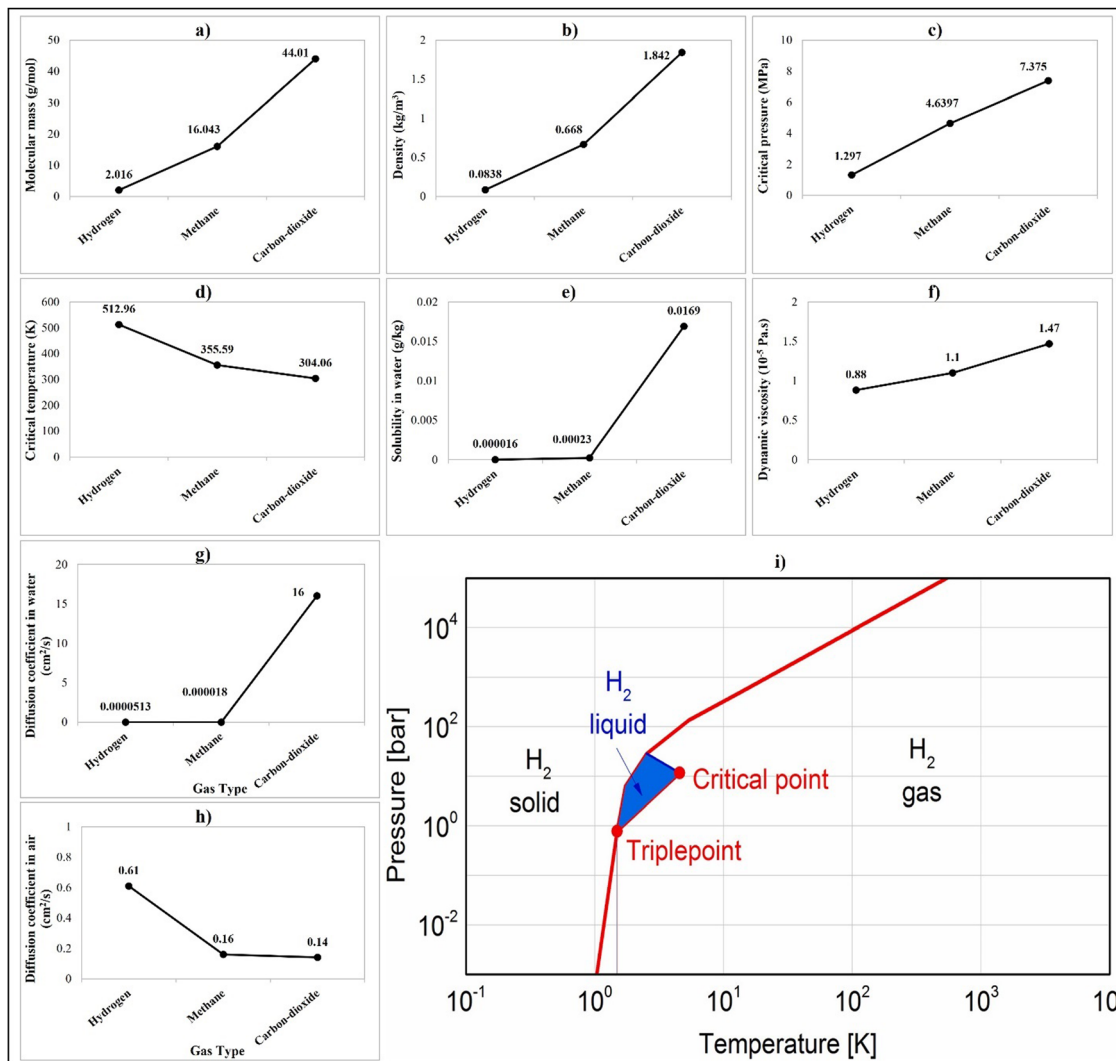


Fig. 5 Hydrogen (H<sub>2</sub>) phase diagram and comparison of physical properties of H<sub>2</sub> with methane (CH<sub>4</sub>) and carbon dioxide (CO<sub>2</sub>). This figure was modified from ref. 95 and 99, and data are from ref. 100–104. (a)–(h) Comparison of the molecular mass, density (293 K and 0.1 MPa), critical pressure, critical temperature, water solubility, dynamic viscosity (293 K and 0.1 MPa), diffusion coefficient in water, and diffusion coefficient in air for H<sub>2</sub>, CO<sub>2</sub>, and CH<sub>4</sub>. Understanding these physical properties is essential for predicting the thermodynamics and behavior of gas in a respective environment. (i) This figure illustrates how H<sub>2</sub> changes its physical state under temperature and pressure conditions.

required to evaluate how H<sub>2</sub> interacts with rock types, how it affects rock wettability, and how critical parameters (*e.g.*, pressure, temperature, and fluid composition) influence these interactions.

### 2.3. Uncertainties of underground hydrogen storage

Rock storage potential, H<sub>2</sub> containment safety, and H<sub>2</sub> injection capacity and rates of withdrawal are significantly influenced by the pore-scale behavior of H<sub>2</sub> in the storage rock and caprock pore network<sup>35,115,116</sup> at realistic downhole geo-storage conditions.<sup>18,21,95,101,117</sup> Fig. 6 summarizes the geological uncertainties that influence H<sub>2</sub> storage in porous media, revealing that the role of critical parameters, such as fluid–rock interaction, microbial activities, and trapping mechanisms, in ensuring successful large-scale UHS cannot be overemphasized. Hydrogen storage is crucial in the H<sub>2</sub> economy value chain.<sup>43</sup>

Thus, the inability to achieve large-scale H<sub>2</sub> storage could create a wide gap between the increasing energy demand and the climate change dilemma. The successful implementation of UHS depends on innovative research outcomes and field applications, which have been extensively discussed in prior reviews.<sup>16,118</sup>

### 2.4. Underground hydrogen storage media

Hydrogen storage capacity describes the capacity of a location or storage site to store H<sub>2</sub> at downhole conditions and for the H<sub>2</sub> to be effectively withdrawn during peak demand.<sup>119</sup> Geological storage of H<sub>2</sub> in depleted hydrocarbon reservoirs, salt caverns, deep aquifers, and subsurface coal seams on a large scale has been identified as the primary blueprint, a plan for achieving energy sustainability and ensuring a balance between energy demand and supply and attaining a zero-carbon energy economy.<sup>17,33</sup> This balance is also pertinent for successfully



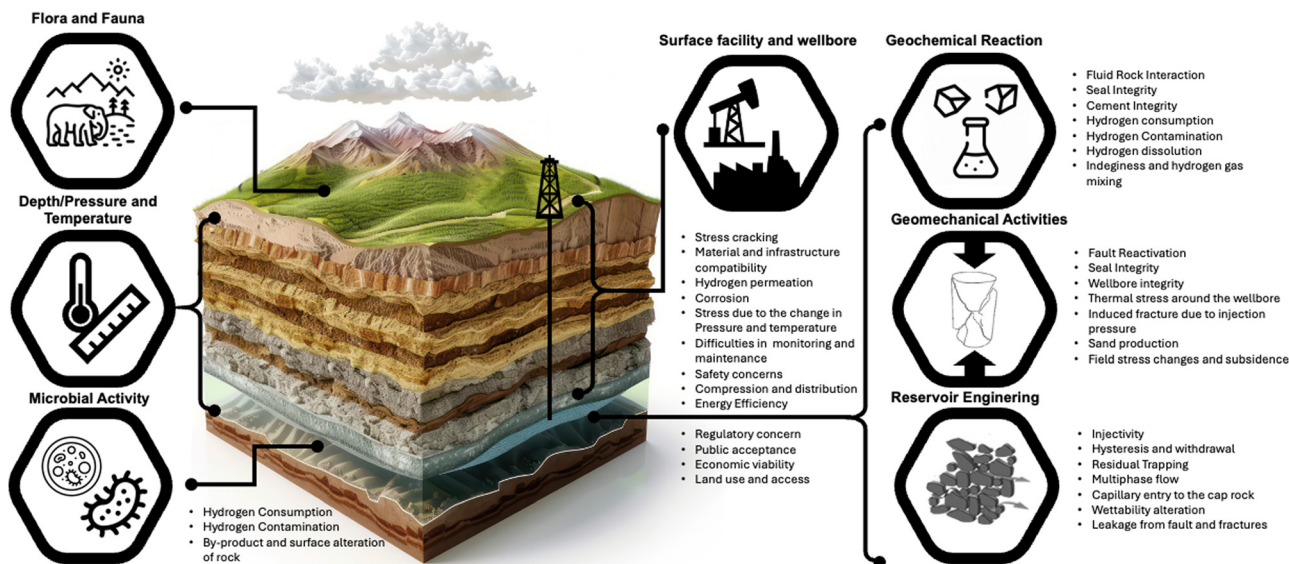


Fig. 6 Geological uncertainties of hydrogen ( $H_2$ ) storage in porous media. Factors influencing the feasibility and safety of underground  $H_2$  storage: the influence of depth, pressure, and temperature on storage integrity, microbial activity leading to  $H_2$  consumption and contamination, and geochemical reactions affecting rock–fluid interactions and seal integrity. Geomechanical activities include fault reactivation, wellbore integrity, and engineering considerations (e.g., injectivity, multiphase flow, and leakage risks). Surface facility and wellbore concerns include stress cracking,  $H_2$  permeation, safety protocols, and regulatory, economic, and public acceptance challenges. Understanding these uncertainties is critical for developing reliable and efficient  $H_2$  storage systems.

integrating and incorporating the  $H_2$  economy into renewable energy schemes.<sup>95,118,120</sup> The UHS time could span months or years, subject to the seasonal energy demand.

Salt caverns are promising UHS sites.<sup>42</sup> The highly saline environments of salt caverns could inhibit microbial consumption of  $H_2$ ,<sup>41</sup> maximizing retrieval. Iordache *et al.*<sup>121</sup> assessed the possibility of UHS in salt caverns in Romania. Simon *et al.*<sup>122</sup> studied the feasibility of large-scale UHS in Europe (Spain). Other storage sites have been investigated, such as depleted oil and gas reservoirs, deep aquifers, and coal beds. Depleted hydrocarbon reservoirs might be promising and more economical storage sites due to their established structure with a deep porous matrix, existing wells, known caprock integrity, and defined geological conditions compared to salt caverns.<sup>32,41</sup>

A comparison of underground  $H_2$  media (Table 1) suggests that the reaction between liquid hydrocarbons and  $H_2$  could restrict the pure storage of  $H_2$  in depleted oil and gas fields.<sup>95</sup> Successful pure  $H_2$  storage in depleted hydrocarbon fields, salt caverns, and deep aquifers is also limited by the inaccessibility of appropriate technology and equipment for constructing and operating a storage system.<sup>95</sup> Coal seams have also been suggested as promising storage sites for  $H_2$  due to their nanopore structure, enhancing their capacity to adsorb higher quantities of  $H_2$ .<sup>72,123</sup> Compared to conventional reservoirs,  $H_2$  gas could be stored as an adsorbed phase in coal seams, minimizing the possibility and rate of  $H_2$  leakages.<sup>72</sup>

Engineering and geological assessments of storage sites are critical and should be conducted to assess the feasibility of  $H_2$  leakages across UHS facilities and the caprock integrity. Successful UHS is only possible if the interaction/reactivity

between the injected  $H_2$ , host rocks, and formation brines is adequately understood. Other essential parameters for successful UHS include biotic  $H_2$  consumption because the injected  $H_2$  could be employed as an electron donor by acetogenic, methanogenic, and sulfate-reducing bacteria (SRB). However, the low solubility of  $H_2$  can prevent consumption at the liquid–gas interface, curtailing biotic consumption effects.<sup>41,124</sup>

The literature review regarding UHS facilities suggests that future studies should focus on biological, mineralogical, and chemical interactions or reactions between  $H_2$ , host-reservoir rocks, and formation fluids. Geomechanical stresses could result in significant leakage into aquifers during UHS. The microbial activity of methanogenic bacteria significantly influences large-scale UHS because these bacteria can use  $H_2$ , reduce  $CO_2$ , and produce  $CH_4$ . In abiotic reactions, corrosive and other reactive chemicals can be created. In microbial  $H_2$  consumption, the geochemical environment can be altered.<sup>18,115,124–127</sup> Moreover, abiotic reactions between storage or host rock minerals and the injected  $H_2$  can cause sulfate and carbonate minerals to dissolve into clay minerals and feldspar in the chlorite group.<sup>21</sup>

Abiotic processes can cause mineral precipitations that block permeability by blocking gas transport channels.<sup>21</sup> The literature review also revealed that the field feasibility of large-scale geological storage of pure  $H_2$  is rarely reported because of a limited understanding of the pore-scale behavior of  $H_2$  in the host rock and the dynamics of  $H_2$  in porous media. The economic assessment of the construction costs and UHS facilities management has primarily been based on what was learned from storing natural gas ( $CH_4$ ),  $CO_2$ , and crude oil. However, the behavior of  $H_2$  stored underground is more



Table 1 Comparison of underground hydrogen (H<sub>2</sub>) storage (UHS) in depleted hydrocarbon fields, salt caverns, and deep aquifers

Storage type	Global UHS involvement	H <sub>2</sub> storage capacity	Recognition/development	Construction and operation costs	Long-term leakage rates	Regional economic feasibility
Depleted hydrocarbon reservoirs	Widely used in regions with mature oil and gas industries  The US, Europe (e.g., the UK, Norway), the Middle East	Large-scale storage potential (hundreds of kilotons to megatons of H <sub>2</sub> )  Varies based on reservoir size and geological conditions	Significant research and development, especially in Europe (e.g., Norway) and North America (the US)  Some countries have early-stage demonstration projects (e.g., US Department of Energy's H <sub>2</sub> storage initiatives)	Initial costs can be high due to repurposing existing infrastructure  Ongoing operational costs are moderate, with maintenance and monitoring requirements	Leakage risks depend on reservoir seal integrity; lower than aquifers if well-maintained  Estimated leakage rates of about 0.1% to 1% per year	High feasibility in regions with existing oil and gas infrastructure (e.g., North America, Europe, Middle East).  Moderate feasibility in regions with limited oil/gas reserves  Economically viable in regions with existing hydrocarbon infrastructure but higher costs in regions without it
Salt caverns	Widely recognized and deployed for natural gas storage; H <sub>2</sub> storage is gaining attention globally  US (Texas), Germany, Canada, and emerging interest in Asia (China, Japan)	High storage density: individual caverns can store up to 10 000+ tons of H <sub>2</sub>  Suitable for regions with favorable salt geology but limited by cavern size and geology	Advanced in Europe (e.g., Germany) and North America (e.g., the US); emerging in Asia  Ongoing advancements in storage efficiency and H <sub>2</sub> compatibility	High capital costs for cavern construction; Operational costs are typically lower than aquifers or hydrocarbon reservoirs  High upfront costs but low operational and maintenance costs	Minimal leakage due to salt impermeability; leakage rates < 0.1% in well-maintained caverns  Long-term leakage rates are negligible when caverns are properly sealed and maintained	Most cost-effective in regions with salt formations (e.g., US Midwest, Northern Europe); feasible in areas with significant natural salt deposits  Feasible in regions with salt domes (e.g., the US, Northern Europe, and parts of China); less feasible in regions without salt deposits
Aquifers	Increasing global research and pilot projects  The US, Australia, Europe (e.g., Germany, Netherlands)	Substantial capacity (potentially millions of tons)  Vast storage potential in aquifers with suitable geology	Emerging recognition with pilot projects in Europe, Australia, and the US  Recognition is growing, with interest in multi-purpose storage solutions	Lower construction costs than salt caverns or depleted reservoirs but still significant  Lower operational costs once established; ongoing monitoring costs	Higher leakage risk than salt caverns and hydrocarbon reservoirs, depending on geological conditions  Leakage rates vary significantly, 0.5% to 5% per year, depending on aquifer integrity	Economically feasible in regions with large porous aquifers (e.g., the US, parts of Australia, and some European countries); less feasible in regions without suitable aquifers  Most economically feasible in areas with available aquifer geology and water resources (e.g., the US, Australia, and parts of Europe)

complex than that of CH<sub>4</sub>, crude oil, N<sub>2</sub>, and CO<sub>2</sub> because H<sub>2</sub> is highly reactive, volatile, and compressible, and it also weakens metals used in underground storage facilities.<sup>21,33,90</sup>

## 2.5. Trapping mechanisms of hydrogen in geo-storage media

Research on greenhouse gas storage in the Earth's subsurface and the H<sub>2</sub> economy to actualize a carbon-free global economy is gaining global prominence. Nevertheless, UHS is a relatively new technology that has yet to be convincingly demonstrated at an industrial scale. Hence, potential associated risks are still unclear. Hydrogen is buoyant, and the stored H<sub>2</sub> in the Earth's subsurface could leak into the atmosphere through natural or artificial channels at geo-storage conditions. Residual/capillary trapping in storage rocks, structural trapping by caprock, and adsorption trapping in coal bed CH<sub>4</sub> and clay surfaces are trapping mechanisms responsible for keeping the stored buoyant H<sub>2</sub> immobilized in storage formations. The literature on H<sub>2</sub> geo-storage increasingly emphasizes the importance of structural and residual trapping mechanisms for gas storage in geological formations.<sup>27,49,99,125,128–133</sup> Fig. 7 depicts caprock, the impermeable closing layer that stops buoyant gases, such as H<sub>2</sub>, CH<sub>4</sub>, and CO<sub>2</sub>, from moving upward, keeping the H<sub>2</sub> in the storage formation.<sup>38,109,134,135</sup>

When H<sub>2</sub> is injected into the formation, its upward migration is prevented by the reservoir structural seal, whose integrity is influenced by the buoyancy *versus* capillary pressure effects, which are a function of wettability, as indicated in eqn (1)–(4):

$$P_b = \Delta\rho gh \quad (1)$$

$$P_c = P_{\text{nwet}} - P_{\text{wet}} \quad (2)$$

$$P_c = \frac{2\gamma \cos \theta}{r} \quad (3)$$

$$h = \frac{2\gamma \cos \theta}{\Delta\rho gr} \quad (4)$$

where  $P_b$  denotes the buoyancy pressure,  $P_c$  is the capillary pressure,  $P_{\text{nwet}}$  represents the pressure of the nonwetting phase,  $P_{\text{wet}}$  represents the wetting phase pressure,  $\gamma$  denotes the IFT between water and H<sub>2</sub>,  $r$  signifies the largest pore throat radius, and  $\theta$  represents the contact angle measured in degrees in the denser phase.

During H<sub>2</sub> injection into the subsurface storage formation, it displaces fluids initially occupying the pores (wetting phase), influenced by the receding contact angle  $\theta_r$ . If  $\theta_r$  exceeds 90° in rock/H<sub>2</sub>/brine systems, capillary leakage can occur, resulting in reduced structural trapping efficiency because of high upward suction forces in the caprock. After the H<sub>2</sub> injection stops, the pores previously filled with the H<sub>2</sub> plume are reoccupied with formation brine, a process related to the advancing contact angle  $\theta_a$ . The primary drainage is unaffected by wettability if  $\theta_a$  is below 50°. This reinvasion is crucial in enhancing the containment security *via* residual trapping.<sup>136</sup>

**2.5.1. Structural and stratigraphic trapping.** The H<sub>2</sub> passages and leakages across caprock are prevented *via* structural trapping, which provides a geological seal that stops the permeation of the buoyant H<sub>2</sub> arising from high capillary pressure.<sup>134</sup> However, the stored H<sub>2</sub> tends to become mobile

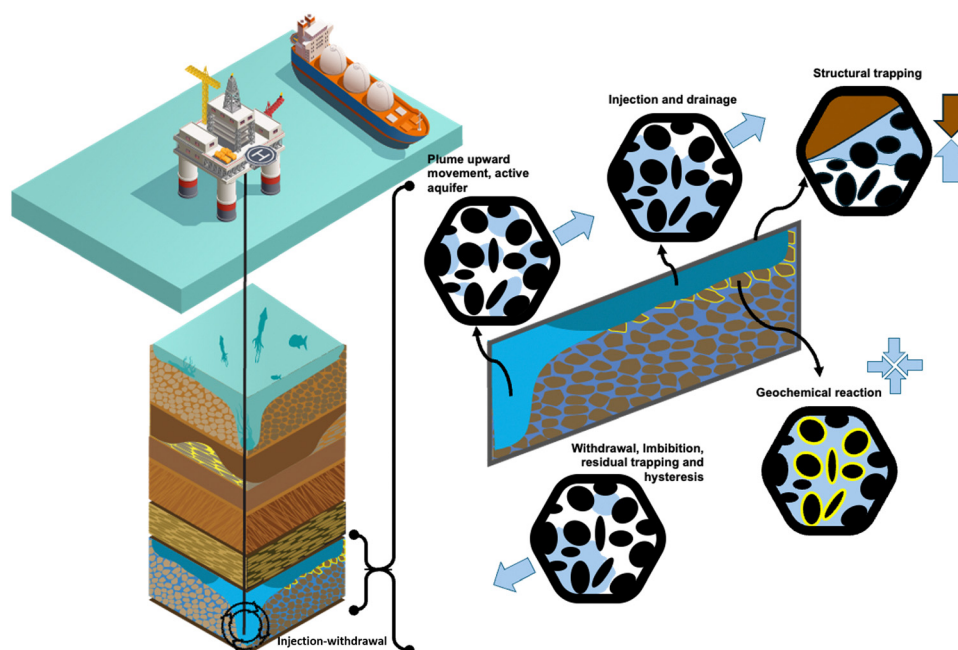


Fig. 7 Diagram of trapping mechanisms for underground hydrogen storage (UHS). Processes of H<sub>2</sub> injection, drainage, and trapping mechanisms in a geological formation, including structural trapping, where impermeable layers trap H<sub>2</sub>; geochemical reactions that alter the chemical composition of the storage environment; and the upward movement of H<sub>2</sub> plumes in active aquifers. Withdrawal, imbibition, residual trapping, and hysteresis are also depicted, which are critical for understanding H<sub>2</sub> retention and retrieval. These mechanisms are essential for optimizing the efficiency and security of UHS systems.



or movable when the force of buoyancy equals the capillary force or when the capillary force is less than the buoyancy force.

Without a structural trap, the H<sub>2</sub> plume could increase in the H<sub>2</sub>-water system when the rock becomes hydrophobic and more H<sub>2</sub>-wet. A higher H<sub>2</sub> column height suggests that the mobility of H<sub>2</sub> increases, increasing the H<sub>2</sub>-induced caprock pressure and reducing the containment safety of H<sub>2</sub>. The caprock integrity and stability of the overlying seal are essential parameters for the success of UHS.

Generally, caprock is assumed to be initially fully water-wet and hydraulically firm to prevent H<sub>2</sub> leakages. Previous studies have suggested that caprock provides a geological barrier to H<sub>2</sub> leakages if the threshold capillary pressure is not surpassed.<sup>20,137</sup> The buoyant H<sub>2</sub> cannot diffuse across caprock at a high capillary entry pressure.<sup>9,11,134</sup> However, caprock is not fully water-wet at the initial conditions in realistic geo-storage conditions, as presumed due to organic contamination.<sup>35,109,138</sup> At H<sub>2</sub>-wet conditions, the buoyancy forces overwhelm the oppositely acting capillary forces because the capillary entry is far lower than the buoyancy pressure, resulting in H<sub>2</sub> gas leakages and overpredictions of H<sub>2</sub> storage capacities. The buoyancy-capillary force balance relationship can be inferred from eqn (5):<sup>134,139</sup>

$$H = \frac{2\gamma \cos \theta}{rg\Delta\rho} \quad (5)$$

The variable  $H$  represents the H<sub>2</sub> column height, the height at which H<sub>2</sub> can be permanently stopped from migrating below the caprock,  $\theta$  represents the rock-brine-H<sub>2</sub> wettability,  $\gamma$  denotes the H<sub>2</sub>-brine IFT, and  $\Delta\rho$  is the gas density-water density difference ( $\rho_w - \rho_g$ ). Recently, Iglauer<sup>134,139</sup> assessed the optimum storage depth where the highest quantity of H<sub>2</sub> can be stored in geological formations, such as CO<sub>2</sub> storage. Iglauer<sup>134</sup> suggested that the maximum theoretical amount of H<sub>2</sub> can be stored at a depth of 1100 m. The H<sub>2</sub> column height ( $H$ ) drops uniformly with depth, reaching a value of zero at a depth of 3700 m. Long-term H<sub>2</sub> storage below this depth threshold is discouraged because the buoyant forces would exceed the capillary forces as the caprock wettability is modified from the water-wet to the H<sub>2</sub>-wet system.

Hydrogen withdrawal during UHS significantly relies on structural and stratigraphic trapping mechanisms to ensure secure containment and efficient recovery of the stored H<sub>2</sub>.<sup>9,11,134</sup> Structural trapping occurs when H<sub>2</sub> is confined by impermeable geological structures, such as anticlines, fault-bound traps, or salt domes, preventing upward migration. These structural features act as physical barriers, enabling the safe accumulation and retrieval of H<sub>2</sub> over time. Stratigraphic trapping involves variations in rock permeability and porosity, such as pinch-outs, unconformities, or lithological changes, creating natural traps in the storage reservoir. These mechanisms combine to retain H<sub>2</sub> in the storage formation and minimize leakage, ensuring a controlled withdrawal. Effective withdrawal during UHS depends on understanding these trapping dynamics and optimizing operational strategies to maximize recovery while maintaining reservoir integrity.

Iglauer<sup>134</sup> assessed the optimum geo-storage depths for structural UHS at 0.1 to 20 MPa, 300 to 360 K, a 30-k km<sup>-1</sup> geothermal gradient, and a 10-MPa km<sup>-1</sup> hydrostatic gradient.<sup>134</sup> Further research is required to assess the optimum storage depth where the maximum amount of H<sub>2</sub> can be stored and the threshold depth during UHS beyond the conditions assumed in this study.<sup>134</sup> Hydrogen structural trapping capacities of rock are typically deduced from the contact angle datasets of shale-brine-H<sub>2</sub>, mica-brine-H<sub>2</sub>, and clayey rock-brine-H<sub>2</sub> systems and relative permeabilities and capillary pressure measurements.

Al-Yaseri *et al.*<sup>110</sup> demonstrated that the wetting state of shale and clayey caprock remained strongly water-wet at H<sub>2</sub> geo-storage conditions. Studies have further revealed that the equilibrium contact angles of the shale-H<sub>2</sub>-brine system were lower than those of shale-CO<sub>2</sub>-brine and shale-N<sub>2</sub>-brine systems. Yekeen *et al.*<sup>140</sup> demonstrated that H<sub>2</sub>-clay IFTs were higher at geo-storage conditions than clay-N<sub>2</sub> and clay-CO<sub>2</sub> IFTs.<sup>140</sup> Compared to CO<sub>2</sub> and N<sub>2</sub> storage, these results imply that caprock tends to remain hydraulically tight, acting as a geological barrier to prevent H<sub>2</sub> escape during UHS.

However, these research studies were conducted without considering organic contamination in geo-storage formations. Moreover, the higher solubility, diffusivity, and chemical modifications by H<sub>2</sub> of the host rock due to the reaction between H<sub>2</sub> and caprock minerals were not considered. The extent of geochemical effects on caprock hydraulic integrity arising from H<sub>2</sub>-caprock mineral reactivity is recommended for future studies. The stored H<sub>2</sub> could dissolve in the formation brine and diffuse into the caprock or storage rock formation because of high H<sub>2</sub> diffusivity. The loss *via* diffusion could be higher at the commencement of the geo-storage processes and reduce with time as the formation brine becomes saturated with H<sub>2</sub>.<sup>21</sup>

**2.5.2. Residual/capillary trapping.** Capillary or residual trapping is a crucial mechanism in geological H<sub>2</sub> storage, where H<sub>2</sub> gas is immobilized in the pore spaces of rock formations. This process relies on the capillary forces due to the differences in wetting properties between the H<sub>2</sub> gas and the surrounding brine or residual hydrocarbon. When H<sub>2</sub> is injected into a geological formation, it displaces the brine and occupies the pore spaces. As the pressure is reduced or flow stops, capillary forces trap H<sub>2</sub> as disconnected, immobile gas bubbles in the pores. This trapping mechanism is crucial for preventing H<sub>2</sub> migration, enhancing storage security, and reducing leakage risk.<sup>141-143</sup>

The effectiveness of residual trapping depends on several factors, including the wettability of the rock surface, pore-size distribution, and IFT between H<sub>2</sub> and the brine. Rocks with hydrophilic surfaces and a wide range of pore sizes are typically more effective at trapping H<sub>2</sub> because they promote the formation of smaller, more stable gas bubbles.<sup>144-147</sup> The lower IFT between H<sub>2</sub> and brine can enhance capillary trapping by making it easier for the gas to be retained in the pore spaces. Understanding and optimizing these factors is vital in designing efficient and secure H<sub>2</sub> storage sites.

Residual trapping helps secure H<sub>2</sub> in the geological formation and aids in the long-term stability of the storage site



and the H<sub>2</sub> withdrawal process. By preventing the free movement of H<sub>2</sub>, residual trapping reduces the likelihood of gas migrating to the surface or other unintended zones, maximizing the retrievable H<sub>2</sub>. This approach is critical to ensure that H<sub>2</sub> storage is environmentally safe and economically viable. Moreover, strategic injection and withdrawal protocols<sup>145</sup> and selecting geological formations with favorable trapping properties can enhance residual trapping effectiveness. Residual trapping is a critical component of a successful H<sub>2</sub> storage strategy, providing reliability for containing and preserving H<sub>2</sub> in subsurface environments.

**2.5.3. Adsorption trapping.** Adsorption trapping is a crucial mechanism in geological H<sub>2</sub> storage, where H<sub>2</sub> molecules adhere to the surface of porous materials, such as rocks or minerals.<sup>148</sup> This process occurs at the microscopic level, where H<sub>2</sub> gas interacts with the solid surfaces in the storage formation. This interaction on these surfaces retains H<sub>2</sub> through chemical or physical adsorption. Physical adsorption (physisorption) involves weaker van der Waals forces, whereas chemical adsorption (chemisorption) involves stronger ionic or covalent bonds. Several factors influence the success of adsorption trapping. These factors include surface area, porosity, chemical composition of the geological media, and temperature and pressure conditions.<sup>72,149,150</sup>

The type of geological material in the storage formation can significantly influence the efficiency of adsorption trapping in H<sub>2</sub> storage. For instance, rock minerals with high surface areas and favorable adsorption sites, such as certain clay minerals and organic-rich shale types, tend to have a higher H<sub>2</sub> storage capacity.<sup>151,152</sup> Kerogen, an organic matter in sedimentary rock, can enhance adsorption due to its porous nature and large surface area.<sup>151–153</sup> Conversely, materials with a lower surface area or less favorable adsorption properties (*e.g.*, some types of sandstone or carbonate) may offer less effective trapping. Understanding the adsorption characteristics of geological materials is crucial for selecting optimal storage sites and maximizing storage efficiency.

In addition to rock properties, storage environment conditions are crucial in adsorption trapping. Higher pressure generally enhances the adsorption capacity by increasing the number of H<sub>2</sub> molecules that can be held on the surface. However, temperature effects are more complex. Lower temperatures can increase adsorption capacity by reducing the kinetic energy of H<sub>2</sub> molecules.<sup>149</sup> Extremely low temperatures might not be feasible for practical storage operations. Moreover, other gases, such as CO<sub>2</sub>, CH<sub>4</sub>, or N<sub>2</sub>, can influence adsorption dynamics. These gases can compete for adsorption sites or alter the surface properties, influencing the overall effectiveness of H<sub>2</sub> adsorption.<sup>151</sup>

Hydrogen withdrawal during UHS is influenced by adsorption trapping, where H<sub>2</sub> molecules adhere to the surface of porous reservoir rocks, such as shales, coals, or clay-rich formations.<sup>151,152</sup> This interaction can reduce the mobility of H<sub>2</sub>, affecting its recovery efficiency. During withdrawal, desorption must occur for the stored H<sub>2</sub> to be released into the gas phase. The extent of adsorption/desorption depends on the pressure, temperature, and mineral composition of the

reservoir. Proper reservoir selection and operational strategies are crucial in minimizing H<sub>2</sub> retention and maximizing withdrawal efficiency.

Generally, the residual, adsorption, and structural trapping potential of geo-storage rock is considerably affected by rock-wetting tendency behavior in contact with formation brines and the stored H<sub>2</sub>. The wetting phenomenon also depends on the pore heterogeneity and morphology. Therefore, careful management of these environmental factors is essential to optimize adsorption trapping and ensure the stability and efficiency of H<sub>2</sub> storage systems.

## 2.6. Methods for underground hydrogen storage assessment

The techniques to determine rock-wetting characteristics, rock-H<sub>2</sub> and H<sub>2</sub>-fluid interfacial interactions, sorption behavior, biogeochemical interactions, and the injectivity and retrieval of H<sub>2</sub> during UHS are analogous to those in studies of rock-CO<sub>2</sub>-brine systems. These methods typically involve measuring contact angles, IFTs, and capillary pressure and conducting core-flooding experiments to evaluate H<sub>2</sub> injectivity and withdrawal. Other techniques include advanced imaging techniques, such as nuclear magnetic resonance (NMR), microcomputed tomography (micro-CT), scanning electron microscopy (SEM), and the use of molecular dynamic (MD) simulations to assess how H<sub>2</sub> and fluids interact with rock surfaces under simulated subsurface conditions of pressure and temperature. Moreover, machine learning (ML) techniques have recently been used to predict wetting behavior and interfacial properties of rock and fluids.<sup>154,155</sup>

Hydrogen withdrawal during UHS depends on accurate assessment methods to evaluate the reservoir capacity, trapping mechanisms, and gas recovery efficiency.<sup>109,111</sup> Reservoir modeling, core analysis, and geophysical monitoring are crucial for predicting withdrawal performance and optimizing storage operations. The primary challenges arise from the distinct properties of H<sub>2</sub>. The low density, high diffusivity, and flammability of H<sub>2</sub> require stringent safety protocols during experimentation. The high volatility and potential for rapid diffusion of H<sub>2</sub> into rock pores and brine distinguish its behavior from that of other gases, such as CO<sub>2</sub>, CH<sub>4</sub>, and N<sub>2</sub>. Consequently, although the foundational evaluation techniques remain consistent, the assessment method must account for the unique interactions of H<sub>2</sub> with rock and brine, ensuring accurate assessments of wettability and the overall feasibility of H<sub>2</sub> storage and withdrawal in geological formations.

The methods employed to determine rock/H<sub>2</sub>/brine wettability could be qualitative (indirect) or quantitative (direct methods).<sup>156,157</sup> These methods provide data to assess the feasibility of H<sub>2</sub> storage in porous sedimentary rocks<sup>19,35,158,159</sup> and the sealing or trapping potential of caprocks (mica and shale were employed as representatives).<sup>109,111</sup> The possibility of H<sub>2</sub> storage in coal seam gas reservoirs *via* adsorption has also been investigated.<sup>72,123</sup>

The wettability of rock/H<sub>2</sub>/brine systems at geological storage conditions has been determined using qualitative and quantitative techniques in the literature. Yekta *et al.*<sup>19</sup> measured the



capillary pressure and relative permeability for a water/H<sub>2</sub> system to evaluate the viability of UHS in sandstone at representative shallow (293 K and 5.5 MPa) and deep (318 K and 10 MPa) geological storage conditions.

### 3. Rock wettability and interfacial interactions during underground hydrogen storage

Wettability is the tendency of a fluid to wet a solid surface in the presence of another fluid. It controls fluid distribution and saturation in rock pores, affecting the overall displacement of fluids in porous media.<sup>3,160–163</sup> In H<sub>2</sub> geo-storage, wettability is critical; it determines whether H<sub>2</sub> or other formation fluids, such as oil or gas (for UHS in depleted hydrocarbon reservoirs)<sup>164,165</sup> or brine (for UHS in aquifers),<sup>166</sup> contacts the

rock.<sup>89,167–170</sup> Wettability determines the H<sub>2</sub> distribution in geo-storage formations for UHS applications. Moreover, it affects the fluid-flow dynamics and H<sub>2</sub> withdrawal and injection rates.<sup>165,171</sup> Thus, wettability determines the rock storage potential and H<sub>2</sub> containment safety. Hence, a thorough investigation of wettability is necessary to estimate the storage and withdrawal potential and possibility of H<sub>2</sub> loss accurately.

Despite the increasing attention to large-scale UHS, the details of the pore-scale fluid distribution and flow properties of H<sub>2</sub> in porous media are not well known. Hydrogen storage capacities of subsurface formations are typically inferred from contact angle measurements.<sup>35,170,172,173</sup> Fig. 8 illustrates a detailed setup for studying rock/H<sub>2</sub>/brine wettability and interfacial tension. The figure schematically represents an underwater geological storage site, highlighting the magnified view of porous rock structures and measuring contact angles to understand the interactions between liquid, solid, and gas phases.

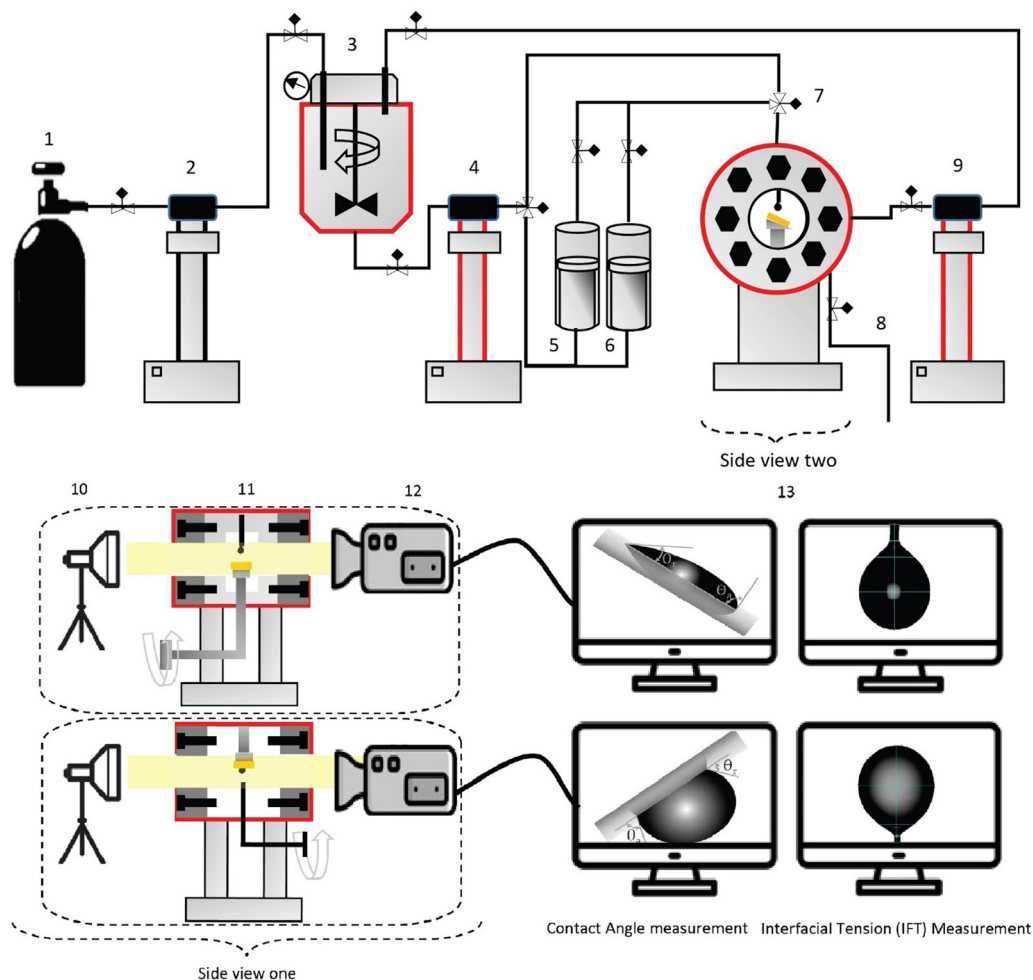


**Fig. 8** Schematic setup for studying rock wettability and interfacial tension (IFT) in geological storage systems. Detailed experimental configuration for investigating rock–fluid interactions under subsurface storage conditions and precise contact angle and IFT measurements. Apparatuses include a gas supply system (1) connected to pressure controllers (2, 4, 9) and a high-pressure mixing reactor (3) for acquiring equilibrium conditions between the rock and fluids. Additional fluid management is maintained via reservoirs (5, 6), ensuring stable conditions for testing. High-precision imaging components (10, 11, 12) capture the dynamics of the fluid–rock interactions, inputting real-time data into monitoring stations (13) to analyze the contact angle and IFT values. Further, a liquid droplet is regulated via a valve (7), and the gas exhaust is operated by a valve (8). This setup replicates subsurface pressures and temperatures, providing critical insight into fluid behavior in porous media for underground hydrogen storage applications.



The bottom section details the experimental apparatus, including a gas cylinder, valves, mixing chambers, humidification containers, and a pressure chamber. The figure also features an observation chamber with a sample holder, a camera for capturing contact angles and interfacial properties, and a computer for data analysis. This setup is designed to simulate subsurface conditions of pressure, temperature, and fluid composition, providing valuable insight into rock–fluid interactions essential for effective H<sub>2</sub> storage.

Rock–fluid interfacial interactions and the wetting behavior of the rock during UHS significantly influence the residual and structural trapping capacities of the storage and caprock. The relationship between the rock wettability and the interface between fluids and the host rock during UHS are expressed in eqn (6):

$$\theta = \arccos \frac{\gamma_{SG} - \gamma_{SL}}{\gamma_{LG}} \quad (6)$$

The rock–brine–H<sub>2</sub> contact angles ( $\theta$ ) were computed using Young's equation if the values of the liquid–solid ( $\gamma_{SL}$ ), gas–solid ( $\gamma_{SG}$ ), and gas–liquid ( $\gamma_{LG}$ ) IFTs are known.<sup>116,118</sup> However, only gas–liquid IFTs ( $\gamma_{LG}$ ) can be measured conveniently in the laboratory. Gas–solid ( $\gamma_{SG}$ ) and liquid–solid ( $\gamma_{SL}$ ) IFTs cannot be determined experimentally; hence, these parameters are determined through semi-empirical methods.<sup>116,118</sup> Young's equilibrium contact angle ( $\theta_e$ )<sup>174</sup> was computed from the values of the advancing contact angle ( $\theta_a$ ) and receding contact angle ( $\theta_r$ ) using Tadmor's correlation<sup>175</sup> (eqn (7)):

$$\theta_e = \arccos \left( \frac{r_a \cos \theta_a + r_r \cos \theta_r}{r_A + r_R} \right) \quad (7)$$

$$r_A = \sqrt[3]{\frac{(\sin \theta_a)^3}{2 - 3 \cos \theta_a + (\cos \theta_a)^3}} \quad \text{and} \quad r_R = \sqrt[3]{\frac{(\sin \theta_r)^3}{2 - 3 \cos \theta_r + (\cos \theta_r)^3}}$$

Next, Neumann's equations of state (eqn (8) and (9))<sup>108,176,177</sup> were combined with eqn (6) (Young's equation) to derive eqn (10):

$$\gamma_{SG} = \gamma_{SL} + \gamma_{LG} - 2\sqrt{\gamma_{SL}\gamma_{LG}} \left[ 1 - \beta(\gamma_{SL} - \gamma_{LG})^2 \right] \quad (8)$$

$$\gamma_{SL} = \gamma_{SG} + \gamma_{LG} - 2\sqrt{\gamma_{SG}\gamma_{LG}} \left[ 1 - \beta(\gamma_{SG} - \gamma_{LG})^2 \right] \quad (9)$$

$$\cos \theta_e = 1 - 2\sqrt{\frac{\gamma_{SL}}{\gamma_{LG}}} \left[ 1 - \beta(\gamma_{SL} - \gamma_{LG})^2 \right] \quad (10)$$

In eqn (10),  $\theta_e$  and  $\gamma_{LG}$  represent input parameters;  $\gamma_{SL}$  (assumed independent of pressure)<sup>178–180</sup> and  $\beta$  are the fitting parameters. Finally,  $\theta_e$  is determined using eqn (10). Although several studies<sup>138,175–177</sup> have reported the rock–fluid IFT at geological storage conditions, very few publications have reported such measurements for rock–H<sub>2</sub> interfacial interactions.<sup>108</sup>

Experimental rock–H<sub>2</sub>–brine contact angle measurements are often conducted to ascertain rock-wetting behavior during

H<sub>2</sub> storage.<sup>108</sup> Several studies have attempted to measure the contact angles of rock–brine–H<sub>2</sub> systems despite the high compressibility, volatility, and reactivity of H<sub>2</sub> at geo-storage conditions and the possibility of embrittlement damage caused by H<sub>2</sub> to metallic investigation apparatuses.<sup>20,39,108,111,158,181</sup>

Owing to these challenges, researchers have developed empirical correlations using the known contact angles of other geo-storage gases, such as CO<sub>2</sub>, N<sub>2</sub>, helium (He), CH<sub>4</sub>, and argon (Ar), and their densities at various pressure and temperature values to compute the three-phase contact angles of H<sub>2</sub> at similar conditions. To this end, several methods and techniques have been employed to evaluate UHS.

### 3.1. Wettability and H<sub>2</sub>–brine interactions using quantitative experimental methods

Contact angle measurement is a prominent method of directly assessing the H<sub>2</sub> wettability of storage and caprock.<sup>156</sup> The existing literature contains contact angle datasets for H<sub>2</sub> from laboratory experiments.<sup>35,109,111,158,182</sup>

If rock-pore structures are known, contact angle data can express the capillary pressure and relative permeability functions, which could be useful for conducting simulations at the reservoir scale and predicting H<sub>2</sub> containment security and storage optimization.<sup>109</sup> Contact angles in rock–gas–brine systems are primarily determined using the captive-bubble method (the gas bubble technique) or the sessile-drop method (the pendant drop).<sup>147,156,183</sup>

In the sessile-drop method, a droplet of the assessment fluid is introduced onto the rock surface, and the droplet is introduced underneath the rock substrate, where it rises due to buoyancy in the captive-bubble technique (Fig. 8). The angle at the three-phase contact line is measured to assess wetting behavior.

The sessile-drop technique is applied when the surrounding fluid or medium density is lower than the “drop fluid,” whereas the captive-bubble configuration is for cases where the lower-density fluid is the “drop fluid.” For the contact angle of rock/H<sub>2</sub>/brine, H<sub>2</sub> gas bubbles are introduced at the rock–brine interface during contact angle measurement. In contrast, brine droplets are introduced on gas–solid interfaces during sessile-drop procedures.<sup>117,147,156,183</sup> Some studies have suggested that captive-bubble techniques could be more advantageous than sessile-drop configurations because the dispersion of brine droplets into permeable (porous) hydrophilic rock substrates during sessile-drop measurement can yield unreliable contact angle datasets.<sup>182,184</sup>

In addition, H<sub>2</sub> bubbles have been monitored over time using the captive-bubble contact angle method, and the average contact angles have been reported. This approach has advantages because it avoids external viscous forces that could displace fluid and gas phases, allowing for static contact angle measurements for H<sub>2</sub> on saturated porous reservoir rock. This approach also measures intrinsic contact angles using a gas bubble at a solid–liquid interface, with synthetic seawater as the surrounding phase. This approach has an advantage over the sessile-drop method, where brine spreading and diffusion



into porous hydrophilic substrates present experimental challenges and reduce data reliability.<sup>117,185</sup>

Advancing and receding contact angles can be determined using tilted-plate or drop-removal techniques. Hashemi *et al.*<sup>117</sup> employed the captive-bubble setup to measure contact angles of H<sub>2</sub>/brine systems on Berea and Bentheimer sandstone samples. The methods for the contact angle measurements are similar to those employed for rock contact angles in CO<sub>2</sub>/brine systems in previous studies;<sup>138,186–188</sup> however, H<sub>2</sub> gas is employed instead of CO<sub>2</sub> for UHS.

Accordingly, Iglauer *et al.*<sup>158</sup> and Ali *et al.*<sup>35</sup> conducted a quantitative wettability measurement of quartz/H<sub>2</sub>/brine *via* the contact angle at geological storage temperatures and pressures using tilted-plate configurations. Emphasis was placed on the sample preparation procedure before contact angle measurements because it determines data consistency, reliability, and repeatability. Advancing contact angles correlated with the residual trapping potential of storage rocks, whereas the receding angles correspond to the structural trapping capacity or sealing potential of the caprock. The pre-equilibration of brine with the H<sub>2</sub> and rock is usually conducted under the assessment condition to prevent mass transfer effects due to interactions between the brine and quartz surface.

Using similar methods, Ali *et al.*<sup>109,111</sup> presented contact angle datasets of mica/H<sub>2</sub>/brine systems at geo-storage temperature and pressure values in the presence and absence of organic-acid contamination. The contact angles were measured in the high-pressure, high-temperature cell using the tilted-plate technique (at 17°) at pressures of 0.1 to 25 MPa and temperatures of 308–343 K. The contact angles were determined using an ImageJ analysis of the acquired image.

Although wettability assessment *via* contact angle measurement is a significant method for directly quantifying rock-wetting characteristics in H<sub>2</sub>/brine systems, many of the limitations reported for contact angle measurements in rock/CO<sub>2</sub>/brine systems also apply to rock/H<sub>2</sub>/brine systems.<sup>189</sup> These limitations include sample preparation procedures—specifically, the lack of standardized cleaning procedures and experimental protocols and potential alterations in the physical and chemical properties of rock substrates due to cleaning procedures, equilibration time, surface-roughness variability, surface contamination, and rock-substrate chemical heterogeneity.<sup>182,190–195</sup> Contact angle measurements for rock–H<sub>2</sub>–brine systems could also be affected by the difficulty of achieving equilibration and saturation conditions, H<sub>2</sub> bubble solubility, and dissolution in brine or brine-droplet diffusion into porous rock surfaces. These parameters must be accounted for to ensure successful laboratory measurements and unbiased results.

Furthermore, measuring wetting behavior and interfacial interactions experimentally *via* contact angles in rock/H<sub>2</sub>/brine systems is challenging due to the high reactivity and volatility of H<sub>2</sub> and stringent safety requirements. Properties of H<sub>2</sub> necessitate specialized handling and controlled environments, complicating experimental setups and increasing operational risks and data uncertainty. Hence, researchers often explore alternative methods to assess these properties for UHS applications. These methods

may include using empirical correlations to infer the rock/H<sub>2</sub>/brine interfacial interactions computational simulations, such as MD or pore-scale modeling, which offer insight into fluid behavior at a microscopic level without the constraints and safety considerations associated with experimental setups involving H<sub>2</sub>. Additionally, ML and advanced analytical techniques, such as spectroscopy and surface characterization, indirectly infer wetting and sorption characteristics and interfacial interactions, providing valuable data for optimizing UHS strategies while ensuring safety and efficiency.

### 3.2. Wettability and H<sub>2</sub>-brine interactions using empirical correlation

Empirical correlations are employed to circumvent the problems of experimental measurement of rock contact angles in an H<sub>2</sub>/brine environment because of the high compressibility and reactivity of H<sub>2</sub> at geological storage conditions. For example, Al-Yaseri and Jha<sup>108</sup> and Al-Yaseri *et al.*<sup>110</sup> applied the measured contact angles and densities of other relevant geo-storage gases (*e.g.*, CO<sub>2</sub>, N<sub>2</sub>, He, CH<sub>4</sub>, and Ar) at various temperatures and pressures to compute H<sub>2</sub>-brine equilibrium contact angles.<sup>108,110</sup>

From Young's equation,<sup>174</sup> a rock–fluid IFT can be correlated with the contact angle as presented in eqn (11):

$$\cos \theta_1 = \frac{(\gamma_{gs} - \gamma_{ls})}{\gamma_{gl}} \quad (11)$$

where  $\gamma_{gl}$ ,  $\gamma_{ls}$ , and  $\gamma_{gs}$ , denote the gas–liquid, liquid–solid, and gas–solid IFTs, respectively. The macroscopic equation in eqn (12)<sup>72,196–199</sup> can be derived from the combination of eqn (11) and the sharp-kink approximation,<sup>200</sup> as presented below:

$$\cos \theta_1 = \frac{I}{\gamma_{lg}} \Delta\rho - 1 \quad (12)$$

where  $I = -\int_{z_{\min}}^{\infty} V(z) dz$  represents the van der Waals potential integral,<sup>198,199</sup> and  $\Delta\rho = \rho_{lf} - \rho_g$  (where  $\rho_g$  denotes the density of the gas, and  $\rho_{lf}$  depends on the precise liquid–gas density of the substrate). Substituting the defined parameters into eqn (12) and rearranging eqn (13)<sup>201</sup> yields

$$\cos \theta_1 = -\frac{I}{\gamma_{lg}} \rho_g + \left( \frac{I}{\gamma_{lg}} \rho_{lf} - 1 \right) \quad (13)$$

Then, the Young's equilibrium contact angle ( $\theta_1$ ) is computed using the advancing and receding angle values measured for other gases using eqn (14):<sup>175–177,202</sup>

$$\theta_1 = \cos^{-1} \left( \frac{r_A \cos \theta_A + r_R \cos \theta_R}{r_A + r_R} \right) \quad (14)$$

with

$$r_A = \sqrt[3]{\frac{(\sin \theta_A)^3}{2 - 3 \cos \theta_A + (\cos \theta_A)^3}} \quad \text{and} \quad r_R = \sqrt[3]{\frac{(\sin \theta_R)^3}{2 - 3 \cos \theta_R + (\cos \theta_R)^3}}$$



Afterward,  $\theta_1$  computed in the presence of other gases estimates the rock/H<sub>2</sub>/brine equilibrium contact angle. The linear regression in eqn (13) obtains the relationship between density and  $\cos \theta_1$  and other gases at various thermophysical conditions because gas molecule and rock surface interaction depend on gas density.

Al-Yaseri and Jha<sup>108</sup> and Al-Yaseri *et al.*<sup>110</sup> adopted this method for predicting the equilibrium contact angles of basaltic rock, shale, and clay. Accordingly, Al-Yaseri and Jha<sup>108</sup> conducted contact angle measurements of basalt/gas/brine systems using CO<sub>2</sub>, N<sub>2</sub>, and He at high temperature (323 K) and pressure (5, 10, 15, and 20 MPa) values. The basalt samples were sourced from well KB-01 at the CarbFix injection site in Iceland.<sup>203,204</sup> The basalt/H<sub>2</sub>/water system wettability was determined from empirical correlations with He (with a density near that of H<sub>2</sub>), indicating a strong water-wetting state.

For the clay-H<sub>2</sub>-brine system, contact angle values were less than 40° for kaolinite, montmorillonite, and illite at all studied conditions,<sup>110</sup> suggesting that the residual trapping of H<sub>2</sub> is favorable even with these three minerals in the geo-storage rock. These results indicate that the basalt rock, shale, and rock comprising these three primary clay compositions remained hydrophilic during UHS, indicating that large-scale UHS could be feasible for these rock types. More recently, the potential for H<sub>2</sub> generation from basaltic rocks has been explored, with initial evidence suggesting that H<sub>2</sub> can be produced during geological CO<sub>2</sub> storage.<sup>205</sup>

The results of the laboratory-measured contact angle of the rock/H<sub>2</sub>/brine system were consistent with contact angles predicted by the developed correlations. Hashemi *et al.*<sup>117</sup> measured the three-phase contact angles of Berea and Bentheimer sandstone in H<sub>2</sub>/brine in the geo-storage state using the captive-bubble technique. They found that the contact angle values were between 21.1° and 43°, suggesting the sandstone formation could be water-wet at downhole conditions. The low brine contact angles of storage and caprock in the H<sub>2</sub>/brine system were attributed to the considerably lower density of H<sub>2</sub>. The intermolecular interactions, cohesive surface energy, and forces between the rock surface and H<sub>2</sub> molecules are very weak due to the low H<sub>2</sub> density.<sup>43,108,110,117,158</sup>

The empirical correlation method Al-Yaseri *et al.*<sup>108</sup> developed encounters uncertainty and challenges in certain situations. This method could be due to differing gas-rock interactions, as each gas exhibits unique physicochemical properties and interactions with rock and brine. Hydrogen has distinct characteristics, including its small molecular size, low density (0.089 kg m<sup>-3</sup> in standard conditions), and high diffusivity and reactivity. These properties substantially differ from those of CO<sub>2</sub>, N<sub>2</sub>, CH<sub>4</sub>, and Ar. Regarding surface chemistry differences, the chemical properties of H<sub>2</sub>, such as its ability to participate in reduction-oxidation (redox) reactions, differ from those of other gases, potentially leading to distinct surface chemistry dynamics. A comparison of H<sub>2</sub> and N<sub>2</sub> displacement processes revealed that H<sub>2</sub> recovery from porous storage media significantly differs from N<sub>2</sub> recovery, suggesting that N<sub>2</sub> is a poor proxy for H<sub>2</sub>.<sup>143,144,206,207</sup> Therefore, based on other gases,

predictions of empirical correlations of H<sub>2</sub>-wetting behavior and interactions between H<sub>2</sub> and geological materials can be inaccurate.

### 3.3. Parameters for wettability of rock/H<sub>2</sub>/brine systems in ideal geo-storage situations

Rock/H<sub>2</sub>/brine wettability is crucial in determining injectivity, withdrawal rates, storage potentials, and containment safety in H<sub>2</sub> subsurface storage processes. Several parameters influence the wettability of the rock/H<sub>2</sub>/brine system in H<sub>2</sub> geo-storage applications. The wetting characteristics of the rock during underground CO<sub>2</sub> storage are also strongly affected by several critical parameters, such as surface roughness, pressure, salinity, temperature, organic-acid concentrations, and alkyl chain groups.<sup>182,208</sup> Studies on the wettability of the rock-H<sub>2</sub>-brine system suggest that this observation is also valid for the H<sub>2</sub> wettability of storage formations and caprock.

The wetting behavior of rock/H<sub>2</sub>/water systems is assessed *via* contact angle measurements using samples corresponding to ideal geo-storage conditions without surface modifications. Researchers use pure and polished rock surfaces, such as quartz or silica, to represent sandstone reservoirs, pure calcite for carbonate formations, and mica or other minerals for shale formations to replicate subsurface formations. This approach eliminates the effects of other minerals and minimizes the influence of surface roughness. Some studies have applied nonporous and nonpermeable polished rock substrates to reduce the influence of petrophysical properties on the experimental results. By employing such methods, the focus is directed toward understanding the temperature and pressure effects on the wettability of rock/H<sub>2</sub>/water systems.<sup>192,209-212</sup> For example, wettability measurements have been conducted on pure quartz,<sup>158,213</sup> calcite,<sup>136</sup> mica,<sup>111,167</sup> and Bentheimer sandstone<sup>117</sup> to assess the influence of pressure and temperature.

Reports of the influence of temperature and pressure on the wettability of rock-H<sub>2</sub>-brine systems are inconsistent. The trends also depend on the considered rock type. The advancing, receding, and equilibrium contact angles in brine are typically higher at higher pressure and increase with increasing pressure for some reported rock/H<sub>2</sub>/brine systems. The contact angle datasets demonstrate that the H<sub>2</sub> wettability of rock increases with increased pressure because of the growing intermolecular interactions between H<sub>2</sub> molecules and rock surfaces. Hydrogen density increases with increased pressure. Thus, the intermolecular interactions of the H<sub>2</sub> gas molecule-rock surface are enhanced at higher pressure.<sup>111,136,158</sup>

The contact angles of the mica/H<sub>2</sub>/brine system decreased, whereas those of the quartz/H<sub>2</sub>/brine system increased with increased temperature. For example, the advancing and receding contact angles of the pure mica/H<sub>2</sub>/brine system were measured as 39.6° and 34.1°, whereas those of the quartz-H<sub>2</sub>-brine system were measured as 43.7° and 40.3° in similar conditions (20 MPa and 343 K). The hydrogen bonds (H-bonds) between silanol groups, water molecules, and quartz substrates are likelier to be broken with increased pressure. Thus, quartz substrates are increasingly gas-wet at higher temperatures.<sup>35,158</sup>



In contrast, the wetting tendency of the mica surface is significantly influenced by H<sub>2</sub> density considerably more than H-bonding; thus, the increasing temperature reduces the gas molecular cohesive energy density and the interaction between gas molecules and substrate surfaces.<sup>109,214</sup>

Zheng *et al.*<sup>169</sup> noted that a prevailing opinion suggests that the change in contact angle with pressure indicates that the interaction between the gas and solid surface intensifies with a higher gas density, regardless of the gas type. However, other researchers have reported contrasting observations regarding the rock/H<sub>2</sub>/water contact angle trend with increased pressure. For example, Muhammed *et al.*,<sup>47</sup> Hashemi *et al.*,<sup>117</sup> and Higgs *et al.*<sup>170</sup> found no evident trend in the experimental data, covering a broad range of pressure, temperature, and salinity conditions. They attributed the discrepancy between their findings and those of Iglauer *et al.*<sup>158</sup> to variations in experimental methods, sample preparation, and gas-bubble size. Therefore, this section thoroughly explores the literature on rock/H<sub>2</sub>/brine wettability variations under various pressure and temperature conditions.

**3.3.1. Pure mica/H<sub>2</sub>/water systems.** Study results have indicated that the wetting behavior of mica/H<sub>2</sub>/brine systems is significantly affected by temperature and pressure.<sup>109,111</sup> Mica is an appropriate representative of caprock minerals because shale, sedimentary, metamorphic, and igneous rocks are rich in it.<sup>5,142,188,215</sup> Ali *et al.*<sup>111</sup> used mica substrates with a length of 14 mm, width of 12 mm, height of 2.5 mm, and an average roughness of 1 nm to measure and characterize the wetting behavior of the mica/H<sub>2</sub>/brine system. The substrates were cleaned using deionized (DI) water followed by N<sub>2</sub> flow to remove surface contaminants and an air plasma treatment for 20 min to eliminate residual organic molecules.

The  $\theta_a$  and  $\theta_r$  angles of the mica–H<sub>2</sub>–brine (10 wt% NaCl) were measured using the tilted-plate method in various conditions (0.1 to 25 MPa and 308 to 343 K). The contact angles increased with pressure. This behavior is attributed to increased gas density with elevated pressure, enhancing the interaction at the molecular level between the solid surface and gas.<sup>5,48</sup> Specifically, at 323 K, the  $\theta_a$  angle of pure mica increased from 21.7° to 42.9° after increasing the pressure from 5 to 20 MPa (Fig. 9(a)).

A similar change has been noted in studies, although the contact angles for the H<sub>2</sub> systems were higher.<sup>167</sup> At 323 K, the  $\theta_a$  for the mica/H<sub>2</sub>/brine system was 39.1° at 5 MPa, whereas at 20 MPa and the same temperature, the angle increased to 83.5°. Discrepancies in the H<sub>2</sub>/mica contact angles compared to those reported by Ali *et al.*<sup>111</sup> can be attributed to differences in measurement procedures, sample preparation, and properties.<sup>167</sup>

Regarding temperature, the mica/H<sub>2</sub>/brine contact angle values reduced with temperature, indicating a higher sealing potential of caprock at elevated temperatures. For example, at 15 MPa, the advancing contact angle was 53.1° at 308 K, compared to 35.4° at 343 K. This result can be attributed to the density reduction of H<sub>2</sub> gas at an elevated temperature due to the lower molecular cohesive energy density of H<sub>2</sub>. Moreover, H<sub>2</sub> gas molecules acquired more kinetic energy when heated, moving faster and resulting in more collisions and faster

diffusion.<sup>167</sup> This approach reduces the mica–H<sub>2</sub> surface molecular interactions, decreasing the contact angle with rising temperatures.

**3.3.2. Pure calcite/H<sub>2</sub>/water systems.** Calcite is an analogous mineral for carbonate formations and is typically found as a constituent of caprock and reservoir rock.<sup>138,221</sup> Thus, understanding carbonate-rich rock wettability in geo-storage conditions is critical to evaluating the structural and residual trapping of calcite-rich caprock and reservoir rock during UHS.<sup>136,222</sup> The wetting behavior of H<sub>2</sub>/water systems on pure calcite substrates (comprising 56.03% CaO and 43.97% CO<sub>2</sub>) was assessed using the tilted-plate contact angle technique. The result revealed that the system remained strongly hydrophilic at ambient states, but the wetting state transitioned to intermediate-wet at high pressure. Moreover, the contact angle decreased as the temperature increased from 298 to 353 K, and the pressure dropped (0.1 to 20 MPa). The conditions suggest that high temperature and lower pressure are ideal for minimizing UHS risks in carbonate formations.<sup>136</sup>

The  $\theta_a$  and  $\theta_r$  values increased as the pressure increased, suggesting that the water wettability of calcite decreased at 298, 323, and 353 K (Fig. 9(b)). For instance, under ambient conditions (0.1 MPa and 298 K),  $\theta_a$  increased from water-wet to 83.6° (intermediate-wet) at 298 K and 20 MPa.<sup>136</sup> This trend is attributable to the increased intermolecular forces between H<sub>2</sub> and calcite at higher pressure due to the increased gas density, consistent with other investigations.<sup>217,223,224</sup>

Conversely, and slightly contradictorily, Fig. 9(b) reveals that the contact angles ( $\theta_a$  and  $\theta_r$ ) decreased with increasing temperature, indicating improved water wettability.<sup>136</sup> For instance, at 15 MPa,  $\theta_a$  and  $\theta_r$  decreased from 80.35° to 57.85° at 298 K and from 76.6° to 53.15° at 353 K, respectively. Similarly, Hou *et al.*<sup>223</sup> reported a decrease in  $\theta_a$  and  $\theta_r$  for carbonate/H<sub>2</sub>/brine rock with increased temperature, lowering the density of H<sub>2</sub> gas due to a decrease in its molecular cohesive energy density. The authors emphasized that the kinetic energy increased as H<sub>2</sub> molecules were heated, causing more frequent collisions between H<sub>2</sub> molecules; thus, the molecular interactions between the carbonate rocks and H<sub>2</sub> decreased.

In contrast, other studies have reported higher contact angles with increasing temperatures from 293 to 353 K,<sup>217</sup> for instance, the contact angle changed from 43.9° at 293 K to 88.3° at 353 K and 10 MPa. This observation was credited to the increase in the rock–H<sub>2</sub> IFT with temperature, as the molecular cohesive energy density of H<sub>2</sub> decreases with temperature while remaining constant for the rock. Higher temperatures increase kinetic energy and accelerate the diffusion of H<sub>2</sub> gas molecules, reducing molecular interactions between the calcite surface and H<sub>2</sub>. These conditions increase water wettability (reduced contact angle) with higher temperatures, indicating a higher H<sub>2</sub> storage capacity of carbonate formations with increasing temperature and decreasing pressure. Conversely, Esfandiyari *et al.*<sup>217</sup> argued that the H-bonds between the silanol groups of mica or calcite surfaces and water molecules break at high temperatures, reducing the rock–water affinity and increasing the H<sub>2</sub> wettability.<sup>158,197,216,225,226</sup>



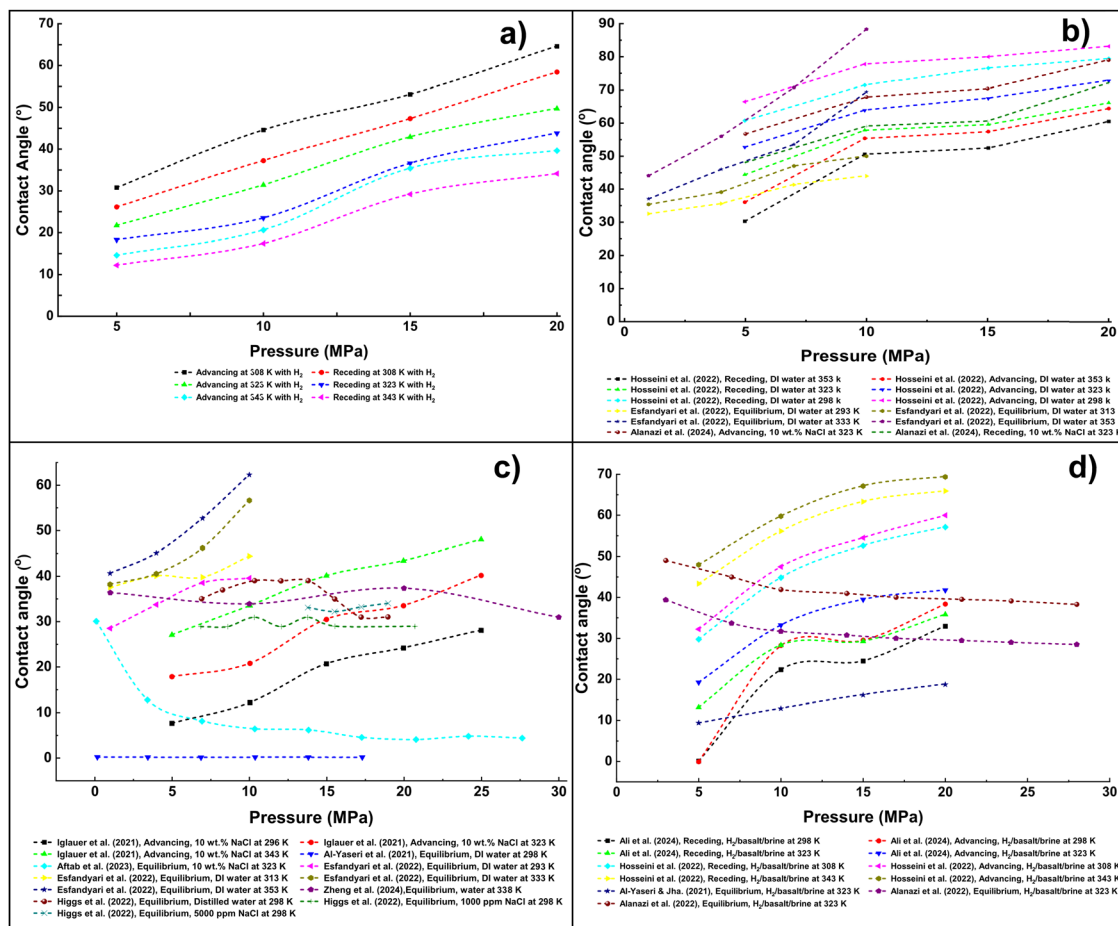


Fig. 9 Contact angle variation as a function of pressure and temperature for rock/H<sub>2</sub>/brine systems. Influence of pressure and temperature on the wettability of rock surfaces in contact with H<sub>2</sub> and brine. (a) Mica/H<sub>2</sub>/brine systems exhibit increasing contact angles with pressure, suggesting enhanced gas-wetting behavior at higher pressure.<sup>111</sup> (b) Calcite/H<sub>2</sub>/brine systems display a similar trend with increasing contact angles, indicating reduced brine-wetting under elevated pressure.<sup>136,216,217</sup> (c) Quartz/H<sub>2</sub>/brine systems display varied responses, with contact angles fluctuating based on experimental conditions, reflecting the sensitivity of quartz to temperature and pressure.<sup>158,168–170,217,218</sup> (d) Basalt/H<sub>2</sub>/brine systems display increasing contact angles with pressure, signifying stronger gas-wetting properties at an elevated pressure.<sup>108,172,219,220</sup> All system data were collected from the literature and replotted to provide a comprehensive overview of wettability trends across rock types.

**3.3.3. Pure quartz/H<sub>2</sub>/water systems.** Pristine quartz substrates are commonly employed as representatives for sandstone formations because the principal constituents are quartz minerals.<sup>227</sup> Several authors have reported the influence of pressure and temperature on H<sub>2</sub>/brine/quartz wettability.<sup>158,213</sup> However, reports regarding quartz/H<sub>2</sub>/brine wettability changes with pressure have conflicted. For instance, Iglauer *et al.*<sup>158</sup> demonstrated that, regarding pure quartz substrates, contact angles significantly increased with increased pressure for H<sub>2</sub> storage conditions (0.1 to 25 MPa and 296 to 343 K), as illustrated in Fig. 9(c). This trend resulted from increasing intermolecular interactions between quartz and gas due to the higher molecular gas density at elevated pressure.<sup>3,224</sup>

Conversely, other studies have observed a decreasing trend in contact angles with increasing pressure. For example, Aftab *et al.*<sup>168</sup> reported that a contact angle of around 10° to 30° for the quartz–H<sub>2</sub>–brine system as pressure rose from 0 to 27 MPa at 323 K. In contrast, some studies have not observed significant changes in the quartz/H<sub>2</sub>/brine contact angle with

pressure.<sup>169,170</sup> Due to these discrepancies, Al-Yaseri *et al.*<sup>218</sup> conducted validation experiments using the same experimental procedure (sessile-drop method) and cleaning and experimental conditions as reported in the literature.<sup>158</sup> The authors found zero quartz–H<sub>2</sub>–brine contact angle values under all pressure and temperature conditions (Fig. 9(c)). These results were supported by MD simulations and are aligned with some data on the wettability of rock/H<sub>2</sub>/water systems in the literature. For instance, *via* contact angle measurements, Hashemi *et al.*<sup>117</sup> discovered no correlation between temperature, pressure, and sandstone/H<sub>2</sub> wettability. Moreover, using MD simulation, Zeng *et al.*<sup>213</sup> noted that increasing pressure and temperature did not affect quartz wetting behavior in the H<sub>2</sub>/brine system.

Literature on quartz/H<sub>2</sub>/brine wettability variation with temperature and pressure presents conflicting trends. For example, Iglauer *et al.*<sup>158</sup> noted that quartz is weak-to-intermediate-wet in an H<sub>2</sub>/brine environment due to increased temperature regardless of pressure. Notably, at 10 MPa, the contact angle rose from



12.3° at 296 K to 33.7° at 343 K.<sup>158</sup> This increase was attributed to the higher possibility of breaking H-bonds between quartz surface silanol groups and water molecules at higher temperatures. As the H-bond concentration decreases, the affinity between water and quartz diminishes, reducing the quartz surface hydrophilicity and enhancing H<sub>2</sub> wettability.<sup>158,169</sup>

Using a subsurface complexation model, Zeng *et al.*<sup>213</sup> found that elevated storage temperatures make the sandstone surface more H<sub>2</sub>-wet. The variation was reportedly due to the increasing rock surface potential induced by the increased availability of surface species concentration. However, a conflicting observation regarding the effect of temperature on H<sub>2</sub> wetting *via* the predicted disjoining pressure suggests that anticipated incremental temperatures have an insignificant influence. The model predictions revealed that increasing the temperature and pressure has a trivial effect on the disjoining pressure between H<sub>2</sub>/brine and pure quartz/brine and on the H<sub>2</sub> wettability of pure quartz. This result contrasts with previous experimental observations,<sup>158</sup> documenting that increasing the temperature significantly increases the H<sub>2</sub>/brine contact angle of pure quartz. However, these observations are inconsistent with the findings by Hashemi *et al.*,<sup>117</sup> who observed no significant relationship between temperature and the H<sub>2</sub>/brine contact angle on the sandstone surface.

Similarly, Zheng *et al.*<sup>169</sup> conducted an MD simulation of quartz/H<sub>2</sub>/water using the large-scale atomic/molecular massively parallel simulator (LAMMPS). The outcome indicated that the quartz/H<sub>2</sub>/water contact angle at 1 to 30 MPa fluctuated between 30.7° and 37.1° (Fig. 9(c)). This finding aligns with some experimental observations in the literature, indicating no clear correlation between the water contact angle and pressure in this range, suggesting that pressure does not significantly affect quartz wettability (see above). The primary argument for the increasing water contact angle with pressure is the critical interaction between H<sub>2</sub> and the quartz surface at a higher pressure due to the higher density of the gas phase.<sup>158</sup> Although the total interaction energy between H<sub>2</sub> and quartz increases with pressure, this does not consistently increase the quartz/H<sub>2</sub>/water contact angle.<sup>169</sup>

The authors argued that the hypothesis that a stronger gas-quartz interaction at higher pressure leads to a larger contact angle does not fully explain all experimental observations due to the unique properties of H<sub>2</sub> compared to other gases.<sup>169</sup> The interaction energy between water and hydroxyl groups displays the opposite trend to that between water and quartz (hydrophilicity increases with increased interaction), suggesting that a stronger interaction between water and hydroxyl groups leads to a higher water contact angle. This result implies that the interaction between water and the surface hydroxyl groups on quartz is crucial in altering quartz wettability with pressure. The water contact angle on the quartz surface does not follow a monotonic trend with pressure. Instead, the angle is influenced by the pinning effect caused by microstructures on the quartz surface and the adsorption of water and H<sub>2</sub> on the substrate rather than by the interaction between H<sub>2</sub> and the quartz substrate.<sup>169</sup>

**3.3.4. Pure basalt/H<sub>2</sub>/water systems.** The literature on the variations in basalt/H<sub>2</sub>/brine contact angles with pressure is inconsistent, reporting different trends and extents. However, a significant portion of the literature indicates an increasing trend with pressure. For example, Al-Yaseri and Jha<sup>108</sup> documented that the CarbFix basalt-H<sub>2</sub>-brine contact angle increased with pressure, although the contact angle values were less than 60°. Similarly, Esfandiyari *et al.*<sup>217</sup> demonstrated that the contact angle of basalt stayed strongly water-wet, ranging from 17° to 35°, over a wide range of conditions (0.1 to 10 MPa and 293 to 353 K) in DI water and formation brine.

Likewise, Hosseini *et al.*<sup>172</sup> demonstrated that the water contact angles ( $\theta_a$  and  $\theta_r$ ) at 308 and 343 K increased with pressure due to the increased intermolecular forces between Iranian basalt and H<sub>2</sub>. At 5 MPa and 308 K, the basalt surface was strongly water-wet with  $\theta_a$  at 32.29°.<sup>172</sup> The surface became weakly water-wet, with  $\theta_a$  rising to 59.31° as the pressure changed to 20 MPa. Under the same pressure conditions, at 343 K, the contact angles were 47.86° (moderately water-wet) and 68.61° (weakly water-wet), as depicted in Fig. 9(d).

Furthermore, the reported  $\theta_a$  and  $\theta_r$  values of the intact Saudi Arabian Basalt (SAB) at 298 and 323 K increased with rising pressure and temperature (see Fig. 9(d)). At a pressure of 20 MPa,  $\theta_a$  and  $\theta_r$  rose from 38.5° and 33.2° at 298 K to 42.1° and 36.3° at 323 K, respectively.<sup>220</sup> This result suggests that intermolecular interactions between H<sub>2</sub> and basalt surfaces intensify with increasing H<sub>2</sub> storage depth and calefaction.<sup>220</sup> The authors contested that higher  $\theta_a$  and  $\theta_r$  values of the H<sub>2</sub>/brine system on SAB at elevated temperatures and pressures are due to increased H<sub>2</sub> density and enhanced basalt-H<sub>2</sub> intermolecular interactions. Although this may hold for other systems, such as rock/CO<sub>2</sub>/brine, the variations in H<sub>2</sub> density with pressure are insignificant compared to other rock-gas-brine systems, and the basalt/H<sub>2</sub>/brine reactivity is also minimal. Therefore, the variations in  $\theta_a$  and  $\theta_r$  with elevated pressure and temperature for H<sub>2</sub> are insufficient to render the surface of pure basalt H<sub>2</sub>-wet, leading to poor H<sub>2</sub>-wetting.<sup>140,173,220</sup>

Regarding the extent of the wetting behavior, compared to the contact angles reported in the basalt/H<sub>2</sub>/brine system,<sup>172</sup>  $\theta_a$  and  $\theta_r$  indicated weakly water-wet conditions ( $\theta_a = 68.8^\circ$  and  $\theta_r = 65.4^\circ$ ) at 343 K and 20 MPa. Ali *et al.*<sup>220</sup> emphasized that the difference in the wetting states of SAB (strongly water-wet state) and Iranian basalt (weakly water-wet state) observed by Hosseini *et al.*<sup>172</sup> at high temperatures and pressures can be attributed to variations in the mineralogical compositions of the basalt type. Table 2 details the compositions of the basalts discussed in this section.

Specifically, the plagioclase (CaAl<sub>2</sub>Si<sub>2</sub>O<sub>8</sub>) composition of SAB is 51 wt%, whereas it was 55 wt% in the other basalt substrates.<sup>172</sup> Therefore, basalt substrates with a higher plagioclase content are expected to exhibit higher gas-brine-rock contact angles.<sup>220,228</sup> In addition, basalt surfaces are often rich in silica,<sup>229</sup> analogous to the quartz/H<sub>2</sub>/brine system. The wettability of the basalt/H<sub>2</sub>/brine system depends on H-bonding between silanol groups and water molecules on the rock surface.<sup>158,172</sup>



**Table 2** Mineralogical compositions of basalts, offering insight into basaltic formation diversity in underground hydrogen (H<sub>2</sub>) storage. Critical minerals, such as olivine, plagioclase, and pyroxene, are compared, highlighting the varying proportions of these components. Data from multiple sources were compiled to clarify the role of mineralogy in H<sub>2</sub>–rock interactions and storage feasibility

Sample	Mineralogy	Composition	Abundance wt%	Ref.
Saudi basalt-1	Anorthite	CaAl <sub>2</sub> Si <sub>2</sub> O <sub>8</sub>	44.1	219
	Olivine	(Mg <sup>2+</sup> , Fe <sup>2+</sup> ) <sub>2</sub> SiO <sub>4</sub>	14.7	
	Diopside-ferrian	MgCaSi <sub>2</sub> O <sub>6</sub>	24.8	
	Nepheline	Na <sub>3</sub> KAl <sub>4</sub> Si <sub>4</sub> O <sub>36</sub>	16.3	
Saudi basalt-2	Anorthite	CaAl <sub>2</sub> Si <sub>2</sub> O <sub>8</sub>	57.1	219
	Olivine	(Mg <sup>2+</sup> , Fe <sup>2+</sup> ) <sub>2</sub> SiO <sub>4</sub>	24.4	
	Magnesianoferrite	Mg(Fe <sup>3+</sup> ) <sub>2</sub> O <sub>4</sub>	17.6	
	Albite	(NaAlSi <sub>3</sub> O <sub>8</sub> )	0.8	
CarbFix basalt	Labradorite	(Na,Ca) <sub>1–2</sub> Si <sub>3–2</sub> O <sub>8</sub>	59.0	108
	Montmorillonite	(Na,Ca) <sub>0.33</sub> (Al,Mg) <sub>2</sub> (Si <sub>4</sub> O <sub>10</sub> )	4.0	
	Augite	Ca(Fe,Mg)Si <sub>2</sub> O <sub>6</sub>	37.0	
	Quartz	SiO <sub>2</sub>	0.3	
Iranian basalt	Anorthite	CaAl <sub>2</sub> Si <sub>2</sub> O <sub>8</sub>	55.0	172
	Augite	Ca(Fe,Mg)Si <sub>2</sub> O <sub>6</sub>	25.0	
	Orthoclase	KAlSi <sub>3</sub> O <sub>8</sub>	16.0	
	Lizardite	Mg <sub>3</sub> (Si <sub>2</sub> O <sub>5</sub> )(OH) <sub>4</sub>	4.0	
Saudi Arabian basalt	Plagioclase	CaAl <sub>2</sub> Si <sub>2</sub> O <sub>8</sub>	51.0	220
	Others	—	49.0	

Lower CaAl<sub>2</sub>Si<sub>2</sub>O<sub>8</sub> content in SAB (50 wt%) was responsible for the lower  $\theta_a$  and  $\theta_r$  values of the SAB–CO<sub>2</sub>–brine systems compared to the Icelandic (59 wt%) and Western Australian basalt (80 wt%), supporting this finding.<sup>228</sup> These results highlight the significant influence of the plagioclase composition on basalt wettability because rocks with a higher plagioclase content demonstrated higher hydrophobicity.<sup>228,230,231</sup>

Conversely, the contact angles of two SAB samples measured at pressures of 3, 7, 10, 14, 17, 21, 24, and 28 MPa and a temperature of 323 K exhibited strong-to-intermediate water-wet behavior. The contact angles slightly decreased with increased pressure, attributed to reduced interfacial forces between the brine and H<sub>2</sub> gas.<sup>219</sup> Saudi basalt-1 demonstrated more hydrophilic behavior than Saudi basalt-2, which was linked to the higher presence of siloxane (Si–O–Si) groups and O–H bonds in Saudi basalt-1 than basalt-2.

**3.3.5. Pure porous sandstone/H<sub>2</sub>/water systems.** Hashemi *et al.*<sup>117</sup> evaluated the wetting characteristics of Bentheimer and Berea sandstone under various pressure and temperature values to simulate reservoir conditions. The authors employed captive-bubble contact angle measurements of sandstone with an average roughness of 0.030 and 0.025 mm for Bentheimer and Berea slabs, respectively. The sandstone was water-wet, with contact angles varying from 25° to 45°. In addition, no significant connection was established with changes in pressure and temperature. Fig. 10(a and b) illustrates the effect of pressure and temperature on the contact angles of the Berea/H<sub>2</sub>/water and Bentheimer/H<sub>2</sub>/water systems, respectively, with and without NaCl (5000 ppm). No apparent correlation was reported. Moreover, Yekta *et al.*<sup>19</sup> computed the receding contact angle of H<sub>2</sub>/water on sandstone under various conditions from the capillary pressure and relative permeability measurements, where contact angle values were obtained as 21.6° at 5.5 MPa and 34.9° at 10 MPa.

**3.3.6. Pure clay mineral/H<sub>2</sub>/water systems.** Clays are common secondary minerals in most natural underground environments (besides salt caverns), including sandstone and igneous rock, where clays replace primary feldspar or mafic minerals, such as pyroxenes.<sup>234,235</sup> A significant portion of UHS reservoirs and caprock comprises clays, significantly influencing the wetting behavior and affecting the overall storage and containment security of the reservoir and caprock, respectively.

Al-Yaseri *et al.*<sup>110</sup> investigated the wettability of the H<sub>2</sub>/brine clay system. The wettability of H<sub>2</sub> on three clay surfaces representing 1:1, 2:1 nonexpansive, and 2:1 expansive clay groups was measured using synthetic brine (comprising 20 wt% NaCl and 1 wt% KCl).<sup>110</sup> Before conducting wettability tests, kaolinite, illite, and montmorillonite clays were mechanically compacted into consolidated substrates. All three clays (kaolinite, illite, and montmorillonite) exhibited water-wet behavior, with contact angles consistently lower than 40° across all investigated conditions, as presented in Fig. 10(c). This observation suggests that residual and structural trapping of H<sub>2</sub> is favorable in clay-rich caprock and host rock. The kaolinite was the most water-wet clay, followed by illite, and montmorillonite was the most H<sub>2</sub>-wet clay.<sup>110</sup> This trend in wetting behavior aligns with MD modeling, indicating that the basal plane of kaolinite's octahedral sheet is easily accessible by brine, greatly hydrophilic, and can form strong H-bonds. However, the same octahedral sheets in montmorillonite and illite are easily accessible to brine, resulting in lower hydrophilicity.

Rather than measuring the clay/H<sub>2</sub>/brine contact angles directly, other gases, such as He, CO<sub>2</sub>, N<sub>2</sub>, CH<sub>4</sub>, and Ar, were employed in the clay/gas/brine system at specific storage conditions, including temperature (333 K) and pressure (5, 10, 15, and 20 MPa). The clay/H<sub>2</sub>/brine contact angle can be derived by comparing these gases to H<sub>2</sub> and applying empirical



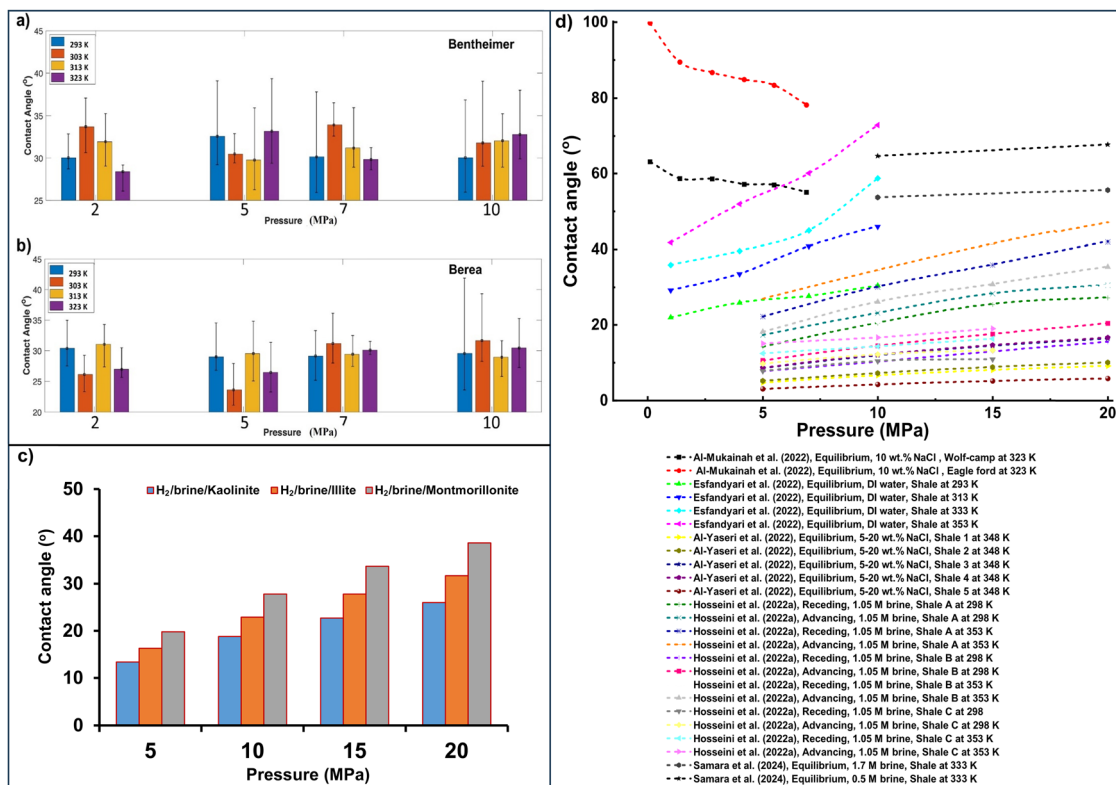


**Fig. 10** Contact angle variation with pressure and temperature for sandstone, clay, and shale in hydrogen ( $H_2$ )/brine systems. The contact angle variation is a function of pressure and temperature across rock types in  $H_2$ /brine environments. (a) and (b) Contact angles for pure porous sandstone (Bentheimer and Berea) demonstrate relatively stable behavior across pressures and temperatures, displaying slight increases in the contact angle with higher pressure, modified from ref. 117. (c) Clay/ $H_2$ /brine systems display a notable increase in the contact angle with pressure, indicating a stronger gas-wetting tendency at higher pressures.<sup>110</sup> (d) Shale/ $H_2$ /brine systems display significant variability in the contact angle based on pressure, temperature, and shale composition, compiled from several studies.<sup>173,217,225,232,233</sup> Data from these studies were collected and replotted to compare wettability trends comprehensively in underground  $H_2$  storage conditions.

relationships, and the wetting characteristics of  $H_2$  on rock surfaces can be deduced using mathematical techniques.<sup>108,110</sup>

The contact angle increased with pressure for all clay/ $H_2$ /brine systems (Fig. 10(c)), consistent with observed trends.<sup>236</sup> This result is attributed to the increased intermolecular interactions between gas molecules and the clay surface at higher pressure.<sup>3,237</sup> The wetting characteristic variations of these clay minerals are attributed to their surface chemistry, structure, and basal surfaces. Hydrophilic surfaces produce smaller water-gas contact angles, whereas hydrophobic surfaces produce larger angles.<sup>3</sup> Kaolinite, a 1:1 clay mineral, has two distinct basal surfaces: a tetrahedral siloxane surface (T-sheet) and an octahedral hydroxide surface (O-sheet), allowing water to adsorb to both.

In contrast, montmorillonite and illite, which are 2:1 clays, have an O-sheet sandwiched between two T-sheets (forming TOT layers), meaning the water interacts only with the T-sheets. The octahedral layer in kaolinite contributes to its higher water wettability due to its hydrophilic nature and strong H-bonds. The siloxane T-sheet is less hydrophilic with weaker H-bonds.

However, studies have found that siloxane surfaces can become hydrophilic in saline solutions, making all basal surfaces hydrophilic enough for intimate water contact regardless

of the TO or TOT structure. Although montmorillonite and illite have more H-bonds on their T-sheets than kaolinite, the additional H-bonds from kaolinite's O-sheet result in a higher degree of hydrophilicity and water-wetting capability.<sup>110,238,239</sup> The water-wetting behavior of kaolinite, illite, and montmorillonite implies that the potential of structural and residual  $H_2$  trapping is enhanced in clays (see also ref. 3). Kaolinite exhibited significantly higher water-wetting properties compared to illite and montmorillonite. This difference is attributed to the accessible basal O-sheet sites in kaolinite, which are highly polar and hydrophilic. In contrast, the O-sheets of illite and montmorillonite are not basal and, therefore, inaccessible to water.

**3.3.7. Pure shale/ $H_2$ /water systems.** Shale is complex due to the wide range of minerals present. Iglaier *et al.*<sup>187</sup> and Hosseini *et al.*<sup>225</sup> conducted an X-ray diffraction (XRD) study, demonstrating that shale can be rich in clay. In terms of trend and extent and, therefore, the wetting behavior of shales, different contact angles have been reported for  $H_2$ /brine systems, even under the same physicochemical conditions of temperature and pressure. Some mineral compositions tend to influence the wetting state toward a more water-wet state and, in some reported cases, a more  $H_2$ -wet state.<sup>187,225</sup>



Therefore, understanding the trend, deriving parameters, and extent of wetting disparities in shale for H<sub>2</sub> geo-storage is paramount.

Furthermore, mineral compositions include calcite, feldspar, mica, and other clay, including kaolinite and chlorite (see shale compositions in Table 3). Shale can be a caprock or a reservoir rock in H<sub>2</sub> subsurface storage. Thus, the wetting behavior of shale/H<sub>2</sub>/water is crucial because it determines the sealing integrity and stored H<sub>2</sub> capacity (primarily by adsorption).

The predicted shale/H<sub>2</sub>/brine contact angles indicated that, at a constant temperature of 343 K (Fig. 10(d)), the equilibrium contact angles for the H<sub>2</sub>/brine system increased with rising pressure from 5 to 20 MPa. Despite this, the shale samples shale 1 to 5 (Table 3) remained water-wet at high pressures, with the highest contact angle for the shale/H<sub>2</sub>/brine system not exceeding 16.7°. <sup>232</sup> Likewise, multiple authors have documented increased contact angles of shale/H<sub>2</sub>/water systems with pressure, <sup>217,225</sup> although contrasting findings have also been reported.

Samara *et al.* <sup>233</sup> observed no significant variation in the contact angle with pressure for Sultani shale, and the system remained water-wet under all experimental conditions. For example, with 0.5 mol kg<sup>-1</sup> brine, the average contact angle changes from 53° at 0.1 MPa to 56° at 20 MPa. This slight increase is ascribed to the significant adsorption of gas molecules on the rock surface and the change in the gas-brine IFT.

In addition, Al-Mukainah *et al.* <sup>173</sup> measured the contact angle of shale/H<sub>2</sub>/brine systems at 323 K with changing pressure (0.10 to 6.89 MPa) using the sessile-drop technique. In this technique, a 10 wt% NaCl solution was employed as the drop phase in an H<sub>2</sub> environment. Measurements at different pressure values were achieved by gradually pressurizing the cell containing the brine droplet on the shale substrate with H<sub>2</sub> gas. The Eagle Ford shale, with a root mean squared (RMS) surface roughness of 302 μm and a TOC of 3.83%, demonstrated an H<sub>2</sub>-wet state at 0.10 MPa. However, the Wolfcamp shale, with an RMS surface roughness of 183 μm and a TOC of 0.30%, was weakly water-wet in the same conditions. These data suggest that the rock TOC content could significantly influence shale caprock wettability during UHS. However, no noticeable increase in the contact angle was observed with pressure. <sup>173</sup> The authors emphasized that the drop in contact values with pressure was due to the lower H<sub>2</sub> density than that of CO<sub>2</sub> and CH<sub>4</sub>, resulting in insignificant variations in H<sub>2</sub> density at elevated pressure. <sup>169,173</sup> Thus, increasing the H<sub>2</sub> storage depth may not significantly influence UHS due to the H<sub>2</sub> density.

### 3.4. Organics in underground hydrogen storage formations

Geological and caprock formations often contain organic acids. Moreover, organic acids, including carboxylic and fatty acids, are present in crude oil streams. <sup>243</sup> Fatty acids in several geological formations have been reported, ranging from the Precambrian age to the present. <sup>243–245</sup> Organic acids comprise unsaturated branched and straight-chain fatty acids and saturated straight-chain dicarboxylic and monocarboxylic acids. Organic acid in geological formations is linked to hydrocarbon

**Table 3** Mineralogy and total organic carbon (TOC) of shale. Mineralogical composition and TOC content for shale samples, highlighting the diverse shale composition, which is critical in determining the wettability and interaction with hydrogen (H<sub>2</sub>) and brine during underground storage. Understanding these factors is essential for assessing the feasibility and performance of shale in H<sub>2</sub> storage applications

Sample	Mineralogy	Percentage wt%	TOC wt%	Ref.
Eagle Ford	Calcite	89.3	3.83	173
	Quartz	10.2		
	Pyrite	0.5		
Wolfcamp	Calcite	98.6	0.3	
	Quartz	1.3		
	Pyrite	0.1		
Shale 1	Quartz	31.0	0.081	187
	Calcite	—		
	Clay	41.0		
	Others	28.0		
Shale 2	Quartz	62.0	11.0	
	Calcite	8.0		
	Clay	20.0		
	Others	10.0		
Shale 3	Quartz	12.0	23.4	240
	Calcite	28.0		
	Dolomite	28.0		
	Clay	7.0		
	Others	25.0		
Shale 4	Quartz	19.0	3.0	241
	Calcite	49.0		
	Clay	16.0		
	Others	16.0		
Shale 5	Quartz	31.0	0.081	242
	Calcite	33.0		
	Ankerite	15.0		
	Others	21.0		
Shale A	Quartz	28.0	0.08	225
	Calcite	58.0		
	Dolomite	3.0		
	Clay	10.0		
	Others	1.0		
Shale B	Quartz	30.0	0.1	
	Siderite	6.0		
	Albite	4.0		
	Clay	56.0		
	Others	4.0		
Shale C	Quartz	25.0	0.09	
	Siderite	2.0		
	Albite	10.0		
	Clay	52.0		
	Others	11.0		
Sultani shale	Calcite	67.25	15.87	233
	Quartz	18.38		
	Apatite	6.50		
	dolomite	3.62		
	pyrite	4.25		

formation due to organic substances in biological materials and their similar molecular structures. <sup>245–247</sup>

Previous experiments have demonstrated that organic acids are innate in geological storage formations, and a minute concentration of such acids could increase rock hydrophobicity. <sup>244,248,249</sup> Lundegard and Kharaka <sup>245</sup> demonstrated that Cenozoic sedimentary basins contain sufficient (about



3000 mg L<sup>-1</sup>) monocarboxylic short-chain fatty acids (*i.e.*, acetate) at 353 and 413 K.

Akob *et al.*<sup>244</sup> studied the microbiology and organic matter composition of shale gas wells in Pennsylvania. They found that organic-acid anions, such as acetate, pyruvate, and formate, are abundant in geo-storage media in the range of 66 to 9400 cells per mL owing to microbial activity. The carbon atom of organic acids in fossils varies from C<sub>2</sub> to C<sub>32</sub>.<sup>246,250,251</sup> Hydrocarbons were further biodegraded to produce heavy molecular weight (>C<sub>20</sub>) branched and cyclic-chain organic acids. In 1984, Cyr and Strausz similarly reported the chemisorption of monocarboxylic acid (with concentrations from 1% to 14%) onto an inorganic matrix for Alberta oil sands (Canada).<sup>252</sup>

Previous research has focused on the role of organic acids on rock wettability and interfacial interactions of rock–oil–brine systems, primarily for applications in improving oil recovery.<sup>245,248,253–262</sup> Investigations on how organic acids affect rock–H<sub>2</sub>–brine systems and UHS have been limited. Therefore, this section systematically reviews the effects of organics on H<sub>2</sub>–brine interfacial interactions across rock types, highlighting areas for further research.

### 3.5. Wettability parameters of rock/H<sub>2</sub>/brine systems in geo-storage conditions with organic acids

The H<sub>2</sub> geo-storage capacity of rock formations depends on the wetting characteristics, which influence the withdrawal rate, residual saturation, and containment security. However, due to the prevalent atmospheric reduction, realistic geological and caprock formations often contain organic content. A quantitative evaluation of H<sub>2</sub> geo-storage must consider the wettability of H<sub>2</sub> in natural reservoir conditions. An anoxic, reductive environment is produced by organic acids found in natural geological formations.<sup>188,244,245,263</sup>

For a complete understanding and benchmarking of natural geological settings, the influence of small concentrations of organics on rock-wetting properties in downhole conditions and their interactions with the host rock in distinct heterogeneous formations must be considered. Silanes have been employed in studies to alter the wetting properties from water-wet to oil-wet states to simulate the oil-wet (hydrophobic) nature of reservoir rock.<sup>264–266</sup> Due to their highly reactive nature, silanes cannot be present in actual geo-storage circumstances. Measuring and replicating actual geological storage settings on a laboratory scale is necessary to establish the organic thresholds for wettability investigations.

Subsurface formations are anoxic due to organic molecules; organic traces are even found in aquifers.<sup>244,245</sup> Organic materials containing acid functional groups (*e.g.*, –COOH) can create surfaces more wetted by H<sub>2</sub>.<sup>267</sup> Therefore, this section explores the influence of pressure and temperature on the wetting behavior of reservoir and caprock formations with organic acids. This section covers various rock types, including sandstones, carbonates, and formations representative of caprock.

**3.5.1. Organic-aged quartz-, mica-, and calcite/H<sub>2</sub>/water systems.** Research has demonstrated that pressure and

temperature significantly influence the wetting characteristics of quartz, a representative mineral of sandstone, in the presence of organic compounds in the formation. Igaluer *et al.*<sup>158</sup> demonstrated that the wettability of quartz/H<sub>2</sub>/brine systems, as determined by the contact angle, varies with increasing pressure (0.1 to 25 MPa) and temperature (296 to 343 K). They employed 10 wt% NaCl brine and quartz substrates aged in stearic acid, and the wettability shifted from initial water-wet conditions (0° to 50° for pure quartz) to intermediate-wet conditions. At stearic acid concentrations ranging from 10<sup>-2</sup> to 10<sup>-9</sup> mol L<sup>-1</sup>, under conditions of 25 MPa and 323 K,  $\theta_a$  and  $\theta_r$  were 76.9° and 70.7°, respectively.

This result indicates that the wettability of the quartz/H<sub>2</sub>/brine system decreases as the stearic acid concentration decreases. The decrease in the contact angle is attributed to the reduced hydrophilicity of the quartz surface caused by the adsorption of organic acid, leading to the lower wettability of the quartz surface.<sup>237</sup> Table 4 lists the properties of the organic acids. Notably, saline aquifers can contain higher concentrations of organic acid, significantly affecting trapping capacities.<sup>244–246</sup>

The adsorption of organic acids on quartz substrates was confirmed by the increased carbon concentrations on the surfaces (+1.6 wt% for hexanoic acid, +1.7 wt% for lauric acid, and +2.2 wt% for lignoceric acid).<sup>263,268</sup> Fig. 11 illustrates that the brine contact angle increased as the organic-acid concentration increased. Pure quartz exhibited strong water-wet characteristics in the presence of H<sub>2</sub> ( $\theta_a$  at 40.8° and  $\theta_r$  at 35.1°) but shifted to an intermediate water-wet state ( $\theta_a$  at 91.3° and  $\theta_r$  at 82.7°) at 323 K and 25 MPa when the rock substrates were treated with organic acids containing longer alkyl chains (10<sup>-2</sup> M lignoceric acid).

Moreover, the quartz/H<sub>2</sub>/brine contact angles increased with higher pressure, indicating enhanced H<sub>2</sub> wettability. This increase is associated with the increased H<sub>2</sub> density as pressure increases.<sup>35,158</sup> When quartz substrates are treated with 10<sup>-9</sup> M hexanoic acid,  $\theta_a$  is 42.9° and  $\theta_r$  is 38.6° (at 323 K and 25 MPa), indicating water-wet conditions on the quartz surface (Fig. 11(a)). Exposure to 10<sup>-2</sup> M hexanoic acid resulted in an increase in  $\theta_a$  and  $\theta_r$  to 68.2° and 61.5°, respectively, suggesting a weakly water-wet state. This state could lead to a decrease in the residual trapping capacities of H<sub>2</sub> ( $\theta_a > 50^\circ$ ).<sup>138,187</sup> A similar trend in quartz/H<sub>2</sub>/brine wettability alteration was observed for quartz treated with other organic acids (Fig. 11(a)). For example, the contact angle of quartz/H<sub>2</sub>/brine for 10<sup>-2</sup> M lauric acid was higher than that for quartz aged in 10<sup>-9</sup> M lauric acid. This result indicates an increased adsorption of carbon atoms with a higher acid concentration, resulting in more hydrophobic quartz surfaces.

With the chemical formula KAl<sub>2</sub>(AlSi<sub>3</sub>O<sub>10</sub>)(OH)<sub>2</sub>, mica is analogous to caprock due to its prevalence in shale caprock.<sup>215,269,270</sup> A typical reservoir caprock is water-wet, impeding the upward migration of gas during geological storage. Fig. 11(b) indicates that increasing organic-acid concentrations increases contact angles. The rock achieved a fully H<sub>2</sub>-wet state at 383 K and 25 MPa, with 10<sup>-2</sup> mol L<sup>-1</sup> lignoceric acid ( $\theta_a$  of 106.2° and



**Table 4** Properties of organic acids. The critical properties of organic acids relevant to underground hydrogen storage (UHS) applications, modified from ref. 35. These properties influence interactions between organic acids and rock formations in UHS. Understanding these characteristics is crucial for predicting how organic contaminants affect the wettability and overall efficiency of geological storage systems

Acids	pH (pK <sub>a</sub> )	State	Molar mass (g mol <sup>-1</sup> )	No. of carbon atoms	Molecular formula	Molecular structure
Lignoceric	7.4	Solid	368.630	24	C <sub>24</sub> H <sub>48</sub> O <sub>2</sub>	
Stearic	—	Solid	284.480	18	C <sub>18</sub> H <sub>36</sub> O <sub>2</sub>	
Lauric	5.3	Solid	200.318	12	C <sub>12</sub> H <sub>24</sub> O <sub>2</sub>	
Hexanoic	4	Liquid	116.158	6	C <sub>6</sub> H <sub>12</sub> O <sub>2</sub>	

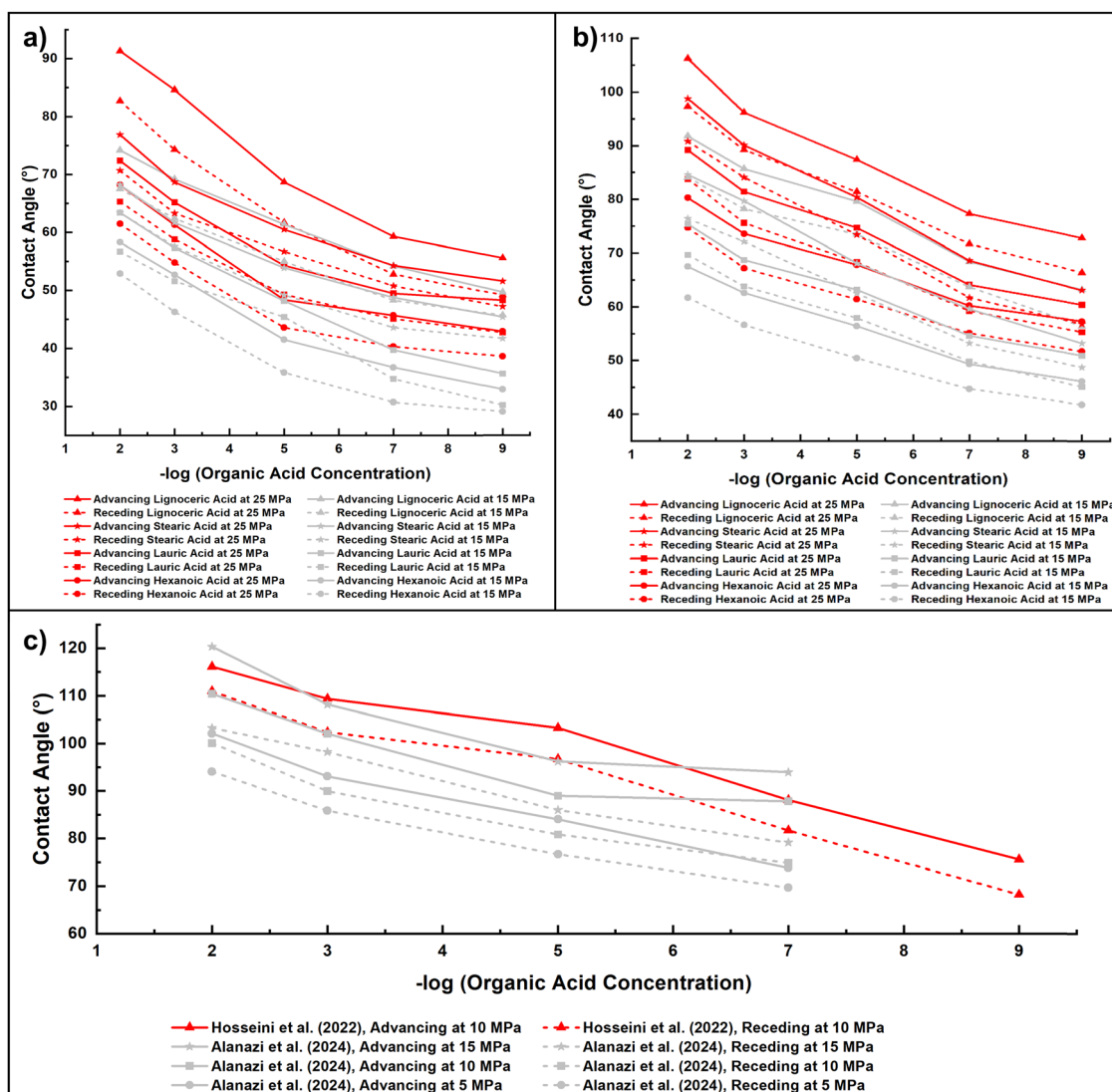


**Fig. 11** Organic-acid concentration effects on the advancing and receding contact angles in rock/H<sub>2</sub>/brine systems. Varying concentrations of organic acids influence the contact angles of H<sub>2</sub> and brine on rock. (a) In the quartz/H<sub>2</sub>/brine system, contact angles increase with increasing organic-acid concentrations, indicating a stronger gas-wetting tendency at higher concentrations.<sup>35,158</sup> (b) Mica/H<sub>2</sub>/brine systems display a similar trend with increasing advancing and receding contact angles as organic-acid concentrations increase.<sup>109,111</sup> (c) The calcite/H<sub>2</sub>/brine system exhibits the most significant rise in contact angles as organic-acid concentration increases, suggesting enhanced gas-wetting behavior with higher organic content.<sup>136,216</sup> All system data were collected from the literature and replotted to compare organic-acid effects comprehensively on wettability in H<sub>2</sub> storage environments.



$\theta_r$  of  $97.3^\circ$ ) as indicated in Fig. 11(b).<sup>109</sup> The alteration in wetting characteristics of the organic-acid-aged mica substrates was attributed to the organic esterification on hydroxyl groups of mica substrates,<sup>180,271</sup> forming covalent bonds between the -OH group on the mica surface and organic acids, rendering the mica H<sub>2</sub>-wet.<sup>138,263,272</sup> Such an alteration of caprock wetting behavior to H<sub>2</sub>-wet (with the receding contact angle exceeding  $90^\circ$ ) could decrease the mica-caprock structural trapping ability and H<sub>2</sub> leakage during UHS.<sup>111</sup>

Calcite is a common mineral in caprock and reservoir rock,<sup>273,274</sup> and its wettability substantially influences structural and capillary trapping during UHS. In calcite-rich caprock, H<sub>2</sub>-wettability produces a low structural trapping capacity resulting from an increased upward suction force, potentially leading to caprock leakage.<sup>187,270</sup> Conversely, in calcite-rich reservoir rock, H<sub>2</sub> wettability could lead to a high structural storage capacity as H<sub>2</sub> occupies most of the pore volume (PV), forming a thicker column.<sup>136</sup> However, this condition can complicate H<sub>2</sub> withdrawal because the reservoir rock is wetted by H<sub>2</sub>. Organic acids can render calcite-rich surfaces more H<sub>2</sub>-wet, affecting their storage potential and stability.

Several studies have reported the effects of pressure and temperature on the wettability of H<sub>2</sub>/calcite in the presence of organic acids.<sup>111,136,216</sup> Fig. 11(c) reveals that the water wettability of calcite decreased with an increasing organic-acid concentration due to the adsorption of the organic acid on the rock surface.<sup>237</sup> For clean calcite surfaces,  $\theta_a$  and  $\theta_r$  are  $64.6^\circ$  and  $55.4^\circ$ , which increased to  $75.9^\circ$  and  $68.7^\circ$  respectively, when the substrate was treated with  $10^{-9}$  mol L<sup>-1</sup> stearic acid.<sup>136</sup> The decreasing trend of calcite hydrophilicity with increasing organic-acid concentrations is consistent with observations for quartz-H<sub>2</sub>-brine<sup>35</sup> and mica/H<sub>2</sub>/brine systems.<sup>111</sup> However, calcite displays higher hydrophobicity than mica and quartz due to its less hydrophilic surface, reducing rock-H<sub>2</sub> interfacial energy.<sup>111,162</sup>

**3.5.2. Influence of organic-acid type, mineralogy, and pressure on hydrogen wettability.** The molecular composition of organic acids, particularly the number of carbon atoms, is critical in modifying reservoir and caprock H<sub>2</sub> wettability.<sup>263</sup> Fig. 11 presents how mica/H<sub>2</sub>/brine wettability varies with organic acids. Longer alkyl chain lengths correspond to higher  $\theta_a$  and  $\theta_r$  values, with lignoceric acid (24 carbon atoms) exhibiting the highest wetting state, followed by lauric acid (12 carbon atoms) and hexanoic acid (six carbon atoms).

Organic acids with a higher number of carbon atoms were more effective in altering the mica substrate wettability toward H<sub>2</sub>-wet conditions.<sup>138,272</sup> For instance, at 15 MPa and  $10^{-2}$  mol L<sup>-1</sup>,  $\theta_a$  was measured as  $67.5^\circ$ ,  $75.4^\circ$ , and  $91.8^\circ$  for hexanoic, lauric, and lignoceric acids, respectively. These results suggest that rock becomes H<sub>2</sub>-wet when the alkyl chain length increases in the following sequence: lignoceric acid > stearic acid > lauric acid > hexanoic acid. In addition, higher pressure results in higher contact angles due to the increased gas density and molecular interaction.<sup>158,275,276</sup>

Similar findings were reported regarding the influence of the alkyl chain length on the H<sub>2</sub> wettability of quartz. Notably, the extent of wettability change for the quartz/H<sub>2</sub>/brine system

is also significantly greater for organic acids with longer alkyl chains, with the most pronounced effects in lignoceric acid, followed by lauric acid and hexanoic acid (see also ref. 35). The authors highlighted that H<sub>2</sub> could leak *via* the caprock with longer alkyl chain lengths, higher organic-acid concentrations, and elevated H<sub>2</sub> pressure. Thus, assuming an initial condition of fully water-wet surfaces for caprock and storage rocks leads to overpredicting structural and residual trapping capabilities of rock during UHS in realistic reservoir conditions.<sup>109</sup>

The literature has documented the wetting behavior of rock minerals aged in organic acids. The contact angles vary with pressure and temperature for minerals under similar geo-storage conditions.<sup>217</sup> The most substantial increase in the contact angle was for calcite, with an almost  $45^\circ$  increase when the pressure increased from 1.0 to 10.0 MPa at 353 K (Fig. 12). In contrast, the contact angle for basalt exhibited the lowest change with a shift of just  $4^\circ$  in the same conditions.

Generally,  $\theta_a$  and  $\theta_r$  of H<sub>2</sub>-brine on mica and quartz substrates increased with the organic-acid concentration and increased alkyl chain length (from C<sub>6</sub> to C<sub>24</sub>).<sup>35,109</sup> The standard energy of adsorption values increased with an increased organic acids alkyl chain length, suggesting enhanced interactions of H<sub>2</sub> molecules with rock surfaces.<sup>35,109,263,277</sup> These studies indicate that organic contaminations intrinsic to reservoir rocks can increase their H<sub>2</sub> wettability. Hence, the effect of intrinsic organic acids on rock wettability must be accurately accounted for to predict storage capacity and containment security during UHS.

The organic contaminants in UHS sites can promote microbial growth by providing nutrients for microorganisms naturally in the underground formation, such as SRB and methanogens. These microbes can produce gases, such as hydrogen sulfide (H<sub>2</sub>S) or CH<sub>4</sub>, as metabolic by-products, contaminating and reducing the purity of the stored H<sub>2</sub>. Moreover, H<sub>2</sub>S is highly corrosive and could damage and corrode pipelines and well casings in the UHS infrastructure. This situation can result in H<sub>2</sub> leakages and reduce the storage infrastructure integrity.<sup>278</sup> Microbes formed in the presence of organic contamination can form biofilms on well casings or reservoir rock surfaces, clogging pores and decreasing the permeability and storage capacity of the reservoir rock. In addition, biofilms can create preferential flow paths, affecting H<sub>2</sub> recovery and injectivity.<sup>279</sup>

Moreover, organic contamination in geo-storage formations can interfere with monitoring systems and sensors for tracking the concentration of H<sub>2</sub> and other gases, such as H<sub>2</sub>S and CH<sub>4</sub>. This interference prevents the timely detection of leakages or other problems during UHS. Moreover, the microbial degradation of organic contaminants in geo-storage sites can produce exothermic reactions, increasing the localized temperature and altering the reservoir pressure and phase behavior of the stored H<sub>2</sub>. This outcome makes it challenging to manage the long-term storage conditions and stability effectively.<sup>280,281</sup>

### 3.6. Mineralogy, surface roughness, salinity, and droplet size on hydrogen wettability

Multiple factors affect rock wettability, such as brine salinity, surface roughness, and rock type. The reservoir water salinity,



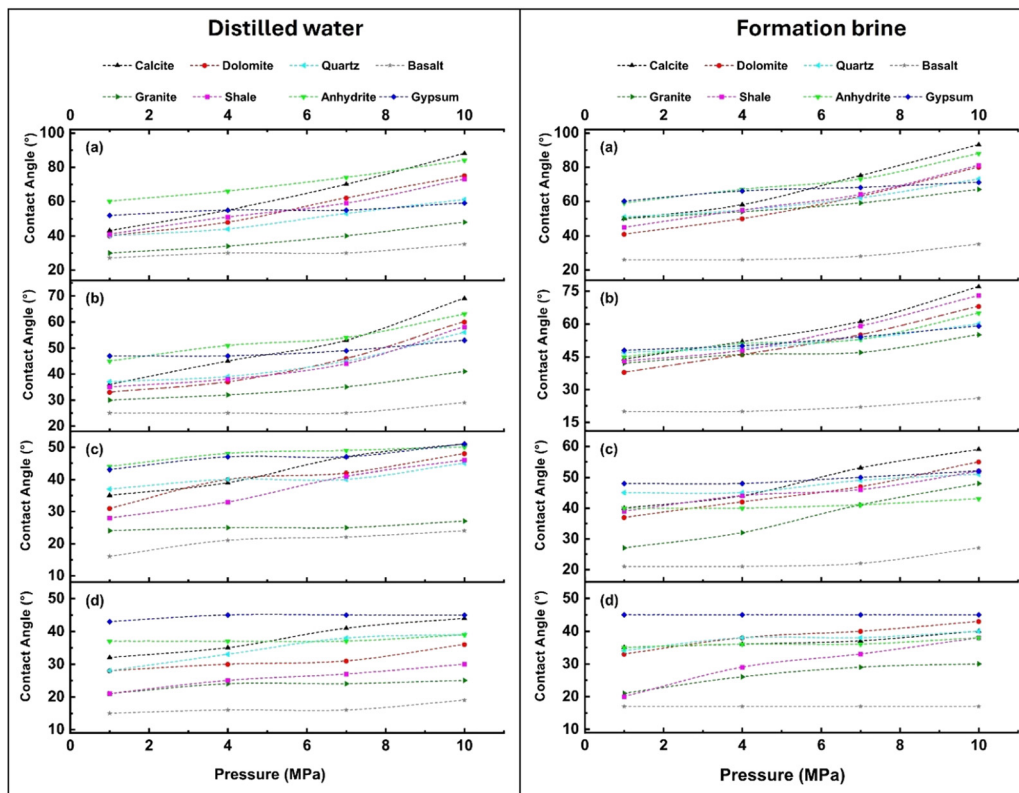


Fig. 12 Experimental contact angle measurements for  $H_2$ /brine systems on minerals aged in  $10^{-2}$  mol  $L^{-1}$  of stearic acid by pressure and temperature. Contact angles vary with pressure for minerals (calcite, dolomite, quartz, basalt, granite, shale, anhydrite, and gypsum) with distilled water (left) and formation brine (right) at (a) 353 K, (b) 333 K, (c) 313 K, and (d) 293 K. Data were measured experimentally at 1 to 10 MPa, finding significant differences between behavior in distilled water and formation brine. These results highlight the influence of mineralogy and fluid composition on wettability, which is critical for understanding underground  $H_2$  storage (UHS) in geological formations.<sup>217</sup> All data were collected from the literature and replotted to compare organic-acid effects comprehensively on wettability in UHS environments.

surface roughness, and rock type all play critical roles in determining the wetting characteristics of the rock/ $H_2$ /brine system. Each rock type, with its unique mineral composition and structure, responds differently to changes in environmental conditions, necessitating customized approaches for practical  $H_2$  storage. Understanding these factors and their links with physical properties, such as pressure, temperature, and organics, is essential for optimizing the UHS, containment capability, and withdrawal efficiency of storage operations in geological formations. Therefore, this section discusses the effects of reservoir water salinity, rock type, and surface roughness on the wetting behavior of rock/ $H_2$ /brine systems.

**3.6.1. Effect of mineralogy on rock/ $H_2$ /brine systems.** Rock types, such as carbonate, sandstone, basalt, and shale, exhibit unique wetting behavior due to their distinct mineral compositions and surface properties. Carbonate is typically composed of various minerals, such as calcite and dolomite, and often displays a high affinity for organic-acid adsorption, significantly altering wettability.

The predominant constituents of sandstone are quartz and other silicate minerals. Sandstone usually exhibits water-wet characteristics. However, organic acids can modify the surface properties, potentially making sandstone more  $H_2$ -wet and

influencing its effectiveness in  $H_2$  storage. In contrast, shale is rich in minerals, such as mica and clay (*e.g.*, illite, kaolinite, and montmorillonite), often displaying complex wetting behavior. The interaction of these clays with  $H_2$ , brine, hydrocarbon, or organic acid can significantly alter wettability, affecting the capillary and structural trapping capacities of shale formations. Surface chemistry, weathering products, and organic acid can influence the wettability of basalt.<sup>110,172,282</sup>

Studies on rock/ $H_2$ /brine systems have reported less wettability on the quartz surface than on mica. These results have been attributed to the higher hydrophilic site content on quartz surfaces than mica.<sup>35,218</sup> Accordingly, Ali *et al.*<sup>35,109,111</sup> and Iglauer *et al.*<sup>158</sup> measured  $\theta_a$  and  $\theta_r$  for pure and organic-acid-modified mica and quartz substrates. These studies found that contact angles increased at higher pressure for mica and quartz. However, contact angles were higher at lower temperatures for mica but at higher temperatures for quartz. These findings indicate that the temperature effect on the wettability of quartz differs from that of mica. Researchers have observed higher contact angle values with increased pressure for several rock types, including mica, quartz, calcite, and shale.<sup>223,232,283,284</sup>

In contrast, Hashemi *et al.*<sup>117</sup> found no clear correlation between the contact angle and rock type in a sandstone/ $H_2$ /water



system for Bentheimer and Berea sandstone, and all estimated contact angle values were within the accuracy range. Similarly, Aghaei *et al.*<sup>285</sup> demonstrated that varying pressures (3.44, 10.34, and 17.23 MPa) and temperatures (303 and 348 K) did not significantly influence the contact angle. For example, at 303 K, the brine contact angle on the S-1 sample was 26.5° at 3.44 MPa and 25.0° at 17.23 MPa. According to the XRD, the sample composition of the reservoir rocks is rich in calcite and dolomite with traces of ankerite and siderite, whereas the caprock is pure anhydrite.<sup>285</sup> Likewise, the brine contact angles for samples S-2 to S-5 exhibited no notable change with pressure. For the S-5 sample, contact angles were 21.5° and 22.5° at 3.44 MPa and 17.23 MPa, respectively. All rock samples remained strongly water-wet in H<sub>2</sub>, with contact angles between 17° and 28°, indicating that storage rock and caprock remained strongly water-wet under all tested

conditions despite variations in pressure and temperature (Fig. 13(a)).

Moreover, Aghaei *et al.*<sup>285</sup> revealed no significant variation in the H<sub>2</sub> wettability of storage (carbonate) and caprock (anhydrite) formations with changes in pressure and temperature. The authors argued that the wetting state of the rock was not sensitive to changes in pressure. Noting that H<sub>2</sub> has a considerably lower density at high pressure than other geo-storage gases, they emphasized that the insignificant change in the H<sub>2</sub> density with pressure could not have caused such a substantial change in the contact angle.<sup>173,283</sup>

**3.6.2. Effect of salinity on rock/H<sub>2</sub>/brine systems.** Reservoir formation water is typically saline, and the salinity level significantly influences rock–fluid interactions, affecting the wetting properties of the caprock and reservoir formation. Saline water

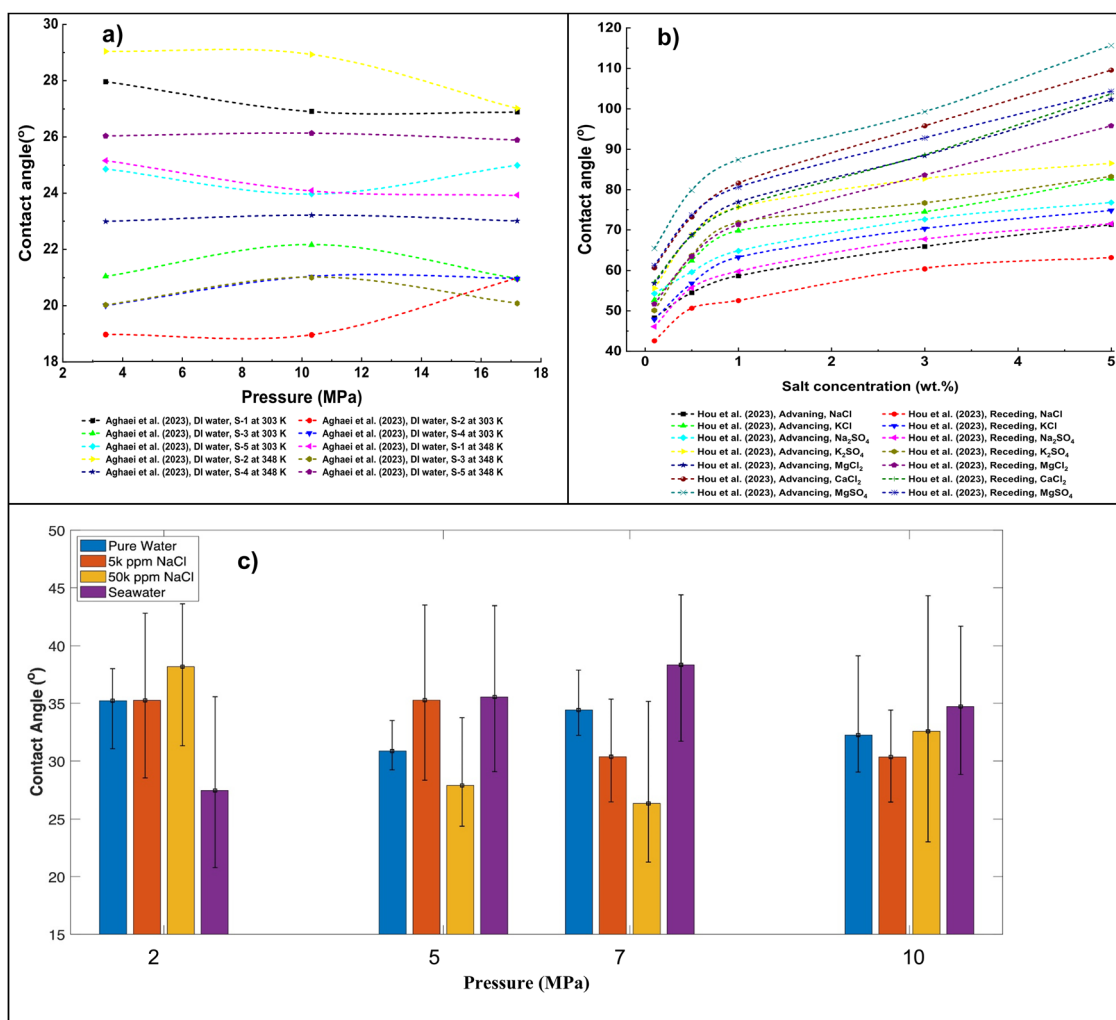


**Fig. 13** Contact angle measurements by rock mineralogy and salinity effects on wettability in hydrogen (H<sub>2</sub>)/brine systems. (a) Contact angles for rock samples (S-1 to S-5) were measured at varying pressures and temperatures, revealing the influence of pressure on the wettability behavior, modified from ref. 285. (b) Effects of monovalent ions (NaCl, KCl, Na<sub>2</sub>SO<sub>4</sub>, and K<sub>2</sub>SO<sub>4</sub>) and divalent ions (MgCl<sub>2</sub>, CaCl<sub>2</sub>, and MgSO<sub>4</sub>) on carbonate/H<sub>2</sub>/brine wettability, indicating a significant increase in the contact angle at higher salinity levels.<sup>223</sup> (c) Influence of salinity on Bentheimer sandstone wettability using pure water, 5000 ppm NaCl brine, 50 000 ppm NaCl brine, and seawater, measured at 303 K under 2, 5, 7, and 10 MPa, illustrating that higher salinity increases the contact angle, especially at elevated pressure.<sup>117</sup> Data were collected and replotted to offer a comprehensive understanding of the pressure, temperature, and salinity effects on wettability in H<sub>2</sub> storage applications.



affects wettability by altering the interfacial forces between the rock and fluids, modifying the contact angles, and influencing the capillary forces in the reservoir. Due to their availability and storage capacity, deep saline aquifers are prime candidates for H<sub>2</sub> geo-storage applications. Therefore, varying brine salinity levels play a crucial role in controlling the rock/H<sub>2</sub> wettability because higher salinity can enhance or diminish the hydrophilicity of the rock surface, affecting the H<sub>2</sub> storage efficiency and stability in these formations.

In this context, Hosseini *et al.*<sup>136</sup> studied the effect of brine salinity with monovalent ions (NaCl) on the water wettability of calcite/H<sub>2</sub>/brine systems. They found that, as the salinity increased,  $\theta_a$  and  $\theta_r$  also increased, indicating a decrease in water wettability. For example, at 323 K and 15 MPa, increasing the salinity from 0 mol kg<sup>-1</sup> to 4.95 mol kg<sup>-1</sup> raised  $\theta_a$  from 69.8° to 80.65° and  $\theta_r$  from 63.35° to 73.3°. This result occurs because a higher salinity requires more ions to neutralize the surface charge of the sample, reducing the surface polarity and promoting de-wetting.<sup>222,286</sup>

A similar trend was also reported for monovalent and divalent cations. For instance, Al-Yaseri *et al.*<sup>287</sup> demonstrated the effect of salt type and salinity on the advancing and receding contact angle for quartz/gas/water systems. Divalent ions cause a more significant increase in  $\theta_a$  and  $\theta_r$  than monovalent ions. As ion valency or salt concentration increases, the zeta potential also rises, leading to more efficient guarding and strong de-wetting of the surface.<sup>136,286,288</sup> In Fig. 13(b), salts containing divalent cations (Ca<sup>2+</sup>, Mg<sup>2+</sup>) increase the contact angle of carbonate/H<sub>2</sub>/brine systems more than those with monovalent ions (Na<sup>+</sup>, K<sup>+</sup>) due to their higher zeta potential. With increasing ion concentration (salinity), advancing and receding contact angles increase due to the compression of the electric double layer.<sup>223</sup>

Following a series of contact angle measurements on rock minerals, Esfandyari *et al.*<sup>217</sup> also demonstrated that salinity and brine ionic composition significantly influence altering the wettability of rock minerals. In formation brine, ions (*e.g.*, K<sup>+</sup>, Mg<sup>2+</sup>, Ca<sup>2+</sup>, and Na<sup>+</sup>) can change the wetting behavior of mineral surfaces compared to distilled water.<sup>109,116,289</sup> In many rock mineral substrates (*e.g.*, basalt, granite, dolomite, gypsum, anhydrite, quartz, and calcite), the rock/H<sub>2</sub>/brine system had higher contact angle values than the rock/H<sub>2</sub>/distilled water system.<sup>217</sup>

The decreased water wettability with increased salinity is consistent for various systems, such as quartz/H<sub>2</sub>/brine,<sup>218</sup> calcite/H<sub>2</sub>/brine,<sup>136,223</sup> and other rock minerals.<sup>217</sup> However, conflicting results regarding the variation in rock/H<sub>2</sub>/brine wettability have also been reported. To assess the influence of salinity, Hashemi *et al.*<sup>117</sup> used brines with three salinity levels: 0, 5000, and 50 000 ppm NaCl, at a constant temperature of 303 K and four pressures from 2 to 10 MPa. The authors measured the contact angles of the Bentheimer/H<sub>2</sub>/brine system at various salinity conditions (pure water, seawater, 5000 ppm, and 50 000 ppm NaCl) at a constant temperature and varying pressure (2, 5, 7, and 10 MPa). They found that salinity, pressure, and temperature did not significantly affect the

sandstone/H<sub>2</sub> wettability, as determined by contact angle measurements. The contact angle datasets are within the experimental expected standard deviation. The variation in salinity did not result in a meaningful change in the measured contact angles, indicating that the wetting state of the rock was insensitive to salinity in the presence of H<sub>2</sub>, as presented in Fig. 13(c). They emphasized that this result is due to the variation in measurement techniques, sample preparation methods, and preparation conditions.

More recently, Al-Yaseri *et al.*<sup>218</sup> studied the wettability of sandstone and limestone using experimental methods and MD simulations. The contact angles for quartz/H<sub>2</sub>/water and calcite/H<sub>2</sub>/water systems were entirely water-wet (contact angle = 0) under all conditions, regardless of salinity, pressure, and temperature variations. The varying brine compositions can significantly influence the long-term safety and stability of UHS in aquifers, depleted hydrocarbon reservoirs, and salt caverns.<sup>267</sup> The solubility of H<sub>2</sub> in brines is dependent on salt type. The solubility of H<sub>2</sub> is reduced with increasing ionic strength and salt concentration, suggesting that in high-salinity brines, H<sub>2</sub> remains in the gas phase instead of dissolving in brine.<sup>290</sup> This process potentially reduces the effectiveness of the UHS system.

In storage sites or zones where the composition of brine varies with time, H<sub>2</sub> solubility in brine could fluctuate, resulting in unpredictable fluid-flow behavior during UHS. Brine containing a high salt concentration and chlorides, such as CaCl<sub>2</sub> and NaCl, are corrosive to metals and can hasten the corrosion processes of UHS materials, such as metallic valves, pipes, and well casings, by forming corrosion cells on steel surfaces, rapidly degrading storage infrastructure and causing failure. The storage site integrity can also be compromised by the corrosion of the well casing and other infrastructure, causing contamination and potential leakages of the stored H<sub>2</sub>.<sup>290,291</sup>

Moreover, the geomechanical stability of the UHS site can be affected by pressure build-up due to the varying density of brine compositions. For instance, a denser, high-salinity brine could result in higher pressure in the storage formation. This process could stress the rock formation and rupture containment structures if the pressure exceeds the strength of the geological formation.<sup>292</sup> Changes in brine composition with time can cause salinity-driven precipitation or dissolution, altering the rock permeability and porosity and the geological formation pore structure. Clogged pores can reduce the rock storage capacity due to salt precipitation.

In some instances, brine containing sulfur (S) or iron (Fe) could react with the stored H<sub>2</sub>, causing contamination, such as H<sub>2</sub>S, that could degrade the purity of the stored H<sub>2</sub>. Organic acids or nutrients in the brine could enhance microbial growth, producing CH<sub>4</sub> and H<sub>2</sub>S. Microbial by-products can contribute to corrosion, further affecting the storage infrastructure. Moreover, the varying brine composition and changes in its chemistry can affect the mechanical properties of the salt and the rate of “salt creep” in a cavern, where the surrounding salt formation deforms under pressure, reducing the cavern stability.<sup>293,294</sup>



**3.6.3. Effect of drop size on rock/H<sub>2</sub>/brine systems.** During measurement, the bubble or droplet size influenced the experimental contact angle values. The literature presents varying perspectives regarding how the drop size affects the experimental values of the contact angle. Hashemi *et al.*<sup>117</sup> reported on the effect of droplet size on the contact angle of the sandstone/H<sub>2</sub>/brine system. The measured contact angles increased with decreased bubble sizes. The progressive decrease in bubble sizes was attributed to the diffusion or dissolution of H<sub>2</sub> gas into the brine. The dependence of the contact angle on the drop size diminishes as the volume increases (Fig. 14(a and b)). Studies have reported similar observations while measuring the contact angles of rock/CO<sub>2</sub>/brine systems.<sup>184,295–297</sup> This variation was attributed to gravity effects for larger fluid bubbles and the influence of the rock-surface composition.<sup>117</sup> The implications of the bubble size on contact angle measurement could be minimized by taking several images of the injected bubble for each experimental run and determining the mean contact angle of the droplets.

As a drop becomes larger, the influence of gravity on the drop shape increases. This effect is accounted for by the Young–Laplace equation of axisymmetric drop shapes attached to a needle or resting on a solid surface. From the Young–Laplace relation, the IFT can be deduced based on the balance between gravitational and interfacial forces. Regarding the contact angle at the three-phase contact of a drop resting on a solid surface, gravity can distort the macroscopic value.<sup>295</sup> The ratio of gravitational to interfacial forces is given by the Eötvös or bond number, as indicated in eqn (15):

$$B_o = \frac{g\Delta\rho d^2}{\sigma} \quad (15)$$

where  $g$  denotes the gravity constant in  $\text{m s}^{-2}$ ,  $\Delta\rho$  represents the density difference between two adjacent phases in  $\text{kg m}^{-3}$ ,  $d$  indicates the drop diameter in m, and  $\sigma$  denotes the IFT in  $\text{mN m}^{-1}$ .

For tiny drops and a relatively high IFT,  $B_o$  is smaller than unity, leading to relatively spherical drops. Therefore, small

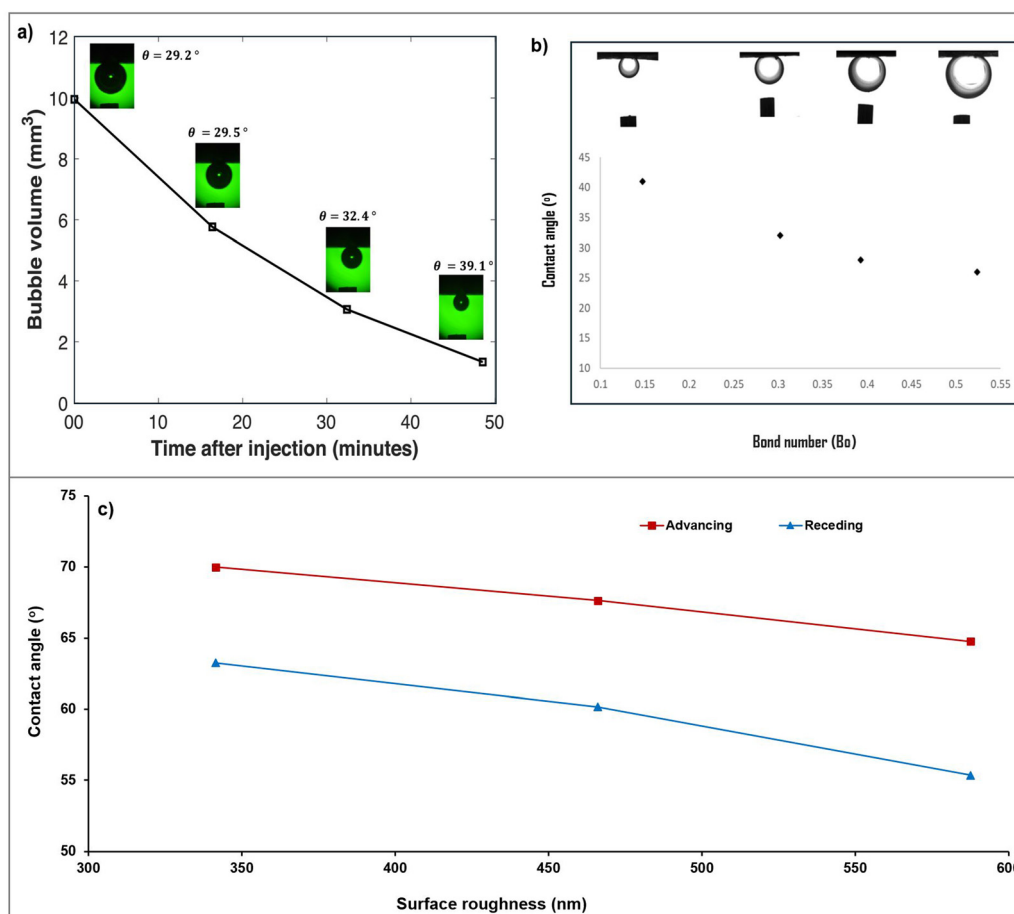


**Fig. 14** Effect of bubble size and surface roughness on the contact angles in hydrogen (H<sub>2</sub>)/brine systems. (a) Influence of bubble size on the contact angle in the Bentheimer sandstone/H<sub>2</sub>/water system at 296.5 K and 5.12 MPa, illustrating how the bubble volume changes over time, affecting wettability.<sup>117</sup> (b) Contact angle measured using the captive-bubble method as a function of the bond number, demonstrating how the buoyancy of different-sized bubbles affects the angle at the three-phase contact line.<sup>295</sup> (c) Variation in calcite/H<sub>2</sub>/deionized water wettability with changes in surface roughness at 323 K and 15 MPa, where increased roughness yields lower contact angles, indicating a stronger brine-wetting tendency.<sup>136</sup> The data were collected from the literature and replotted to provide insight into the effects of bubble size and surface roughness on wettability behavior in underground H<sub>2</sub> storage.



drops are preferred because the influence of gravity on the contact angle is reduced. A threshold value of  $B_0$  is arbitrarily set to unity. This finding was also demonstrated for shale surfaces in DI water and  $\text{CO}_2$  at 10 MPa and 333 K. Therefore, sessile or captive-bubble drops should have base diameters of no less than 5 mm.<sup>295</sup>

#### 3.6.4. Effect of surface roughness on rock/ $\text{H}_2$ /brine systems.

The surface roughness of rock, which defines its topography, also has a pronounced effect on the wettability of rock/ $\text{H}_2$ /brine systems. Rougher surfaces increase the surface area and have more contact points that can trap fluids differently than smoother surfaces.<sup>298</sup> Surface roughness can cause variations in local wettability, creating heterogeneous wetting conditions that affect fluid distribution and flow in the reservoir and the capillary trapping efficiency.<sup>146,299</sup>

Hosseini *et al.*<sup>136</sup> investigated contact angles on three pure calcite substrates with varying surface roughness values (RMS = 341, 466, and 588 nm) to examine the relationship between wettability and surface roughness.<sup>136</sup> Fig. 14(c) illustrates that  $\theta_a$  and  $\theta_r$  for the calcite/ $\text{H}_2$ /DI water system exhibited a decreasing trend as the RMS roughness value increased at 323 K and 15 MPa. For example, for a surface roughness of 341 nm,  $\theta_a$  and  $\theta_r$  were 69.8° and 63.35°, respectively. However, for a surface roughness of 588 nm,  $\theta_a$  and  $\theta_r$  decreased to 64.6° and 55.4°, respectively, suggesting that smoother surfaces are less water-wet than coarser surfaces. Eqn (16) illustrates how Wenzel's equation can account for this observation.<sup>300</sup>

$$\cos \theta_{\text{rough}} = r \cos \theta_{\text{smooth}} \quad (16)$$

where  $r$  denotes the roughness ratio between the ideal and actual surfaces,  $\theta_{\text{rough}}$  represents the contact angle measured on the rough surface, and  $\theta_{\text{smooth}}$  indicates the ideal contact angle recorded on a perfectly smooth surface. This effect occurs because the liquid penetrates the grooves on the surface,<sup>301,302</sup> influencing wettability.

#### 3.7. Effect of pressure and temperature on interfacial tension for underground hydrogen storage

Studying the effects of pressure and temperature on interfacial properties is critical for understanding UHS. Variations in pressure and temperature can significantly influence the interactions between  $\text{H}_2$ , rock, and brine, specifically, the  $\text{H}_2$ -fluid, rock/ $\text{H}_2$ /fluid interactions, and the overall stability of  $\text{H}_2$  in subsurface environments. Analyzing how pressure and temperature affect these interfacial properties allows for optimizing storage strategies, enhances the efficiency of  $\text{H}_2$  containment, and reduces potential losses due to leakages. Therefore, this section compiles data on  $\text{H}_2$ /fluids and rock/ $\text{H}_2$ /fluids IFT for UHS and provides a comparative discussion.

**3.7.1. Hydrogen-fluid interfacial tension.** The general trend observed across assorted studies is that the IFT between  $\text{H}_2$  and aqueous solutions tends to decrease with increasing pressure. This observation suggests that higher-pressure environments enhance  $\text{H}_2$ -fluid interactions, lowering IFTs. Disparities in these study trends can be attributed to specific properties of the aqueous solutions and experimental conditions, such as

temperature and salinity. Higher temperatures and salt concentrations affect IFT differently than pure water, with  $\text{H}_2$ -aqueous solutions often exhibiting a more pronounced increase in IFT under pressure, indicating the significant roles of ionic strength and temperature in  $\text{H}_2$  interfacial behavior. Understanding these variations is crucial for optimizing  $\text{H}_2$  storage and transport in diverse subsurface geological conditions, where pressure and temperature gradients can substantially vary and affect storage efficiency and safety measures, particularly concerning caprock integrity.

Fig. 15 presents the datasets of the IFT between  $\text{H}_2$  and aqueous solutions as a function of pressure and temperature, with data from multiple studies. The figure reveals the relationship between pressure (from 0 to 35 MPa) and IFT (from 30 to 90  $\text{mN m}^{-1}$ ) for specific combinations of  $\text{H}_2$  and aqueous solutions under various conditions, including temperatures from 293 to 423 K, and several salt concentrations. The general trend is that IFT decreases with increasing pressure for most  $\text{H}_2$ -aqueous solution combinations. This trend is noticeable in the lower-pressure range (0 to 15 MPa), where significant reductions in IFT are evident for many solutions. For example, with increasing pressure, the IFT significantly reduced in the data series for  $\text{H}_2$  in 1.05 M  $\text{H}_2\text{O}$  at 373 K (from ref. 303) and  $\text{H}_2$  in water at 298 K (from ref. 304). This finding suggests that higher-pressure environments may facilitate better  $\text{H}_2$ -fluid interactions and lower IFTs.

Differences in trends in studies can be ascribed to the specific properties of the aqueous solutions and the experimental conditions. For instance, elevated temperature and salt (*e.g.*, NaCl) affect IFT differently than pure water. The  $\text{H}_2$ -NaCl solutions typically exhibit a more pronounced increase in IFT with increased pressure compared to pure water, suggesting that ionic strength and temperature play significant roles in the interfacial behavior of  $\text{H}_2$  in aqueous environments.<sup>170,217,305</sup> Salt affects the interfacial behavior of  $\text{H}_2$ , possibly due to changes in ionic strength and interactions at the molecular level. These variations are critical for understanding and optimizing  $\text{H}_2$  storage and transport in subsurface geological formations, where pressure and temperature widely vary.<sup>306</sup>

The effect of temperature is also evident in Fig. 15. For instance, studies involving  $\text{H}_2$ -water at elevated temperatures (*e.g.*,  $\geq 373$  K) display lower IFT values than those at lower temperatures (*e.g.*, 298 K). This trend implies that higher temperatures may enhance the interaction between  $\text{H}_2$  and the aqueous phase, reducing IFT. This trend is crucial for subsurface conditions where temperature gradients can significantly influence storage efficiency.

Although most studies have indicated a decreased IFT with increasing pressure, some have exhibited relatively stable or less pronounced changes (see ref. 170, 305 and 307). For example, Omrani *et al.*<sup>305</sup> documented that temperature and pressure have the greatest and least influence, respectively, on the IFT of the  $\text{H}_2$ -water/brine system. Temperature changes are more noticeable at lower salinities, whereas salinity significantly influences IFT values at higher temperatures. The reduction in IFT due to pressure changes is relatively insignificant



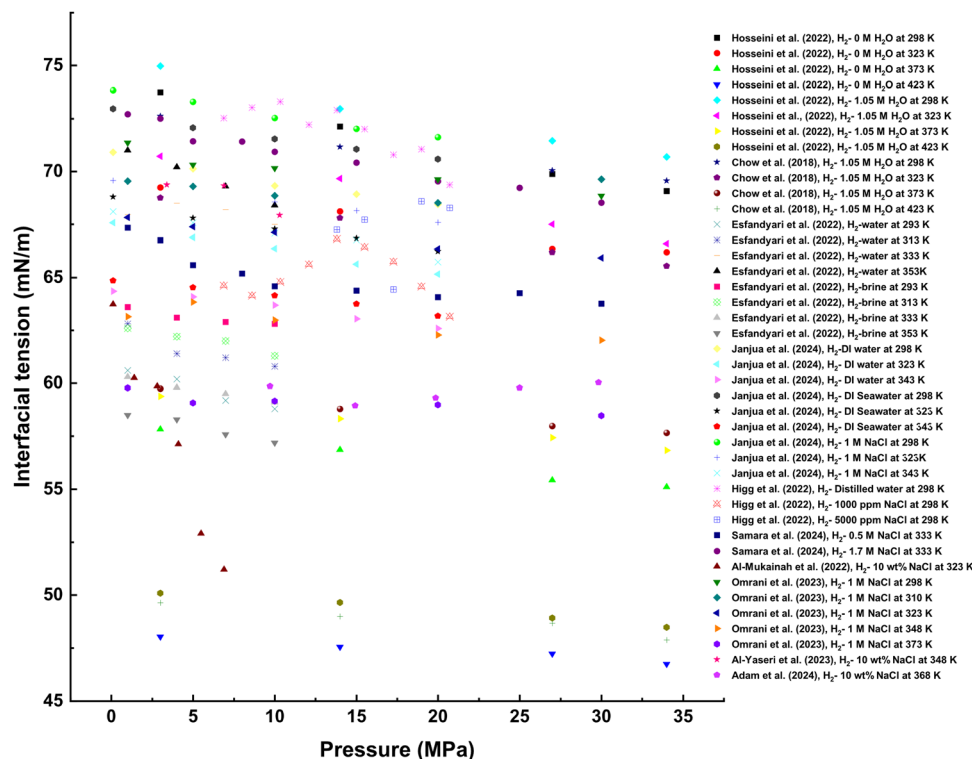


Fig. 15 Interfacial tension (IFT) between hydrogen ( $H_2$ ) and aqueous solutions by pressure and temperature. The IFT varies between  $H_2$  and aqueous solutions with increasing pressure and temperature across multiple datasets. Data are from several studies<sup>170,173,217,233,304–308</sup> and were replotted to offer a comprehensive understanding of how pressure and temperature affect  $H_2$  interaction by brine composition, which is vital for optimizing  $H_2$  storage and retrieval in subsurface environments.

primarily because the density dependence on pressure is lower in the system.

Similarly, the IFT data for  $H_2$  in 1000 and 5000 ppm NaCl at various temperatures (from ref. 170) does not correlate with the IFT values across the pressure range. This stability could imply that specific experimental methods or solution compositions offer more predictable and stable interactions with  $H_2$ . Understanding these trends and differences is essential for optimizing UHS in geological formations, ensuring efficient and safe storage capacities while maintaining the caprock seal integrity.

**3.7.2. Rock/hydrogen/fluid interfacial tension.** The interactions between rock types, such as shale, sandstone, carbonate, basalt, evaporite, and clay, with  $H_2$  and water display varying IFT values at specific pressures, highlighting the significance of the rock type and fluid composition on interfacial interactions. The consensus on the trend of rock- $H_2$ -water IFT with varying temperatures and pressure is that, as pressure increases, IFT generally decreases, indicating improved wettability and fluid-flow characteristics that could enhance  $H_2$  storage efficiency. However, the extent of IFT reduction differs between rock types and temperatures, demonstrating the need for customized approaches in designing UHS facilities to maximize storage capacity and recovery rates.

Esfandyari *et al.*<sup>309</sup> presented the results of changing the rock-gas and gas-water IFT in distilled and formation water systems. The rock-fluid IFT cannot be directly measured in the

laboratory; therefore, the solid-liquid IFT ( $\gamma_{SL}$ ) and solid-gas IFT ( $\gamma_{SG}$ ) for rock/ $H_2$ /water minerals were evaluated with Neumann's equations of state (see Section 3).

Generally,  $\gamma_{SG}$  values decrease with pressure. For example, at 293 K, the quartz- $H_2$  IFT system reduced over the pressure range from 75.06 to 67.47 mN m<sup>-1</sup>. However, mineralogy is a crucial factor responsible for varying mineral- $H_2$  IFTs due to the influence of temperature. For instance, at a constant pressure of 5 MPa, the quartz- $H_2$  IFT increased by 15 units as the temperature rose from 293 to 353 K. In contrast, anhydrite, basalt, and gypsum marginally decreased in  $\gamma_{SG}$  with an increased temperature.<sup>309</sup>

Comparable tendencies in the rock/ $H_2$ /formation brine system were found in the rock/ $H_2$ /distilled water system. For instance, at a constant temperature of 313 K, the  $\gamma_{SG}$  value of the basalt- $H_2$  system dropped from 72.01 to 68 mN m<sup>-1</sup> as the pressure rose from 1.0 to 10.0 MPa. However, as the temperature increased from 293 to 353 K at a constant pressure of 4.0 MPa, it dropped from 60.35 to 71.75 mN m<sup>-1</sup>. Anhydrite, basalt, and gypsum displayed the lowest  $\gamma_{SG}$  values, and shale, dolomite, and calcite exhibited the highest. Rising gas density and rock-gas intermolecular forces, connected to the cohesive energy of the gas and rock due to an increase in pressure, are responsible for the decreased IFT of the rock-gas system with rising pressure, strengthening the interactions between the gas and solid.<sup>48,167,196,197,309–311</sup> This finding underscores the



importance of rock–liquid and rock–gas IFT for the H<sub>2</sub> geo-storage potential of rock minerals, highlighting the variations in these factors according to mineralogy.

Fig. 16 presents IFT datasets from the literature for rock/H<sub>2</sub>/brine systems under various pressures, temperatures, and brine compositions. The data represent the IFT of rock types (e.g., shale, quartz, basalt, mica, calcite, evaporite, illite, montmorillonite, and kaolinite) with H<sub>2</sub> and either water or brine.<sup>109,116,225,309</sup> A prominent trend is that rock/H<sub>2</sub>/brine systems have varying IFT values at a given pressure, revealing the influence of rock type and fluid composition on interfacial interactions. For instance, the IFT for quartz/H<sub>2</sub>/brine systems<sup>116</sup> is typically lower than that for shale/H<sub>2</sub>/water systems,<sup>309</sup> signifying that the quartz surface has a different affinity for H<sub>2</sub> and brine than shale.

As pressure increases, the general trend for most studies is decreased IFT in rock/H<sub>2</sub>/fluid system. For instance, different temperatures indicate a noticeable drop in IFT with increasing pressure.<sup>309</sup> The IFT drop suggests that higher pressure reduces the IFT between rock/H<sub>2</sub>/fluid interfaces, which could affect UHS and recovery in formations. Reducing IFT with increasing pressure could facilitate better wettability and fluid-flow characteristics in the porous media, enhancing the H<sub>2</sub> storage efficiency. Lower IFT values indicate more favorable conditions

for H<sub>2</sub> trapping and storage efficiency. However, such values might not be favorable for H<sub>2</sub> withdrawal. A higher H<sub>2</sub> column height implies that more H<sub>2</sub> becomes mobile, increasing the pressure exerted on the caprock and reducing the expected containment security of the H<sub>2</sub>. These findings emphasize the need for tailored approaches when designing UHS facilities, considering the specific rock and fluid types and the operational pressure and temperature to optimize storage capacity and recovery rates.

As the pressure increases from 5 to 20 MPa, the IFT of most rock/H<sub>2</sub>/brine systems decreases, which is consistent across temperatures. For example, Esfandiyari *et al.*<sup>309</sup> observed a reduction in IFT for shale/H<sub>2</sub>/water at 298 and 353 K as the pressure increased. Similar trends were noted for other rock types at various temperatures, such as calcite–H<sub>2</sub>–brine at 298 and 353 K<sup>312</sup> and clay,<sup>140</sup> indicating a general tendency for the IFT to decrease with pressure in rock/H<sub>2</sub>/brine systems.

However, the rate and extent of the IFT reduction with increasing pressure vary among rock types and temperatures. For instance, the IFT reduction for mica/H<sub>2</sub>/brine at 343 K found by Ali *et al.*<sup>167</sup> is less pronounced than quartz–H<sub>2</sub>–brine at 343 K.<sup>116</sup> Clays, such as montmorillonite–H<sub>2</sub>–brine at 333 K, exhibit lower IFT values across the pressure range than other systems.<sup>140</sup> These differences highlight the importance of rock

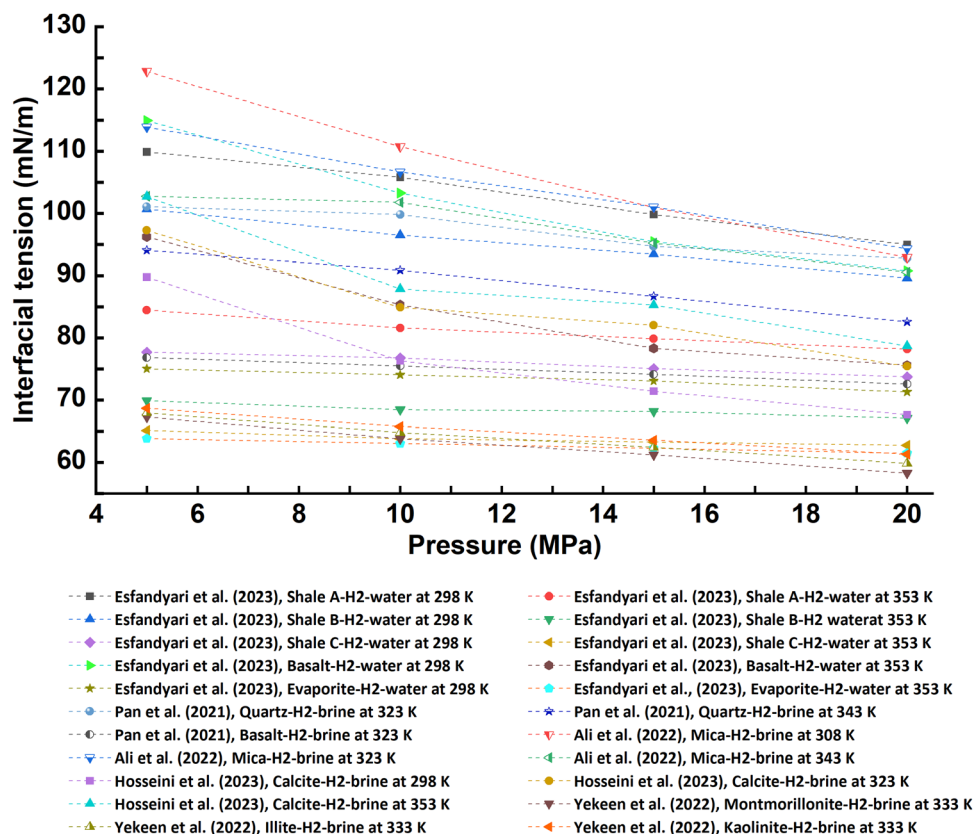


Fig. 16 Rock mineral/H<sub>2</sub> interfacial tension (IFT) values in distilled water and formation brine by pressure and temperature. The IFT between hydrogen (H<sub>2</sub>) and rock minerals (e.g., calcite, dolomite, quartz, basalt, and others) in distilled water and formation brine vary under varying pressure and temperature conditions. The data were collected and replotted from multiple studies<sup>118,140,167,309,312</sup> to provide a detailed comparison of how pressure and fluid composition influence rock–fluid IFT, which is critical for assessing the feasibility of H<sub>2</sub> storage in geological formations.



type, temperature, and pressure in determining the interfacial properties of rock/H<sub>2</sub>/brine systems, which are crucial for optimizing UHS strategies. Additionally, the temperatures at which the experiments were conducted are significant because higher temperatures (*e.g.*, 353 K) tend to have lower IFT values across all systems, highlighting the effect of thermal conditions on IFT.

### 3.8. Role of cushion gas in underground hydrogen storage

In H<sub>2</sub> storage, cushion gas refers to the portion of gas that remains in the storage medium to maintain adequate pressure and ensure efficient and safe operation. Hydrogen loss is prevented *via* a cushion gas that acts as a buffer; unlike the “working” gas (the H<sub>2</sub> actively used or withdrawn), the cushion gas is not intended for regular extraction.<sup>46,89,313,314</sup> The cushion gas is essential for maintaining the structural integrity of the storage system, providing pressure support, and facilitating the withdrawal of the working gas *via* wettability and interfacial force modification. In H<sub>2</sub> storage, cushion gas can be either H<sub>2</sub> itself or another gas, such as CH<sub>4</sub>, N<sub>2</sub>, or CO<sub>2</sub>, depending on the storage requirements and design. Other fluids (oil, water, CH<sub>4</sub>, N<sub>2</sub>, and CO<sub>2</sub>) in the reservoirs must be in the wetting phase to keep H<sub>2</sub> confined in the reservoir pores, preventing its escape or migration due to its low density, small molecular size, and high diffusive nature into the rock formation.<sup>39,128,315</sup>

Hydrogen up-coning has been identified as a danger of UHS in saline aquifers without preinjection of cushion gas. Some studies have suggested that this problem could be curtailed using shallow extraction wells.<sup>21,29,41,270</sup> Cushion gas is meant to maintain formation pressure and provide the required pressure for the steady and stable withdrawal of the stored H<sub>2</sub> during high demand. Gases with a high propensity to wet the rock more than H<sub>2</sub> are usually used as cushion gas for UHS.<sup>40,316,317</sup> Research has generally revealed that N<sub>2</sub> and CO<sub>2</sub> are more gas-wet than H<sub>2</sub> on storage and caprock surfaces, suggesting that they are favorable for maintaining the formation pressure to ease the displacement and withdrawal of H<sub>2</sub> during UHS.<sup>35,46,108,110,318,319</sup> Formation gas has been suggested as cushion gas for H<sub>2</sub> storage. In previous case studies, the recovery of H<sub>2</sub> was reported to increase when the formation gas was preinjected as cushion gas. However, this approach was at the expense of H<sub>2</sub> purity.<sup>29,33,41,320</sup>

**3.8.1. Effects of cushion gas on rock/H<sub>2</sub>/brine system wettability.** The wetting characteristics at the solid–liquid–gas interface are immensely influenced by fluid composition and rock-surface characteristics. Ali *et al.*<sup>236</sup> underscored the role of gas adsorption at solid–gas and solid–liquid interfaces in defining wettability. The wettability of kaolinite–H<sub>2</sub>–brine was investigated with the influence of varying compositions of cushion gases (CO<sub>2</sub> and CH<sub>4</sub>) using MD simulations with the Groningen Machine for Chemical Simulation (GROMACS) package. Simulations computed the liquid–gas IFT and contact angles for 10% NaCl brine at 323 K with pressure ranging from 5 to 40 MPa, illustrating that the addition of CO<sub>2</sub> or CH<sub>4</sub> reduces the density of H<sub>2</sub> molecules adsorbed near the surface, as indicated in Fig. 17(a). Additionally, CO<sub>2</sub> displaced some water molecules

from the surface. An associated decrease in the contact angle was noted with increasing CH<sub>4</sub> or CO<sub>2</sub> in the H<sub>2</sub> phase due to the more vital interaction of CH<sub>4</sub> or CO<sub>2</sub> with the solid surface than H<sub>2</sub>–surface interactions.

The kaolinite surface becomes less water-wet due to the cushion gases CO<sub>2</sub> and CH<sub>4</sub>, which cause larger contact angles. In pure H<sub>2</sub>, the kaolinite siloxane surface is intermediate-wet under subsurface gas storage conditions, with contact angles from 91° to 106°. Nevertheless, CO<sub>2</sub> yields a substantial increase in contact angles, suggesting that CO<sub>2</sub> or CH<sub>4</sub> facilitates more efficient H<sub>2</sub> recovery. These buffer gases also decrease the gas–brine IFT, with CH<sub>4</sub> having a less pronounced effect than CO<sub>2</sub>.<sup>236</sup>

An IFT decrease may result in lower capillary sealing pressure, allowing H<sub>2</sub> to be extracted at reduced pressure. The effectiveness of the cushion gas is linked to the density difference between the resulting gas mixture and water. Both CO<sub>2</sub> and CH<sub>4</sub> in kaolinite/H<sub>2</sub>/brine systems decreased the water wettability of the clay, suggesting that CO<sub>2</sub> and CH<sub>4</sub> reduce the sealing capacity of kaolinite while potentially improving H<sub>2</sub> recovery.<sup>236</sup>

Most cushion gases exhibit higher wetting tendencies than H<sub>2</sub>; thus, their presence in reservoirs increases the brine–gas contact angle, enhancing the wettability of the gas mixture. Several studies have investigated the effects of cushion gases, such as CH<sub>4</sub>, CO<sub>2</sub>, and N<sub>2</sub>, on the wetting characteristics of rock–H<sub>2</sub> systems. Contact angles of H<sub>2</sub>, CH<sub>4</sub>, and H<sub>2</sub>–CH<sub>4</sub>/brine mixture systems and interfacial properties were examined using organic-rich shale samples. The contact angles between rock and CH<sub>4</sub> with brine were higher than those between rock and H<sub>2</sub> with brine (Fig. 17(b)). Gas mixture testing at a 50:50 ratio revealed less influence on wettability than pure gases.<sup>284</sup> In addition, the rock/H<sub>2</sub>/gas contact angles for mixtures of brine and H<sub>2</sub> with CH<sub>4</sub> or CO<sub>2</sub> fell between those for pure gases.<sup>149,236,284</sup>

### 3.8.2. Cushion gas effects on H<sub>2</sub>–fluid interfacial tension.

The IFT datasets against H<sub>2</sub> content (mole %) for H<sub>2</sub> + CO<sub>2</sub> + H<sub>2</sub>O, H<sub>2</sub> + CH<sub>4</sub> + H<sub>2</sub>O, and H<sub>2</sub> + N<sub>2</sub> + H<sub>2</sub>O systems at comparable pressure and temperature values indicated that H<sub>2</sub> increases the IFT. This increase in IFT enhances capillary trapping and reduces the penetration into caprock.<sup>236,308</sup>

Introducing cushion gases, such as CH<sub>4</sub>, CO<sub>2</sub>, and N<sub>2</sub>, into the H<sub>2</sub> phase decreases the H<sub>2</sub>/cushion gas/water IFT (Fig. 18). This result is due to the unique properties of H<sub>2</sub>, which interacts differently with these gases than with brine alone. The small molecular size and high diffusivity of H<sub>2</sub> complicate mixing with cushion gases, increasing IFT with a higher H<sub>2</sub> mole percentage.<sup>321–324</sup> Hence, cushion gases in the H<sub>2</sub> phase can enhance H<sub>2</sub> storage efficiency by improving the wettability and H<sub>2</sub>-flow characteristics of the reservoir.

Moreover, IFT is critical to understanding fluid behavior in subsurface environments, particularly in scenarios involving H<sub>2</sub>–water systems with cushion gases, such as CO<sub>2</sub>, CH<sub>4</sub>, and N<sub>2</sub>. Literature data on H<sub>2</sub>–cushion gas–water IFT reveal a consistent trend where IFT decreases with increasing pressure across these gas mixture–water systems (Fig. 19). This trend is significant because it influences the ease of H<sub>2</sub> extraction,



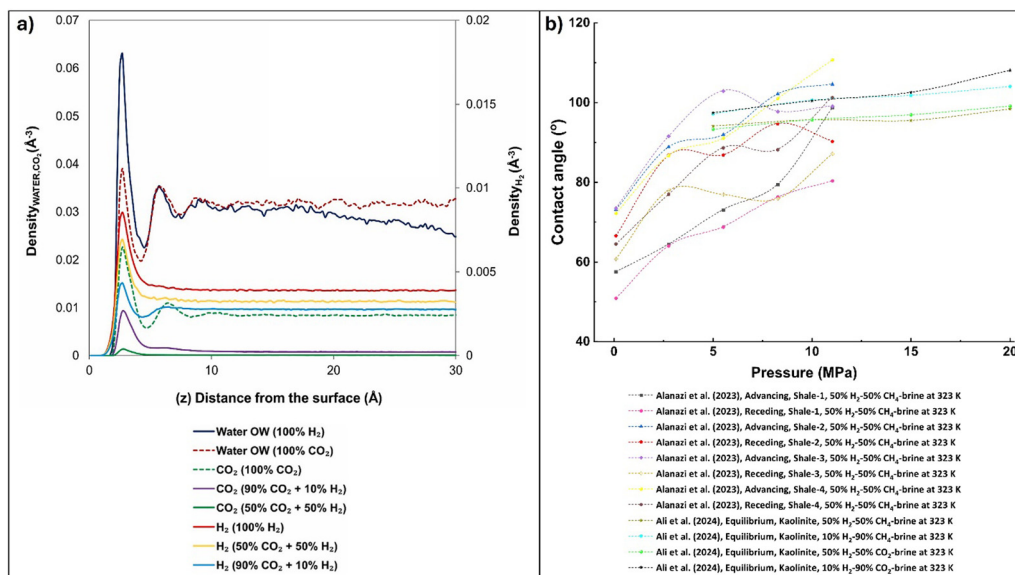


Fig. 17 Atomic density profiles and contact angle variations in rock/H<sub>2</sub>/cushion gas/liquid systems. (a) Profiles of atomic density along the z-axis, perpendicular to the surface, for carbon atoms in CO<sub>2</sub>, oxygen (O<sub>2</sub>) atoms in water, and H<sub>2</sub> at 323 K and 20 MPa. A single-site model was employed to simulate H<sub>2</sub>, with the compositions expressed as mass percentages. The reference plane,  $z = 0$ , aligns with the uppermost O atoms on the silica tetrahedra at the kaolinite surface.<sup>236</sup> (b) Contact angles for rock types and cushion gas mixtures in rock/H<sub>2</sub>/cushion gas/liquid systems, providing insight into how gas and rock compositions influence wettability. The data were collected and replotted from ref. 236 and 284 to provide a detailed comparison of how pressure and fluid composition affect the wettability of rock–fluid systems, which is critical for assessing the feasibility of H<sub>2</sub> storage in geological formations.

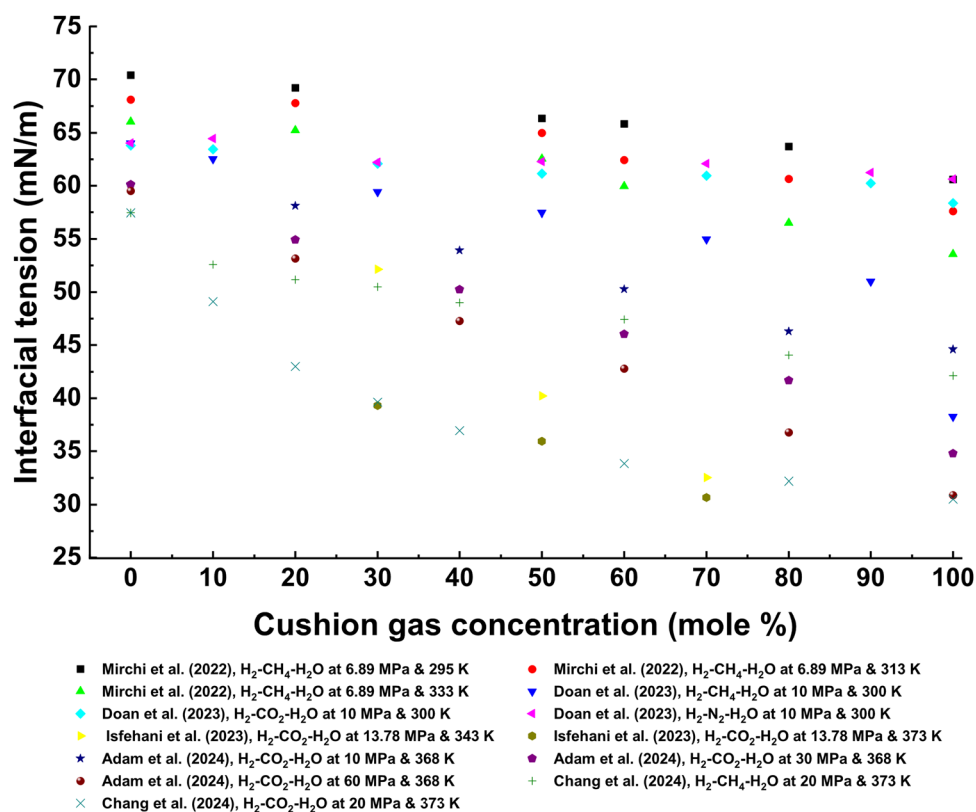


Fig. 18 Cushion gas effects on hydrogen (H<sub>2</sub>)–water interfacial tension (IFT). Introducing cushion gases (e.g., CH<sub>4</sub>, CO<sub>2</sub>, and N<sub>2</sub>) into the H<sub>2</sub> phase reduces the H<sub>2</sub>–cushion gas–water IFT. Data were collected from studies and replotted to illustrate the influence of gases on the interfacial behavior of H<sub>2</sub> in water systems.<sup>307,321,324–326</sup> This information is crucial for optimizing gas mixtures in underground H<sub>2</sub> storage applications.



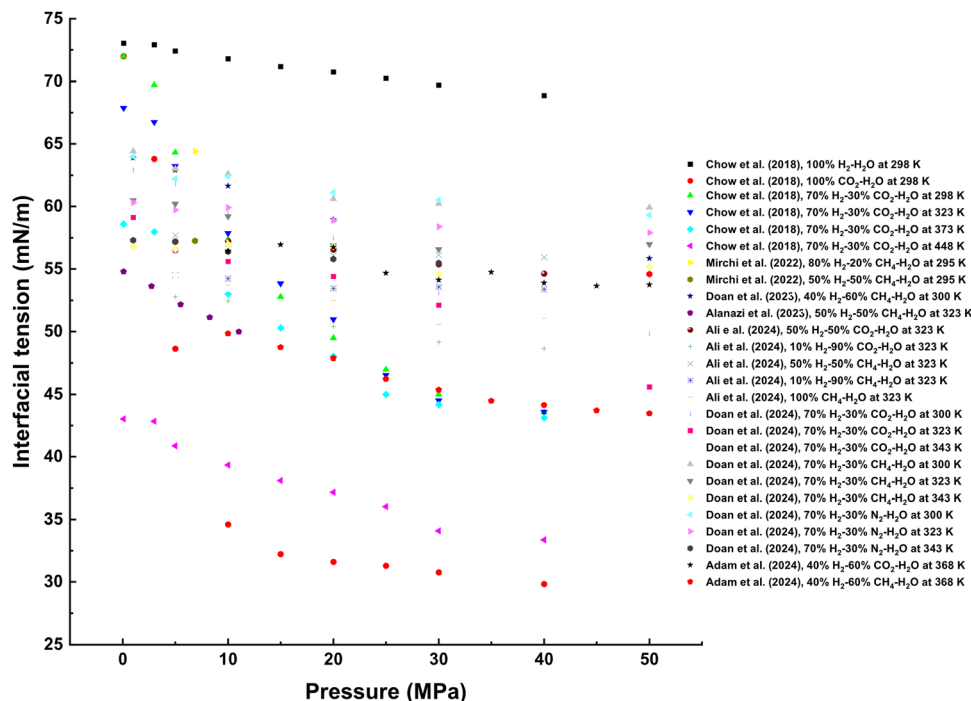


Fig. 19 Interfacial tension (IFT) trends in hydrogen ( $\text{H}_2$ )/cushion gas/water systems by pressure and temperature. The IFT consistently decreases with increasing pressure and temperature across  $\text{H}_2$  and cushion gas mixtures in water systems. This trend highlights the influence of pressure and temperature on the interfacial properties of gas compositions, which is critical for optimizing underground  $\text{H}_2$  storage. The data were collected from multiple studies<sup>236,284,307,308,321,322,325</sup> and replotted to provide a comprehensive comparison.

capillary trapping dynamics, and caprock penetration, which are crucial for  $\text{H}_2$  storage and geological carbon sequestration.

For instance, the IFT of pure  $\text{H}_2$  is about  $73 \text{ mN m}^{-1}$ .<sup>308</sup> The IFT datasets of  $\text{H}_2 + \text{CO}_2 + \text{H}_2\text{O}$  and  $\text{H}_2 + \text{H}_2\text{O}$  systems at pressures ranging from 0.1 to 50 MPa and temperatures from 298.15 to 448.15 K indicate that  $\text{H}_2$  increases the IFT between  $\text{CO}_2$ -rich and  $\text{H}_2\text{O}$ -rich phases. This increase in IFT causes higher pressure, displacing brine from the pore space in aquifer storage, enhancing capillary trapping, and reducing caprock penetration.<sup>308</sup> Although  $\text{CH}_4$  and  $\text{CO}_2$  decrease IFT between brine and gas,  $\text{CO}_2$  has a more pronounced effect than  $\text{CH}_4$  across all pressure levels, influencing wettability and IFT.<sup>236,322,325</sup>

The reduced IFT in  $\text{CO}_2$  suggests the improved mobility and extraction efficiency of  $\text{H}_2$  from subsurface storage media. This result is attributed to  $\text{CO}_2$  altering the surface properties and intermolecular interactions at the gas-liquid interface, facilitating easier displacement of  $\text{H}_2$  and enhancing capillary trapping mechanisms. Moreover, the reduced IFT decreases the likelihood of caprock penetration, enhancing the containment and storage security of  $\text{H}_2$ .

Similarly, the effects of  $\text{CH}_4$  and  $\text{N}_2$  as cushion gases on the  $\text{H}_2$  IFT with brine are comparable to those of  $\text{CO}_2$ . When  $\text{CH}_4$  or  $\text{N}_2$  is introduced as a cushion gas in the  $\text{H}_2$ -water system, the resulting IFT values fall between those observed for pure gases. This intermediary reduction in IFT indicates that  $\text{CH}_4$  and  $\text{N}_2$  contribute to modifying the interfacial properties, albeit to a lesser extent than  $\text{CO}_2$ . Doan *et al.*<sup>322</sup> demonstrated that while all three gases,  $\text{CH}_4$ ,  $\text{CO}_2$ , and  $\text{N}_2$ , reduce  $\text{H}_2$ -water IFT,  $\text{CO}_2$  has

a more pronounced effect across pressure values. This finding underscores the effectiveness of  $\text{CO}_2$  in altering interfacial characteristics and enhancing fluid mobility compared to  $\text{CH}_4$  and  $\text{N}_2$ .

The implications of these findings extend beyond fundamental understanding to practical applications in UHS. Lower IFT values with cushion gases facilitate more efficient  $\text{H}_2$  recovery and influence storage strategies and the design of geological reservoirs for carbon sequestration. Understanding how gases affect IFT helps optimize processes, such as enhanced oil recovery, where controlling fluid behavior in porous media is crucial for maximizing resource extraction and minimizing economic effects. The data in the literature indicate the importance of cushion gases, such as  $\text{CO}_2$ ,  $\text{CH}_4$ , and  $\text{N}_2$ , in modulating IFT in  $\text{H}_2$ -water systems.

**3.8.3. Effect of cushion gas on hydrogen sorption, storage, and recovery.** Understanding the role of cushion gas in  $\text{H}_2$  sorption, storage, and recovery is essential in optimizing the efficiency and stability of geological  $\text{H}_2$  storage systems. These gases can influence the adsorption characteristics of  $\text{H}_2$  on geological surfaces and the overall storage capacity and ease of  $\text{H}_2$  recovery.<sup>99,133,319,323,327</sup>

Additionally, cushion gas can influence competitive adsorption effects, where other gases might occupy adsorption sites on rock surfaces, ensuring that a higher proportion of the storage capacity is available for  $\text{H}_2$ .<sup>151,153</sup> In addition,  $\text{CH}_4$  enhances the relative permeability of gas, significantly boosting  $\text{H}_2$  storage and recovery efficiency.<sup>47,323</sup> Being inert,  $\text{N}_2$  is a



pressure-maintaining cushion gas without much chemical interaction with H<sub>2</sub>.<sup>319</sup> Careful selection and utilization of these cushion gases improves the performance and stability of H<sub>2</sub> storage systems.<sup>89,164,323,327</sup>

Cushion gas maintains reservoir pressure and stable withdrawal rates for several ongoing UHS projects worldwide.<sup>328,329</sup> For instance, in an H<sub>2</sub> storage project in depleted hydrocarbon reservoirs in Utah in the US, about 30% to 50% of the total reservoir storage volume is allocated for H<sub>2</sub> storage, suggesting that approximately 3 to 5 million m<sup>3</sup> of the total storage capacity (10 million m<sup>3</sup>) is allocated to cushion gas. The cushion gas for this project helps maintain stable pressure and H<sub>2</sub> withdrawal rates of about 500 000 to 800 000 m<sup>3</sup> per day. A significant pressure drop is expected without the cushion gas, which could lead to flow restrictions, higher operational costs, and lower recovery efficiency. In UHS projects in salt caverns in Germany (the EWE storage facility), about 25 000 m<sup>3</sup> of the salt cavern H<sub>2</sub> storage capacity (100 000 m<sup>3</sup>) was allocated to cushion gas. Cushion gas enabled a more than 30% increase in the withdrawal rate compared to scenarios without cushion gas, ensuring consistent H<sub>2</sub> withdrawal rates of 5000 to 7000 m<sup>3</sup> per day during the peak demand period.

Fig. 20 indicated that H<sub>2</sub> exhibits stronger adsorption on kerogen surfaces than montmorillonite, suggesting that kerogen

may serve as a more effective reservoir for H<sub>2</sub> storage due to its higher affinity for H<sub>2</sub> molecules. However, CH<sub>4</sub> or CO<sub>2</sub> can significantly alter these adsorption dynamics. Studies suggest that CH<sub>4</sub> and CO<sub>2</sub> reduce the surface adsorption capacity and the overall storage amount of H<sub>2</sub>. This reduction is attributed to competitive adsorption effects, where CH<sub>4</sub> and CO<sub>2</sub> molecules occupy available adsorption sites on the kerogen or montmorillonite surfaces, limiting the space and interactions available for H<sub>2</sub> molecules.<sup>153</sup>

Further, CO<sub>2</sub> emerges as a potentially preferable cushion gas to CH<sub>4</sub> for optimizing H<sub>2</sub> adsorption and storage efficiency in coal seams and shale reservoirs. Moreover, CO<sub>2</sub> appears to interfere less with H<sub>2</sub> adsorption on geological surfaces, which may allow for a higher storage capacity and more favorable adsorption-desorption characteristics for H<sub>2</sub>.

Accordingly, Mirchi *et al.*<sup>323</sup> conducted flow-through experiments to evaluate the influence of CH<sub>4</sub> cushion gas on the effectiveness of formation pressurization and fluid displacement for H<sub>2</sub> storage and recovery. Hydrogen storage was assessed *via* H<sub>2</sub>-brine steady-state drainage and imbibition-relative permeability experiments with and without CH<sub>4</sub> as cushion gas using oil-wet Berea sandstone cores at elevated temperature and pressure values. The effect of H<sub>2</sub> exposure on the petrophysical properties of rock in subsurface conditions

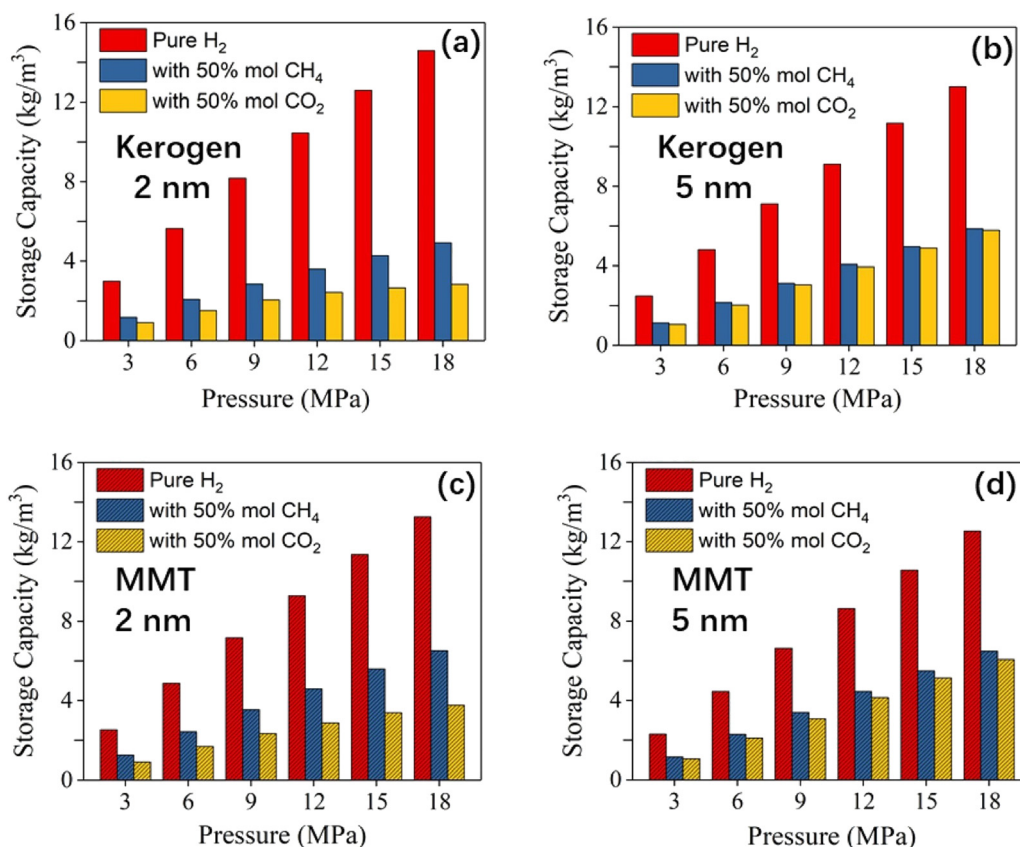


Fig. 20 Storage capacity of hydrogen (H<sub>2</sub>) and gas mixtures in kerogen and montmorillonite (MMT) nanopores by pressure. (a) and (b) Storage capacity of pure H<sub>2</sub>, H<sub>2</sub> with 50 mol% CH<sub>4</sub>, and H<sub>2</sub> with 50 mol% CO<sub>2</sub> in kerogen at nanopores of 2 nm (a) and 5 nm (b) at 333.15 K. (c) and (d) Storage capacity of the same gas mixtures in MMT nanopores of 2 nm (c) and 5 nm (d) under similar conditions. The results illustrate the significant influence of pressure and pore size on gas storage behavior across materials.<sup>153</sup>



slightly changed the permeability and porosity of the core plugs due to the pure  $H_2$  and  $H_2$ - $CH_4$  mixture (50–50%). After gas flooding, the gas saturation increased to 0.611 from 0.277 with the 50–50%  $H_2$ - $CH_4$  mixture. In addition, the gas relative permeability improved by 70.5% by adding 50%  $CH_4$  to  $H_2$ , indicating that the recovery and storage of  $H_2$  are significantly enhanced with  $CH_4$ .<sup>323</sup>

Recently, studies have evaluated the effects of varying  $CH_4$ ,  $CO_2$ , and  $H_2$  concentrations in gas mixtures on rock types.<sup>72,152,330,331</sup> Fig. 21 compares  $H_2$  and  $H_2$ - $CH_4$  uptake in water-wet and oil-wet sandstone under varying pressure and temperature values.<sup>149</sup> Fig. 21(a–d) illustrates the adsorption and desorption behavior ( $cm^3 g^{-1}$ ) of these gases at 298, 313, and 333 K across pressure from 0 to 9 MPa. This result quantifies the gas volume adsorbed or desorbed per gram of sandstone. Notably, adsorption and desorption curves differ significantly, suggesting hysteresis. At 298 K,  $H_2$  uptake is highest, with a pronounced increase as pressure rises, followed by lower uptakes at 313 and 333 K. This trend implies that lower temperatures favor higher  $H_2$  adsorption in water-wet sandstone, likely due to the reduced kinetic energy of  $H_2$  molecules, allowing them to adhere more readily to sandstone surfaces. The overall uptake values are typically lower than in water-oil sandstone (Fig. 21(b)).

The binary gas mixture of  $H_2$ - $CH_4$  in Fig. 21(c and d) displays the sorption behavior in water-wet and oil-wet sandstone, indicating different sorption characteristics. All rock samples exhibited positive hysteresis in the adsorption and desorption isotherms at various temperatures. The Freundlich, Redlich–Peterson, and Sips models better describe adsorption characteristics, indicating multilayer adsorption on the rock surface.<sup>149</sup> The  $H_2$  storage capacity can be underestimated when the storage rocks and caprock are assumed to be initially hydrophilic during UHS.

A case study of Cretaceous Cameo coal samples from outcrops in Colorado with a high TOC value of 72.2% revealed a weak affinity for  $H_2$ . The adsorption of  $H_2$  was significantly lower than that of  $CH_4$  and  $CO_2$ . The injection of  $CH_4$  or  $CO_2$  as cushion gas can considerably reduce  $H_2$  loss by adsorption during geological storage. The empirical calculations suggest that  $H_2$  adsorption is negligible if the chemical composition includes more than 8%  $CH_4$  or 2%  $CO_2$  at storage sites, such as abandoned mines and depleted coal seams.<sup>331</sup>

More recently, Ho *et al.*<sup>151</sup> provided insight into the  $H_2$ - $CH_4$  dynamics in depleted gas reservoirs upon  $H_2$  injection, along with quantifying the  $H_2$  loss and  $CH_4$  desorption in  $H_2$  storage. In a depleted gas reservoir with low  $CH_4$  pressure, approximately 30% of the residual  $CH_4$  can be desorbed when  $H_2$  is

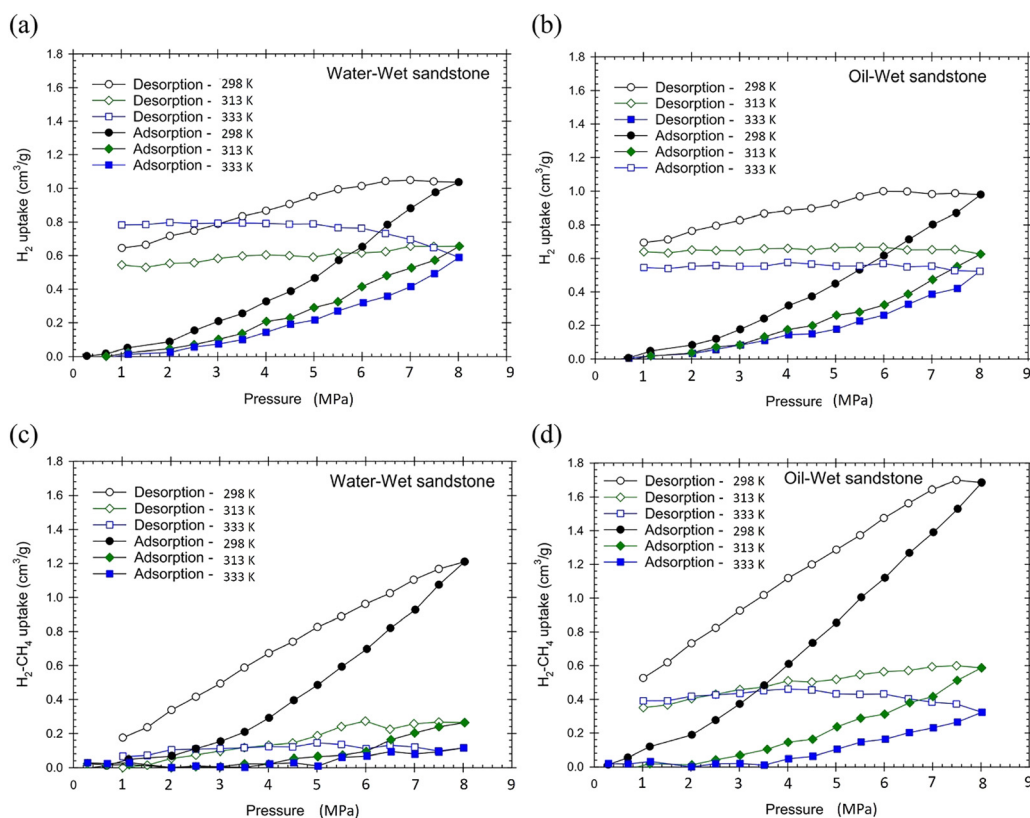


Fig. 21 Sorption hysteresis for pure hydrogen ( $H_2$ ) and  $H_2$ -methane ( $CH_4$ ) mixtures on the water- and oil-wet sandstone. (a) and (b) Sorption hysteresis for pure  $H_2$  on water-wet (a) and oil-wet (b) sandstone samples, revealing  $H_2$  uptake as a function of the equilibrium pressure at various temperatures. (c) and (d) Sorption hysteresis for  $H_2$ - $CH_4$  mixtures on water-wet (c) and oil-wet (d) sandstone samples under similar conditions, highlighting the influence of wetting conditions on gas uptake. These measurements were taken at multiple temperature and pressure values to assess sorption and desorption behavior on water and oil-wet sandstone samples.<sup>149</sup>



injected. Additionally, the diffusion coefficient of H<sub>2</sub> in porous kerogen is about 10 times higher than that of CH<sub>4</sub> and CO<sub>2</sub>.

## 4. Advanced imaging and core flooding for underground hydrogen storage

Notably, UHS is critical in advancing the viability of H<sub>2</sub> as a sustainable energy source. As H<sub>2</sub> demand increases, practical storage solutions become critical for balancing supply and demand, especially for energy-intensive applications. Evaluating potential storage sites involves carefully assessing geological formations to ensure their suitability for H<sub>2</sub> storage. This assessment requires a comprehensive understanding of the methods and techniques to evaluate underground reservoir integrity, capacity, and safety. Advanced imaging, core flooding, and modern tools and methods play crucial roles in characterizing the subsurface environment and determining the storage feasibility.

Several methods can evaluate the physical and chemical properties of potential storage sites to assess UHS sites accurately. Measurements of interfacial interactions and core-flooding techniques provide data on rock formations, including their porosity, permeability, and structural stability. Advanced imaging techniques, such as micro-CT, SEM, NMR, and magnetic resonance imaging (MRI), offer insight into subsurface conditions and help visualize and map the extent of potential storage reservoirs.<sup>151,206,332–335</sup> Core and laboratory analyses refine these assessments by providing detailed information

on rock and fluid properties, including how H<sub>2</sub> interacts with the geological matrix of the formation and other fluids.

### 4.1. Advanced imaging techniques for rock/H<sub>2</sub>/brine interactions

Researchers have employed advanced imaging technology to analyze how H<sub>2</sub> and fluids interact with rock surfaces under simulated pressure and temperature subsurface conditions. Imaging techniques (*e.g.*, NMR, micro-CT, and SEM) before, during, and after core flooding<sup>336</sup> and static and batch reactions of H<sub>2</sub> and fluids with rocks<sup>337–339</sup> facilitate the assessment of biogeochemical alterations following H<sub>2</sub> exposure. This integrated approach aids in visually understanding how H<sub>2</sub>, fluids, and rock influence underground formations, particularly regarding storage capacity and caprock sealing integrity. Such assessments are crucial for evaluating potential geological storage formations.

Moreover, H<sub>2</sub> reactivity with calcite could reduce the storage capacity of carbonate formations during UHS. Al-Yaseri *et al.*<sup>336</sup> observed significant expansion of calcite in limestone using X-ray micro-CT scans of limestone and dolomite cores before and after exposure to H<sub>2</sub> for 75 days at 4.83 MPa and 348 K, resulting in a 47% reduction in effective porosity (storage capacity; Fig. 22(a)). In dolomite rock, the storage capacity slightly increased (approximately 6%), which was attributed to the grain dissolution outweighing the expansion effects.

Recently, Al-Yaseri *et al.*<sup>339</sup> employed SEM imaging to investigate dissolution and precipitation reactions caused by H<sub>2</sub> interaction with limestone. The rock samples were subjected to a pressure of 10.3 MPa and a temperature of 348 K for durations ranging from 6 to 13 months. The experimental

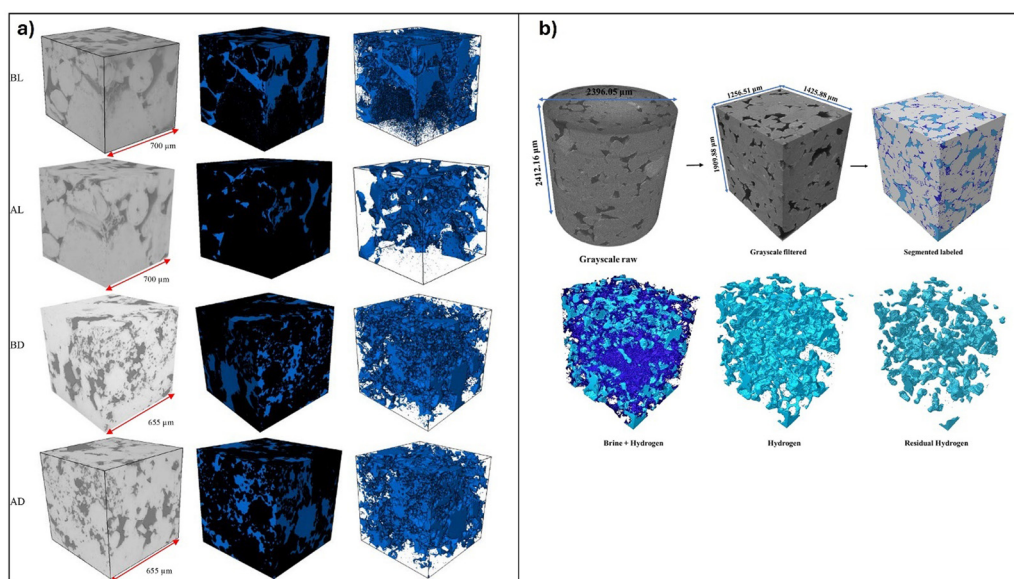


**Fig. 22** Three-dimensional (3D) microcomputed tomography ( $\mu$ CT) images of rock samples before and after exposure to hydrogen (H<sub>2</sub>) and segmented saturation profiles. (a) 3D  $\mu$ CT images of limestone (BL and AL) and dolomite (BD and AD) samples, captured at 1.5  $\mu$ m resolution before (BL and BD) and after (AL and AD) exposure to pressurized H<sub>2</sub>. In raw grayscale images, the rock grain is gray, and the open pore space is black. In segmented images, the grain is black, and the open pore space is blue, indicating porosity changes after H<sub>2</sub> injection.<sup>336</sup> (b) Segmented 3D saturation profiles of H<sub>2</sub> and brine from raw  $\mu$ CT images, with H<sub>2</sub> and brine visualized in separate phases, providing insight into fluid distribution in the pore space.<sup>159</sup>



results demonstrated that  $H_2$  treatment had no significant effect on the surface morphology or pore structure even after six months, indicating that abiotic reactions in carbonate rock are unlikely during the early stages of UHS. Additionally, no geochemical reactions between  $H_2$  and calcite were observed with brine, and no gases were detected after 13 months of treatment. Similarly, the SEM analysis of evaporite mineral (anhydrite, gypsum, and halite) geochemical reactivity with  $H_2$  demonstrated high stability (Fig. 22(b)). After  $H_2$  treatment, minimal cracks and fractures were reported on the gypsum surfaces, which can be attributed to the dehydration process of gypsum at elevated temperatures.<sup>338,340,341</sup>

#### 4.2. Core flooding of hydrogen in geological porous media

Core-flooding experiments provide a realistic representation of rock/ $H_2$ /fluid interactions in subsurface storage media. Typically performed on cylindrical rock plugs from consolidated outcrops or quarried rock, these experiments inject  $H_2$  and other fluids to mimic subsurface injection and withdrawal processes (Fig. 23(a)). Three primary methods for conducting

and interpreting these experiments include pressure profile analysis, effluent analysis, and tracer measurements using advanced imaging techniques. Pressure profile analyses can quantify interactions, where an increase in the pressure gradient suggests pore plugging *via* precipitation, and a decrease indicates increased flow paths due to rock mineral dissolution, affecting permeability and porosity. Effluent analyses involve determining the concentrations of individual components using ion chromatography and TOC content analysis, comparing them to injected values to assess adsorption, precipitation, or dissolution.<sup>157</sup> This technique effectively evaluates rock/ $H_2$ /fluid interactions under reservoir pressure and temperature conditions and realistic flow rates and stresses. Core-flooding experiments and fluid-saturation imaging in  $H_2$ -flooded cores include NMR, micro-CT, X-ray CT, and microfluidics and other indirect methods of estimating the wettability of rock- $H_2$ -brine systems.<sup>99,125,132,141,144,159,336</sup>

Some of these experiments have been conducted to assess the possibility of  $H_2$  storage in sandstone formations (saline aquifer).<sup>159,344,345</sup> Jha *et al.*<sup>159</sup> conducted X-ray CT imaging of

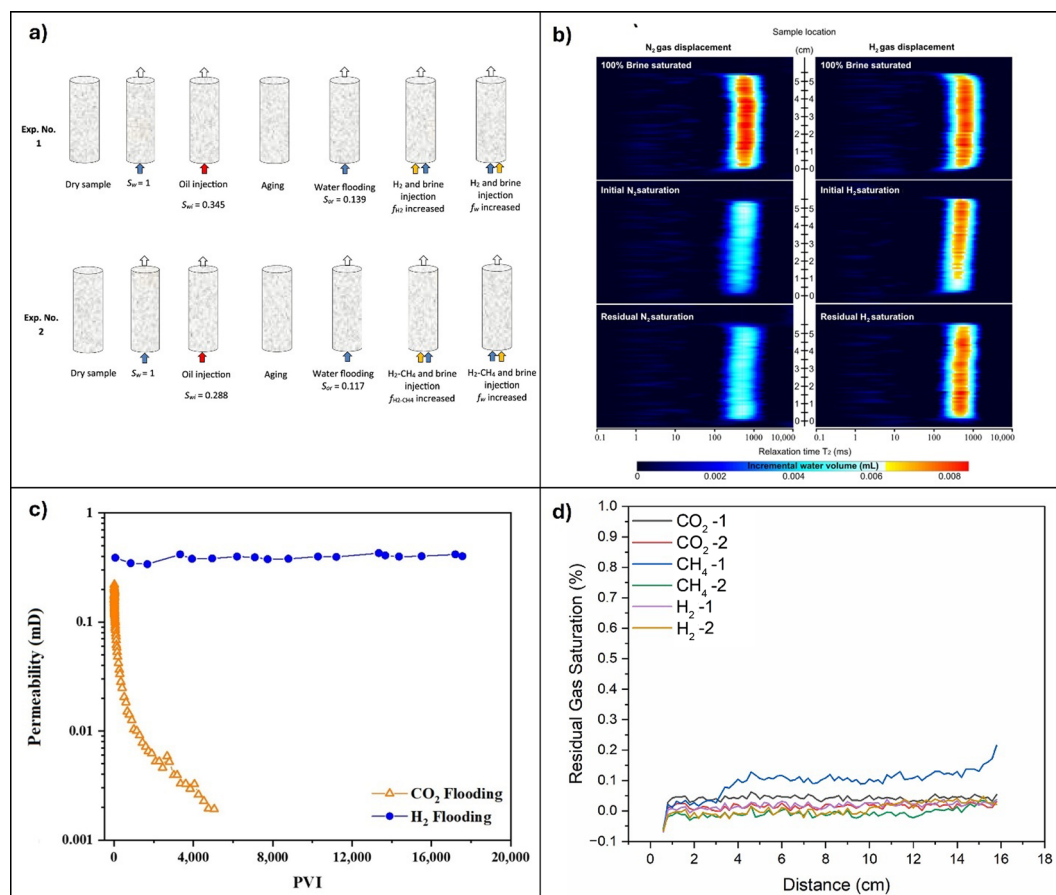


**Fig. 23** Core-flooding experiments, nuclear magnetic resonance (NMR) distributions, permeability measurements, and residual gas saturation comparisons. (a) Core-flooding experimental steps for assessing relative permeability and hydrogen ( $H_2$ ) storage in rock samples, including oil injection, water flooding, and gas injection phases.<sup>323</sup> (b) NMR spatial  $T_2$  distribution along Fontainebleau sandstone displaying the drainage and imbibition processes for  $N_2$  (left) and  $H_2$  (right) at a displacement flow rate of  $2 \text{ mL min}^{-1}$  and  $0.37 \text{ MPa}$  pore pressure, highlighting the water distribution during gas displacement.<sup>143</sup> (c) Dynamic coal permeability measurements during  $H_2$  and  $CO_2$  flooding, with permeability plotted against injected pore volumes.<sup>342</sup> (d) X-ray-based comparison of residual gas saturation for  $H_2$ ,  $CH_4$ , and  $CO_2$ , demonstrating the differences in gas trapping in the pore space after injection.<sup>343</sup>



the brine and H<sub>2</sub> saturation profile in a Gosford standard core, suggesting that about 65% of the core PV could be occupied by injected H<sub>2</sub> at a flow rate of 0.01 mL min<sup>-1</sup>. After the brine injection, almost 41% of the core was still saturated by H<sub>2</sub>. Jha *et al.*<sup>159</sup> further noted that the H<sub>2</sub>-brine pair was strongly water-wet compared to the CO<sub>2</sub>-brine pair at similar geo-storage conditions. The pore-level observation revealed that the brine occupied pore throats, miniature pores, and corners.

In contrast, the larger pores were primarily occupied by H<sub>2</sub>, suggesting that H<sub>2</sub> storage is promising in sandstone reservoirs (saline aquifers). However, these experiments were conducted in ambient conditions not representative of geological H<sub>2</sub> storage conditions. The pore-scale investigation of residual H<sub>2</sub> saturation in storage formation, pre- and post-brine injection at geological storage temperature and pressure conditions is a knowledge gap that must be bridged. Insight into the fluid saturation at the pore scale can be gained from NMR,<sup>346,347</sup> micro-CT techniques, and X-ray-CT imaging of the flooded cores.

Integrating core-flooding techniques with NMR enables the assessment of the initial and residual H<sub>2</sub> saturation values and their distribution in the core samples. This approach helps clarify how wettability influences H<sub>2</sub> migration and residual trapping in potential geological storage formations.<sup>348</sup> Accordingly, Al-Yaseri *et al.*<sup>143</sup> employed NMR to observe fluid distribution in a 38-mm diameter cylindrical clean Fontainebleau sandstone rock (primarily quartz; 99.8%) during core-flooding (drainage and imbibition) experiments. The study revealed that the initial and residual saturation values of H<sub>2</sub> were 4% and 2%, respectively. In comparison, N<sub>2</sub> displayed a high initial and residual saturation of about 26% and 17% for clean sandstone, as indicated in Fig. 23(b). However, the authors noted that the presence and type of clay minerals in sandstone could influence these results.

In another study, Al-Yaseri *et al.*<sup>348</sup> applied an NMR core-flooding setup to explore the influence of clay minerals on H<sub>2</sub> saturation in clay-rich Bandera Grey (BA-G) sandstone. Samples were tested in their natural state and after heating to 973 K for 12 h in an air environment to remove clay minerals.<sup>348</sup> The XRD analyses confirmed the transformation of kaolinite into illite and the disappearance of clinocllore due to the firing process (see ref. 349 and 350). A PV of 10 mL was injected and withdrawn during drainage and imbibition cycles at 298 K with a 6.89 MPa confining pressure and 0.41 MPa injection pressure. The results indicated minor changes in the initial and residual H<sub>2</sub> saturation post-firing (initial saturation increased from 16% to 18%, and residual saturation decreased from 14% to 13%), suggesting that the clay content and type slightly affect the wettability of the BA-G sandstone-H<sub>2</sub>-brine system.

Studies have demonstrated that injecting gases, such as CO<sub>2</sub>, CH<sub>4</sub>, and N<sub>2</sub>, into rocks can lead to swelling, significantly reducing their permeability and porosity.<sup>342,351-353</sup> This finding underscores the importance of examining coal swelling behavior under pressurized H<sub>2</sub> gas and its influence on coal permeability and porosity. Iglauer *et al.*<sup>342</sup> conducted experiments where a PV of 18 000 cc of H<sub>2</sub> gas was injected into coal cores under constant temperature (296 K) and 3.447 MPa effective

stress, using *in situ* three-dimensional (3D) X-ray micro-CT to image the cores under reservoir conditions. Their findings indicated that coal could adsorb large quantities of H<sub>2</sub> without altering the cleat porosity, morphology, size distribution, or permeability. The authors concluded that the geo-storage of H<sub>2</sub> in deep coal seams is feasible from a petrophysical perspective because the coal permeability, crucial for H<sub>2</sub> injectivity and extraction capacity, remains unaffected by H<sub>2</sub> flooding, as illustrated in Fig. 23(c).

In contrast, CO<sub>2</sub> injection causes significant swelling of the maceral phase, and exposure to CH<sub>4</sub> and N<sub>2</sub> gases results in varying degrees of maceral swelling.<sup>150,351,352,354</sup> The order of the swelling propensity of gases follows CO<sub>2</sub> > CH<sub>4</sub> > N<sub>2</sub> > H<sub>2</sub>, influenced by their polarizability and van der Waals forces in the maceral phase. The interaction affinity and adsorption capacity of coal for gases are determined by their respective polarizabilities: CO<sub>2</sub> (29.1 × 10<sup>-25</sup> cm<sup>3</sup>), CH<sub>4</sub> (25.9 × 10<sup>-25</sup> cm<sup>3</sup>), N<sub>2</sub> (17.4 × 10<sup>-25</sup> cm<sup>3</sup>), and H<sub>2</sub> (8 × 10<sup>-25</sup> cm<sup>3</sup>).<sup>72,123</sup> Additionally, CO<sub>2</sub> forms H-bonds with carbonyl and alcohol groups in coal, further enhancing the CO<sub>2</sub>-coal affinity compared to H<sub>2</sub>.<sup>150,355-357</sup> Al-Yaseri *et al.*<sup>343</sup> reported similar findings using X-rays for H<sub>2</sub>, CH<sub>4</sub>, and CO<sub>2</sub> (Fig. 23(d)).

**4.2.1. Capillary pressure and number and relative permeability.** Understanding the capillary pressure, capillary number, and relative permeability is crucial in UHS. These parameters govern fluid-flow dynamics, influencing the efficiency of H<sub>2</sub> injection, storage, and extraction processes in porous media.

Coupled core-flooding experiments using micromodels and numerical simulations (computational fluid dynamics [CFD]) have been employed to understand H<sub>2</sub> multiphase dynamics in subsurface media. For example, Dehury *et al.*<sup>207</sup> observed unstable displacement patterns of H<sub>2</sub> leading to snap-off effects, which increased the structural and residual trapping of H<sub>2</sub> in pore spaces. A comparison of the H<sub>2</sub>-brine two-phase flow with N<sub>2</sub>-brine using coupled core-flooding CFD revealed significantly varied displacement patterns, breakthrough times, and gas saturations at breakthrough. For H<sub>2</sub>-brine flow, gas saturation increased by 10.25%, and the breakthrough time increased by 11.27%. However, the N<sub>2</sub>-brine flow exhibited a 47% increase in gas saturation at breakthrough and a 58% increase in breakthrough time under subsurface aquifer conditions compared to atmospheric conditions. At low capillary numbers (~10<sup>-6</sup>), a higher H<sub>2</sub> saturation at breakthrough and longer breakthrough times were reported due to snap-off effects and low velocity, indicating greater storage capacity. These results emphasize that N<sub>2</sub> cannot be a proxy for H<sub>2</sub> because it inaccurately projects a higher storage potential.<sup>207</sup>

Capillary pressure leads to capillary trapping. Minimizing capillary trapping is desirable in UHS applications to facilitate H<sub>2</sub> extraction during withdrawal.<sup>118</sup> Capillary pressure influences surface wettability, which is crucial in determining the phase saturation distribution in porous media, affecting relative permeability curves that regulate the H<sub>2</sub>-brine two-phase flow.<sup>358</sup>

Fig. 24(a-d) presents the multiphase flow model simulating capillary pressure-saturation ( $P_c$ - $S_w$ ) and relative permeability



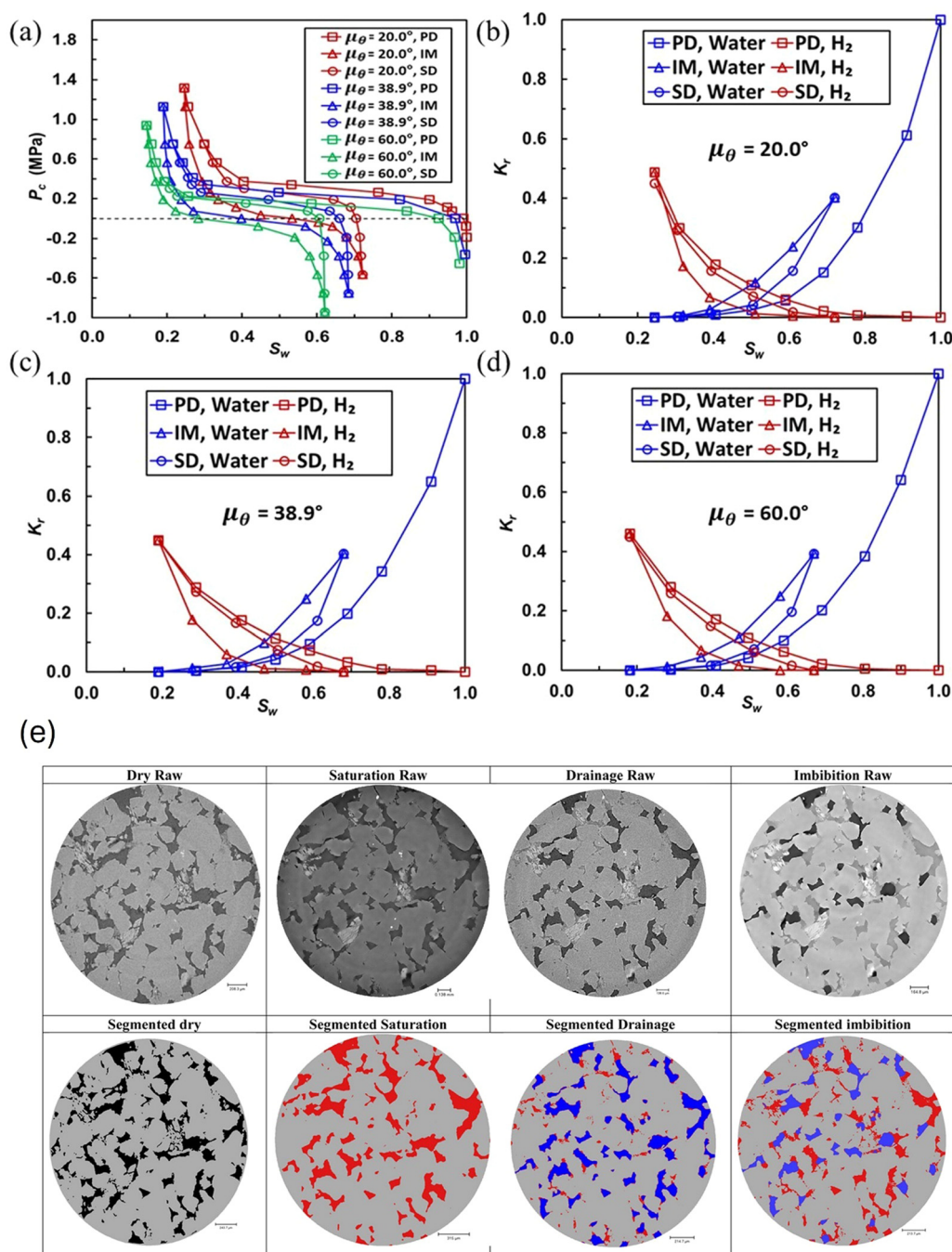


**Fig. 24** Capillary pressure ( $P_c$ )–water saturation ( $S_w$ ) curves, relative permeability, and microcomputed tomography (CT) images of hydrogen ( $H_2$ ) and brine distributions. (a)  $P_c$  versus  $S_w$  curves for mean contact angle values ( $20.0^\circ$ ,  $38.9^\circ$ , and  $60.0^\circ$ ), revealing the influence of the contact angle on the drainage and imbibition (IM) processes. (b)–(d) Relative permeability ( $K_r$ ) curves for water and  $H_2$  at contact angles of  $20.0^\circ$ ,  $38.9^\circ$ , and  $60.0^\circ$  during primary drainage (PD), IM, and secondary drainage (SD) processes. These results reveal the relationship between wettability and fluid flow in porous media, with a standard deviation of  $38.5^\circ$  and spatial correlation length of  $54.06 \mu\text{m}$  for the surface contact angle.<sup>358</sup> (e) Raw and segmented two-dimensional micro-CT images of brine and  $H_2$  distribution in the pore space. Brine is red;  $H_2$  is blue, highlighting the fluid saturation behavior during flow stages.<sup>141</sup>

curves under three contact angles ( $20.0^\circ$ ,  $38.9^\circ$ , and  $60.0^\circ$ ). The  $P_c$ – $S_w$  curves shifted leftward as the mean value of the rock-surface contact angle increased from  $20.0^\circ$  to  $60.0^\circ$ . This shift signifies a decrease in the brine retained in the pores following the drainage phase and increased  $H_2$  pore retention after the imbibition phase. Furthermore, the  $P_c$ – $S_w$  curves transitioned

from an upward to a downward trajectory, indicating reduced capillary pressure as the rock surface transitioned to a less water-wet state.<sup>358</sup>

The relative permeability for water ( $K_{r,w}$ ) increased. In contrast, the relative permeability for  $H_2$  ( $K_{r,H_2}$ ) decreased when the core-flooding process shifted from primary drainage to imbibition



because water flowed back into the rock during imbibition, filling the small pores and pore throats and displacing H<sub>2</sub> into larger pores. This occurrence created isolated H<sub>2</sub> globules, reducing H<sub>2</sub> mobility and Kr<sub>H<sub>2</sub></sub>. Conversely, when the process shifted from imbibition to primary drainage, Kr<sub>w</sub> decreased, whereas Kr<sub>H<sub>2</sub></sub> increased. During primary drainage, H<sub>2</sub> was forced into the rock under capillary pressure, forming connected flow channels for H<sub>2</sub> and reducing the water mobility and Kr<sub>w</sub>. This pattern was observed for all reported contact angles.<sup>358</sup>

Injecting brine at higher capillary numbers decreases capillary trapping and enhances H<sub>2</sub> recovery.<sup>159</sup> Lysy *et al.*<sup>132,359</sup> noted that H<sub>2</sub> saturation after injection (drainage) increases as the capillary number increases. Furthermore, shallow and lower-pressure sites were recommended for H<sub>2</sub> storage in porous media. Thaysen *et al.*<sup>144</sup> recently employed micro-CT to examine H<sub>2</sub> flow and displacement processes in Clashach sandstone (96% quartz), investigating capillary numbers ranging from 1.2 to  $6.8 \times 10^{-8}$  for H<sub>2</sub> and 2.4 to  $9.5 \times 10^{-6}$  for brine, and pore fluid pressures from 2 to 7 MPa at a constant temperature.<sup>144</sup> They found that H<sub>2</sub> saturation during flooding was independent of the pore fluid pressure, with about 50% of the pore space saturated with H<sub>2</sub> during drainage at all pressures. During imbibition, 20%, 22%, and 43% of the initially injected H<sub>2</sub> was trapped at 2, 5, and 7 MPa, respectively, with a capillary number of  $2.4 \times 10^{-6}$ . This result suggests that higher pressures (*i.e.*, deeper reservoirs) are less promising for H<sub>2</sub> storage.<sup>144</sup>

Flooded cores monitored using  $\mu$ CT indicated that, after injecting a PV of 5 mL of H<sub>2</sub> gas at a rate of 0.01 mL min<sup>-1</sup> into a Gosford sandstone formation, large interconnected stable H<sub>2</sub> clusters formed after the drainage process, with an initial H<sub>2</sub> saturation of about 53% and residual H<sub>2</sub> saturations of 44% (Fig. 24(e)). This finding indicates that water-wet H<sub>2</sub> storage formations could produce high H<sub>2</sub> residual saturation that is unfavorable for H<sub>2</sub> withdrawal due to the disconnection and trapping of the nonwetting phase. This finding also implies that H<sub>2</sub> is likely to fill a substantial fraction of the PV while being stored. The significant residual trapping of H<sub>2</sub> in the strongly water-wet sandstone matrix presents considerable challenges for mobilization, leading to an estimated recovery of merely 9% of the stored H<sub>2</sub>.<sup>141</sup> This recovery suggests that water-wet H<sub>2</sub> storage formations may yield higher H<sub>2</sub> residual saturations, posing challenges for H<sub>2</sub> extraction due to the disconnection and entrapment of the nonwetting phase.

**4.2.2. Ostwald ripening in core flooding for underground hydrogen storage.** In core-flooding studies, local capillary pressure differences create varying dissolved gas concentrations according to Henry's law.<sup>334</sup> The dissolved gas variance results in concentration gradients in the aqueous phase, causing dissolved gas to diffuse from areas of high capillary pressure. This process, known as Ostwald ripening, continues until the capillary pressure is uniform throughout the system and affects the fluid distribution in porous media.<sup>334</sup>

Several studies have examined the effect of Ostwald ripening on gas distribution, including CO<sub>2</sub>, N<sub>2</sub>, air,<sup>360–366</sup> and more recently, H<sub>2</sub>.<sup>206,334</sup> For example, Garing *et al.*<sup>363</sup> and

De Chalendar *et al.*<sup>364</sup> conducted experimental and theoretical studies on gas pore-scale distribution. In contrast, Blunt<sup>365</sup> quantified the gas configuration in capillary-gravity equilibrium and estimated the timescales to reach these states. These studies assessed significant gas rearrangement over hours to months and millimeter-to-centimeter scales. In regular pore networks, Ostwald ripening can lead to a more uniform distribution of trapped ganglia (clusters of trapped gas),<sup>362,366</sup> but multiple equilibrium positions may occur in heterogeneous porous rock.<sup>364</sup>

Fig. 25(a and b) illustrates bubble rearrangement, where smaller bubbles tend to merge into larger ones.<sup>206,360,365</sup> In a comparative study of H<sub>2</sub> and N<sub>2</sub> core flooding, after a 12-h halt in injection, Zhang *et al.*<sup>206</sup> observed significant H<sub>2</sub> ganglia rearrangement. Although the total H<sub>2</sub> mass remained constant, smaller ganglia disappeared while larger ones expanded. The average contact angle between the H<sub>2</sub> and brine increased by about 10°, indicating H<sub>2</sub> aggregation in less water-wet regions with lower local capillary pressure. No significant change was observed for N<sub>2</sub>.

This behavior aligns with Ostwald ripening, where trapping primarily occurs through snap-offs in the most water-wet regions of the pore space. Smaller contact angles lead to higher interfacial curvature, more significant local capillary pressure, and increased solubility. A new equilibrium is reached with higher contact angles and volumes of ganglia. Initially, N<sub>2</sub> traps larger numbers of ganglia, demonstrating no significant rearrangement. The contact angle distributions for N<sub>2</sub> remain similar after drainage, imbibition, and a 12-h wait.<sup>206</sup> The authors further hypothesized that ganglia rearrangement results from Ostwald ripening. The diffusion of dissolved gas in the aqueous phase due to local concentration gradients drives the system toward equilibrium with constant local capillary pressure. This interpretation aligns with other studies using two-dimensional (2D) micromodels.<sup>362,364,365</sup>

Ostwald ripening equilibrates the local capillary pressure, reducing capillary pressure hysteresis. While significant effects on a geological timescale may take years,<sup>365</sup> substantial rearrangement occurs locally at the millimeter-to-centimeter scale. This rearrangement could lead to a representative elementary volume with reduced hysteresis, indicating less trapping and more efficient injection and withdrawal, which is beneficial for H<sub>2</sub> storage and extraction.<sup>206,334,365</sup> Capillary pressure and H<sub>2</sub> dissolution in brine can also influence the distribution of H<sub>2</sub> saturation, although they have a minimal effect on the final H<sub>2</sub> recovery factor. The loss of H<sub>2</sub> through dissolution can be offset by minimizing the substantial residual trapping. The cyclic hysteretic effect hinders the distribution of injected H<sub>2</sub> in the formation, leading to a higher ultimate H<sub>2</sub> recovery factor during later withdrawal phases.<sup>45</sup>

Fig. 25(c) illustrates 3D images of gas-phase ganglia sizes, revealing significant movement and redistribution of gas bubbles toward larger ganglia after H<sub>2</sub> injection and a 16-h waiting period.<sup>334</sup> This redistribution facilitates H<sub>2</sub> withdrawal through a connected pathway, highlighting its potential significance in gas remobilization. Similar observations were reported for



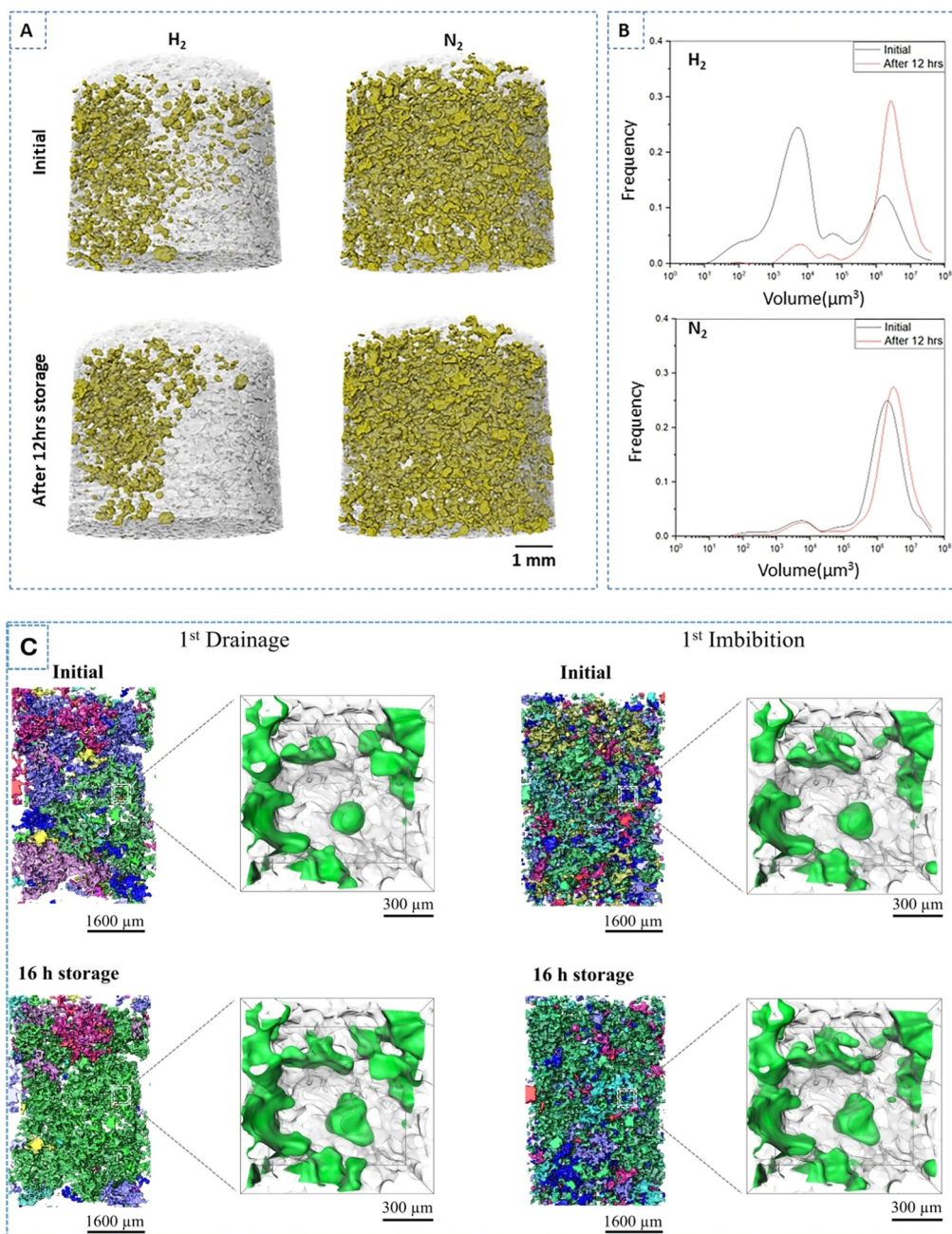


**Fig. 25** Trapped gas ganglia and pore-scale hydrogen ( $H_2$ ) distribution during storage and flooding cycles. (a) Three-dimensional (3D) images depicting trapped gas ganglia before and after 12 h for the  $H_2$  and nitrogen experiments. Trapped gas is marked yellow, indicating no significant change in gas volume after storage.<sup>206</sup> (b) Quantified ganglia size distributions in logarithmic space, using equal bin sizes; the area under the distributions remains constant, confirming no loss in gas volume.<sup>206</sup> (c) 3D images of the  $H_2$  distribution in the pore space during the first gas injection cycle and water flooding. Discrete gas ganglia are visualized by color, with  $H_2$  in green in the zoomed-in images. After 16 h of storage, the gas ganglia merge, improving connectivity, as demonstrated in the close-ups on the right.<sup>334</sup>

gas-brine systems, where trapped gas was significantly rearranged after brine injection.<sup>206,334,366</sup>

These visualization and imaging experiments are typically conducted under standard ambient temperature and pressure conditions, which may not accurately reflect the actual UHS conditions. In addition, micro-CT is a valuable tool for imaging and analyzing porous media at a high resolution, usually on the

micrometer scale during UHS. However, it has some limitations when capturing multiscale heterogeneities in porous media.<sup>367,368</sup> The micro-CT only provides the resolution on the micrometer scale (1–10  $\mu m$ ), which may not be sufficient to capture very fine heterogeneities or features smaller than the resolution limit, such as submicron or nanopore variations. At scales smaller than the micro-CT imaging resolution



capacity, structure variations involving sophisticated pore networks and tiny mineral grains and nanopores may appear blurry or unclear, resulting in the loss of vital multiscale information.<sup>369</sup>

Although micro-CT can provide high-resolution data for a small sample volume, capturing larger volumes required for representing heterogeneous materials across different scales using micro-CT typically leads to trade-offs between the field-of-view size and image resolution. Lower resolutions are often required for capturing large samples, reducing the ability of the micro-CT to capture fine-scale heterogeneities effectively in UHS media. Moreover, only a minimal portion of the large porous media can be scanned using micro-CT. Such a small part may not truly represent the overall heterogeneity of the porous media.<sup>370</sup> Generally, capturing multiscale heterogeneities in porous media requires sophisticated data processing techniques, such as multiscale segmentation, coregistration with other imaging techniques, or combining micro-CT with other methods, such as scanning electron microscopy (SEM).<sup>371</sup>

A comprehensive approach is necessary to address these uncertainties. For example, MD simulations and other advanced modeling techniques can help predict H<sub>2</sub> interactions at the atomic level, providing insight that advanced imaging techniques and empirical correlations may miss. Coupled with the high reactivity of H<sub>2</sub> is the necessity of assessing the individual pore scales (local-contact angles). The MD simulations could provide an alternate route for determining the rock-wetting phenomenon and interfacial interactions between the fluid, cushion gas, and host rocks to predict the success of UHS at geological storage conditions. The MD simulation could be implemented to investigate the rock-wetting phenomenon and rock–fluid IFT and interaction at unfavorable downhole conditions of elevated pressure, temperature, flow rate, and brine salinities that are almost impossible to implement in laboratories.

## 5. Computational methods for Underground hydrogen storage

In UHS, computational methods are essential for evaluating storage capacity, H<sub>2</sub> migration and withdrawal, understanding complex processes, and optimizing storage strategies. Numerical simulations, including MD, CFD, pore network modeling (PNM), and ML, analyze H<sub>2</sub> behavior at various scales. These methods enable modeling large-scale systems and investigating diverse scenarios that would be challenging or impossible to replicate experimentally, providing insight into effective H<sub>2</sub> storage and withdrawal.<sup>169,213,313,326,372–374</sup> Numerical simulations are highly flexible and cost-effective and can provide insight into the system behavior over long time scales and extreme conditions.

Understanding the methods for assessing UHS is vital to optimizing storage efficiency and ensuring long-term stability. This approach facilitates selecting appropriate H<sub>2</sub> storage locations and designing and implementing effective withdrawal strategies.

### 5.1. Molecular dynamic simulation

The MD simulation method models how complex systems behave beyond experiment and theory computationally by mimicking atoms at the molecular scale and numerically solving state equations.<sup>326,375–379</sup> Moreover, MD simulation provides spatial and temporal resolutions of molecular interactions that are unavailable in experiments.<sup>380</sup> Owing to its significance, MD simulation has been implemented in many software packages, including Chemistry at Harvard Macromolecular Mechanics (CHARMM),<sup>381</sup> LAMMPS,<sup>382</sup> GROMACS,<sup>383,384</sup> Nanoscale Molecular Dynamics (NAMD),<sup>385,386</sup> Assisted Model Building and Energy Refinement (AMBER),<sup>387</sup> and Desmond.<sup>388</sup> Recently, several researchers have used the MD to simulate systems down to the nanoscale coulombic and electrostatic forces, which provide more details and save time compared to the classical laboratory experimental approach.

This approach considers the effect of the molecular structure of H<sub>2</sub> and quantifies the energetic interaction of the H<sub>2</sub> with rock surface and fluids. This section discusses and analyzes data available in the literature on MD simulation studies of adsorption, solubility, and wettability for rock/H<sub>2</sub>/brine systems. The wetting characteristics of the rock/H<sub>2</sub>/brine system found using MD simulation studies display some discrepancies in behavior compared to experimental observations.

Ghafari *et al.*<sup>389</sup> employed MD simulations to investigate the wetting behavior of silica surfaces in subsurface H<sub>2</sub> systems, aiming to reconcile inconsistencies in experimental findings. Their study revealed that pure H<sub>2</sub> exhibits minimal sensitivity to pressure and temperature concerning silica wettability. However, in the presence of CO<sub>2</sub>, particularly at higher mole fractions, increased pressure and reduced temperature lead to higher contact angles. The contact angle also increases as the mole fraction of cushion gases increases. Contact angles significantly decrease at higher pH levels, where silica carries a negative charge. Surface charges of  $-0.03$  and  $-0.06$  C m<sup>-2</sup> result in 20% and 80% reductions, respectively, whereas at a pH of about 11 ( $-0.12$  C m<sup>-2</sup>), the contact angle drops to 0° under all conditions, regardless of temperature, pressure, or cushion gas composition (Fig. 26).

The MD simulation by Zheng *et al.*<sup>169</sup> for quartz/H<sub>2</sub>/water systems using LAMMPS revealed that dissolved H<sub>2</sub> tends to migrate to the quartz surface rather than remaining in bulk water. The water contact angle on fully hydroxylated quartz varies from 30.7° to 37.1° as the pressure ranges from 1 to 30 MPa, exhibiting no consistent trend between the water contact angle and pressure in this range.

Similarly, Zheng *et al.*<sup>169</sup> and Zeng *et al.*<sup>213</sup> conducted complexation modeling to understand the wettability of the quartz–H<sub>2</sub>–brine–organic acid system. They calculated the surface potential of pure quartz at several temperatures and pressures. These studies found that increasing the concentration of organic molecules leads to greater H<sub>2</sub>-wetting. The effect of temperature and pressure on the disjoining pressure of the quartz–H<sub>2</sub>–brine system is minimal. The MD results indicated that for pure quartz, increasing pressure and temperature has a negligible effect on H<sub>2</sub> wettability on the pristine quartz



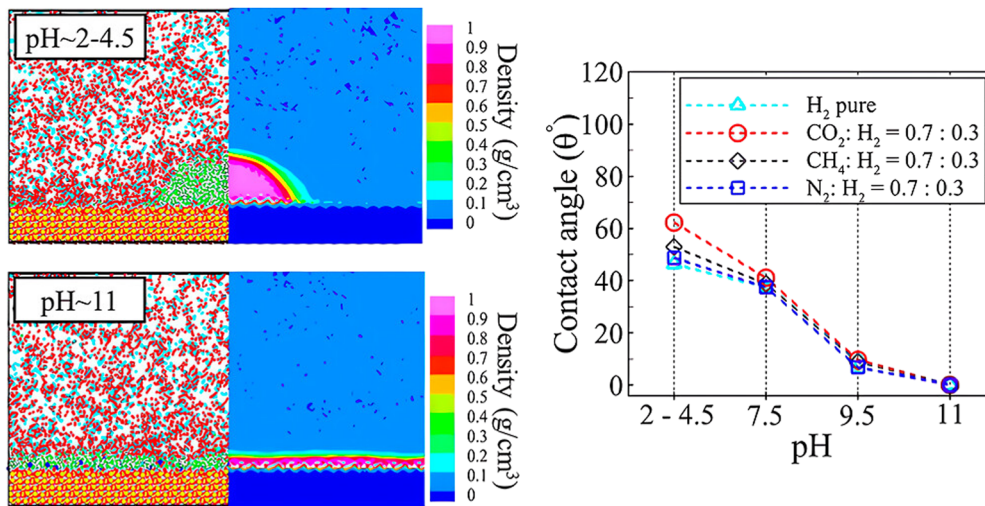


Fig. 26 Two-dimensional gas density distribution in systems containing pure gases by pH. Left panel: Gas density distribution in acidic (pH  $\sim$  2 to 4.5) and basic (pH  $\sim$  11) media, highlighting the density variations. Right panel: Contact angle measurements in systems with negative surface charges at 373 K and 20 MPa for the following cushion gas compositions: (a) N<sub>2</sub>, (b) CH<sub>4</sub>, and (c) CO<sub>2</sub>. The contact angle of the water droplet on the surface remains consistently 0° at a high pH for all gas mixtures. These findings are consistent across the three cushion gases and mole fractions.<sup>389</sup>

surface, aligning with the experimental findings by Hashemi *et al.*<sup>117</sup> but differing from those by Iglauer *et al.*<sup>158</sup> Higher organic-acid concentrations and pressure reduce hydrophilicity and enhance H<sub>2</sub>-wetting, consistent with previous contact angle measurements, demonstrating that an increased organic-acid concentration boosts H<sub>2</sub> wettability.

Conversely, Medina *et al.*<sup>291</sup> used MD simulations to document the contact angle of glass/H<sub>2</sub>/brine (mimicking quartz) systems exhibiting pressure-dependent behavior. As pressure increased from 1.0 to 6.0 MPa, the contact angles at various KCl salinities of 0.5, 2.0, and 4.0 M increased from 22°, 23°, and 23° to 27°, 29°, and 31°, respectively.

The MD simulations of the interfacial properties of H<sub>2</sub>-brine systems exhibit trends similar to those of experimental work. For instance, most experimental results on IFT for UHS reveal an inverse correlation with pressure. As an illustration, the MD simulation conducted by Doan *et al.*<sup>322</sup> using the LAMMPS software for H<sub>2</sub>/cushion gas/water systems demonstrated that IFT decreases with pressure across temperatures ranging from 300 to 343 K. However, similar to experimental methods for assessing rock/H<sub>2</sub>/brine wettability, specific MD simulations display an increase in the contact angle with increasing pressure for quartz/H<sub>2</sub>/brine<sup>291</sup> and carbonate/H<sub>2</sub>/brine systems.<sup>390</sup> This finding contrasts with findings from experimental measurements reported in the literature.<sup>117,168,170</sup> The discrepancy likely stems from differences in assessment methods influencing the surface wettability behavior in these studies. Other examples of MD simulations<sup>307,322,326,391,392</sup> have considered cushion gas, clay,<sup>236,267,379,393</sup> shale,<sup>391,394-396</sup> carbonate, and sandstone.<sup>291,390</sup>

A comprehensive understanding at the molecular level is essential for the advancement of UHS systems that ensure security and efficiency. For example, Ghasemi *et al.*<sup>397</sup> used GROMACS MD simulations to investigate H<sub>2</sub> diffusion across

three clay minerals—pyrophyllite, montmorillonite, and beidelite—considering the charging behavior of the clay. The MD simulation indicated that H<sub>2</sub> diffusion in clay minerals is markedly reduced compared to that in bulk water, attributable to the restrictive conditions presented by the clay matrix. In clay with a negative charge, an increase in pore size of up to 2 nm results in an elevation of the H<sub>2</sub> diffusion coefficient, whereas beyond 2 nm, the coefficient stabilizes and does not change. The authors observed that the presence of interlayer cations and the charging characteristics of clay minerals influence the H<sub>2</sub> diffusion coefficient. The enhanced polarizability of the O-sheet draws in water molecules, elevating the diffusion coefficient.

Regarding the effect of salinity, divalent ions reduce H<sub>2</sub> diffusion in saline aquifers and enhance storage.<sup>398</sup> In addition, CaCl<sub>2</sub> and MgCl<sub>2</sub> are more suitable than NaCl for H<sub>2</sub> storage in reservoirs with a high water content. Among anions, Cl<sup>-</sup> is more favorable than SO<sub>4</sub><sup>2-</sup> because H<sub>2</sub> diffusion changes significantly with Cl<sup>-</sup> at lower anion concentrations than SO<sub>4</sub><sup>2-</sup>.<sup>398</sup> This result highlights the necessity of thoroughly assessing the reservoir and caprock mineralogy to understand potential H<sub>2</sub> diffusion during UHS. Furthermore, MD simulations can model H<sub>2</sub> solubility in underground storage, offering insight into how temperature, pressure, and rock properties influence H<sub>2</sub> behavior at the molecular level.<sup>399</sup>

The MD method provides a better theoretical basis for the relationships involved with wettability and interfacial properties than experimental measurements.<sup>400</sup> Moreover, less human error is involved upon proper execution of the simulation. However, the range MD covers for UHS over rock surfaces is still limited and requires further investigation due to its novelty.

Moreover, improper execution of a simulation study and other limitations associated with MD simulations can also be reasons for inconsistencies. In addition to errors specific to a



particular MD simulation method and potential errors in any approximate computer model, most simulation models are based on a particular model of the considered solid surface, aqueous fluid, or mode and nature of interactions between simulated components. Some MD simulations consider only the most abundant mineral or component and do not consider those present as traces that may influence the outcome by altering the overall flow dynamics.

Moreover, although silica surfaces are net negatively charged, this does not imply positive charges on the natural reservoir surfaces. Positive charge components or minerals may be present, affecting the actual interactions. While simulation models are being developed to incorporate the best available experimental observations and represent the most realistic rock/H<sub>2</sub>/brine interactions, they cannot be guaranteed to mimic real reservoir situations perfectly.<sup>401</sup>

## 5.2. Applications of numerical techniques

Numerical approaches are crucial for analyzing wetting behavior, interfacial interactions, injection strategies, recovery efficiencies, and overall performance in UHS systems. These methods use CFD, PNM/pore-scale modeling, and other advanced simulation techniques to simulate fluid–rock interactions, phase behavior, and transport phenomena in porous media (e.g., ref. 40, 114, 131, 166, 313, 372–374 and 402–405). By integrating these numerical models with experimental data or theoretical frameworks, researchers and industry practitioners can assess operational scenarios, optimize injection and extraction strategies, and predict storage efficiency under diverse geological and operational conditions (Fig. 27(a–d)). This approach enhances the understanding of UHS processes and supports the design and implementation of safe, efficient, and sustainable H<sub>2</sub> storage solutions.

**5.2.1. Computational fluid dynamics.** The CFD model employs numerical techniques to analyze and solve fluid-flow problems, enabling simulations of fluid dynamics, mass transfer, and chemical reactions in diverse systems. Bagheri *et al.*<sup>145</sup> conducted a pore-scale investigation using CFD to study the flow dynamics of H<sub>2</sub>–water systems in aquifers under elevated pressure. The authors observed that optimal injection and production rates for H<sub>2</sub> differ and that capillary and viscous fingering effects could be minimized at moderate flow rates, improving recovery and storability factors. This research highlights the significance of comprehending the transport and trapping mechanisms of H<sub>2</sub> in porous media for practical UHS.

Similarly, Sainz-Garcia *et al.*<sup>41</sup> used COMSOL Multiphysics for simulations investigating the immiscible multiphase flow of water alongside a CH<sub>4</sub>–H<sub>2</sub> gas mixture in the context of CH<sub>4</sub>–H<sub>2</sub> underground storage located in the Lower Triassic of the Paris Basin. Their findings underscored the crucial effect of gas and aquifer characteristics on storage. The researchers created a 3D multiphase numerical model to investigate extraction well configurations, underscoring the potential to attain up to 78% H<sub>2</sub> recovery during underground storage (Fig. 27(e–j)). However, they cautioned that H<sub>2</sub> up-coning could pose challenges in saline aquifers without cushion gas. Applying numerical methods for CFD simulations can yield valuable insight

into complex multiscale phenomena, optimizing the design and operation of UHS facilities.<sup>164,314,399,406–409</sup>

**5.2.2. Pore network modeling.** The PNM simulation method simplifies the complex structure of porous materials into a network of interconnected void spaces, called pores, and the narrow passages between them, known as throats.<sup>399</sup> This approach investigates the phenomenon of fluid transport and flow through porous media by considering crucial characteristics, such as the shape and size of the pore and its connectivity.<sup>399,410,411</sup>

In their investigation of H<sub>2</sub> transport in sandstone reservoirs at varying wetting conditions using direct numerical simulation, Wang *et al.*<sup>412</sup> observed that an increase in H<sub>2</sub> wetting decreased the snap-off effect during the primary drainage process, enhancing H<sub>2</sub> storage capacity. However, increased H<sub>2</sub> wetting impeded the extraction process, leading to a recovery factor of less than 20% during the primary imbibition process. Similarly, in a pore-scale modeling study, Hashemi *et al.*<sup>20</sup> investigated H<sub>2</sub> transport properties in brine-saturated porous rocks for UHS. The sensitivity analysis quantified the effects of relative permeability and capillary pressure on fluid and rock properties, demonstrating the sensitivity of relative permeability and capillary pressure to contact angles. The results indicated that clay content notably affected the endpoint values of the relative permeability curves for drainage and imbibition cycles.

Wang *et al.*<sup>412</sup> and Bagheri *et al.*<sup>145</sup> discussed the influence of wetting conditions and flow rates on H<sub>2</sub> storage and extraction, whereas Hashemi *et al.*<sup>20</sup> and Zhao *et al.*<sup>410</sup> emphasized the necessity of systematically understanding fluid and rock properties in UHS. Accordingly, Zhao *et al.*<sup>410</sup> demonstrated that using H<sub>2</sub> trapping rates simulated by the PNM as training data for ML models enhances predictions of H<sub>2</sub> trapping rates beyond traditional PNM. Integrating pore-scale modeling with ML techniques significantly improved these predictions. Such integrated approaches contribute to a holistic understanding of factors influencing H<sub>2</sub> storage in porous media, offering crucial insight for UHS site selection and design.

Moreover, ML can refine CFD and PNM correlations by incorporating additional variables and interactions specific to H<sub>2</sub>. Applying ML models to a large dataset of experimental measurements can help identify complex patterns and improve prediction accuracy.

## 5.3. Machine learning applications

Using ML for predicting the wettability; rock–fluid interfacial properties; adsorption, injectivity, and withdrawal of H<sub>2</sub> in reservoirs; and caprock integrity for UHS has recently garnered attention within the research community.<sup>413–418</sup> Moreover, ML methods have increasingly been employed to predict the wetting behavior of mineral/H<sub>2</sub>/brine systems,<sup>155,414</sup> H<sub>2</sub>–fluids interfacial properties,<sup>154,419–421</sup> and the sealing integrity and leakage detection<sup>422</sup> in UHS systems.

This advanced technique provides significant advantages in modeling complex interactions that are otherwise challenging to capture using traditional methods. By employing large



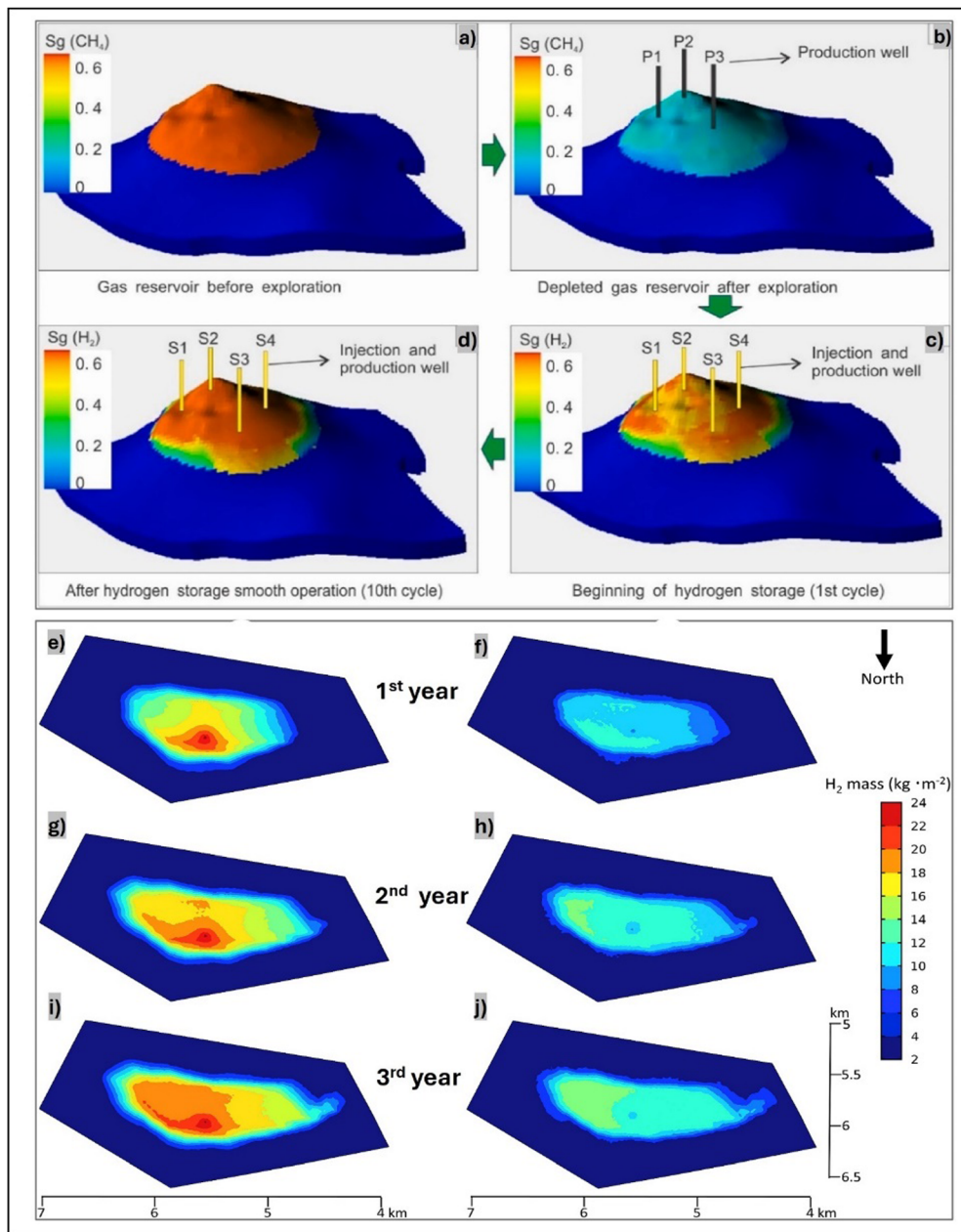


Fig. 27 Reconstruction of depleted gas reservoirs into underground hydrogen ( $H_2$ ) storage (UHS) and  $H_2$  concentration over time. (a)–(d) Simulation of transforming a depleted gas reservoir into a functional UHS site. Gas reservoir (a) before and (b) after exploration and changes in  $H_2$  saturation at the beginning of storage, (c) after smooth operation over one cycle, and (d) after smooth operation over 10 cycles.<sup>402</sup> (e)–(j) Vertically integrated  $H_2$  concentration ( $kg\ m^{-2}$ ) over the aquifer thickness by operational stages. (e) and (f) First year:  $H_2$  injection and extraction, (g) and (h) second year:  $H_2$  injection and extraction, and (i) and (j) third year:  $H_2$  injection and extraction.<sup>41</sup>

datasets, ML algorithms can identify patterns and relationships in data, leading to more accurate predictions and insight.<sup>399</sup> Moreover, ML has made notable strides in predicting wettability,<sup>414</sup> which is a critical factor in determining the efficiency of  $H_2$  storage in geological formations. Traditional methods of assessing wettability typically involve labor-intensive and time-consuming laboratory experiments. However, ML techniques can streamline this process by predicting wettability from existing data, reducing the need for extensive empirical testing. The capability of ML applications in UHS is illustrated in Fig. 28(a–d).

In addition, Tariq *et al.*<sup>413</sup> demonstrated the effectiveness of ML models in predicting advancing and receding contact angles in rock/ $H_2$ /brine systems. Decision trees, random forests, feed-forward neural networks,  $k$ -nearest neighbors, extreme gradient boosting, and adaptive boosting have been employed to create predictive models that achieve high accuracy with mean absolute percentage errors of less than 5% and coefficients of determination ( $R^2$ ) exceeding 0.95. These models offer accurate predictions and provide a practical tool for engineers and scientists to estimate wettability



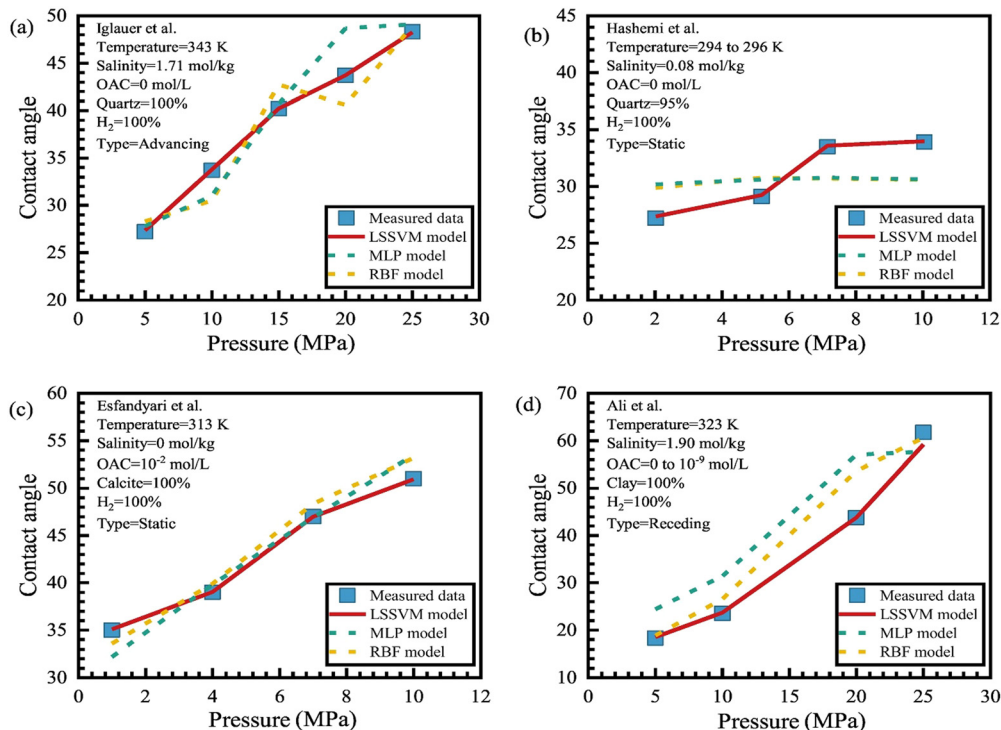


Fig. 28 Predicted and measured contact angles and cyclic evolution of hydrogen ( $H_2$ ) saturation in underground  $H_2$  storage (UHS) operations. (a)–(d) Comparison of predicted and measured contact angles for  $H_2$ –mineral–brine systems as a function of pressure. The data are based on multiple models across experimental conditions, including the least-squares support vector machine (LSSVM), multilayer perceptron (MLP), and radial basis function (RBF).<sup>414</sup>

without specialized ML software using derived mathematical equations.

Similarly, Vo Thanh *et al.*<sup>210</sup> applied ML algorithms (*e.g.*, extreme gradient boosting, random forest, light gradient boosting, and adaptive boosting) to predict  $H_2$  wettability based on input features, such as pressure, temperature, salinity, and rock type. These models have demonstrated excellent performance, with  $R^2$  values over 0.95, further validating the potential of ML in this domain. Taking a different direction, Ansari *et al.*<sup>423</sup> applied ML models, such as the radial basis function and least-squares support vector machine, to predict  $H_2$  solubility in aqueous solutions. These models were benchmarked against traditional equations of state and performed well, highlighting the robustness and accuracy of ML approaches in predicting complex interfacial properties.

The increasing adoption of ML techniques in predicting wetting behavior and rock–fluid interfacial properties signifies a paradigm shift in studying these critical parameters. Moreover, ML is facilitating more effective and economical UHS solutions by enhancing the accuracy and efficiency of predictions. This trend underscores the need for continued research and development in applying ML to UHS, which is essential for advancing the  $H_2$  economy and achieving energy sustainability goals.

In addition, ML models rely on the availability of extensive experimental data. However, obtaining extensive and reliable contact angle data for gases across pressure and temperature

values can be challenging. Experimental limitations (*e.g.*, the difficulty of maintaining stable conditions and accurately measuring small contact angles) add to the uncertainty in the derived correlations. In subsurface storage conditions, multiple phases (solid rock, brine, and gas) add complexity to the wetting behavior, which could lead to uncertain predictions.

#### 5.4. Neural networks, deep learning, and neural operator learning

Scientific ML represents a novel class of solvers that integrate ML techniques with scientific computing principles to address challenges in computational science. These problems are challenging to solve using traditional methods, whereas ML techniques can efficiently manage large datasets. Applying scientific ML techniques to UHS problems can substantially accelerate simulations and optimize storage cycles, uncertainty quantification, and sensitivity analyses.<sup>424–427</sup> Similarly, deep learning models can help mitigate climate change by accelerating the modeling and simulation of  $H_2$  storage projects for better management and risk mitigation.<sup>425,428</sup>

The neural network is an algorithm class loosely modeled after the human brain and designed to recognize patterns and solve complex problems. A notable class of such architectures that have recently gained significant traction is neural operators. A critical advantage of operator learning is that once a model is trained, it can generalize to new input functions. Thus, in inference, a trained operator is orders of magnitude



faster than a numerical solver. Another critical advantage of the operator is that it can train using simulation data, experimental (real or noisy) data, or both.

The DeepONet<sup>429</sup> was the first to use deep learning to train operators directly from data, followed by another algorithm, Fourier neural operators (FNO). More specialized versions of these algorithms were quickly proposed to improve these algorithms. Fig. 29(a) presents a schematic of the U-DeepONet architecture. The U-FNO and U-DeepONet architectures were applied to a CO<sub>2</sub> sequestration dataset for benchmarking.<sup>428,430</sup> Although the objectives of CO<sub>2</sub> sequestration are different from those of UHS, both require subsurface structural entrapment. Moreover, the application has minimal influence in data-driven ML because the data are typically represented in a series of images. Nonetheless, using the CO<sub>2</sub> sequestration dataset presents a valuable gauge of the capabilities of neural operators for gas flow and transport problems in heterogeneous porous media.

The idea is that a trained neural operator should be able to generalize using inputs; given a new combination of variables not in the training dataset, the neural operator should accurately predict the state variables. Fig. 29(b–e) presents four testing examples for gas saturation, and Table 5 compares the performance of the U-FNO and U-DeepONet. Fig. 29(b–e) reveals that the results of neural operator learning are phenomenal, with inference times that cannot be matched using traditional numerics. These advantages can easily be transferred to H<sub>2</sub> storage simulation, with potentially more significant advantages given the cyclic nature of H<sub>2</sub> storage and utilization. For instance, a U-DeepONet can be set up to predict storage efficiency given recurrent instances of production and injection. The U-DeepONet can be trained to consider operational conditions, such as injection and production rates, to maximize storage efficiency at no additional cost during simulation. Moreover, the instantaneous predictive capabilities of neural operators can be valuable in mitigating water production risks and environmental effects.

Carbonero *et al.*<sup>425</sup> addressed the computational challenges impeding large-scale UHS. Their primary contributions include the following:

- Development of autoregressive ML models tailored to UHS, iteratively refining predictions using prior outputs, enabling time extrapolation and adaptability to cyclic injection-withdrawal operations;
- Adaptation of ML frameworks from geological carbon sequestration to UHS by integrating scalar performance metrics (*e.g.*, H<sub>2</sub> recovery factor and gas purity); and
- Generation of a 2D UHS simulation dataset (1000 scenarios) to train models.

Fig. 30 presents an example from this dataset. The authors trained four U-Nets to compare static and autoregressive ML approaches for saturation and pressure. Their results revealed that autoregressive models excel in H<sub>2</sub> saturation prediction (86.1% lower validation error than static models) but struggle with error accumulation in pressure forecasting. The framework achieves scalable predictions across diverse reservoir conditions by incorporating geological parameters (porosity

and permeability) and operational variables (cycle stages and cushion gas). The study also identified critical future steps, such as mitigating error propagation in autoregressive models and extending methods to 3D systems. This research bridged a significant gap in UHS modeling, offering a roadmap for ML-driven tools to accelerate clean energy resilience *via* efficient H<sub>2</sub> storage management.

Mao *et al.*<sup>432</sup> proposed using reduced-order models (ROMs) to focus on the rapid prediction of scalar performance metrics (*e.g.*, withdrawal efficiency and gas purity) by training a neural network to predict critical operational indicators to bypass the complexity of learning on spatial grids and improve computational efficiency. The authors proposed deep neural network-based ROMs, trained on 1000 physics-based simulations to forecast critical metrics, including the H<sub>2</sub> withdrawal efficiency, produced H<sub>2</sub> purity, and gas–water ratio. Their primary contributions include the following:

- Developing ROMs that achieve a 22 000 acceleration over traditional simulations while maintaining high accuracy;
- Conducting global sensitivity analyses *via* Sobol's method to identify critical parameters, such as the injection pressure coefficient, reservoir depth, and initial water saturation; and
- Demonstrating the framework utility *via* a field case study in the Dakota formation, where optimizing the operational parameters reduced the prediction uncertainty by up to 93.8%.

The study underscored the potential of ML ROMs to enable rapid feasibility assessments and operational optimization for UHS.

### 5.5. Coupled computational techniques for underground hydrogen storage

Recently, researchers have adopted coupling techniques integrating MD simulation, ML, and pore-scale simulations to clarify the UHS process. For instance, Wang *et al.*<sup>433</sup> recently adopted these methods for simulating and predicting the density distribution of H<sub>2</sub> in nanoporous media using the improved lattice Boltzmann model, watershed algorithm, and trained artificial neural network. The study evaluated the influence of H<sub>2</sub> adsorption in the nanoscale space due to solid–gas interaction on the efficiency of UHS and H<sub>2</sub> withdrawal from shale reservoirs. The trained artificial neural network predicted the UHS potential in the shale kerogen digital core, indicating that 70.48% of the total gas mass is adsorbed gas.

The combination of the MD, ML, and pore-scale simulations is beneficial in overcoming the limitations of each technique alone. For instance, considerable computational resources are required when pore-scale simulations are used alone. In addition, only the macroscopic adsorption behavior is captured using numerical simulations and macroscopic experiments, whereas single nanopores can only be simulated using MD simulations alone. Combining these techniques allows simulating complex pore structures and elucidating process behavior and mechanisms from a broad-scale perspective.

Recently, MD simulations have been combined with ML techniques to predict the interfacial properties of H<sub>2</sub>–H<sub>2</sub>O–brine



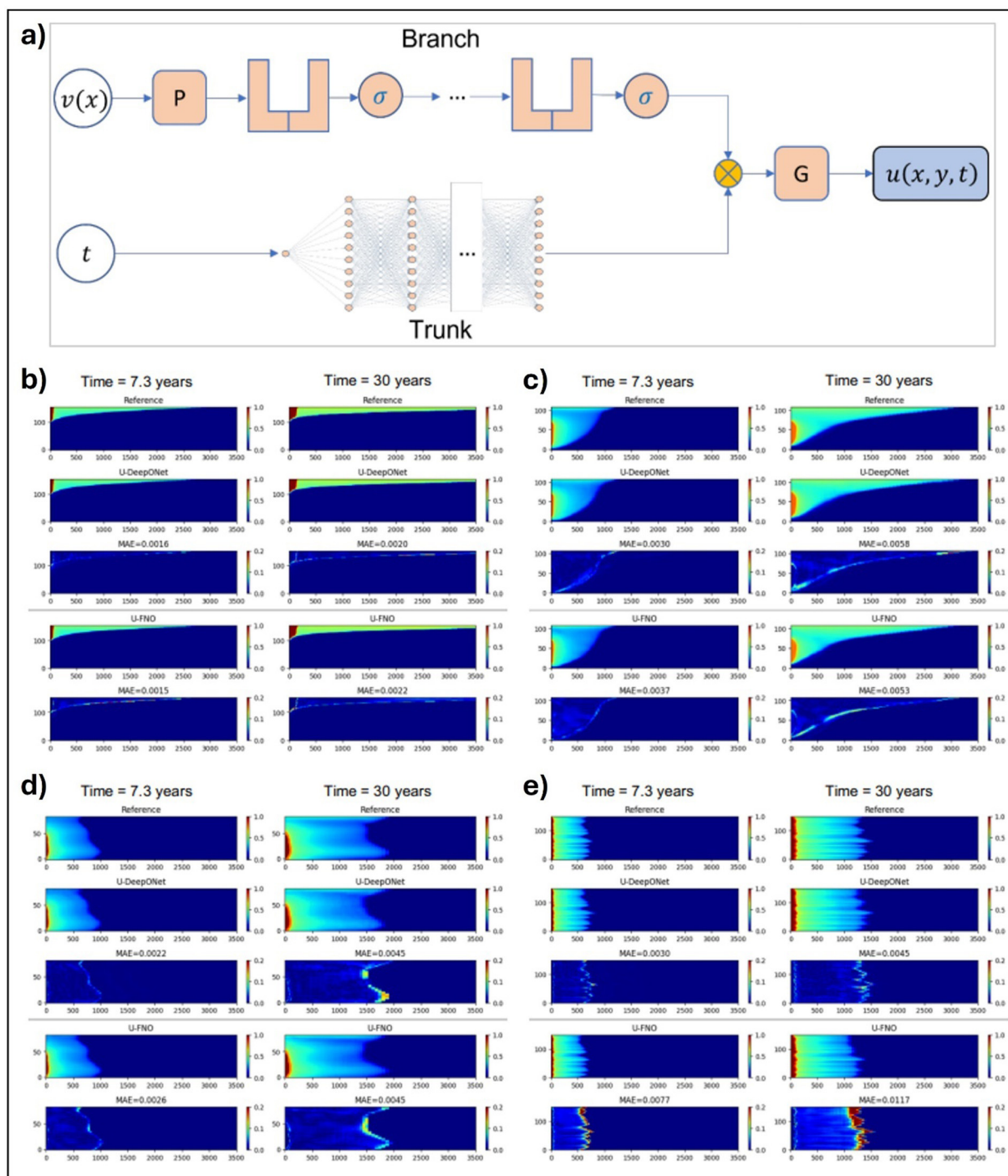


**Fig. 29** U-DeepONet architecture and gas saturation predictions over time. (a) U-DeepONet architecture consisting of trunk and branch networks. The trunk is a feed-forward neural network that takes time ( $t$ ) as input. The branch network contains U-Net blocks with a linear layer ( $P$ ) followed by activation functions ( $\sigma$ ), and the output is passed through a shallow neural network ( $G$ ) to generate the final output.<sup>431</sup> (b)–(e) Visualizations of gas saturation predictions for four test cases. Two snapshots are presented for each case: 7.3 years and 30 years. The reference solutions represent the ground truth generated by a simulator. Predictions made by U-DeepONet and U-FNO are presented alongside their mean absolute error (MAE) maps, indicating the accuracy of the models.<sup>431</sup>

across a broad range of conditions, including temperatures from 298 to 373 K, pressures from 1 to 30 MPa, and NaCl salinities from 0 to 5.02 mol kg<sup>-1</sup>. The influence of cations, determined by their valency and surface configuration, reveals that Ca<sup>2+</sup> can increase

IFT values by up to 12% compared to KCl, with KCl having the most negligible influence. Fig. 31 illustrates the direct relationship between IFT values and salinity and an inverse relationship with temperature and pressure. The IFT between H<sub>2</sub> and brine



**Table 5** Performance comparison of U-FNO and U-DeepONet for gas saturation predictions. The performance of U-FNO and U-DeepONet models is compared using data averaged over the entire testing dataset for gas saturation predictions. The results highlight the differences in accuracy and computational efficiency between the two models. The data are from ref. 430

Training						Testing			
Model	No. of parameters	GPU memory (GiB)	Training time/epoch (s)	Minimum epochs needed	Training time (h)	$R^2$	MPE (%)	MAE	Inference time (s)
U-FNO	33 097 829	15.9	1912	100	53.1	0.981	1.61	0.0031	0.0182
U-DeepONet	1 803 369	4.6	108	100	3.0	0.994	1.58	0.0026	0.0156

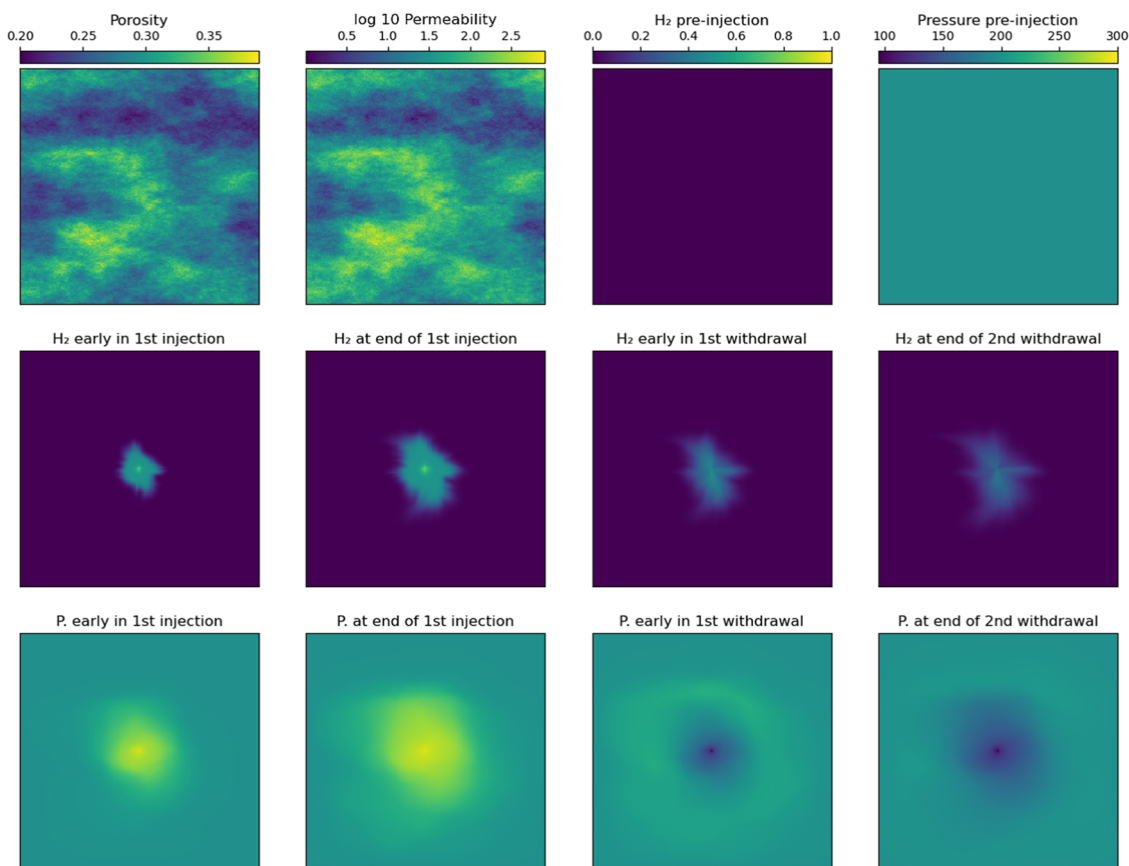


**Fig. 30** Temporal evolution of the spatial distribution of hydrogen ( $H_2$ ) saturation and reservoir pressure in a two-dimensional underground  $H_2$  storage (UHS) simulation. The  $H_2$  is injected and withdrawn from a central well in a depleted gas reservoir over 10 annual cycles comprising a 6-month injection stage followed by a 6-month withdrawal stage. Top row (first two figures): Heterogeneous porosity and permeability of the geological formation. Subsequent figures:  $H_2$  saturation and pressure distributions at time points during UHS operations. 'Early' refers to two months after onset; 'end' is at six months. Porosity and  $H_2$  saturation are dimensionless; permeability is in millidarcies ( $10^{-15} \text{ m}^2$ ); pressure is in bars ( $10^5 \text{ Pa}$ ).<sup>425</sup>

decreases with increasing temperature at all pressures, whereas higher NaCl salinity increases IFT, with a slight decrease observed with increasing pressure.<sup>305</sup>

The IFT datasets predicted using MD simulations were employed to develop correlations using three interpretable ML methods: genetic programming, gene expression programming, and the group method of data handling. Among these, genetic programming yielded the most accurate correlation, achieving an  $R^2$  of 0.9783 and an absolute average relative deviation of 0.9767%. In addition, MD simulation provides atomic-level insight into interfacial phenomena and establishes a reliable dataset that can train ML algorithms for database expansion.<sup>305</sup>

In addition, Zhang *et al.*<sup>434</sup> used a coupled MD-ML approach to evaluate  $H_2$  solubility in brine under various pressure, temperature, and salinity values. The results aligned well with experimental data. Moreover, they discovered that temperature nonlinearly affects  $H_2$  solubility in water.

Zhao *et al.*<sup>410</sup> predicted the influence of pore structure and rock-surface wettability on  $H_2$  withdrawal during UHS using ML and PNM. Two-phase flow ( $H_2$ /brine) in various porous media, such as carbonate, sand packs, and sandstone, was simulated using 3D PNM, whereas two ML techniques (support vector machine and the least square fitting) describe the trapping rate of  $H_2$  in the rock and the trapping capacity of the rock.



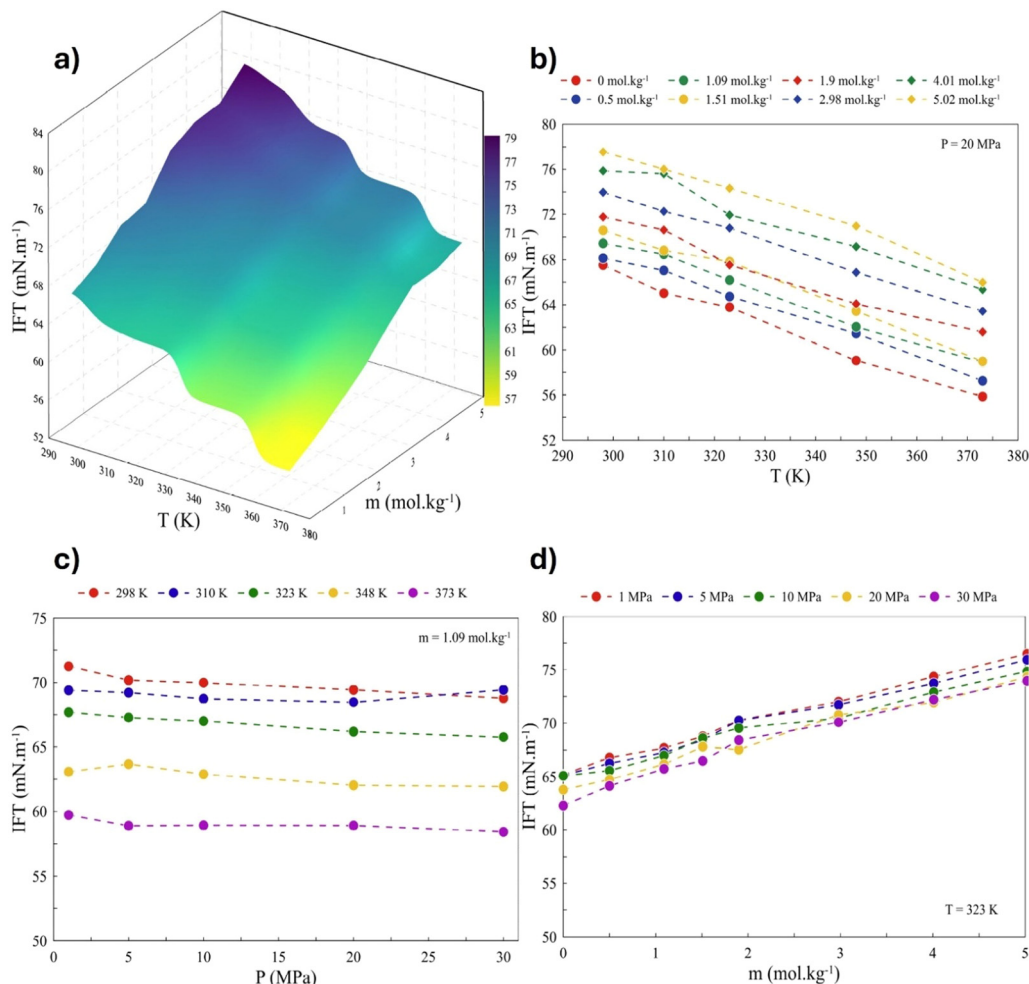


Fig. 31 Molecular dynamic simulations and machine learning-predicted interfacial tension (IFT) values for the hydrogen ( $\text{H}_2$ )-brine system. (a) IFT variations with temperature (298–373 K) and salinity (0–5.02 mol  $\text{kg}^{-1}$ ) at 10 MPa. IFT as a function of (b) temperature and NaCl salinity at 20 MPa, with a decrease in IFT with increasing temperature and salinity; (c) pressure and temperature at 1.09 mol  $\text{kg}^{-1}$  NaCl salinity, where pressure minimally influences IFT compared to temperature; and (d) pressure and NaCl salinity at 323 K, highlighting the dominant influence of salinity on IFT. Salinity and temperature significantly affect IFT, whereas pressure has a less pronounced effect.<sup>305</sup>

The trapping rates of  $\text{H}_2$  simulated *via* PNM were applied as training data in ML models. The findings from ML demonstrated that rocks with high pore connectivity and a low ratio of pore-to-throat size are suitable for ensuring a low  $\text{H}_2$  trapping rate during UHS.

Mao *et al.*<sup>435</sup> combined deep learning and reservoir simulations. The 3D multiphase, compositional reservoir modeling of saline aquifers and depleted gas reservoirs under various cushion gas scenarios was executed using the tNavigator software. The authors proposed critical storage performance metrics, such as  $\text{H}_2$  withdrawal efficiency, produced  $\text{H}_2$  purity, gas-water ratio, and well injectivity. The authors simulated the performance of four cushion gas situations (none,  $\text{CO}_2$ ,  $\text{N}_2$ , and  $\text{CH}_4$ ) using tNavigator in UHS operations in saline aquifers and depleted gas reservoirs (Fig. 32). Based on the simulation results, a unified ROM was developed using a deep neural network. The results indicated that cushion gas barely influences  $\text{H}_2$  purity and recovery efficiency in depleted gas reservoirs. However, cushion gas in saline aquifers reduced  $\text{H}_2$  purity and

recovery efficiency, but the cushion gas considerably improved the injectivity and gas-to-water ratio. Moreover, the ROM correctly predicted the cyclic evolution of the performance metrics at more than 5 000 000 times faster than physics-based reservoir simulations. Overall, artificial intelligence-driven models are valuable for mitigating the high computational cost and are less computationally intensive than multiphysics simulations.

The findings from computational models assist in optimizing  $\text{H}_2$  injection and withdrawal processes from UHS sites, ensuring that UHS processes are cost-effective and efficient. For instance, computational models can help identify injection rates, optimal pressure levels, and well designs to minimize contamination risks or gas leakages and maximize  $\text{H}_2$  storage capacity.<sup>436</sup> The application of advanced computational methods for simulating  $\text{H}_2$  interaction with fluids, cushion gases, and geological formations (*e.g.*, aquifers, depleted gas fields, and salt caverns) can help predict the  $\text{H}_2$  distribution, migration, and interaction with surrounding fluid and rock.



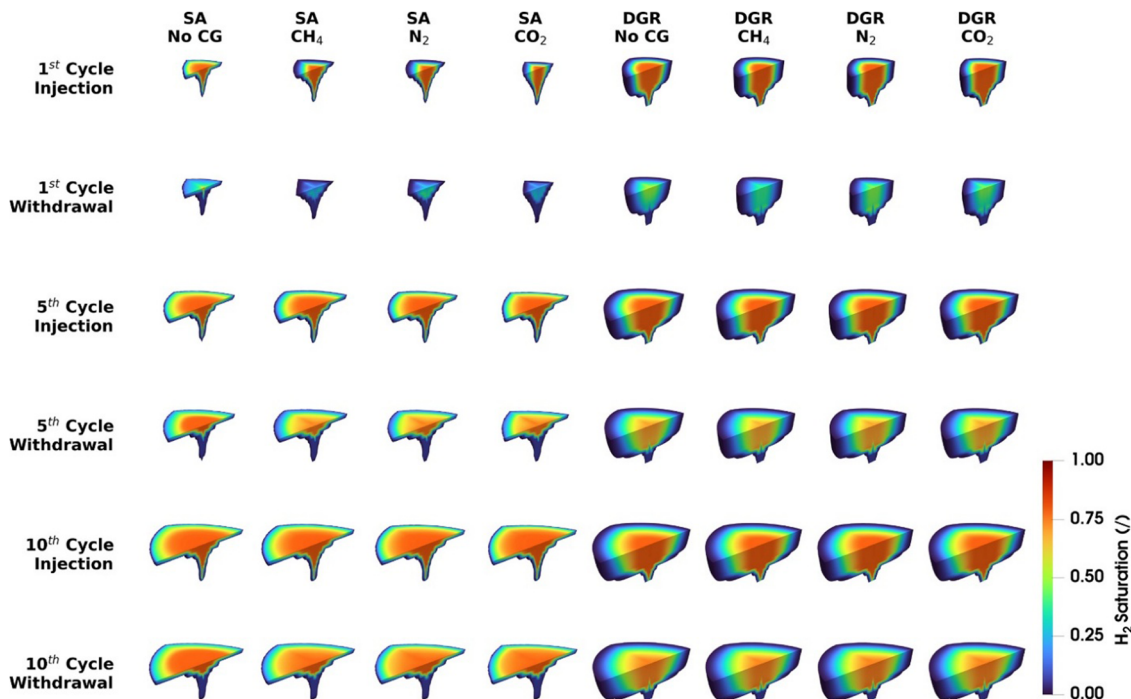


Fig. 32 Cyclic evolution of hydrogen ( $H_2$ ) saturation in underground  $H_2$  storage. Injection and withdrawal operations in saline aquifers (SA) and depleted gas reservoirs (DGR) under cushion gas scenarios (none,  $CH_4$ ,  $N_2$ , and  $CO_2$ ). The distribution of  $H_2$  saturation is presented for the first, fifth, and tenth injection and withdrawal cycles.<sup>435</sup>

Such insight is valuable for ensuring the safety and long-term stability of storage sites. Modeling  $H_2$  behavior in porous rock *via* computational simulations can predict possible leakages and mitigation strategies. The most economically attractive methods for UHS processes can be determined by simulating operational scenarios, identifying cost drivers, and exploring scenarios for scaling up storage capacity.<sup>437</sup>

## 6. Adsorption and desorption of hydrogen in conventional and unconventional reservoirs

Desorption and adsorption of  $H_2$  in unconventional shale and coal seam reservoirs<sup>438</sup> are crucial in the success of UHS. These unconventional reservoirs, characterized by their ultra-tight pore structures and significant organic content, offer unique adsorption sites that enhance  $H_2$  storage capabilities. Coal seams and shale contain smaller, less interconnected pores than conventional reservoirs, increasing the likelihood of gas molecules adhering to rock surfaces. Organic material, such as kerogen, further contributes to higher adsorption capacities, making these reservoirs potential candidates for efficient  $H_2$  storage.<sup>72,152,330,439</sup> Understanding the sorption behavior of  $H_2$  in these geological formations is essential for optimizing storage strategies and improving gas recovery processes.

The feasibility of  $H_2$  geo-storage in coal seams *via* the adsorption of  $H_2$  on coal surfaces has garnered recent attention.<sup>72,123</sup> Experiments have been conducted to demonstrate the feasibility

of UHS in coal seams (*via* adsorption of  $H_2$  on the surface of coal).<sup>72,123,331</sup> Iglauer *et al.*<sup>72</sup> conducted a detailed analysis of subbituminous coal using various analytical techniques. The adsorption capabilities of  $H_2$  in coal seams reach up to 0.6 mol  $H_2$  per kg at 14.3 MPa.<sup>72</sup> In contrast, the rate of  $H_2$  adsorption in coal seams and the diffusion coefficient of  $H_2$  are one order of magnitude larger than the  $CO_2$  diffusion coefficient over a temperature range of 293 to 333 K.<sup>123</sup> These results suggest that a considerable amount of  $H_2$  could be conveniently stored in coal seams.

Keshavarz *et al.*<sup>123</sup> employed similar methods to measure the rate of  $H_2$  adsorption on Australian anthracite coal samples at 1.3 MPa and varying temperatures (293 to 333 K). The diffusion coefficient of  $H_2$  ( $D_{H_2}$ ) was computed using eqn (17), which estimates the adsorption of  $H_2$  on the surface of the coal:

$$D = \frac{R_p^2}{t_0} \quad (17)$$

The variable  $R_p$  represents the coal-particle radius, and  $t_0$  denotes the gas adsorption time.

Fig. 33 compares existing  $H_2$  adsorption data in the literature for unconventional and conventional rock, indicating that  $H_2$  adsorption on conventional formations (*e.g.*, sandstone and carbonate) is lower than in ultra-tight reservoirs (*e.g.*, shale and coal seams), with kerogen displaying the highest adsorption. Conventional rock minerals (*e.g.*, calcite and quartz) demonstrate moderate  $H_2$  adsorption.<sup>440–442</sup> The higher porosity and permeability of Berea sandstone result in larger, well-connected



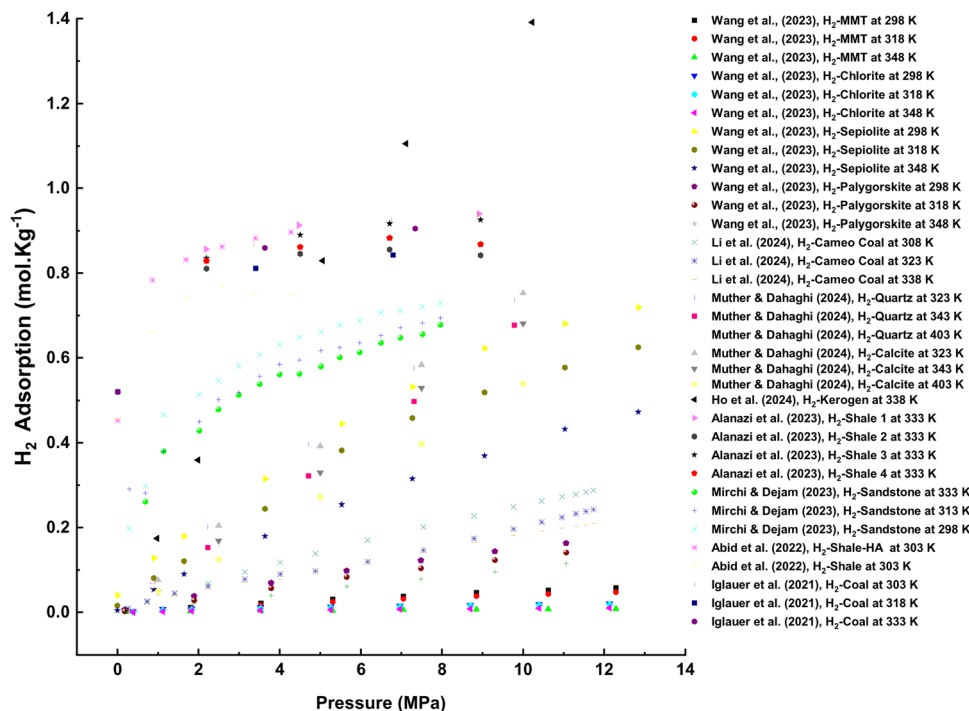


Fig. 33 Comparison of hydrogen (H<sub>2</sub>) adsorption data by rock type (shale, coal, clay, and conventional reservoir rock) as a function of pressure and temperature. Data were collected and replotted from multiple studies,<sup>72,149,151,152,330,331,441–443</sup> providing a comprehensive comparison of adsorption capacity across geological formations as a function of pressure and temperature in H<sub>2</sub> storage environments, which is critical for assessing their potential in underground H<sub>2</sub> storage applications.

pores that facilitate gas flow, reducing adsorption onto rock surfaces.

In contrast, unconventional tight rock, such as shale and coal, have smaller, less interconnected pores, enhancing gas adsorption because gas molecules are more likely to adhere to the rock surface.<sup>149–151,331</sup> Unconventional rock contains organic material, such as kerogen, providing active sites for gas molecule adsorption, increasing the adsorption capacity of these rocks.<sup>439,444,445</sup> This characteristic suggests that conventional rock might lower H<sub>2</sub> loss during retrieval, making H<sub>2</sub> storage in conventional rock a potentially more efficient method for preserving H<sub>2</sub> quantities.

Hydrogen adsorption in clay varies significantly depending on the type of clay mineral. For example, montmorillonite and chlorite typically have low H<sub>2</sub> adsorption capacities. This limited adsorption is attributed to their structural characteristics and surface properties, which do not favor significant H<sub>2</sub> retention. In contrast, the fibrous clay mineral sepiolite demonstrates a moderate H<sub>2</sub> adsorption isotherm. The unique pore structure and higher specific surface area characteristics of sepiolite facilitate better H<sub>2</sub> adsorption than montmorillonite and chlorite. Studies have highlighted these differences,<sup>446,447</sup> emphasizing that the adsorption capacity of clay minerals can be influenced by surface area, pore-size distribution, and functional groups. Various clay minerals can significantly affect the efficiency of H<sub>2</sub> storage.

Furthermore, Wang *et al.*<sup>443</sup> and Ziemiański *et al.*<sup>448</sup> supported these findings, highlighting that variations in H<sub>2</sub> adsorption of

clay minerals are significant and must be considered when evaluating their potential for H<sub>2</sub> storage applications. Understanding these variations is crucial for optimizing H<sub>2</sub> storage systems, particularly in geological formations with various clay minerals.

Using MD simulations and NMR experiments, Ho *et al.*<sup>151</sup> explored H<sub>2</sub> adsorption behavior and diffusion in porous media. They assessed the NMR response of H<sub>2</sub> injected into Duvernay shale and Berea sandstone samples, representing the caprock and storage zones. Gas (H<sub>2</sub> and CH<sub>4</sub>) adsorption at 338 K onto the kerogen porous structure was evaluated using the grand canonical Monte Carlo simulation technique in LAMMPS. Sorption of a gas mixture involving H<sub>2</sub>/CH<sub>4</sub> competitive adsorption and diffusion in kerogen (an essential constituent of shale) was also reported. The NMR response of H<sub>2</sub> in Berea sandstone was similar to that of bulk H<sub>2</sub> gas, suggesting insignificant H<sub>2</sub> adsorption.

However, various H<sub>2</sub> storage mechanisms have been reported for Duvernay shale and Berea sandstone. In Duvernay shale, two distinct NMR T<sub>2</sub> peaks were observed: one representing free gas and the other adsorbed gas (these two storage mechanisms include free H<sub>2</sub> and adsorbed H<sub>2</sub>, with hysteresis H<sub>2</sub> loss). The adsorption or desorption hysteresis was noticeable for shale but not for sandstone (one mechanism, *i.e.*, only free H<sub>2</sub> with no hysteresis H<sub>2</sub> loss). In addition, the MD simulation supports the NMR results, indicating free gas and adsorbed gas in shale and sandstone, which suggests that CH<sub>4</sub> outperforms H<sub>2</sub> in adsorption onto kerogen due to stronger interactions with CH<sub>4</sub> than H<sub>2</sub>.<sup>151</sup>



Critical parameters (*e.g.*, pressure, salinity, temperature, organic contaminations, and cushion gas) affecting rock sorption characteristics during UHS are still unclear. Moreover, the influence of biogeochemical interactions and reactions at the wetted interface, their attendant effects on rock permeability and porosity, and the overall success of UHS require further investigation.

## 7. Biogeochemical reactions of hydrogen in porous media

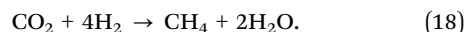
The biogeochemical reactions of H<sub>2</sub> in porous media involve a complex interplay of biological, geological, and chemical processes in porous geological formations. Biological processes involve microbial activities where microorganisms use H<sub>2</sub>, producing it *via* metabolic processes (H<sub>2</sub> generation) or consuming it as an electron donor (H<sub>2</sub> consumption). Geochemical processes entail inorganic reactions where H<sub>2</sub> interacts with rock minerals, formation water, and gases in porous media, potentially altering the reservoir chemistry, porosity, permeability, and overall geochemical environment. Chemical processes include abiotic reactions where H<sub>2</sub> participates in redox reactions independently of biological mediation, interacting with minerals and compounds in the porous media. These interactions are critical in environmental and industrial contexts, affecting energy production, H<sub>2</sub> geo-storage, and subsurface microbial ecosystem dynamics.<sup>89,327,449</sup> The processes involved in generating and consuming H<sub>2</sub> in subsurface environments can be categorized as abiotic (involving nonliving components, such as water, rock minerals, pressure, salinity, and gas composition) and biotic (involving living elements, such as bacteria, including indigenous and anthropogenic microbial life) reactions.<sup>351,450–456</sup>

Subsurface environments typically exhibit high temperature, salinity, pressure, reduced porosity, and limited nutrients.<sup>457–461</sup> Abiotic processes involve inorganic reactions between reservoir rock, native brine, and injected H<sub>2</sub>, influencing petrophysical reservoir properties (*e.g.*, porosity, permeability, pore structure, and composition) and the geomechanical stability of rock formations.<sup>19,457,462</sup> These reactions can occur across a broad temperature range ( $\leq 873$  K), contrasting with typical conditions for ultrahigh-salinity environments.<sup>462</sup> Abiotic H<sub>2</sub> generation, due to its association with high temperature and radiation, may inhibit microbial life near the reservoir.<sup>39,89,449</sup> However, under lower heat or radiation exposure and farther from the reservoir, H<sub>2</sub> may become available for microbial consumption, promoting biotic environments that facilitate H<sub>2</sub> consumption.<sup>460,462</sup> Abiotic and biotic processes involve H<sub>2</sub> generation and consumption; however, abiotic processes focus on H<sub>2</sub> generation, whereas biotic processes predominantly involve H<sub>2</sub> consumption. Fig. 34(a) depicts the biogeochemical reactions involving H<sub>2</sub> during UHS, illustrating the pathways through which H<sub>2</sub> interacts with geological and microbial components.

### 7.1. Methanogenesis and methane production

Methanogens, a group of archaea, are microorganisms that use H<sub>2</sub> to reduce CO<sub>2</sub> into CH<sub>4</sub>. This process, hydrogenotrophic

methanogenesis, is a critical biochemical reaction in subsurface anaerobic environments where methanogens thrive. Three groups of methanogens are typically found: methanobacteriales, methanococcales, and methanomicrobiales.<sup>449,464</sup> The presence of CH<sub>4</sub> indicates the microbial reduction of CO<sub>2</sub> using H<sub>2</sub>. The production of CH<sub>4</sub> from H<sub>2</sub> and CO<sub>2</sub> is an essential consideration for H<sub>2</sub> storage because it could affect the composition and energy content of the stored gas. A typical reaction for methanogenesis is presented in eqn (18):



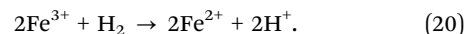
### 7.2. Acetogenesis and acetate production

Acetogens or acetogenic bacteria are another group of microorganisms that use H<sub>2</sub> to reduce CO<sub>2</sub>, producing acetate (CH<sub>3</sub>COO<sup>-</sup>) as a byproduct in a process known as acetogenesis. Common acetogens include *Sporomusa ovata*, *Sporomusa sphaeroides*, *Butyribacterium methylotrophicum*, *Acetobacterium woodii*, *Clostridium acetivum*, *Acetogenium kivui* (*Thermoanaerobacter kivui*), *Clostridium thermoautotrophicum* (*Moorella thermoautotrophica*), and other species.<sup>449,464</sup> This pathway, mediated by acetogens, underscores an additional biogeochemical reaction in which H<sub>2</sub> functions as an electron donor. Acetate generation typically occurs sluggishly in subsurface settings characterized by acidic aqueous aquifers and depleted hydrocarbon reservoirs, predominantly where salinity conditions are notably high.<sup>18,165,327,457,465</sup> However, this generation could influence the microbial community structure and biochemical cycles in the storage formation, as presented in eqn (19):



### 7.3. Iron reducers and transformation

Iron (Fe)-reducing bacteria use H<sub>2</sub> as an electron donor to reduce ferric Fe (Fe<sup>3+</sup>) to its ferrous form (Fe<sup>2+</sup>). Iron reducers may display heterotrophic behavior, using organic carbon as a nutrient source or autotrophic characteristics, where they synthesize their food *via* biochemical processes.<sup>466</sup> Prevalent Fe-reducing bacteria include *Shewanella putrefaciens* and *Geobacter metallireducens*.<sup>449</sup> This biotic reaction changes the oxidation state of Fe in a geological matrix, potentially influencing the mineralogy and geochemical properties and the porosity of the storage formation, affecting its capacity to store H<sub>2</sub> securely. The reduction of Fe<sup>3+</sup> to Fe<sup>2+</sup> can affect the solubility and mobility of Fe minerals, affecting the overall stability of the storage site, as presented in eqn (20):



### 7.4. Sulfate reducers and hydrogen sulfide production

The H<sub>2</sub> to H<sub>2</sub>S pathway involves SRB, found in oil or gas reservoirs,<sup>467,468</sup> saline aquifers,<sup>469,470</sup> and salt caverns.<sup>168,327,471,472</sup> These microorganisms use H<sub>2</sub> as an electron donor to reduce sulfate (SO<sub>4</sub><sup>2-</sup>) into H<sub>2</sub>S. Chang *et al.*<sup>463</sup> described H<sub>2</sub>S generation and mixing in UHS at the field scale, microscale, and



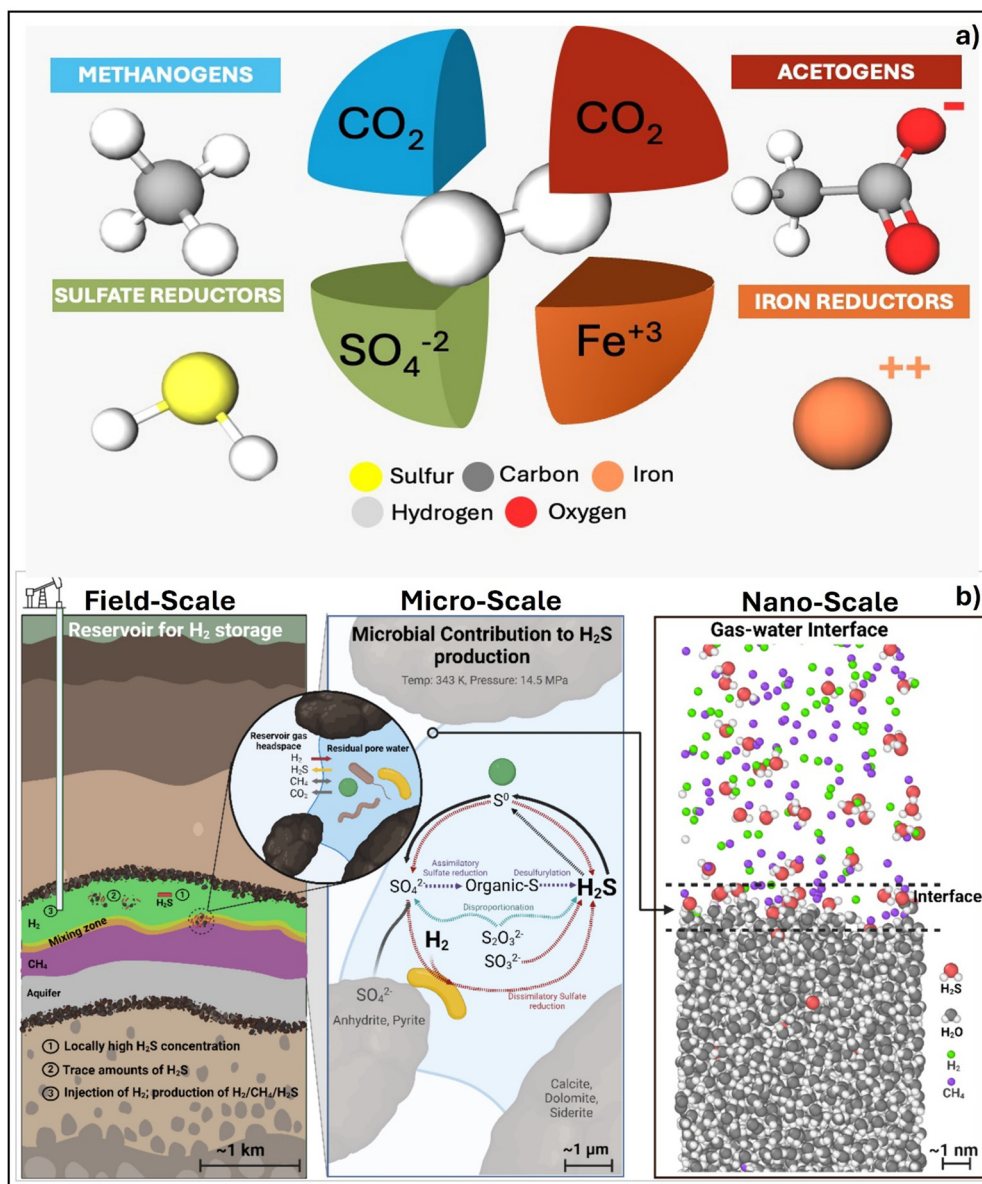


**Fig. 34** Biogeochemical reactions and hydrogen sulfide (H<sub>2</sub>S) generation in underground hydrogen (H<sub>2</sub>) storage (UHS). (a) Biogeochemical reactions involving H<sub>2</sub> in UHS. Interactions between H<sub>2</sub> and geological or microbial components, including methanogens, acetogens, sulfate reducers, and iron reducers, highlight the transformation pathways of H<sub>2</sub> in subsurface environments. (b) Schematic of H<sub>2</sub>S generation and mixing in UHS across three scales: field scale (left), illustrating the H<sub>2</sub> injection and microbial activity in the reservoir; microscale (center), depicting the microbial contribution to H<sub>2</sub>S production, red lines denote anoxic dissimilatory pathways, blue lines represent anoxic disproportionation, purple lines indicate oxitic or anoxic pathways, and black lines signify aerobic oxidation pathways; and nanoscale (right), illustrating the gas–water interface at the molecular level. The schematic in (b) is modified from ref. 463.

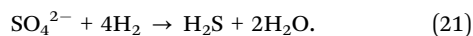
nanoscale, as illustrated in Fig. 34(b). At the field scale (Fig. 34(b), left panel), H<sub>2</sub> is at the top of the reservoir due to its lower density, above a cushion gas layer of CH<sub>4</sub>, which rests above the reservoir aquifer. In the microbial S cycle (Fig. 34(b), center), S is an energy source present in residual formation water as SO<sub>4</sub><sup>2-</sup> or in surrounding rocks as anhydrite or pyrite. Sulfate can undergo reduction to form H<sub>2</sub>S *via* several pathways, including assimilatory or dissimilatory reduction, disproportionation (oxidation or reduction of S<sub>2</sub>O<sub>3</sub><sup>2-</sup>), and desulfurization (organic-S reduction). At the gas–water interface (Fig. 34(b), right

panel), molecular interactions, such as adsorption, absorption, and orientation, influence interfacial properties, such as IFT.<sup>463</sup>

These reactions can occur in sulfate-rich environments and are significant because H<sub>2</sub>S is a corrosive and toxic gas, posing risks to storage integrity and safety and affecting overall UHS performance. The reaction predominantly occurs in hydrocarbon reservoirs where incompatible water is injected during flooding, influenced by sulfate-reducing ions.<sup>455,461,473</sup> The reaction typically occurs at temperatures ranging from 311 to 383 K.<sup>39,327,449,453,455,457,460,461,464,465</sup>



Besides microbial activities, H<sub>2</sub> can directly interact with sulfate (SO<sub>4</sub><sup>2-</sup>) and ferric Fe (Fe<sup>3+</sup>). These geochemical reactions, indicated by the arrows from H<sub>2</sub> to SO<sub>4</sub><sup>2-</sup> and Fe<sup>3+</sup>, can alter the chemical composition and physical properties of the storage formation, as indicated in eqn (21):



Microbial processes, such as sulfate reduction, acetogenesis, methanogenesis, and Fe reduction, alongside direct geochemical reactions and the potential production of gases (*e.g.*, H<sub>2</sub>S and CH<sub>4</sub>), changes in stored H<sub>2</sub> composition, geo-storage formation mineralogy, and shifts in microbial communities are critical factors that must be considered in the design and management of UHS projects. These microbial and geochemical interactions can influence the integrity and efficiency of UHS by altering reservoir permeability, affecting gas injectivity and withdrawal rates, and potentially leading to the formation of biofilms or mineral precipitates that may impact long-term storage stability.

### 7.5. Implications of biogeochemical reactions on underground hydrogen storage

Microorganisms can be found in all potential UHS sites, making it essential to assess microbial activity on a field-specific basis before implementation. Comprehensive investigations of biogeochemical interactions during UHS, the multiphase flow of H<sub>2</sub> in porous formation, and contact angle measurements estimating the H<sub>2</sub> wettability of storage rocks and caprock are essential for assessing the containment safety of storage or caprock formations.

Microbial-associated risks include H<sub>2</sub> loss, souring, corrosion, and clogging.<sup>168,282,327,462,474</sup> The interactions between H<sub>2</sub> and subsurface minerals and microorganisms can affect the storage capacity by altering the rock-pore structure and chemistry, as illustrated in Fig. 35(a). For instance, CH<sub>4</sub> and CH<sub>3</sub>COO<sup>-</sup> formation could lead to rock permeability and porosity variation. Studies have indicated that mineral oxidation due to pre-existing O<sub>2</sub> dissolved in formation fluid has a minimal influence on H<sub>2</sub>-brine-rock interactions. The redox reactions between H<sub>2</sub>, brine, and minerals (*e.g.*, quartz, siderite, calcite, and pyrite) in relation to dissolved O<sub>2</sub> revealed that increasing the concentration of the dissolved O<sub>2</sub> from 5.5 to 5500 ppm has a negligible effect on H<sub>2</sub> solubility and pH levels in reservoirs. Carbonates, such as siderite and calcite, can act as electron acceptors, reacting with H<sub>2</sub> through redox processes, leading to H<sub>2</sub> loss at a pressure of 20 MPa, whereas quartz and pyrite are relatively insensitive to H<sub>2</sub>, resulting in less than a 0.2% H<sub>2</sub> loss under the same conditions.<sup>475</sup> These rocks with reactivity and non-reactivity nature may result in abiotic geochemical reactions which could contribute to the loss of H<sub>2</sub> during UHS operations.

Another report suggested that carbonate rocks are likely to exhibit high geochemical stability in the presence of H<sub>2</sub>. A CT-scan analysis of the geochemical reaction of carbonate rock with H<sub>2</sub> revealed that the extent of mineral dissolution and

precipitation caused by H<sub>2</sub> treatment is minimal. Pore spaces and grain expansion following H<sub>2</sub> treatment did not significantly alter, with porosity values decreasing by less than 2% after 150 days of H<sub>2</sub> exposure.<sup>476</sup>

The production of gases, such as CH<sub>4</sub> and H<sub>2</sub>S, could affect the integrity of the caprock, potentially leading to leakage and compromising the storage site, affecting the behavior and safety of stored H<sub>2</sub>. Methane generation might increase storage capacity, whereas H<sub>2</sub>S can pose risks due to its toxicity and corrosiveness. Experiments involving 12 cylindrical core samples from an active California utility natural gas storage site (including samples from the storage zone, caprock, and cement from different wells) reported swelling upon H<sub>2</sub> exposure.<sup>351</sup> The results indicated minor changes in porosity and mineralogy due to H<sub>2</sub>/CH<sub>4</sub> exposure, but the changes in permeability were more significant. However, no direct evidence of geochemical reactions involving H<sub>2</sub> was found.<sup>351</sup> Understanding these biogeochemical reactions is crucial for predicting the long-term stability and integrity of the storage site. Biogeochemical reactions could enhance or undermine the ability of the storage formation to retain H<sub>2</sub> (for storage) effectively.

Al-Yaseri *et al.*<sup>477</sup> investigated basalt/H<sub>2</sub>/water wettability and geochemical interactions using basalt from the CarbFix site in Iceland after treatment with H<sub>2</sub> and water for 108 days at 348 K and 9.65 MPa. The results indicated a slight dissolution of plagioclase minerals due to H<sub>2</sub> redox reactions. The contact angle data suggested that the basalt surface remained water-wet after treatment with H<sub>2</sub>.<sup>477</sup>

Furthermore, H<sub>2</sub>S produced by SRB can release organic metabolite acids and alter the wettability of the reservoir rock. After bacterial influence, the wettability of the quartz surface *via* contact angle was modified from 4.2° to 14.4° at 27 MPa and 323 K, as illustrated in Fig. 35(b). It is evident from these findings that strongly water-wet quartz changes to a less water-wet state due to microbial activity, suggesting that SRB contributes to a slight reduction in the residual trapping effect, possibly enhancing the efficiency of withdrawing H<sub>2</sub> from sandstone reservoirs affected by microbial processes.<sup>168</sup>

Employing MD simulations using LAMMPS, Chang *et al.*<sup>463</sup> explored the IFT dynamics between residual pore water and gas mixtures containing H<sub>2</sub>, CH<sub>4</sub>, and H<sub>2</sub>S in subsurface porous media for UHS systems. The authors established IFT correlations for H<sub>2</sub>S concentrations ranging from 5% to 80%, under 14.5 MPa and 343 K. In the absence of H<sub>2</sub>S (0% concentration), the IFT of the equimolar (50% H<sub>2</sub> + 50% CH<sub>4</sub>)/H<sub>2</sub>O mixture logically falls between the IFT values of the binary H<sub>2</sub>-H<sub>2</sub>O and CH<sub>4</sub>-H<sub>2</sub>O systems (Fig. 35(c)). The IFT decreases with increasing H<sub>2</sub>S concentrations.<sup>463</sup> At a low H<sub>2</sub>S concentration of 5%, the IFT reduction is significant at about 12% for the (H<sub>2</sub>S + H<sub>2</sub>)/H<sub>2</sub>O system. In contrast, the (H<sub>2</sub>S + CH<sub>4</sub>)/H<sub>2</sub>O system exhibits only a 6% IFT reduction at the same concentration, suggesting that CH<sub>4</sub> counteracts the H<sub>2</sub>S-induced reduction in IFT. This comparative analysis indicates that H<sub>2</sub>S has a more pronounced effect on IFT when interacting with H<sub>2</sub> than with CH<sub>4</sub> in an aqueous environment.<sup>463</sup>

The assessment of H<sub>2</sub>-rock geochemical reactions and potential CH<sub>4</sub> production indicated that the interaction between H<sub>2</sub> and



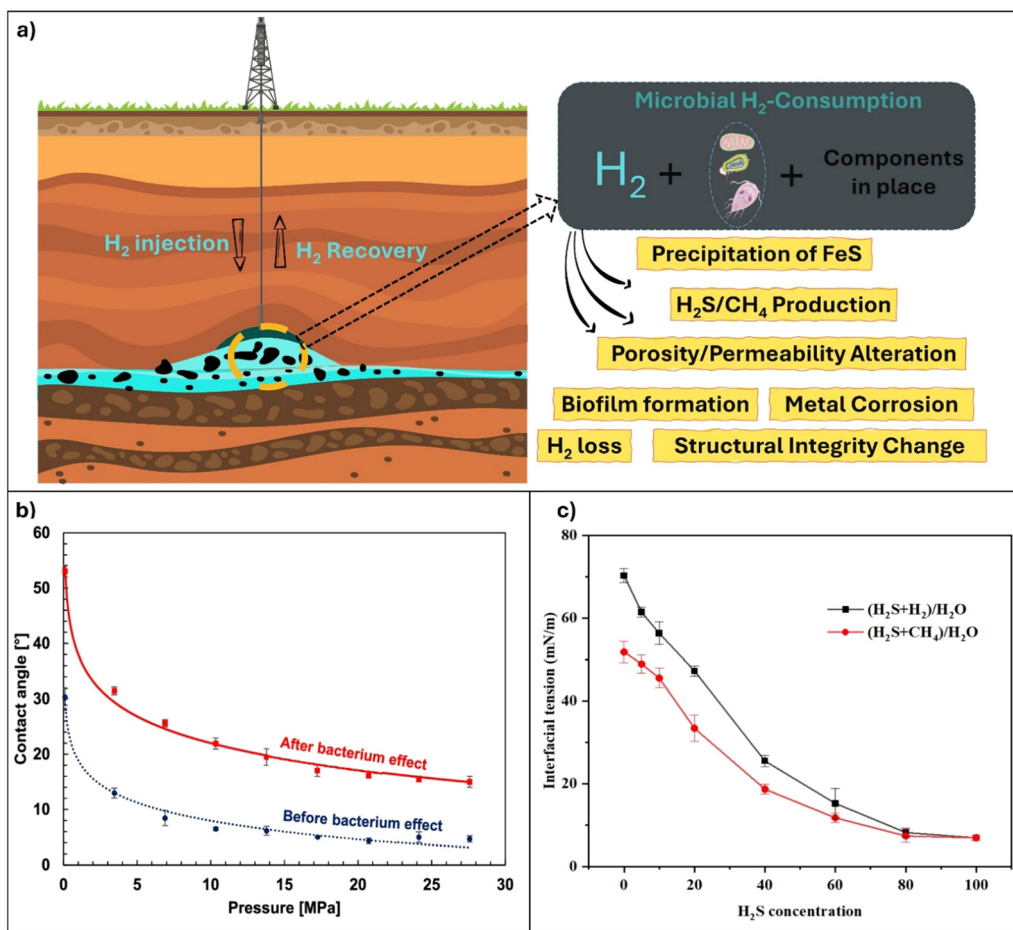


Fig. 35 Microbial effect on hydrogen ( $H_2$ ) consumption, wettability, and interfacial tension (IFT) in underground  $H_2$  storage (UHS). (a) Microbial interactions with injected  $H_2$  can result in the precipitation of iron sulfide (FeS), production of  $H_2$  sulfide ( $H_2S$ ) and methane ( $CH_4$ ), alterations in porosity and permeability, biofilm formation, metal corrosion,  $H_2$  loss, and structural integrity changes. (a) Extended and modified from ref. 457. (b) Contact angle of brine before and after the bacterium effect as a function of pressure on quartz substrates.<sup>168</sup> (c) Effect of  $H_2S$  concentration on the IFT of  $H_2$  in  $CH_4$  cushion gas.<sup>465</sup> Understanding these microbial effects is essential for managing and optimizing UHS systems.

organic matter in shale (with a high TOC of 14.07%) resulted in only a small amount of  $CH_4$  after 85 days of exposure to  $H_2$  at 348 K and 10.3 MPa. A gas chromatography analysis after the experiment detected no  $H_2S$ , but a small amount of  $CH_4$  (0.018%) was reported.<sup>478</sup>

Achieving high UHS efficiency requires careful site selection, an understanding of reservoir dynamics, and a well-designed operational plan to minimize loss and enhance recoverability. Okoroafor *et al.*<sup>37</sup> analyzed  $H_2$  recovery efficiency and round-trip efficiency (RTE), measuring the recoverable power relative to the energy input for  $H_2$  production and storage. The RTE is determined by comparing the curtailed energy converted into stored  $H_2$  with the energy generated from extracted  $H_2$ , expressed as a percentage. The primary limitation of overall process efficiency is not in  $H_2$  recovery from storage but in the conversion steps between renewable power,  $H_2$  production, and power generation.<sup>37</sup> However,  $H_2$  extraction efficiency can significantly enhance RTE by improving the withdrawal efficiency *via* optimal site selection. Increasing withdrawal efficiency, turbine efficiency, and electrolyzer efficiency to 100%

leads to RTE gains of 8%, 24%, and 33%, respectively, highlighting the critical factors in the cycle of power to  $H_2$  to power. The RTE for UHS reported in the literature ranges from 18% to 46%.<sup>37,479,480</sup>

Several factors in this review affect the RTE of UHS. Wettability and capillary trapping significantly influence RTE in the storage reservoir. For example, the  $H_2$  interaction with brine and the rock surface can lead to irretrievable  $H_2$  due to capillary forces and adsorption. Cushion gases, such as  $CO_2$ ,  $CH_4$ , or  $N_2$ , are also vital in reducing  $H_2$  retention by adsorption. Although these gases improve pressure maintenance, reduce  $H_2$  adsorption, and mitigate  $H_2$  loss during cycling, they can lead to gas mixing, complicating withdrawal and purification processes and reducing RTE.

Reservoir conditions (*e.g.*, temperature and pressure) influence  $H_2$  solubility, diffusion, and the phase-change potential, affecting retrievability.<sup>480–483</sup> Subsurface geochemical and microbial reactions may consume or react with stored  $H_2$ , reducing recoverable quantities.<sup>481</sup> Table 6 summarizes studies on quantifying microbial loss during  $H_2$  storage. Operational



Table 6 Summary of the literature on quantifying microbial loss during underground hydrogen storage (adapted from ref. 481)

References	Hydrogen loss due to microbial interaction			Remarks/operational conditions
	Methanogenesis	Acetogenesis	Sulfate	
Pan <i>et al.</i> <sup>484</sup>			29.4% 3.7%	Microfluidics study at 3.5 MPa and 37 °C in the presence of microbes
Haddad <i>et al.</i> <sup>485</sup>	~ 40%			Microfluidics study of H <sub>2</sub> gas at 3.5 MPa and 37 °C considering microbes
Jahanbani	3.4%		0.5%	Study at 9.5 MPa, 47 °C, and 7.9 pH
Veshareh <i>et al.</i> <sup>482</sup>	30%	26%		Simulation studies with temperature values of 50, 75, 100, and 122 °C and pressure of 35.1 MPa
Thaysen <i>et al.</i> <sup>457</sup>	0.6% < 0.01–1.3%, < 0.01–2.3%	< 0.01–3.2%, < 0.01–2.0%	< 0.01–1.3%, < 0.01–0.5%	Simulations considering the maximum theoretical H <sub>2</sub> consumption rate Field study at Frigg reservoir at 19.5 MPa, 61 °C, 0.07–0.53 M salinity, and 6.5–7.4 pH Field study at Hamilton reservoir at 9.6 MPa, 30 °C, 1.59–4.18 M salinity, and 5.8 pH
Pichler, <sup>486</sup>	~ 3%			Reactors operated at 45 bar and 45 °C replicating the Sun storage project field conditions
Hemme & van Berk, <sup>483</sup>			32.9%	Hydrogeochemical, 1D reactive mass transport modeling approach at 40 °C and 4.05 MPa
Flesch <i>et al.</i> <sup>337</sup>			2–4%	Static H <sub>2</sub> reactor experiments on samples from the field in Ketzin, Germany, at 40 °C and 1 MPa
Truche <i>et al.</i> <sup>487</sup>			0.01%	Experimental study of the effect of H <sub>2</sub> in a clay-rich rock containing 1–2 wt% framboidal pyrite at 90–250 °C and 0.3–3 MPa
Amigan <i>et al.</i> <sup>488</sup>	17%			Gas storage site case study with 0.03 M salinity, 20–45 °C, 6.7 pH, and 4 MPa

strategies, such as optimizing injection and withdrawal cycles, can mitigate loss and improve RTE.

## 8. Recommendations

An H<sub>2</sub> economy could significantly reduce global carbon emissions, employing the existing oil and gas infrastructure for H<sub>2</sub> storage and transport. Addressing the economic, social, technological, and geological challenges associated with large-scale H<sub>2</sub> storage is essential to advance this goal. Further research is necessary to clarify H<sub>2</sub> behavior in subsurface conditions, including its interactions with rock formations, brines, and other gases. Developing reliable and efficient H<sub>2</sub> storage systems can facilitate the transition to a sustainable energy future, aligning with global efforts to combat climate change and achieve decarbonization goals. Therefore, prioritizing research and development in H<sub>2</sub> storage technology is critical for meeting the increasing global energy demands while minimizing environmental effects. The following recommendations for future research in UHS are outlined. These areas require further exploration to optimize storage strategies, enhance H<sub>2</sub> containment efficiency, and ensure the safety and sustainability of H<sub>2</sub> as an energy carrier.

Although UHS offers significant potential, several critical challenges remain unresolved. One crucial limitation is the uncertainty in long-term storage integrity, particularly the effects of repeated injection and withdrawal cycles on reservoir stability and gas retention. The unique properties of H<sub>2</sub>, including its low molecular weight and high diffusivity, raise concerns regarding potential leakage through caprock and faults, requiring further investigation *via* advanced geomechanical modeling and long-term field monitoring studies. Moreover, H<sub>2</sub> reactivity with reservoir minerals remains poorly assessed, with limited experimental and field-scale validation. Developing real-time monitoring systems and refining predictive

models is essential to ensure UHS safety and efficiency. Several recommendations are provided below.

### 8.1. Comprehensive experimental setups

Research should explore additional parameters in more representative experimental setups, such as core-flooding experiments. These experiments can assess the injectivity and retrieval of H<sub>2</sub>, considering the effects of injection flow rates, temperature, pressure, confining stress, and pore pressure (adequate pressure). The insight gained from real-time imaging can aid in optimizing operational parameters, such as injection rates, pressure conditions, and temperature profiles, to maximize storage capacity and efficiency while ensuring safe and sustainable operations.

Research should incorporate *in situ* and real-time advanced imaging techniques into core-flooding systems to enhance understanding and accuracy in observing H<sub>2</sub> dynamics during injection and withdrawal in UHS. Various techniques, such as X-ray CT, MRI (see ref. 333 and 343), and optical coherence tomography,<sup>335</sup> can visualize the spatial distribution of H<sub>2</sub> and monitor its movement, providing insight into interactions with geological formations under various pressure, temperature, and injection rates. These methods help analyze flow patterns, saturation levels, and interactions with rock matrices and fluids, which are crucial for optimizing UHS efficiency and safety.

### 8.2. Advanced underground hydrogen storage evaluation methods

Several researchers have employed MD simulations to model systems at the nanoscale, capturing detailed coulombic and electrostatic forces. This approach offers greater detail and efficiency than traditional laboratory experiments. However, MD studies must be expanded to include H<sub>2</sub> interfacial properties, such as wettability, IFT, solubility, density, and storage efficiency. Few studies have considered the effect of cushion



gas, and none have examined the influence of diverse mineralogy and ternary mixtures involving H<sub>2</sub> and other gas impurities in UHS applications using MD simulations.

### 8.3. Utilization of nanoparticles

Research should investigate using nanoparticles in the wettability reversal of rock/H<sub>2</sub>/brine systems to enhance storage and recovery efficiency, significantly improving the interaction between H<sub>2</sub> and the storage media and facilitating better containment and retrieval.

### 8.4. Biochemical activities

Research should explore the influence of microbial activities and organic compounds on H<sub>2</sub> storage, which may include investigating the effects of biochemical activities, such as methanogenesis, acetogenesis, sulfate, and Fe-reducing agents, on H<sub>2</sub> consumption and production in the presence of bacteria. These activities can significantly affect H<sub>2</sub> consumption and production, influencing the overall efficiency of UHS.

### 8.5. Adsorption and desorption studies

Research should conduct adsorption and desorption studies considering influential parameters, such as cushion gas and other gas impurities (*e.g.*, N<sub>2</sub>, CH<sub>4</sub>, and CO<sub>2</sub>). Understanding these interactions is crucial for optimizing storage capacity and ensuring the stability of H<sub>2</sub> in subsurface conditions.

### 8.6. Economic evaluation

Comprehensive economic evaluations of UHS processes and procedures must be performed, including cost analyses of developing and maintaining the storage infrastructure and the potential financial benefits of H<sub>2</sub> as an energy carrier. Understanding the economic feasibility is essential for the widespread adoption and implementation of UHS.

### 8.7. Summary

Future research should focus on improving H<sub>2</sub> recovery efficiency, particularly under varying pressure and temperature conditions. Optimizing withdrawal techniques, such as pressure-management strategies or gas-cycling approaches, could help reduce residual H<sub>2</sub> trapping and improve RTE. Advanced cushion gas selection should be explored to minimize H<sub>2</sub> retention while maintaining reservoir pressure. From an economic perspective, integrating technoeconomic models with geological assessments is necessary to establish the viability of UHS at larger-scale. Further interdisciplinary collaboration, combining insight from geochemistry, microbiology, reservoir engineering, and computational modeling is required to unlock the potential of UHS as a long-term energy solution.

## 9. Final remarks

The projected increase in the global population and the rapid industrialization underscores the urgency of transitioning from fossil fuels to sustainable energy sources. Fossil fuels meet

nearly 80% of global energy demands and contribute significantly to environmental degradation through greenhouse gas emissions and climate change. The challenge of reducing global CO<sub>2</sub> emissions and limiting the global temperature rise to below 2 °C necessitates a paradigm shift toward renewable and low-carbon energy alternatives. Anthropogenic CO<sub>2</sub> emissions continue to outpace the Earth's natural capacity to absorb and recycle CO<sub>2</sub>, exacerbating environmental degradation and global warming. Transitioning to sustainable and low-carbon energy sources is imperative to mitigate climate change and limit the rise in global temperature.

Renewable energy options, such as solar, wind, bio-, and geothermal energy, hold promise but face intermittent and seasonal variability challenges, creating supply-demand imbalances. In response, the concept of an H<sub>2</sub> economy has gained traction as a viable solution to decarbonize energy systems and phase out fossil fuels. Hydrogen, primarily green H<sub>2</sub> produced from renewable sources *via* electrolysis, presents a clean energy alternative that emits only water vapor upon combustion, offering substantial environmental benefits. Integrating H<sub>2</sub> into global energy frameworks underscores its potential to achieve significant greenhouse gas emission reductions and enhance energy security. However, successfully implementing an H<sub>2</sub> economy hinges on addressing several challenges, including economic viability, societal acceptance, technological advancements in storage and retrieval systems, and the geological suitability of storage sites. Critical research gaps persist, particularly concerning understanding H<sub>2</sub> interaction with geological formations, its wettability under diverse conditions and sorption behavior, and the influence of cushion gases and organic compounds on storage dynamics.

Compared to alternative large-scale energy storage technology, such as pumped hydro storage, compressed air storage, and grid-scale battery storage, UHS offers a unique advantage due to its high energy density and large storage capacity. However, UHS faces operational and technical barriers, including uncertain long-term sealing efficiency, geochemical interactions, and withdrawal loss. In contrast to compressed air or hydro storage, UHS requires a detailed understanding of site-specific geological factors to ensure minimal leakage and efficient gas cycling. Although advances in reservoir engineering and cushion gas optimization may improve performance, further validation *via* large-scale demonstration projects is critical before UHS can be widely deployed.

Accordingly, this review highlights the reported inconsistencies regarding the influence of various parameters on the effectiveness of UHS. For instance, some literature has reported a positive correlation between pressure and the contact angle in rock/H<sub>2</sub>/brine systems, contrasting a significant portion of the literature. This discrepancy also extends to the rock/H<sub>2</sub>/water contact angle relationship with temperature and salinity. However, the trend for IFT with physical parameters is more consistent, typically displaying an inverse relationship with pressure and temperature.

The perspective of the current authors is that, while assessment errors cannot be entirely dismissed, the primary reasons



for these discrepancies could be differences in measurement methods, diverse rock mineralogy, and fluid composition. Moreover, disparities in the reported data could also be due to different sample preparation procedures, specifically, the lack of standardized cleaning protocols, experimental inconsistencies, physical and chemical alterations during measurement, and variances in equilibration time, substrate surface roughness, surface contamination, and chemical heterogeneity of the rock substrate. Addressing these factors is crucial for obtaining unbiased results and reliable data.

Furthermore, advanced methods, such as ML and MD simulations, have garnered attention for predicting the interfacial properties of rock/H<sub>2</sub>/brine systems, sorption properties, and the injectivity and withdrawal of H<sub>2</sub> in reservoirs and assessing caprock integrity for subsurface storage. Integrated approaches also hold promise in improving UHS assessments. For example, integrating experimental data into molecular and pore-scale modeling with ML techniques has significantly enhanced prediction accuracy.

Moreover, core-flooding experiments combined with advanced imaging techniques, such as NMR, MRI, and micro-CT, allow a precise evaluation of rock/H<sub>2</sub>/fluid interactions under simulated subsurface conditions and facilitate the assessment of biogeochemical alterations following H<sub>2</sub> exposure. This integrated approach helps visualize interactions between H<sub>2</sub>, fluids, and rock, promoting a complete understanding of parameters influencing the storage of H<sub>2</sub> in geo-storage media and providing valuable insight into the selection and design of the UHS site.

However, improper execution of simulation models can lead to data inconsistencies. Each simulation method, whether physical or numerical, has specific errors and limitations in accurately mimicking natural reservoir conditions, which must be considered to avoid misleading results.

While significant strides have been made in exploring H<sub>2</sub> storage technology, comprehensive reviews and targeted research efforts are essential to resolve knowledge disparities and optimize storage efficiency. This research includes a deeper understanding of rock/H<sub>2</sub>/brine interactions across mineralogy and environmental conditions, which is crucial for developing robust and reliable storage solutions.

Beyond technical challenges, regulatory and economic considerations play a critical role in determining the feasibility of large-scale UHS deployment. Clear regulatory frameworks for H<sub>2</sub> storage in geological formations are currently lacking, leading to uncertainty regarding permitting processes and long-term liability. Standardized safety protocols and environmental risk assessments must be developed to ensure secure operation and public acceptance. Moreover, economic viability remains uncertain due to high infrastructure costs and limited commercial-scale demonstrations. Incentives (e.g., carbon credits, government subsidies, and H<sub>2</sub> market integration policies) are critical in bridging the gap between research and commercialization. Addressing these regulatory and economic challenges is as critical as overcoming the scientific and technical barriers to UHS.

Finally, advancing H<sub>2</sub> storage technology and infrastructure is pivotal in realizing a sustainable energy future. After addressing

the current research gaps, implementing recommendations, and applying technological innovations, the widespread adoption of H<sub>2</sub> as a clean and efficient energy carrier can play a pivotal role in mitigating climate change and achieving global energy security goals.

## Data availability

No primary research results, software or code has been included and no new data were generated or analyzed as part of this review.

## Conflicts of interest

The authors declare no conflicts of interest.

## References

- 1 V. Popovich, P. Zeile, P. Elisei, C. Beyer, J. Ryser, G. Stöglehner, M. Padilla, K. Swamygowda and R. Sheoran, *CITIES 20.50—Creating Habitats 3rd Millenn. Smart—Sustainable—Climate Neutral. Proc. REAL CORP 2021, 26th Int. Conf. Urban Dev. Reg. Plan. Inf. Soc. CORP—Competence Cent. Urban Reg.*, 2021, pp. 241–249.
- 2 N. Salari, A. Hosseinian-Far, R. Jalali, A. Vaisi-Raygani, S. Rasoulpoor, M. Mohammadi, S. Rasoulpoor and B. Khaledi-Paveh, *Global Health*, 2020, **16**, 1–11.
- 3 S. Iglauer, *Acc. Chem. Res.*, 2017, **50**, 1134–1142.
- 4 M. Bui, C. S. Adjiman, A. Bardow, E. J. Anthony, A. Boston, S. Brown, P. S. Fennell, S. Fuss, A. Galindo, L. A. Hackett, J. P. Hallett, H. J. Herzog, G. Jackson, J. Kemper, S. Krevor, G. C. Maitland, M. Matuszewski, I. S. Metcalfe, C. Petit, G. Puxty, J. Reimer, D. M. Reiner, E. S. Rubin, S. A. Scott, N. Shah, B. Smit, J. P. M. Trusler, P. Webley, J. Wilcox and N. Mac Dowell, *Energy Environ. Sci.*, 2018, **11**, 1062–1176.
- 5 S. Iglauer, C. H. Pentland and A. Busch, *Water Resour. Res.*, 2015, **51**, 729–774.
- 6 C. Armstrong, *Political Studies*, 2020, **68**(3), 671–688.
- 7 I. Bucur, G. Posea, A. Bulmez and P. Axinte, *Bull. Transilvania Univ. Brasov, Ser. I*, 2019, **11**, 309–316.
- 8 M. S. Okundamiya, *Int. J. Hydrogen Energy*, 2021, **46**, 30539–30546.
- 9 N. F. Jariah, M. A. Hassan, Y. H. Taufiq-Yap and A. M. Roslan, *Processes*, 2021, **9**, 1198.
- 10 K. T. Nguyen, N. Y. Xu, J. Y. Zhang, T. Shang, A. Y. DuBord, L. Heinemann, E. P. Krisiunas, T. Stumpe, D. A. Seid and D. C. Klonoff, *J. Diabetes Sci. Technol.*, 2022, **16**, 233–247.
- 11 M. S. Islam and E. Kieu, *Int. Polit. Econ. Ser.*, 2021, 1–16.
- 12 M. A. Clark, N. G. G. Domingo, K. Colgan, S. K. Thakrar, D. Tilman, J. Lynch, I. L. Azevedo and J. D. Hill, *Science*, 2020, **370**, 705–708.
- 13 K. O'Brien, *Curr. Opin. Environ. Sustainability*, 2018, **31**, 153–160.
- 14 M. Á. Sanjuán, C. Andrade, P. Mora and A. Zaragoza, *Appl. Sci.*, 2020, **10**, 339.



- 15 K. O. Yoro and M. O. Daramola, *Adv. Carbon Capture*, 2020, 3–28.
- 16 N. Heinemann, J. Alcalde, J. M. Miocic, S. J. T. Hangx, J. Kallmeyer, C. Ostertag-Henning, A. Hassanpouryouzband, E. M. Thaysen, G. J. Strobel, C. Schmidt-Hattenberger, K. Edlmann, M. Wilkinson, M. Bentham, R. Stuart Haszeldine, R. Carbonell and A. Rudloff, *Energy Environ. Sci.*, 2021, **14**, 853–864.
- 17 E. Yates, A. Bischoff, M. Beggs and N. Jackson, Hydrogen Geo-storage in Aotearoa–New Zealand, 2021, DOI: [10.13140/RG.2.2.27113.21603](https://doi.org/10.13140/RG.2.2.27113.21603).
- 18 A. E. Yekta, M. Pichavant and P. Audigane, *Appl. Geochem.*, 2018, **95**, 182–194.
- 19 A. E. Yekta, J. C. Manceau, S. Gaboreau, M. Pichavant and P. Audigane, *Transp. Porous Media*, 2018, **122**, 333–356.
- 20 L. Hashemi, M. Blunt and H. Hajibeygi, *Sci. Rep.*, 2021, **11**, 1–13.
- 21 V. Reitenbach, L. Ganzer, D. Albrecht and B. Hagemann, *Environ. Earth Sci.*, 2015, **73**, 6927–6937.
- 22 A. Jahanbakhsh, A. Louis Potapov-Crighton, A. Mosallanezhad, N. Tohidi Kaloorazi and M. M. Maroto-Valer, *Renewable Sustainable Energy Rev.*, 2024, **189**, 114001.
- 23 S. E. Hosseini and M. A. Wahid, *Int. J. Energy Res.*, 2020, **44**, 4110–4131.
- 24 G. Bel and S. Joseph, *Renewable Sustainable Energy Rev.*, 2018, **82**, 3798–3807.
- 25 A. Lenschow, P. Bocquillon and L. Carafa, *Environ. Policy Gov.*, 2018, **28**(5), 323–328.
- 26 A. Hassanpouryouzband, M. Wilkinson and R. S. Haszeldine, *Chem. Soc. Rev.*, 2024, **53**, 2258–2263.
- 27 S. Snæbjörnsdóttir, B. Sigfússon, C. Marieni, D. Goldberg, S. R. Gislason and E. H. Oelkers, *Nat. Rev. Earth Environ.*, 2020, **12**(1), 90–102.
- 28 A. I. Osman, N. Mehta, A. M. Elgarahy, M. Hefny, A. Al-Hinai, A. H. Al-Muhtaseb and D. W. Rooney, *Environ. Chem. Lett.*, 2022, **20**, 153–188.
- 29 B. A. Franco, P. Baptista, R. C. Neto and S. Ganilha, *Appl. Energy*, 2021, **286**, 116553.
- 30 A. Majumdar, J. M. Deutch, R. S. Prasher and T. P. Griffin, *Joule*, 2021, **5**, 1905–1908.
- 31 N. Mac Dowell, N. Sunny, N. Brandon, H. Herzog, A. Y. Ku, W. Maas, A. Ramirez, D. M. Reiner, G. N. Sant and N. Shah, *Joule*, 2021, **5**, 2524–2529.
- 32 A. Hassanpouryouzband, E. Joonaki, K. Edlmann and R. S. Haszeldine, *ACS Energy Lett.*, 2021, **6**, 2181–2186.
- 33 R. Tarkowski, *Int. J. Hydrogen Energy*, 2017, **42**, 347–355.
- 34 A. Hassanpouryouzband, M. J. Veshareh, M. Wilkinson, H. M. Nick, B. T. Ngwenya and R. S. Haszeldine, *Joule*, 2025, **9**(2), 101809.
- 35 M. Ali, N. K. Jha, A. Al-Yaseri, Y. Zhang, S. Iglauer and M. Sarmadivaleh, *J. Pet. Sci. Eng.*, 2021, **207**, 109081.
- 36 H. Bin Navaid, H. Emadi and M. Watson, *Int. J. Hydrogen Energy*, 2023, **48**, 10603–10635.
- 37 E. R. Okoroafor, N. Nazari, T. W. Kim, H. Y. Watkins, S. D. Saltzer and A. R. Kavscek, *Int. J. Hydrogen Energy*, 2024, **71**, 982–998.
- 38 S. Khandoozi, R. Hazlett and M. Fustic, *Earth-Sci. Rev.*, 2023, **244**, 104515.
- 39 D. Zivar, S. Kumar and J. Foroozesh, *Int. J. Hydrogen Energy*, 2021, **46**, 23436–23462.
- 40 F. Feldmann, B. Hagemann, L. Ganzer and M. Panfilov, *Environ. Earth Sci.*, 2016, **75**(16), 1165.
- 41 A. Sainz-Garcia, E. Abarca, V. Rubi and F. Grandia, *Int. J. Hydrogen Energy*, 2017, **42**, 16657–16666.
- 42 R. Tarkowski and G. Czapowski, *Int. J. Hydrogen Energy*, 2018, **43**, 21414–21427.
- 43 C. J. Quarton and S. Samsatli, *Appl. Energy*, 2020, **257**, 113936.
- 44 M. Al-Shafi, O. Massarweh, A. S. Abushaikha and Y. Bicer, *Energy Rep.*, 2023, **9**, 6251–6266.
- 45 H. Zhang, Y. Zhang, M. Al Kobaisi, S. Iglauer and M. Arif, *Int. J. Hydrogen Energy*, 2024, **49**, 336–350.
- 46 N. S. Muhammed, B. Haq and D. Al Shehri, *Int. J. Hydrogen Energy*, 2024, **50**, 1281–1301.
- 47 N. S. Muhammed, B. Haq and D. Al Shehri, *Int. J. Hydrogen Energy*, 2023, **48**, 29663–29681.
- 48 M. Arif, A. Barifcani and S. Iglauer, *Int. J. Greenhouse Gas Control*, 2016, **53**, 263–273.
- 49 A. Raza, M. Arif, G. Glatz, M. Mahmoud, M. Al Kobaisi, S. Alafnan and S. Iglauer, *Fuel*, 2022, **330**, 125636.
- 50 P. J. Linstrom and W. G. Mallard, *J. Chem. Eng. Data*, 2001, **46**, 1059–1063.
- 51 M. R. Dehghani, S. F. Ghazi and Y. Kazemzadeh, *Sci. Rep.*, 2024, **14**, 1–25.
- 52 B. C. Tashie-Lewis and S. G. Nnabuife, *Chem. Eng. J. Adv.*, 2021, **8**, 100172.
- 53 A. Hassanpouryouzband, J. Yang, B. Tohidi, E. Chuvilin, V. Istomin, B. Bukhanov and A. Cheremisin, *Environ. Sci. Technol.*, 2018, **52**, 4324–4330.
- 54 S. Cloete, O. Ruhnau and L. Hirth, *Int. J. Hydrogen Energy*, 2021, **46**, 169–188.
- 55 J. Cader, R. Koneczna and P. Olczak, *Energies*, 2021, **14**, 4811.
- 56 M. K. Kazi, F. Eljack, M. M. El-Halwagi and M. Haouari, *Computers Chem. Eng.*, 2021, **145**, 107144.
- 57 P. M. Falcone, M. Hiete and A. Sapio, *Curr. Opin. Green Sustainable Chem.*, 2021, **31**, 100506.
- 58 C. Salah, S. Cobo, J. Pérez-Ramírez and G. Guillén-Gosálbez, *ACS Sustainable Chem. Eng.*, 2023, **11**, 3238–3247.
- 59 T. N. From, B. Partoon, M. Rautenbach, M. Østberg, A. Bontien, K. Aasberg-Petersen and P. M. Mortensen, *Chem. Eng. J.*, 2024, **479**, 147205.
- 60 L. Barelli, G. Bidini, F. Gallorini and S. Servili, *Energy*, 2008, **33**, 554–570.
- 61 S. A. Bhat and J. Sadhukhan, *AIChE J.*, 2009, **55**, 408–422.
- 62 E. M. A. Mokheimer, M. I. Hussain, S. Ahmed, M. A. Habib and A. A. Al-Qutub, *J. Energy Resour. Technol.*, 2015, **137**(1), 012001.
- 63 S. Zolghadri, M. R. Kiani, R. Kamandi and M. R. Rahimpour, *J. Energy Inst.*, 2024, **113**, 101541.
- 64 S. U. Batgi and I. Dincer, *Comput. Chem. Eng.*, 2024, **180**, 108514.



- 65 M. Wójcik, Ł. Szablowski and O. Dybiński, *Int. J. Hydrogen Energy*, 2024, **52**, 965–982.
- 66 Z. Navas-Anguita, D. García-Gusano, J. Dufour and D. Iribarren, *Sci. Total Environ*, 2021, **771**, 145432.
- 67 F. Salahi, F. Zarei-Jelyani, M. Farsi and M. R. Rahimpour, *J. Energy Inst.*, 2023, **108**, 101208.
- 68 A. P. Simpson and A. E. Lutz, *Int. J. Hydrogen Energy*, 2007, **32**, 4811–4820.
- 69 Y. Ding and E. Alpay, *Chem. Eng. Sci.*, 2000, **55**, 3929–3940.
- 70 O. S. Alade, M. Mahmoud and A. Al-Nakhli, *Energy Fuels*, 2023, **37**, 17411–17427.
- 71 J. E. Lee, I. Shafiq, M. Hussain, S. S. Lam, G. H. Rhee and Y. K. Park, *Int. J. Hydrogen Energy*, 2022, **47**, 4346–4356.
- 72 S. Iglauer, H. Abid, A. Al-Yaseri and A. Keshavarz, *Geophys. Res. Lett.*, 2021, **48**, e2021GL092976.
- 73 B. Pandey, Y. K. Prajapati and P. N. Sheth, *Int. J. Hydrogen Energy*, 2019, **44**, 25384–25415.
- 74 C. K. R. Pocha, W. Y. Chia, T. A. Kurniawan, K. S. Khoo and K. W. Chew, *Fuel*, 2023, **340**, 127472.
- 75 N. Wu, K. Lan and Y. Yao, *Resour., Conserv. Recycl.*, 2023, **188**, 106693.
- 76 H. Balat and E. Kirtay, *Int. J. Hydrogen Energy*, 2010, **35**, 7416–7426.
- 77 B. Senthil Rathi, P. Senthil Kumar, G. Rangasamy and S. Rajendran, *Int. J. Hydrogen Energy*, 2024, **52**, 115–138.
- 78 V. Sridevi, D. V. Surya, B. R. Reddy, M. Shah, R. Gautam, T. H. Kumar, H. Puppala, K. S. Pritam and T. Basak, *Int. J. Hydrogen Energy*, 2024, **52**, 507–531.
- 79 V. G. Nguyen, T. X. Nguyen-Thi, P. Q. Phong Nguyen, V. D. Tran, Ü. Ağbulut, L. H. Nguyen, D. Balasubramanian, W. Tarelko, S. A. Bandh and N. D. Khoa Pham, *Int. J. Hydrogen Energy*, 2024, **54**, 127–160.
- 80 K. Guerra, A. Welfle, R. Gutiérrez-Alvarez, M. Freer, L. Ma and P. Haro, *Appl. Energy*, 2024, **357**, 122447.
- 81 A. Tleubergenova, B. C. Han and X. Z. Meng, *Int. J. Hydrogen Energy*, 2024, **49**, 349–355.
- 82 S. Czernik, R. Evans and R. French, *Catal. Today*, 2007, **129**, 265–268.
- 83 D. B. Levin and R. Chahine, *Int. J. Hydrogen Energy*, 2010, **35**, 4962–4969.
- 84 E. Kirtay, *Energy Convers. Manage.*, 2011, **52**, 1778–1789.
- 85 J. Bourdet, C. D. Piane, C. Wilske, D. Mallants, A. Suckow, D. Questiaux, C. Gerber, P. Crane, A. Deslandes, L. Martin and M. Aleshin, *Chem. Geol.*, 2023, **638**, 121698.
- 86 A. S. Templeton, E. T. Ellison, P. B. Kelemen, J. Leong, E. S. Boyd, D. R. Colman and J. M. Matter, *Front. Geochem.*, 2024, **2**, 1366268.
- 87 G. Etiope, *Int. J. Hydrogen Energy*, 2024, **78**, 368–372.
- 88 M. Masoudi, A. Hassanpouryouzband, H. Hellevang and R. S. Haszeldine, *J. Energy Storage*, 2024, **84**, 110927.
- 89 N. S. Muhammed, B. Haq, D. Al Shehri, A. Al-Ahmed, M. M. Rahman and E. Zaman, *Energy Rep.*, 2022, **8**, 461–499.
- 90 M. Sofian, M. B. Haq, D. Al Shehri, M. M. Rahman and N. S. Muhammed, *Int. J. Hydrogen Energy*, 2024, **60**, 867–889.
- 91 F. Chen, Z. Ma, H. Nasrabadi, B. Chen, M. Z. Saad Mehana and J. Van Wijk, *Int. J. Hydrogen Energy*, 2023, **48**, 9008–9022.
- 92 W. F. Giaucque, *J. Am. Chem. Soc.*, 1930, **52**, 4816–4831.
- 93 C. Spiegel, N. York, C. San, F. Lisbon, L. Madrid, M. City, M. New, D. San and J. Seoul, *Designing and building fuel cells*, 2007.
- 94 L. M. Das, *Compend. Hydrog. Energy Hydrog. Energy Convers.*, 2015, **3**, 177–217.
- 95 R. Tarkowski, *Renewable Sustainable Energy Rev.*, 2019, **105**, 86–94.
- 96 X. Li, B. M. Krooss, P. Weniger and R. Littke, *Int. J. Coal Geol.*, 2015, **137**, 152–164.
- 97 P. Gabrielli, A. Poluzzi, G. J. Kramer, C. Spiers, M. Mazzotti and M. Gazzani, *Renewable Sustainable Energy Rev.*, 2020, **121**, 109629.
- 98 Z. Yanxing, G. Maoqiong, Z. Yuan, D. Xueqiang and S. Jun, *Int. J. Hydrogen Energy*, 2019, **44**, 16833–16840.
- 99 M. S. A. Perera, *Fuel*, 2023, **334**, 126677.
- 100 A. Züttel, *Naturwissenschaften*, 2004, **91**, 157–172.
- 101 E. R. Ugarte and S. Salehi, *J. Energy Resour. Technol.*, 2022, **144**(4), 042001.
- 102 D. T. Pritchard and J. A. Currie, *J. Soil Sci.*, 1982, **33**, 175–184.
- 103 F. L. Dryer, M. Chaos, Z. Zhao, J. N. Stein, J. Y. Alpert and C. J. Homer, *Combust. Sci. Technol.*, 2007, **179**, 663–694.
- 104 R. Tarkowski, B. Uliasz-Misiak and P. Tarkowski, *Int. J. Hydrogen Energy*, 2021, **46**, 20010–20022.
- 105 A. Goodman Hanson, B. Kutchko, G. Lackey, D. Gulliver, B. R. Strazisar, K. A. Tinker, R. Wright, F. Haeri, N. Huerta, S. Baek, C. Bagwell, J. de Toledo Camargo, G. Freeman, W. Kuang, J. Torgeson, J. White, T. A. Buscheck, N. Castelletto and M. Smith, Subsurface hydrogen and natural gas storage (state of knowledge and research recommendations report), 2022, DOI: [10.2172/1846632](https://doi.org/10.2172/1846632).
- 106 E. I. Epelle, W. Obande, G. A. Udourioh, I. C. Afolabi, K. S. Desongu, U. Orivri, B. Gunes and J. A. Okolie, *Sustainable Energy Fuels*, 2022, **6**, 3324–3343.
- 107 S. Alafnan, *Int. J. Hydrogen Energy*, 2024, **83**, 1099–1106.
- 108 A. Al-Yaseri and N. K. Jha, *J. Pet. Sci. Eng.*, 2021, **200**, 108387.
- 109 M. Ali, N. Yekeen, N. Pal, A. Keshavarz, S. Iglauer and H. Hoteit, *J. Colloid Interface Sci.*, 2022, **608**, 1739–1749.
- 110 A. Al-Yaseri, D. Wolff-Boenisch, C. A. Fauziah and S. Iglauer, *Int. J. Hydrogen Energy*, 2021, **46**, 34356–34361.
- 111 M. Ali, N. Yekeen, N. Pal, A. Keshavarz, S. Iglauer and H. Hoteit, *Energy Rep.*, 2021, **7**, 5988–5996.
- 112 D. Van Der Spoel, P. J. Van Maaren, P. Larsson and N. Timneanu, *J. Phys. Chem. B*, 2006, **110**, 4393–4398.
- 113 V. Tietze and D. Stolten, *Int. J. Hydrogen Energy*, 2015, **40**, 11530–11537.
- 114 E. Sarı and E. Çiftçi, *Fuel*, 2024, **358**, 130310.
- 115 S. Henkel, D. Pudlo, L. Werner, F. Enzmann, V. Reitenbach, D. Albrecht, H. Würdemann, K. Heister, L. Ganzer and R. Gaupp, *Energy Procedia*, 2014, **63**, 8026–8035.



- 116 B. Pan, X. Yin and S. Iglauer, *Int. J. Hydrogen Energy*, 2021, **46**, 25578–25585.
- 117 L. Hashemi, W. Glerum, R. Farajzadeh and H. Hajibeygi, *Adv. Water Resour.*, 2021, **154**, 103964.
- 118 B. Pan, X. Yin, Y. Ju and S. Iglauer, *Adv. Colloid Interface Sci.*, 2021, **294**, 102473.
- 119 A. Aftab, A. Hassanpouryouzband, H. Naderi, Q. Xie and M. Sarmadivaleh, *J. Energy Storage*, 2023, **65**, 107252.
- 120 A. Aftab, A. Hassanpouryouzband, A. Martin, J. E. Kendrick, E. M. Thaysen, N. Heinemann, J. Utley, M. Wilkinson, R. S. Haszeldine and K. Edlmann, *Environ. Sci. Technol. Lett.*, 2023, **10**, 551–556.
- 121 I. Iordache, D. Schitea, A. V. Gheorghie and M. Iordache, *Int. J. Hydrogen Energy*, 2014, **39**, 11071–11081.
- 122 J. Simon, A. M. Ferriz and L. C. Correias, *Energy Procedia*, 2015, **73**, 136–144.
- 123 A. Keshavarz, H. Abid, M. Ali and S. Iglauer, *J. Colloid Interface Sci.*, 2022, **608**, 1457–1462.
- 124 A. Ebigo, F. Golfier and M. Quintard, *Adv. Water Resour.*, 2013, **61**, 74–85.
- 125 M. Bai, K. Song, Y. Sun, M. He, Y. Li and J. Sun, *J. Pet. Sci. Eng.*, 2014, **124**, 132–136.
- 126 S. Bartel and G. Janssen, *Tunn. Undergr. Space Technol.*, 2016, **55**, 112–117.
- 127 S. Bauer, C. Beyer, F. Dethlefsen, P. Dietrich, R. Duttmann, M. Ebert, V. Feeser, U. Görke, R. Köber, O. Kolditz, W. Rabbel, T. Schanz, D. Schäfer, H. Würdemann and A. Dahmke, *Environ. Earth Sci.*, 2013, **70**, 3935–3943.
- 128 P. O. Carden and L. Paterson, *Int. J. Hydrogen Energy*, 1979, **4**, 559–569.
- 129 C. Sambo, A. Dudun, S. A. Samuel, P. Esenenjor, N. S. Muhammed and B. Haq, *Int. J. Hydrogen Energy*, 2022, **47**, 22840–22880.
- 130 L. Zeng, M. Sarmadivaleh, A. Saeedi, Y. Chen, Z. Zhong and Q. Xie, *Earth-Sci. Rev.*, 2023, **247**, 104625.
- 131 R. Ershadnia, M. Singh, S. Mahmoodpour, A. Meyal, F. Moeini, S. A. Hosseini, D. M. Sturmer, M. Rasoulzadeh, Z. Dai and M. R. Soltanian, *Int. J. Hydrogen Energy*, 2023, **48**, 1450–1471.
- 132 M. Lysy, N. Liu, C. M. Solstad, M. A. Fernø and G. Ersland, *Int. J. Hydrogen Energy*, 2023, **48**, 31294–31304.
- 133 S. R. Thiyagarajan, H. Emadi, A. Hussain, P. Patange and M. Watson, *J. Energy Storage*, 2022, **51**, 104490.
- 134 S. Iglauer, *J. Pet. Sci. Eng.*, 2022, **212**, 109498.
- 135 S. Flude and J. Alcalde, Carbon Capture and Storage Has Stalled Needlessly—Three Reasons Why Fears of CO<sub>2</sub> Leakage are Overblown.
- 136 M. Hosseini, J. Fahimpour, M. Ali, A. Keshavarz and S. Iglauer, *J. Colloid Interface Sci.*, 2022, **614**, 256–266.
- 137 M. A. Sutton, C. M. Howard, J. W. Erisman, G. Billen, A. Bleeker, P. Grennfelt, H. Van Grinsven and B. Grizzetti, The European Nitrogen Assessment: Sources, Effects and Policy Perspectives.
- 138 M. Ali, S. Al-Anssari, M. Arif, A. Barifcani, M. Sarmadivaleh, L. Stalker, M. Lebedev and S. Iglauer, *J. Colloid Interface Sci.*, 2019, **534**, 88–94.
- 139 S. Iglauer, *Int. J. Greenhouse Gas Control*, 2018, **77**, 82–87.
- 140 N. Yekeen, A. Al-Yaseri, B. M. Negash, M. Ali, A. Giwelli, L. Esteban and J. Sarout, *Int. J. Hydrogen Energy*, 2022, **47**, 19155–19167.
- 141 A. Al-Yaseri, N. Yekeen, H. Al-Mukainah, M. Sarmadivaleh and M. Lebedev, *Energy Fuels*, 2024, **38**, 2983–2991.
- 142 E. A. Al-Khdheawi, D. S. Mahdi, M. Ali, C. A. Fauziah and A. Barifcani, *Offshore Technol. Conf. Asia 2020, OTCA*, 2020, DOI: [10.4043/30094-ms](https://doi.org/10.4043/30094-ms).
- 143 A. Al-Yaseri, L. Esteban, A. Giwelli, J. Sarout, M. Lebedev and M. Sarmadivaleh, *Int. J. Hydrogen Energy*, 2022, **47**, 22482–22494.
- 144 E. M. Thaysen, I. B. Butler, A. Hassanpouryouzband, D. Freitas, F. Alvarez-Borges, S. Krevor, N. Heinemann, R. Atwood and K. Edlmann, *Int. J. Hydrogen Energy*, 2023, **48**, 3091–3106.
- 145 M. Bagheri, H. Mahani, S. Ayatollahi and D. Zivar, *Adv. Water Resour.*, 2023, **181**, 104547.
- 146 B. Zulfiqar, H. Vogel, Y. Ding, S. Golmohammadi, M. Kuchler, D. Reuter and H. Geistlinger, *Water Resour. Res.*, 2020, **56**, e2020WR027965.
- 147 N. Yekeen, E. Padmanabhan, H. Abdulelah, S. A. Irfan, O. A. Okunade, J. A. Khan and B. M. Negash, *J. Pet. Sci. Eng.*, 2021, **196**, 107673.
- 148 Q. Zhang, M. Masoudi, L. Sun, L. Zhang, L. Yang, Y. Song and A. Hassanpouryouzband, *ACS Appl. Mater. Interfaces*, 2024, **16**, 53994–54006.
- 149 V. Mirchi and M. Dejam, *J. Energy Storage*, 2023, **73**, 109152.
- 150 F. Zhou, F. Hussain, Z. Guo, S. Yanici and Y. Cinar, *Energy Explor. Exploit.*, 2013, **31**(4), 645–665.
- 151 T. A. Ho, S. T. Dang, N. Dasgupta, A. Choudhary, C. S. Rai and Y. Wang, *Int. J. Hydrogen Energy*, 2024, **51**, 158–166.
- 152 A. Alanazi, H. Rasool Abid, M. Usman, M. Ali, A. Keshavarz, V. Vahrenkamp, S. Iglauer and H. Hoteit, *Fuel*, 2023, **346**, 128362.
- 153 M. Zhang, Y. Yang, B. Pan, Z. Liu, Z. Jin and S. Iglauer, *Fuel*, 2024, **361**, 130621.
- 154 B. Pan, T. Song, X. Yin, Y. Jiang, M. Yue, H. Hoteit, H. Mahani and S. Iglauer, *Soc. Pet. Eng. – GOTECH Conf.*, 2024, DOI: [10.2118/219225-MS](https://doi.org/10.2118/219225-MS).
- 155 M. Ali, Z. Tariq, M. Mubashir, M. S. Kamal, B. Yan and H. Hoteit, *Int. Pet. Technol. Conf. IPTC 2024*, 2024, pp. 12–14.
- 156 M. Ali, N. K. Jha, N. Pal, A. Keshavarz, H. Hoteit and M. Sarmadivaleh, *Earth-Sci. Rev.*, 2022, **225**, 103895.
- 157 A. Isah, M. Arif, A. Hassan, M. Mahmoud and S. Iglauer, *Energy Rep.*, 2022, **8**, 6355–6395.
- 158 S. Iglauer, M. Ali and A. Keshavarz, *Geophys. Res. Lett.*, 2021, **48**, e2020GL090814.
- 159 N. K. Jha, A. Al-Yaseri, M. Ghasemi, D. Al-Bayati, M. Lebedev and M. Sarmadivaleh, *Int. J. Hydrogen Energy*, 2021, **46**, 34822–34829.
- 160 W. G. Anderson, *J. Pet. Technol.*, 1987, **39**, 1453–1468.
- 161 H. J. Deglint, C. R. Clarkson, A. Ghanizadeh, C. DeBuhr and J. M. Wood, *J. Nat. Gas Sci. Eng.*, 2019, **62**, 38–67.



- 162 V. Alipour Tabrizy, R. Denoyel and A. A. Hamouda, *Colloids Surf., A*, 2011, **384**, 98–108.
- 163 T. D. Donaldson, D. Donaldson and E. C. Wettability, *Petrophysics*, 2012, **6**, 371–418.
- 164 M. Kanaani, B. Sedae and M. Asadian-Pakfar, *J. Energy Storage*, 2022, **45**, 103783.
- 165 N. S. Muhammed, M. B. Haq, D. A. Al Shehri, A. Al-Ahmed, M. M. Rahman, E. Zaman and S. Iglauer, *Fuel*, 2023, **337**, 127032.
- 166 N. Heinemann, J. Scafidi, G. Pickup, E. M. Thaysen, A. Hassanpouryouzband, M. Wilkinson, A. K. Satterley, M. G. Booth, K. Edlmann and R. S. Haszeldine, *Int. J. Hydrogen Energy*, 2021, **46**, 39284–39296.
- 167 M. Ali, B. Pan, N. Yekeen, S. Al-Ansari, A. Al-Anazi, A. Keshavarz, S. Iglauer and H. Hoteit, *Int. J. Hydrogen Energy*, 2022, **47**, 14104–14120.
- 168 A. Aftab, A. Al-Yaseri, A. Nzila, J. Al Hamad, A. O. Amao and M. Sarmadivaleh, *Energy Fuels*, 2023, **37**, 5623–5631.
- 169 R. Zheng, T. C. Germann, M. Gross and M. Mehana, *ACS Sustainable Chem. Eng.*, 2024, **12**, 5555–5563.
- 170 S. Higgs, Y. Da Wang, C. Sun, J. Ennis-King, S. J. Jackson, R. T. Armstrong and P. Mostaghimi, *Int. J. Hydrogen Energy*, 2022, **47**, 13062–13075.
- 171 M. Aslannezhad, M. Ali, A. Kalantariasl, M. Sayyafzadeh, Z. You, S. Iglauer and A. Keshavarz, *Prog. Energy Combust. Sci.*, 2023, **95**, 101066.
- 172 M. Hosseini, M. Ali, J. Fahimpour, A. Keshavarz and S. Iglauer, *J. Energy Storage*, 2022, **52**, 104745.
- 173 H. Al-Mukainah, A. Al-Yaseri, N. Yekeen, J. Al Hamad and M. Mahmoud, *Energy Rep.*, 2022, **8**, 8830–8843.
- 174 T. Young, *Philos. Trans. R. Soc. London*, 1805, **95**, 65–87.
- 175 R. Tadmor, *Langmuir*, 2004, **20**, 7659–7664.
- 176 E. Chibowski and K. Terpilowski, *J. Colloid Interface Sci.*, 2008, **319**, 505–513.
- 177 K. Terpilowski, L. Hołysz, M. Chodkowski and D. C. Guinarte, *Colloids Interfaces*, 2021, **5**, 4.
- 178 B. Pan, C. Gong, X. Wang, Y. Li and S. Iglauer, *Fuel*, 2020, **262**, 116461.
- 179 N. Shojai Kaveh, A. Barnhoorn and K. H. Wolf, *Int. J. Greenhouse Gas Control*, 2016, **49**, 425–435.
- 180 S. Al-Ansari, A. Barifcani, S. Wang, L. Maxim and S. Iglauer, *J. Colloid Interface Sci.*, 2016, **461**, 435–442.
- 181 G. R. Abbasi, A. Al-Yaseri, A. Isah, A. Keshavarz and S. Iglauer, *J. Phys. Chem. C*, 2021, **125**, 17323–17332.
- 182 N. Yekeen, E. Padmanabhan, T. A. Sevo, K. A. Kanesen and O. A. Okunade, *J. Ind. Eng. Chem.*, 2020, **88**, 1–28.
- 183 Y. Xu, Y.-B. Ma, F. Gu, S.-S. Yang and C.-S. Tian, *Nature*, 2023, **621**(7979), 506–510.
- 184 N. Shojai Kaveh, E. S. J. Rudolph, P. Van Hemert, W. R. Rossen and K. H. Wolf, *Energy Fuels*, 2014, **28**, 4002–4020.
- 185 A. V. Prydatko, L. A. Belyaeva, L. Jiang, L. M. C. Lima and G. F. Schneider, *Nat. Commun.*, 2018, **9**, 1–7.
- 186 L. M. Lander, L. M. Siewierski, W. J. Britain and E. A. Vogler, *Langmuir*, 1993, **9**, 2237–2239.
- 187 S. Iglauer, A. Z. Al-Yaseri, R. Rezaee and M. Lebedev, *Geophys. Res. Lett.*, 2015, **42**, 9279–9284.
- 188 M. Ali, A. Aftab, Z. U. A. Arain, A. Al-Yaseri, H. Roshan, A. Saeedi, S. Iglauer and M. Sarmadivaleh, *ACS Appl. Mater. Interfaces*, 2020, **12**, 39850–39858.
- 189 H. Esfandyari, A. Safari, A. Hashemi, A. Hassanpouryouzband, M. Haghighi, A. Keshavarz and A. Zeinijahromi, *Renew. Energy*, 2024, **237**, 121726.
- 190 M. Jafari and J. Jung, *Sustainability*, 2017, **9**, 2352.
- 191 F. J. M. Ruiz-Cabello, M. A. Rodríguez-Valverde and M. A. Cabrerizo-Vilchez, *Adv. Colloid Interface Sci.*, 2014, **206**, 320–327.
- 192 A. Al-Yaseri, G. R. Abbasi, N. Yekeen, F. Al-Shajalee, A. Giwelli and Q. Xie, *J. Pet. Sci. Eng.*, 2022, **208**, 109555.
- 193 P. K. Bikkina, *Int. J. Greenhouse Gas Control*, 2011, **5**, 1259–1271.
- 194 J. Mahadevan, *Int. J. Greenhouse Gas Control*, 2012, **7**, 261–262.
- 195 S. Saraji, M. Piri and L. Goual, *Int. J. Greenhouse Gas Control*, 2014, **28**, 147–155.
- 196 A. Z. Al-Yaseri, H. Roshan, M. Lebedev, A. Barifcani and S. Iglauer, *Geophys. Res. Lett.*, 2016, **43**, 3771–3776.
- 197 B. Pan, Y. Li, L. Xie, X. Wang, Q. He, Y. Li, S. H. Hejazi and S. Iglauer, *J. Pet. Sci. Eng.*, 2019, **172**, 511–516.
- 198 R. Garcia, K. Osborne and E. Subashi, *J. Phys. Chem. B*, 2008, **112**, 8114–8119.
- 199 S. M. Gatica, J. K. Johnson, X. C. Zhao and M. W. Cole, *J. Phys. Chem. B*, 2004, **108**, 11704–11708.
- 200 S. Dietrich and M. Napiarkowski, *Phys. Rev. A:At., Mol., Opt. Phys.*, 1991, **43**, 1861–1885.
- 201 Abstr. Pap. Print., *Philos. Trans. R. Soc. London*, 1832, vol. 1, pp. 171–172.
- 202 H. J. Butt, D. S. Golovko and E. Bonaccorso, *J. Phys. Chem. B*, 2007, **111**, 5277–5283.
- 203 S. Snæbjörnsdóttir, E. H. Oelkers, K. Mesfin, E. S. Aradóttir, K. Dideriksen, I. Gunnarsson, E. Gunnlaugsson, J. M. Matter, M. Stute and S. R. Gislason, *Int. J. Greenhouse Gas Control*, 2017, **58**, 87–102.
- 204 S. R. Gislason, D. Wolff-Boenisch, A. Stefansson, E. H. Oelkers, E. Gunnlaugsson, H. Sigurdardottir, B. Sigfusson, W. S. Broecker, J. M. Matter, M. Stute, G. Axelsson and T. Fridriksson, *Int. J. Greenhouse Gas Control*, 2010, **4**, 537–545.
- 205 A. Al-Yaseri, M. Desouky, M. S. Aljawad and A. Hassanpouryouzband, *Int. J. Hydrogen Energy*, 2025, **101**, 1183–1190.
- 206 Y. Zhang, B. Bijeljic, Y. Gao, S. Goodarzi, S. Foroughi and M. J. Blunt, *Geophys. Res. Lett.*, 2023, **50**, e2022GL102383.
- 207 R. Dehury, S. Chowdhury and J. S. Sangwai, *Int. J. Hydrogen Energy*, 2024, **69**, 817–836.
- 208 M. Arif, S. A. Abu-Khamsin and S. Iglauer, *Adv. Colloid Interface Sci.*, 2019, **268**, 91–113.
- 209 A. Isah, M. Mahmoud, M. Arif, M. S. Aljawad and M. S. Kamal, *Energy Fuels*, 2023, **37**, 12744–12761.
- 210 H. Vo Thanh, M. Rahimi, Z. Dai, H. Zhang and T. Zhang, *Fuel*, 2023, **345**, 128183.
- 211 P. Soltani, S. Sadeghnejad, A. H. S. Dehaghani and R. Ashena, *SPE Reservoir Eval. Eng.*, 2019, **22**, 1334–1345.
- 212 A. Isah, M. Mahmoud, M. Arif, M. Al Jawad and A. O. Amao, *Fuel*, 2023, **351**, 128908.



- 213 L. Zeng, A. Keshavarz, N. Kumar Jha, A. Al-Yaseri, M. Sarmadivaleh, Q. Xie and S. Iglauer, *J. Mol. Liq.*, 2023, **371**, 121076.
- 214 R. A. Nasralla, M. A. Bataweel and H. A. Nasr-El-Din, *Soc. Pet. Eng. – Offshore Eur. Oil Gas Conf. Exhib. 2011, OE 2011*, 2011, vol. 2, pp. 978–989.
- 215 P. Chiquet, D. Broseta and S. Thibeau, *Geofluids*, 2007, **7**, 112–122.
- 216 A. Alanazi, M. Ali, M. Ali, A. Keshavarz, S. Iglauer and H. Hoteit, *Fuel*, 2024, **370**, 131842.
- 217 H. Esfandyari, M. Sarmadivaleh, F. Esmailzadeh, M. Ali, S. Iglauer and A. Keshavarz, *J. Energy Storage*, 2022, **52**, 104866.
- 218 A. Al-Yaseri, S. Abdel-Azeim and J. Al-Hamad, *Int. J. Hydrogen Energy*, 2023, **48**, 34897–34905.
- 219 A. Alanazi, M. Al Malallah, M. Mowafi, W. Badeghaish, H. Hoteit, A. Al-Yaseri and J. Al-Hamad, Hydrogen wettability measurement of Saudi basaltic rocks at underground storage conditions, in *ARMA/DGS/SEG International Geomechanics Symposium*, ARMA-IGS, ARMA, 2022, DOI: [10.56952/igs-2022-110](https://doi.org/10.56952/igs-2022-110).
- 220 M. Ali, N. Yekeen, M. Ali, A. Alanazi, M. Shahzad Kamal, A. Keshavarz and H. Hoteit, *Fuel*, 2024, **371**, 132045.
- 221 C. N. Trueman, K. J. Rodgers, I. S. McLellan and A. S. Hursthouse, *Encycl. Anal. Sci.*, 2019, 271–282.
- 222 M. Arif, M. Lebedev, A. Barifcani and S. Iglauer, *Int. J. Greenhouse Gas Control*, 2017, **62**, 113–121.
- 223 J. Hou, S. Lin, M. Zhang and W. Li, *Int. J. Hydrogen Energy*, 2023, **48**, 11303–11311.
- 224 S. Iglauer, M. S. Mathew and F. Bresme, *J. Colloid Interface Sci.*, 2012, **386**, 405–414.
- 225 M. Hosseini, J. Fahimpour, M. Ali, A. Keshavarz and S. Iglauer, *Energy Fuels*, 2022, **36**, 4065–4075.
- 226 C. Chen, N. Zhang, W. Li and Y. Song, *Environ. Sci. Technol.*, 2015, **49**, 14680–14687.
- 227 P. A. Scholle and D. Spearing, Sandstone Depositional Environments: AAPG Memoir, 31 (No. 31). AAPG.
- 228 M. Ali, N. Yekeen, A. Alanazi, A. Keshavarz, S. Iglauer, T. Finkbeiner and H. Hoteit, *J. Energy Storage*, 2023, **62**, 106921.
- 229 *Encyclopedia of Geology*, ed. R. C. Selley, L. R. M. Cocks and I. R. Plimer, Elsevier, Amsterdam, 2004, vol. 5.
- 230 A. Al-Yaseri, M. Ali, M. Ali, R. Taheri and D. Wolff-Boenisch, *J. Colloid Interface Sci.*, 2021, **603**, 165–171.
- 231 S. Iglauer, A. Z. Al-Yaseri and D. Wolff-Boenisch, *Int. J. Greenhouse Gas Control*, 2020, **102**, 103148.
- 232 A. Al-Yaseri, N. Yekeen, M. Mahmoud, A. Kakati, Q. Xie and A. Giwelli, *Int. J. Hydrogen Energy*, 2022, **47**, 22510–22521.
- 233 H. Samara, T. V. Ostrowski and P. Jaeger, *J. Supercrit. Fluids*, 2024, **205**, 106124.
- 234 M. A. Verbel, *Am. Mineral.*, 1993, **78**, 405–414.
- 235 J. F. Banfield and W. W. Barker, *Geochim. Cosmochim. Acta*, 1994, **58**, 1419–1429.
- 236 A. Ali, D. R. Cole and A. Striolo, *Int. J. Hydrogen Energy*, 2024, **58**, 668–677.
- 237 A. Abramov, A. Keshavarz and S. Iglauer, *J. Phys. Chem. C*, 2019, **123**, 9027–9040.
- 238 D. Tunega, M. H. Gerzabek and H. Lischka, *J. Phys. Chem. B*, 2004, **108**, 5930–5936.
- 239 D. Tunega, L. Benco, G. Haberhauer, M. H. Gerzabek and H. Lischka, *J. Phys. Chem. B*, 2002, **106**, 11515–11525.
- 240 M. Arif, M. Lebedev, A. Barifcani and S. Iglauer, *Geophys. Res. Lett.*, 2017, **44**, 8769–8775.
- 241 B. Pan, Y. Li, H. Wang, F. Jones and S. Iglauer, *Energy Fuels*, 2018, **32**, 1914–1922.
- 242 H. Roshan, A. Z. Al-Yaseri, M. Sarmadivaleh and S. Iglauer, *J. Colloid Interface Sci.*, 2016, **475**, 104–111.
- 243 K. A. Kvenvolden, *J. Am. Oil Chem. Soc.*, 1967, **44**, 628–636.
- 244 D. M. Akob, I. M. Cozzarelli, D. S. Dunlap, E. L. Rowan and M. M. Lorah, *Appl. Geochem.*, 2015, **60**, 116–125.
- 245 P. D. Lundegard and Y. K. Kharaka, *Org. Acids Geol. Processes*, 1994, 40–69.
- 246 B. Caballero, L. Trugo and P. Finglas, *Encyclopedia of food sciences and nutrition*, 2003, pp. 1–10.
- 247 D. Waples, Burgess Pub. Co.
- 248 D. M. Jones, I. M. Head, N. D. Gray, J. J. Adams, A. K. Rowan, C. M. Aitken, B. Bennett, H. Huang, A. Brown, B. F. J. Bowler, T. Oldenburg, M. Erdmann and S. R. Larter, *Nature*, 2007, **451**, 176–180.
- 249 P. C. Bennett, D. E. Siegel, M. J. Baedeker and M. F. Hult, *Appl. Geochem.*, 1993, **8**, 529–549.
- 250 C. W. McGowan, R. C. Pearce and H. Diehl, *Fuel Process. Technol.*, 1985, **10**, 195–204.
- 251 W. Meredith, S. J. Kelland and D. M. Jones, *Org. Geochem.*, 2000, **31**, 1059–1073.
- 252 T. D. Cyr and O. P. Strausz, *Org. Geochem.*, 1984, **7**, 127–140.
- 253 L. Yang, T. Xu, M. Wei, G. Feng, F. Wang and K. Wang, *Appl. Geochem.*, 2015, **54**, 65–73.
- 254 M. J. Nazarahari, A. K. Manshad, M. Ali, J. A. Ali, A. Shafiei, S. M. Sajadi, S. Moradi, S. Iglauer and A. Keshavarz, *Fuel*, 2021, **298**, 120773.
- 255 J. Amaya, D. Rana and V. Hornof, *J. Solution Chem.*, 2002, **31**, 139–148.
- 256 K. A. Rezaei Gomari and A. A. Hamouda, *J. Pet. Sci. Eng.*, 2006, **50**, 140–150.
- 257 G. Hansen, A. A. Hamouda and R. Denoyel, *Colloids Surf., A*, 2000, **172**, 7–16.
- 258 P. M. Jardine, N. L. Weber and J. F. McCarthy, *Soil Sci. Soc. Am. J.*, 1989, **53**, 1378–1385.
- 259 Y. K. Kharaka, J. J. Thordsen, S. D. Hovorka, H. Seay Nance, D. R. Cole, T. J. Phelps and K. G. Knauss, *Appl. Geochem.*, 2009, **24**, 1106–1112.
- 260 C. Legens, H. Toulhoat, L. Cuiec, F. Villiéras and T. Palermo, *SPE J.*, 1999, **4**, 328–333.
- 261 L. Madsen and I. Lind, *SPE Reservoir Eng.*, 1998, **1**, 47–51.
- 262 L. Stalker, S. Varma, D. van Gent, J. Haworth and S. Sharma, *Aust. J. Earth Sci.*, 2013, **60**, 45–58.
- 263 M. Ali, M. Arif, M. F. Sahito, S. Al-Ansari, A. Keshavarz, A. Barifcani, L. Stalker, M. Sarmadivaleh and S. Iglauer, *Int. J. Greenhouse Gas Control*, 2019, **83**, 61–68.
- 264 J. W. Grate, K. J. Dehoff, M. G. Warner, J. W. Pittman, T. W. Wietsma, C. Zhang and M. Oostrom, *Langmuir*, 2012, **28**, 7182–7188.
- 265 S. C. Vanithakumari, R. P. George and U. Kamachi Mudali, *Appl. Surf. Sci.*, 2014, **292**, 650–657.



- 266 Y. C. Araujo, P. G. Toledo, V. Leon and H. Y. Gonzalez, *J. Colloid Interface Sci.*, 1995, **176**, 485–490.
- 267 Y. Chen, V. Niasar, L. Ma and Q. Xie, *Int. J. Hydrogen Energy*, 2023, **48**, 32839–32848.
- 268 J. J. Zullig and J. W. Morse, *Geochim. Cosmochim. Acta*, 1988, **52**, 1667–1678.
- 269 S. W. Bailey, *Rev. Mineral.*, 1984, **13**, 1–12.
- 270 M. Arif, A. Barifcani, M. Lebedev and S. Iglauer, *Int. J. Greenhouse Gas Control*, 2016, **50**, 112–120.
- 271 P. K. Bikkina, *Int. J. Greenhouse Gas Control*, 2012, **7**, 263–264.
- 272 M. Ali, F. U. R. Awan, M. Ali, A. Al-Yaseri, M. Arif, M. Sánchez-Román, A. Keshavarz and S. Iglauer, *J. Colloid Interface Sci.*, 2021, **588**, 315–325.
- 273 S. K. Haldar, *Introduction to mineralogy and petrology*, Elsevier, 2020.
- 274 N. Tonnet, G. Mouronval, P. Chiquet and D. Broseta, *Energy Procedia*, 2011, **4**, 5422–5429.
- 275 J. McCaughan, S. Iglauer and F. Bresme, *Energy Procedia*, 2013, **37**, 5387–5402.
- 276 A. Ameri, N. Shojai Kaveh, E. S. J. Rudolph, K. H. Wolf, R. Farajzadeh and J. Bruining, *Energy Fuels*, 2013, **27**, 1015–1025.
- 277 M. Ali, M. Arif, M. Sánchez-Román, A. Keshavarz and S. Iglauer, *15th Greenh. Gas Control Technol. Conf. 2021, GHGT*, 2021, DOI: [10.2139/ssrn.3815420](https://doi.org/10.2139/ssrn.3815420).
- 278 L. Wu, Z.-M. Hou, Z.-F. Luo, Y.-L. Fang, L.-C. Huang, X.-N. Wu, Q.-J. Chen and Q.-C. Wang, *Pet. Sci.*, 2024, **21**, 4067–4099.
- 279 T. Ahmad, N. Kumar and M. Mubashir, *Subsurf. Hydrog. Energy Storage Curr. Status, Prospect. Challenges*, 2025, 265–293.
- 280 M. F. Shahriar, A. Khanal, M. I. Khan and R. Pandey, *J. Energy Storage*, 2024, **97**, 112773.
- 281 N. S. Vasile, *Energies*, 2024, **17**, 6094.
- 282 A. Aftab, A. Al-Yaseri, A. Nzila, J. Al Hamad and M. Sarmadivaleh, *Greenhouse Gases:Sci. Technol.*, 2024, **14**, 546–560.
- 283 A. Al-Yaseri, L. Esteban, A. Giwelli, S. Abdel-Azeim, J. Sarout and M. Sarmadivaleh, *Int. J. Hydrogen Energy*, 2023, **48**, 23581–23593.
- 284 A. Alanazi, N. Yekeen, M. Ali, M. Ali, I. S. Abu-Mahfouz, A. Keshavarz, S. Iglauer and H. Hoteit, *J. Energy Storage*, 2023, **62**, 106865.
- 285 H. Aghaei, A. Al-Yaseri, A. Toorajipour, B. Shahsavani, N. Yekeen and K. Edlmann, *Fuel*, 2023, **351**, 129048.
- 286 A. Kaya and Y. Yukselen, *Can. Geotech. J.*, 2005, **42**(5), 1280–1289.
- 287 A. Z. Al-Yaseri, M. Lebedev, A. Barifcani and S. Iglauer, *J. Chem. Thermodyn.*, 2016, **93**, 416–423.
- 288 A. Isah, M. Mahmoud, M. S. Kamal, M. Arif and M. Al Jawad, *SPE Reservoir Eval. Eng.*, 2023, **26**, 592–610.
- 289 J. Mouallem, M. Arif, A. Isah, A. Raza, M. Motiur Rahman, M. Mahmoud and M. Shahzad Kamal, *Fuel*, 2024, **371**, 131986.
- 290 J. G. Arias, *Repos. Gall. Ariasrepositorio.unal.edu.co*.
- 291 O. E. Medina, J. F. Gallego, I. Moncayo-Riascos, M. Lysy, P. N. Benjumea, F. B. Cortés and C. A. Franco, *Int. J. Hydrogen Energy*, 2024, **60**, 959–975.
- 292 B. Uliasz-Misiak and J. Misiak, *Energies*, 2024, **17**, 1666.
- 293 O. A. M. Zamani and D. Knez, *Energies*, 2024, **17**, 3586.
- 294 J. D. Minougou, R. Gholami and P. Andersen, *Earth-Sci. Rev.*, 2023, **247**, 104599.
- 295 H. Samara and P. Jaeger, *SN Appl. Sci.*, 2022, **4**, 1–11.
- 296 F. Haeri, D. Tapriyal, S. Sanguinito, F. Shi, S. J. Fuchs, L. E. Dalton, J. Baltrus, B. Howard, D. Crandall, C. Matranga and A. Goodman, *Energy Fuels*, 2020, **34**, 6085–6100.
- 297 J. W. Jung and J. Wan, *Energy Fuels*, 2012, **26**, 6053–6059.
- 298 N. R. Morrow, *J. Can. Pet. Technol.*, 1975, **14**, 42–53.
- 299 A. Sari, N. S. Al Maskari, A. Saeedi and Q. Xie, *J. Mol. Liq.*, 2020, **299**, 112107.
- 300 R. N. Wenzel, *Ind. Eng. Chem. ACS Publ.*
- 301 P. S. Swain and R. Lipowsky, *Langmuir*, 1998, **14**, 6772–6780.
- 302 A. Marmur, *Soft Matter*, 2006, **2**, 12–17.
- 303 M. Hosseini, J. Fahimpour, M. Ali, A. Keshavarz and S. Iglauer, *J. Pet. Sci. Eng.*, 2022, **213**, 110441.
- 304 A. N. Janjua, M. Ali, M. Murtaza, S. Patil and M. S. Kamal, *J. Energy Storage*, 2024, **95**, 112510.
- 305 S. Omrani, M. Ghasemi, M. Singh, S. Mahmoodpour, T. Zhou, M. Babaei and V. Niasar, *Langmuir*, 2023, **39**, 12680–12691.
- 306 H. Esfandyari, M. Sarmadivaleh, F. Esmaeilzadeh, M. Ali, S. Iglauer and A. Keshavarz, *J. Energy Storage*, 2023, **57**, 106162.
- 307 A. M. Adam, D. Bahamon, M. Al Kobaisi and L. F. Vega, *Int. J. Hydrogen Energy*, 2024, **78**, 1344–1354.
- 308 Y. T. F. Chow, G. C. Maitland and J. P. M. Trusler, *Fluid Phase Equilib.*, 2018, **475**, 37–44.
- 309 H. Esfandyari, M. Hosseini, M. Ali, S. Iglauer, M. Haghghi and A. Keshavarz, *J. Energy Storage*, 2023, **60**, 106637.
- 310 H. Abdullelah, A. Al-Yaseri, M. Ali, A. Giwelli, B. M. Negash and M. Sarmadivaleh, *J. Pet. Sci. Eng.*, 2021, **204**, 108683.
- 311 J. L. Dickson, G. Gupta, T. S. Horozov, B. P. Binks and K. P. Johnston, *Langmuir*, 2006, **22**, 2161–2170.
- 312 M. Hosseini, M. Ali, J. Fahimpour, A. Keshavarz and S. Iglauer, *Energy Fuels*, 2023, **37**, 5986–5994.
- 313 M. Chai, Z. Chen, H. Nourozieh and M. Yang, *Appl. Energy*, 2023, **334**, 120655.
- 314 M. Zamehrian and B. Sedaei, *J. Pet. Sci. Eng.*, 2022, **212**, 110304.
- 315 Z. Bo, L. Zeng, Y. Chen and Q. Xie, *Int. J. Hydrogen Energy*, 2021, **46**, 19998–20009.
- 316 B. Hagemann, M. Rasoulzadeh, M. Panfilov, L. Ganzer and V. Reitenbach, *Environ. Earth Sci.*, 2015, **73**, 6891–6898.
- 317 L. Paterson, *Int. J. Hydrogen Energy*, 1983, **8**, 53–59.
- 318 S. Kobeissi, N. N. A. Ling, K. Yang, E. F. May and M. L. Johns, *Int. J. Hydrogen Energy*, 2024, **60**, 940–948.
- 319 N. S. Muhammed, B. Haq and D. A. Al Shehri, *Int. J. Hydrogen Energy*, 2023, **48**, 38782–38807.
- 320 A. Lemieux, K. Sharp and A. Shkarupin, *Int. J. Hydrogen Energy*, 2019, **44**, 15193–15204.
- 321 V. Mirchi, M. Dejam and V. Alvarado, *Int. J. Hydrogen Energy*, 2022, **47**, 34963–34975.
- 322 Q. T. Doan, A. Keshavarz, C. R. Miranda, P. Behrenbruch and S. Iglauer, *Int. J. Hydrogen Energy*, 2024, **50**, 1607–1615.



- 323 V. Mirchi, M. Dejam, V. Alvarado and M. Akbarabadi, *Energy Fuels*, 2023, **37**, 15231–15243.
- 324 Z. Dalal Isfehiani, A. Sheidaie, M. Hosseini, J. Fahimpour, S. Iglauer and A. Keshavarz, *J. Mol. Liq.*, 2023, **374**, 121279.
- 325 Q. T. Doan, A. Keshavarz, C. R. Miranda, P. Behrenbruch and S. Iglauer, *J. Energy Storage*, 2023, **66**, 107470.
- 326 Q. Chang, D. Dempsey, L. Zhang, Y. Zhao and L. Huang, *Int. J. Hydrogen Energy*, 2024, **64**, 896–905.
- 327 A. Aftab, A. Hassanpouryouzband, Q. Xie, L. L. Machuca and M. Sarmadivaleh, *Ind. Eng. Chem. Res.*, 2022, **61**, 3233–3253.
- 328 S. O. Akpasi, I. Michael, S. Anekwe, E. Kweinor Tetteh, U. O. Amune, S. Ishola Mustapha and S. L. Kiambi, *Clean Energy*, 2025, **9**, 52–88.
- 329 H. Yousefi, *Design considerations for developing an underground hydrogen storage facility in porous reservoirs*, PDEng thesis, University of Twente, 2021.
- 330 H. R. Abid, N. Yekeen, A. Al-Yaseri, A. Keshavarz and S. Iglauer, *J. Energy Storage*, 2022, **55**, 105615.
- 331 X. Li, X. Sun, C. C. Walters and T. Zhang, *Int. J. Hydrogen Energy*, 2024, **50**, 879–892.
- 332 A. Al-Yaseri, H. Al-Mukainah and N. Yekeen, *Fuel*, 2023, **344**, 128000.
- 333 Y. Teng, L. Jiang, Y. Liu, D. Wang and Y. Song, *Int. J. Heat Mass Transfer*, 2018, **119**, 678–687.
- 334 S. Goodarzi, Y. Zhang, S. Foroughi, B. Bijeljic and M. J. Blunt, *Int. J. Hydrogen Energy*, 2024, **56**, 1139–1151.
- 335 S. L. Campello, W. P. Dos Santos, V. F. Machado, C. C. B. O. Mota, A. S. L. Gomes and R. E. De Souza, *Microporous Mesoporous Mater.*, 2014, **198**, 50–54.
- 336 A. Al-Yaseri, H. Al-Mukainah, N. Yekeen and A. S. Al-Qasim, *Int. J. Hydrogen Energy*, 2023, **48**, 3583–3592.
- 337 S. Flesch, D. Pudlo, D. Albrecht, A. Jacob and F. Enzmann, *Int. J. Hydrogen Energy*, 2018, **43**, 20822–20835.
- 338 A. Fatah, A. Al-Yaseri, R. Theravalappil, O. A. Radwan, A. Amao and A. S. Al-Qasim, *Fuel*, 2024, **371**, 131857.
- 339 A. Al-Yaseri, A. Fatah, B. Alsaif, S. Sakthivel, A. Amao, A. S. Al-Qasim and A. A. Yousef, *Energy Fuels*, 2024, **38**(11), 9923–9932.
- 340 A. Isah, M. Arif, A. Hassan, M. Mahmoud and S. Iglauer, *Fuel*, 2022, **320**, 123942.
- 341 A. Isah, M. Mahmoud, M. S. Aljawad, M. Arif, S. R. Hussaini, A. Amao, A. Raza and M. S. Kamal, *Energy*, 2024, **305**, 132323.
- 342 S. Iglauer, H. Akhondzadeh, H. Abid, A. Paluszny, A. Keshavarz, M. Ali, A. Giwelli, L. Esteban, J. Sarout and M. Lebedev, *Geophys. Res. Lett.*, 2022, **49**, e2021GL096873.
- 343 A. Al-Yaseri, A. Fatah, R. Al-Abdrabalnabi, S. Alafnan and A. Salmachi, *Int. J. Hydrogen Energy*, 2024, **78**, 268–278.
- 344 J. Wang, X. Feng, Q. Wanyan, K. Zhao, Z. Wang, G. Pei, J. Xie and B. Tian, *Energy*, 2022, **242**, 123058.
- 345 Z. Jangda, H. Menke, A. Busch, S. Geiger, T. Bultreys, H. Lewis and K. Singh, *J. Colloid Interface Sci.*, 2023, **629**, 316–325.
- 346 A. R. Adebayo, A. Isah, M. Mahmoud and D. Al-Shehri, *Molecules*, 2020, **25**, 3385.
- 347 A. Isah, A. R. Adebayo, M. Mahmoud, L. O. Babalola and A. El-Husseiny, *J. Nat. Gas Sci. Eng.*, 2021, **86**, 103652.
- 348 A. Al-Yaseri, L. Esteban, N. Yekeen, A. Giwelli, J. Sarout and M. Sarmadivaleh, *Int. J. Hydrogen Energy*, 2023, **48**, 5175–5185.
- 349 A. Al-Yaseri, N. Yekeen, A. Isah, S. Abdel-Azeim, A. M. Bello and S. Sakthivel, *Energy Fuels*, 2023, **37**, 9329–9338.
- 350 A. Isah, M. Mahmoud, M. S. Aljawad, M. Arif and M. S. Kamal, Relationship Between Geomechanical Properties and Rock Wetting Behavior, in *ARMA/DGS/SEG International Geomechanics Symposium*, ARMA-IGS, ARMA, 2023.
- 351 Z. Shi, K. Jessen and T. T. Tsotsis, *Int. J. Hydrogen Energy*, 2020, **45**, 8757–8773.
- 352 Y. Zhang, M. Lebedev, M. Sarmadivaleh, A. Barifcani and S. Iglauer, *Geophys. Res. Lett.*, 2016, **43**, 9077–9083.
- 353 Z. Pan, L. D. Connell and M. Camilleri, *Int. J. Coal Geol.*, 2010, **82**, 252–261.
- 354 Y. Zhang, X. Xu, M. Lebedev, M. Sarmadivaleh, A. Barifcani and S. Iglauer, *Int. J. Coal Geol.*, 2016, **165**, 149–156.
- 355 A. Fujii, T. Ebata and N. Mikami, *J. Phys. Chem. A*, 2002, **106**, 10124–10129.
- 356 P. Rallapalli, K. P. Prasanth, D. Patil, R. S. Somani, R. V. Jasra and H. C. Bajaj, *J. Porous Mater.*, 2011, **18**, 205–210.
- 357 E. Ahmed and A. Rothenberger, *J. Mater. Chem. A*, 2015, **3**, 7786–7792.
- 358 Q. Zhao, R. Guo, N. K. Jha, M. Sarmadivaleh, M. Lebedev, A. Al-Yaseri, J. McClure and C. Chen, *Fuel*, 2024, **366**, 131414.
- 359 M. Lysy, G. Ersland and M. Fernø, *Adv. Water Resour.*, 2022, **163**, 104167.
- 360 D. Singh, H. A. Friis, E. Jettestuen and J. O. Helland, *Transp. Porous Media*, 2022, **145**, 441–474.
- 361 A. AlRatrou, A. Q. Raeini, B. Bijeljic and M. J. Blunt, *Adv. Water Resour.*, 2017, **109**, 158–169.
- 362 K. Xu, R. Bonnecaze and M. Balhoff, *Phys. Rev. Lett.*, 2017, **119**, 264502.
- 363 C. Garing, J. A. de Chalendar, M. Voltolini, J. B. Ajo-Franklin and S. M. Benson, *Adv. Water Resour.*, 2017, **104**, 223–241.
- 364 J. A. De Chalendar, C. Garing and S. M. Benson, *J. Fluid Mech.*, 2018, **835**, 363–392.
- 365 M. J. Blunt, *Phys. Rev. E: Stat., Nonlinear, Soft Matter Phys.*, 2022, **106**, 045103.
- 366 N. Joewondo, V. Garbin and R. Pini, *Chem. Eng. Res. Des.*, 2023, **192**, 82–90.
- 367 G. R. Abbasi, M. Arif, A. Isah, M. Ali, M. Mahmoud, H. Hoteit, A. Keshavarz and S. Iglauer, *Earth-Sci. Rev.*, 2022, **234**, 104233.
- 368 S. M. Shah, F. Gray, J. P. Crawshaw and E. S. Boek, *Adv. Water Resour.*, 2016, **95**, 276–287.
- 369 V. Cnudde and M. N. Boone, *Earth-Sci. Rev.*, 2013, **123**, 1–17.
- 370 L. Vásárhelyi, Z. Kónya and R. Vajtai, *Mater. Today Adv.*, 2020, **8**, 100084.



- 371 E. M. Withjack, C. Devier and G. Michael, *SPE West. Reg. Meet.*, 2003, 41–52.
- 372 I. Izadi Amiri, D. Zivar, S. Ayatollahi and H. Mahani, *J. Energy Storage*, 2024, **80**, 110264.
- 373 A. P. Indro and E. R. Okoroafor, *J. Energy Storage*, 2024, **92**, 112228.
- 374 E. R. Okoroafor, S. D. Saltzer and A. R. Kovscek, *Int. J. Hydrogen Energy*, 2022, **47**, 33781–33802.
- 375 S. Bai, J. Kubelka and M. Piri, *Langmuir*, 2021, **37**, 6641–6649.
- 376 T. Fang, M. Wang, C. Wang, B. Liu, Y. Shen, C. Dai and J. Zhang, *Chem. Eng. Sci.*, 2017, **164**, 17–22.
- 377 B. Liu, J. Shi, M. Wang, J. Zhang, B. Sun, Y. Shen and X. Sun, *J. Supercrit. Fluids*, 2016, **111**, 171–178.
- 378 F. Jiménez-Ángeles and A. Firoozabadi, *J. Phys. Chem. C*, 2016, **120**, 11910–11917.
- 379 M. C. Oliver, R. Zheng, L. Huang and M. Mehana, *Int. J. Hydrogen Energy*, 2024, **65**, 540–547.
- 380 M. J. Abraham, T. Murtola, R. Schulz, S. Páll, J. C. Smith, B. Hess and E. Lindahl, *SoftwareX*, 2015, 1–2, 19–25.
- 381 B. R. Brooks, R. E. Bruccoleri, B. D. Olafson, D. J. States, S. Swaminathan and M. Karplus, *J. Comput. Chem.*, 1983, **4**, 187–217.
- 382 S. Plimpton, *J. Comput. Phys.*, 1995, **117**, 1–19.
- 383 B. Hess, C. Kutzner, D. Van Der Spoel and E. Lindahl, *J. Chem. Theory Comput.*, 2008, **4**, 435–447.
- 384 S. Pronk, S. Páll, R. Schulz, P. Larsson, P. Bjelkmar, R. Apostolov, M. R. Shirts, J. C. Smith, P. M. Kasson, D. Van Der Spoel, B. Hess and E. Lindahl, *Bioinformatics*, 2013, **29**, 845–854.
- 385 M. T. Nelson, W. Humphrey, A. Gursoy, A. Dalke, L. V. Kale, R. D. Skeel and K. Schulten, *The International Journal of Supercomputer Applications and High Performance Computing*, 1996, **10**(4), 251–268.
- 386 J. C. Phillips, R. Braun, W. Wang, J. Gumbart, E. Tajkhorshid, E. Villa, C. Chipot, R. D. Skeel, L. Kalé and K. Schulten, *J. Comput. Chem.*, 2005, **26**, 1781–1802.
- 387 D. A. Case, T. E. Cheatham, T. Darden, H. Gohlke, R. Luo, K. M. Merz, A. Onufriev, C. Simmerling, B. Wang and R. J. Woods, *J. Comput. Chem.*, 2005, **26**, 1668–1688.
- 388 K. J. Bowers, E. Chow, H. Xu, R. O. Dror, M. P. Eastwood, B. A. Gregersen, J. L. Klepeis, I. Kolossvary, M. A. Moraes, F. D. Sacchetti, J. K. Salmon, Y. Shan and D. E. Shaw, *Proc. 2006 ACM/IEEE Conf. Supercomput. SC'06*, DOI: [10.1145/1188455.1188544](https://doi.org/10.1145/1188455.1188544).
- 389 M. A. Ghafari, M. Ghasemi, V. Niasar and M. Babaei, *Langmuir*, 2024, **40**, 20559–20575.
- 390 G. Carchini, A. Hamza, I. A. Hussein, M. Saad, M. Mahmoud, R. Shawabkeh and S. Aparicio, *Int. J. Hydrogen Energy*, 2023, **48**, 7419–7430.
- 391 S. Alafnan, *SPE J.*, 2024, **29**, 4471–4485.
- 392 M. Xie, M. Zhang and Z. Jin, *Langmuir*, 2024, **40**, 5369–5377.
- 393 H. Abdullelah, A. Keshavarz, H. Hoteit, H. Abid, E. Goudeli, J. Ennis-King and S. Iglauer, *J. Energy Storage*, 2023, **66**, 107440.
- 394 A. Raza, S. Alafnan, G. Glatz, M. Arif, M. Mahmoud and M. G. Rezk, *Energy Fuels*, 2022, **36**, 15013–15022.
- 395 S. Alafnan, A. Raza and M. Mahmoud, *Fuel*, 2024, **364**, 131073.
- 396 A. Raza, S. Alafnan, G. Glatz, M. Mahmoud and A. Salmachi, *Fuel*, 2024, **359**, 130476.
- 397 M. Ghasemi, S. Omrani, S. Mahmoodpour and T. Zhou, *Int. J. Hydrogen Energy*, 2022, **47**, 24871–24885.
- 398 X. Li, T. Huo, K. Wei, Z. Yan, L. Zhu and Q. Xue, *Fuel*, 2024, **367**, 131469.
- 399 M. Saeed and P. Jadhawar, *Gas Sci. Eng.*, 2024, **121**, 205196.
- 400 A. Phan, V. Barker, A. Hassanpouryouzband and T. A. Ho, *J. Energy Storage*, 2025, **112**, 115477.
- 401 J. Kubelka, S. Bai and M. Piri, *J. Phys. Chem. B*, 2021, **125**, 1293–1305.
- 402 J. Wang, R. Wu, M. Wei, B. Bai, J. Xie and Y. Li, *Gas Sci. Eng.*, 2023, **118**, 205105.
- 403 K. Luboń and R. Tarkowski, *Int. J. Hydrogen Energy*, 2020, **45**, 2068–2083.
- 404 G. Wang, G. Pickup, K. Sorbie and E. Mackay, *Int. J. Hydrogen Energy*, 2022, **47**, 28956–28968.
- 405 J. Wang, R. Wu, K. Zhao and B. Bai, *Int. J. Hydrogen Energy*, 2024, **69**, 1069–1083.
- 406 K. Luboń and R. Tarkowski, *Energies*, 2024, **17**, 1493.
- 407 A. Correnti and M. Verlaan, *Soc. Pet. Eng. – SPE Eur. Energy Conf. Exhib. EURO 2024*, 2024, pp. 26–28.
- 408 A. Salmachi, A. Seyfaee, R. J. Robert, T. Hosseini, G. Nathan, P. Ashman, A. Roberts, M. Jafarian and C. Simon, *Int. J. Hydrogen Energy*, 2024, **50**, 1055–1069.
- 409 E. R. Okoroafor, L. Sampaio, F. Gasanzade, Y. Perez Claro, J. D. Zhou, S. D. Saltzer, S. Bauer and A. R. Kovscek, *Energy Convers. Manage.*, 2023, **292**, 117409.
- 410 Q. Zhao, H. Wang and C. Chen, *Fuel*, 2024, **357**, 130051.
- 411 H. Singh, *Appl. Energy*, 2022, **313**, 118862.
- 412 J. Wang, Y. Yang, S. Cai, J. Yao and Q. Xie, *Int. J. Hydrogen Energy*, 2023, **48**, 13922–13933.
- 413 Z. Tariq, M. Ali, N. Yekeen, A. Baban, B. Yan, S. Sun and H. Hoteit, *Fuel*, 2023, **354**, 129354.
- 414 K. Kohzadvand, M. M. Kouhi, A. Barati, S. Omrani and M. Ghasemi, *J. Energy Storage*, 2023, **72**, 108567.
- 415 S. Kalam, M. Arif, A. Raza, N. Lashari and M. Mahmoud, *Int. J. Coal Geol.*, 2023, **280**, 104386.
- 416 A. Gbadamosi, H. Adamu, J. Usman, A. G. Usman, M. M. Jibril, B. A. Salami, S. L. Gbadamosi, L. O. Oyedele and S. I. Abba, *Int. J. Hydrogen Energy*, 2024, **50**, 1326–1337.
- 417 H. Vo Thanh, Z. Dai, Z. Du, H. Yin, B. Yan, M. R. Soltanian, T. Xiao, B. McPherson and L. Abualigah, *Int. J. Hydrogen Energy*, 2024, **57**, 1000–1009.
- 418 B. Pan, T. Song, M. Yue, S. Chen, L. Zhang, K. Edlmann, C. W. Neil, W. Zhu and S. Iglauer, *Int. J. Hydrogen Energy*, 2024, **56**, 1384–1390.
- 419 C. S. W. Ng, H. Djema, M. Nait Amar and A. Jahanbani Ghahfarokhi, *Int. J. Hydrogen Energy*, 2022, **47**, 39595–39605.
- 420 M. Behnamnia, N. Mozafari and A. Dehghan Monfared, *J. Energy Storage*, 2023, **73**, 108995.
- 421 M. Hosseini and Y. Leonenko, *Int. J. Hydrogen Energy*, 2024, **58**, 485–494.



- 422 K. Gao, N. M. Creasy, L. Huang and M. R. Gross, *Int. J. Hydrogen Energy*, 2024, **61**, 137–161.
- 423 S. Ansari, M. Safaei-Farouji, S. Atashrouz, A. Abedi, A. Hemmati-Sarapardeh and A. Mohaddespour, *Int. J. Hydrogen Energy*, 2022, **47**, 37724–37741.
- 424 J. Vamathevan, D. Clark, P. Czodrowski, I. Dunham, E. Ferran, G. Lee, B. Li, A. Madabhushi, P. Shah, M. Spitzer and S. Zhao, *Nat. Rev. Drug Discovery*, 2019, **18**, 463–477.
- 425 A. Carbonero, S. Mao and M. Mehana, *Work. Pap. "Tackling Clim. Chang. with Mach. Learn. ICLR*.
- 426 D. Rolnick, P. L. Donti, L. H. Kaack, K. Kochanski, A. Lacoste, K. Sankaran, A. S. Ross, N. Milojevic-Dupont, N. Jaques, A. Waldman-Brown, A. S. Luccioni, T. Maharaj, E. D. Sherwin, S. K. Mukkavilli, K. P. Kording, C. P. Gomes, A. Y. Ng, D. Hassabis, J. C. Platt, F. Creutzig, J. Chayes and Y. Bengio, *ACM Comput. Surv.*, 2023, **55**, 96.
- 427 J. Cai, X. Chu, K. Xu, H. Li and J. Wei, *Nanoscale Adv.*, 2020, **2**, 3115–3130.
- 428 G. Wen, Z. Li, Q. Long, K. Azizzadenesheli, A. Anandkumar and S. M. Benson, *Energy Environ. Sci.*, 2023, **16**, 1732–1741.
- 429 L. Lu, P. Jin, G. Pang, Z. Zhang and G. E. Karniadakis, *Nat. Mach. Intell.*, 2021, **3**, 218–229.
- 430 W. Diab and M. Al Kobaisi, Temporal Extrapolation and Reliable Generalization via 2U-Nets Deep Operator Network (2U-DeepONet) for Time-Dependent PDEs, in *ECMOR 2024*, European Association of Geoscientists & Engineers, 2024, vol. 2024, No. 1, pp. 1–16.
- 431 W. Diab and M. Al Kobaisi, *Sci. Rep.*, 2024, **14**(1), 21298.
- 432 S. Mao, B. Chen, M. Malki, F. Chen, M. Morales, Z. Ma and M. Mehana, *Appl. Energy*, 2024, **361**, 122914.
- 433 H. Wang, K. Hu, W. Fan, M. Zhang, X. Xia and J. Cai, *Int. J. Hydrogen Energy*, 2025, **101**, 303–312.
- 434 J. Zhang, M. B. Clennell, A. Sagotra and R. Pascual, *Chem. Phys.*, 2023, **564**, 111725.
- 435 S. Mao, B. Chen, M. Morales, M. Malki and M. Mehana, *Int. J. Hydrogen Energy*, 2024, **68**, 1033–1047.
- 436 S. O. Bade, K. Taiwo, U. F. Ndulue, O. S. Tomomewo and B. Aisosa Oni, *Int. J. Hydrogen Energy*, 2024, **80**, 449–474.
- 437 X. Luo, S. Tveit, R. Gholami and P. Ø. Andersen, *Fuel*, 2024, **364**, 131038.
- 438 Z. Wei, L. Jiang, A. Hassanpouryouzband, S. Chen, Y. Chen, Y. Ju, L. Feng, K. Liu, J. Zhang and Z. Chen, *Energy Convers. Manage.*, 2025, **325**, 119449.
- 439 C. Wang, Y. Zhao, R. Wu, J. Bi and K. Zhang, *Fuel*, 2024, **357**, 129919.
- 440 E. López-Chávez, A. Garcia-Quiroz, Y. A. Peña-Castañeda, J. A. I. Diaz-Gongora, F. de Landa Castillo-Alvarado and W. R. Carbellido, *J. Mol. Model.*, 2020, **26**, 1–14.
- 441 T. Muther and A. K. Dahaghi, *Int. J. Hydrogen Energy*, 2024, **58**, 583–595.
- 442 T. Muther and A. Kalantari Dahaghi, *J. Energy Storage*, 2024, **87**, 111425.
- 443 L. Wang, J. Cheng, Z. Jin, Q. Sun, R. Zou, Q. Meng, K. Liu, Y. Su and Q. Zhang, *Fuel*, 2023, **344**, 127919.
- 444 C. J. Okere, J. J. Sheng and C. Ejike, *Energy Geosci.*, 2024, **5**, 100318.
- 445 M. Ali, N. Yekeen, S. Al-Ansari, A. Hassanpouryouzband, A. Keshavarz and H. Hoteit, *J. Energy Storage*, 2024, **97**, 112768.
- 446 C. Mondelli, F. Bardelli, J. G. Vitillo, M. Didier, J. Brendle, D. R. Cavicchia, J. C. Robinet and L. Charlet, *Int. J. Hydrogen Energy*, 2015, **40**, 2698–2709.
- 447 F. Bardelli, C. Mondelli, M. Didier, J. G. Vitillo, D. R. Cavicchia, J. C. Robinet, L. Leone and L. Charlet, *Appl. Geochem.*, 2014, **49**, 168–177.
- 448 P. P. Ziemiański and A. Derkowski, *Int. J. Hydrogen Energy*, 2022, **47**, 28794–28805.
- 449 M. Panfilov, *Compend. Hydrog. Energy Hydrog. Storage, Distrib. Infrastruct.*, 2015, **2**, 91–115.
- 450 L. C. Stewart, J. H. Jung, Y. T. Kim, S. W. Kwon, C. S. Park and J. F. Holden, *Int. J. Syst. Evol. Microbiol.*, 2015, **65**, 1280–1283.
- 451 S. P. Gregory, M. J. Barnett, L. P. Field and A. E. Milodowski, *Microorganisms*, 2019, **7**, 53.
- 452 Z. Zhou, M. Benbouzid, J. Frédéric Charpentier, F. Scullier and T. Tang, *Renewable Sustainable Energy Rev.*, 2013, **18**, 390–400.
- 453 A. Hassanpouryouzband, E. Joonaki, K. Edlmann, N. Heinemann and J. Yang, *Sci. Data*, 2020, **7**, 1–14.
- 454 G. Strobel, B. Hagemann, T. M. Huppertz and L. Ganzer, *Renewable Sustainable Energy Rev.*, 2020, **123**, 109747.
- 455 V. O'Flaherty, T. Mahony, R. O'Kennedy and E. Colleran, *Process Biochem.*, 1998, **33**, 555–569.
- 456 A. Al-Yaseri, N. Yekeen, H. Al-Mukainah and A. Hassanpouryouzband, *Fuel*, 2024, **361**, 130728.
- 457 E. M. Thaysen, S. McMahan, G. J. Strobel, I. B. Butler, B. T. Ngwenya, N. Heinemann, M. Wilkinson, A. Hassanpouryouzband, C. I. McDermott and K. Edlmann, *Renewable Sustainable Energy Rev.*, 2021, **151**, 111481.
- 458 L. Ganzert, J. Schirmack, M. Alawi, K. Mangelsdorf, W. Sand, A. Hillebrand-Voiculescu and D. Wagner, *Int. J. Syst. Evol. Microbiol.*, 2014, **64**, 3478–3484.
- 459 T. N. Zhilina, D. G. Zavarzina, V. V. Kevbrin and T. V. Kolganova, *Microbiol.*, 2013, **82**, 698–706.
- 460 T. F. Jakobsen, K. U. Kjeldsen and K. Ingvorsen, *Int. J. Syst. Evol. Microbiol.*, 2006, **56**, 2063–2069.
- 461 B. Ollivier, C. E. Hatchikian, G. Prensier, J. Guezennec and J. L. Garcia, *Int. J. Syst. Bacteriol.*, 1991, **41**, 74–81.
- 462 N. Dopffel, S. Jansen and J. Gerritse, *Int. J. Hydrogen Energy*, 2021, **46**, 8594–8606.
- 463 Q. Chang, L. Huang, K. McKenzie, C. Carere, M. Stott, A. Nicol and D. Dempsey, *J. Energy Storage*, 2024, **97**, 112766.
- 464 H. G. Machel, *Sediment. Geol.*, 2001, **140**, 143–175.
- 465 A. Rabii, S. Aldin, Y. Dahman and E. Elbeshbishy, *Energies*, 2019, **12**, 1106.
- 466 K. Porsch, J. Meier, S. Kleinsteuber and K. Wendt-Potthoff, *Microb. Ecol.*, 2009, **57**, 701–717.
- 467 S. R. G. Tiburcio, A. Macrae, R. S. Peixoto, C. T. C. da Costa Rachid, F. R. P. Mansoldo, D. S. Alviano, C. S. Alviano, D. F. Ferreira, F. de Queiroz Venâncio, D. F. Ferreira and A. B. Vermelho, *Sci. Rep.*, 2021, **11**, 1–11.
- 468 P. Rueter, *Oceanogr. Lit. Rev.*, 1995, **5**, 348.



- 469 M. A. Saxton, V. A. Samarkin, M. T. Madigan, M. W. Bowles, W. M. Sattley, C. A. Schutte and S. B. Joye, *Limnol. Oceanogr.*, 2021, **66**, 1804–1818.
- 470 M. Ranchou-Peyruse, M. Guignard, F. Casteran, M. Abadie, C. Defois, P. Peyret, D. Dequidt, G. Caumette, P. Chiquet, P. Cézac and A. Ranchou-Peyruse, *Front. Microbiol.*, 2021, **12**, 688929.
- 471 C. Hemme and W. van Berk, *J. Nat. Gas Sci. Eng.*, 2017, **47**, 114–123.
- 472 L. Lankof, K. Urbańczyk and R. Tarkowski, *Renewable Sustainable Energy Rev.*, 2022, **160**, 112309.
- 473 F. J. Millero, *MariChem*, 1986, **18**, 121–147.
- 474 A. Hassanpouryouzband, K. Adie, T. Cowen, E. M. Thaysen, N. Heinemann, I. B. Butler, M. Wilkinson and K. Edlmann, *ACS Energy Lett.*, 2022, **7**, 2203–2210.
- 475 S. Zhan, L. Zeng, A. Al-Yaseri, M. Sarmadivaleh and Q. Xie, *Int. J. Hydrogen Energy*, 2024, **50**, 19–35.
- 476 A. Al-Yaseri, S. Rizwanullah Hussaini, A. Fatah, A. S. Al-Qasim and P. D. Patil, *Fuel*, 2024, **361**, 130680.
- 477 A. Al-Yaseri, A. Fatah, A. Amao and D. Wolff-Boenisch, *Energy Fuels*, 2023, **37**, 15138–15152.
- 478 A. Al-Yaseri, I. S. Abu-Mahfouz, N. Yekeen and D. Wolff-Boenisch, *J. Energy Storage*, 2023, **63**, 106986.
- 479 A. Escamilla, D. Sánchez and L. García-Rodríguez, *Int. J. Hydrogen Energy*, 2022, **47**, 17505–17525.
- 480 A. Safari, Y. Sugai, M. Sarmadivaleh and M. Imai, *J. Energy Storage*, 2023, **70**, 107679.
- 481 A. P. Indro, L. K. Sekar, G. V. Matey-Korley, C. C. Ikeokwu and E. R. Okoroafor, *Int. J. Hydrogen Energy*, 2024, **78**, 1288–1305.
- 482 M. Jahanbani Veshareh, E. M. Thaysen and H. M. Nick, *Appl. Energy*, 2022, **323**, 119575.
- 483 C. Hemme and W. van Berk, *Appl. Sci.*, 2018, **8**, 2282.
- 484 B. Pan, K. Liu, B. Ren, M. Zhang, Y. Ju, J. Gu, X. Zhang, C. R. Clarkson, K. Edlmann, W. Zhu and S. Iglauer, *Fuel*, 2023, **333**, 126516.
- 485 P. G. Haddad, M. Ranchou-Peyruse, M. Guignard, J. Mura, F. Casteran, L. Ronjon-Magand, P. Senechal, M. P. Isaure, P. Moonen, G. Hoareau, D. Dequidt, P. Chiquet, G. Caumette, P. Cezac and A. Ranchou-Peyruse, *Energy Environ. Sci.*, 2022, **15**, 3400–3415.
- 486 M. Pichler, *EAGE/DGMK Joint Workshop on Underground Storage of Hydrogen*, European Association of Geoscientists & Engineers, 2019, vol. 2019, pp. 1–4.
- 487 L. Truche, M. C. Jodin-Caumon, C. Lerouge, G. Berger, R. Mosser-Ruck, E. Giffaut and N. Michau, *Chem. Geol.*, 2013, **351**, 217–228.
- 488 P. Amigan, M. Greksák, J. Kozánková, F. Buzek, V. Onderka and I. Wolf, *FEMS Microbiol. Ecol.*, 1990, **6**, 221–224.

